



UNIVERSIDAD PÚBLICA DE NAVARRA  
Departamento de Ingeniería Eléctrica y Electrónica  
*NAFARROAKO UNIBERTSITATE PUBLIKOA*  
*Ingeniaritza Elektriko eta Elektroniko Saila*



**MILLIMETER-WAVE EXTRAORDINARY TRANSMISSION:**

CONNECTION TO METAMATERIALS AND  
TECHNOLOGICAL APPLICATIONS

Tesis Doctoral realizada por / Doctoral Thesis by  
Miguel Beruete Díaz

dirigida por / supervised by  
Dr. Mario Sorolla Ayza

Pamplona, 2006

# CONTENTS

---

---

## Chapter 1.

<b>Introduction To Metamaterials .....</b>	<b>1</b>
1.1. Periodic structures .....	2
1.2. The arrival of photonic crystals .....	5
1.3. A surprising effect: Extraordinary Optical Transmission (EOT) .....	6
1.4. Light can reverse Snell's law: Left-Handed Metamaterials (LHM) .....	8
1.5. The pursuit of plasmonic circuits .....	11
1.6. Quasioptical systems and gaussian beam propagation .....	12
1.7. Outline of this document .....	13

## Chapter 2.

<b>Extraordinary Transmission Through Perforated Metallic Plates. ....</b>	<b>15</b>
2.1. Initial state-of-the-art: dichroic filters .....	16
2.2. Origin of the EOT phenomenon and controversy to explain it .....	18
2.3. Millimeter-wave range enhanced transmission: experimental validation of the perfect conductor model .....	21
2.3.1. Fresnel-zone illumination .....	23
2.3.2. Farfield illumination .....	27
2.4. Finite structure effects .....	31
2.5. Dichroic filters and EOT structures .....	35
2.6. Phase response of cut-off metallic hole arrays .....	38
2.7. Double periodicity structures on dielectric slabs .....	39
2.8. Concluding remarks .....	44
APPENDIX 2. Dispersive model of metals .....	45

## Chapter 3.

<b>Enhanced Transmission Through Slits In Corrugated Metallic Planes: Slit + Grooves Structures. ....</b>	<b>51</b>
3.1. Evolution from Ebbesen's experiment towards the understanding of metallic structured surfaces .....	52

3.2. Antecedents in microwaves: corrugated planes .....	54
3.3. Microwave range enhanced transmission and beaming .....	56
3.3.1. Transmission results .....	57
3.3.2. Beaming results .....	62
3.4. Millimeter-wave enhanced transmittance and reflectance: quasioptical illumination .....	65
3.5. Application to all-metallic low-profile antenna feeder prototypes based on "slit +grooves" structures .....	69
3.5.1. High gain and low profile "Slot + 12 grooves" antenna .....	71
3.5.2. Isotropic enhanced "Slot + 2 grooves" antenna .....	77
3.5.3. Towards a thinner metallic antenna .....	82
3.5.4. Dual-band antenna .....	88
3.5.5. High gain "Bull's-Eye" antenna .....	94
3.5.6. Dielectric loaded antenna .....	100
3.5.7. Further improvements: sinusoidal profiles .....	105
3.6. Concluding remarks .....	107

## **Chapter 4.**

### **Stacked Hole Arrays: Merging Photonic Crystals, Enhanced Transmission And Metamaterials In A Single Structure .....**

109

4.1. Introduction .....	110
4.2. Artificial waveguide approach to the hole array problem .....	111
4.2.1. Formulation of the problem .....	111
4.2.2. Simulation results .....	116
4.3. Left-handed propagation in the enhanced transmission band by stacking hole arrays .....	122
4.3.1. Dispersion diagrams: antiparallel phase and group velocities .....	123
4.3.2. Experimental results: LHM .....	126
4.4. EBG over ET band: RHM .....	129
4.4.1. Simulation results: Tuning RHM or LHM with the EBG .....	129
4.4.2. Experimental results: RHM .....	130
4.5. LHM- and RHM-ET: an intuitive explanation .....	132
4.6. Transition from RH to LH (zero group velocity) and other results .....	136
4.7. Gaussian beam compression: lens effect .....	144
4.8. Superprism or anomalous collimation .....	148
4.8.1. Prism in microwaves .....	150
4.8.2. Prism in millimeter waves .....	152
4.9. Parabolic lens .....	155

4.10. Equivalent circuit discussion .....	159
4.11. Metal-dielectric ( $\epsilon > 1$ ) stack .....	162
4.12. Concluding remarks .....	166

## **Chapter 5.**

### **Alternative Structures ..... 169**

5.1. Introduction: SRR, Babinet, bianisotropy .....	170
5.2. Metasurfaces .....	172
5.2.1. SRR/CSRR Metasurfaces under normal incidence .....	172
5.2.2. SRR/CSRR Metasurfaces under oblique incidence .....	178
5.2.3. Concluding remarks .....	190
5.3. Electroinductive waves .....	191
5.3.1. Dispersion relation and duality .....	191
5.3.2. Practical Implementation in planar technology .....	195
5.3.3. UWB filter based on EIW .....	197
5.3.4. Concluding remarks .....	198
5.4. Comparison with Extraordinary Transmission structures .....	199
5.4.1. Metasurfaces vs. Enhanced Transmission Structures .....	199
5.4.2. Electroinductive Waveguides vs. Stacked Hole Arrays .....	201

## **Chapter 6.**

### **Conclusions And Future Work ..... 203**

6.1. Conclusions ..	204
6.2. Future work .....	206

### **References ..... 209**

### **Author's Publications ..... 223**

# Chapter 1

## Introduction To Metamaterials.

---

---

*Three discoveries have altered the state of the art of electromagnetic radiation research over the last years. First, the concept and realisation of photonic band-gap (PBG) structures opened up new original approaches for the control of light flow and confinement with great technological consequences.*

*Second, the demonstration of extraordinary optical transmission (EOT) through sub-wavelength hole arrays and other structures provided the basis for using subwavelength apertures for a variety of potential applications.*

*Third, Negative Refractive Index (NRI) refreshed the classical electrodynamics field by introducing highly unusual properties – so-called left-handed metamaterial (LHM)- leading to a new class of devices.*

*In this chapter a short introduction to these topics is given and some subjects that will be extensively treated in subsequent chapters are briefly advanced. Moreover, the thesis fundamentally deals with phenomena occurring at millimeter wave frequencies, where the gaussian beam formalism fits accurately. Thus, the quasi-optics concept is succinctly presented.*

## 1.1 Periodic structures

The properties of periodic structures have fascinated researchers of many fields for quite some time. A very interesting historical description can be found in the work by Leon Brillouin [BRIL 46], devoted to the analysis of such structures applied in a general fashion. The initial studies were conducted by Netwon in the XVIII century, motivated by the need to obtain a formula that could adequately describe the speed of sound in a medium. To do so, Netwon modeled this problem as an elastic wave that was propagating in a medium of localized point masses, as depicted in Fig. 1.1:

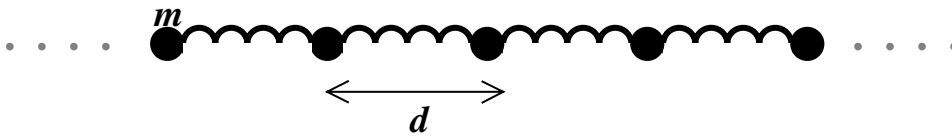


Fig. 1.1. Initial system of point masses  $m$ , linked by springs of length  $d$ .

From the previous model it is possible to obtain the velocity of sound as:

$$v = d \sqrt{\frac{e}{m}} \quad (1.1)$$

where  $d$  is the distance between adjacent particles,  $e$  is the elastic constant of the springs and  $m$  is the mass of the point source. Such a model was chosen since at that time, partial derivatives were unknown, not allowing to solve the continuous problem.

Further research was conducted by Daniel and John Bernouilli, in one dimensional lattices with  $n$  point masses. They showed that such a system has  $n$  proper frequencies (also known as eigenfrequencies), which can be seen as a special case of the Fourier series, as would be shown later on.

The first attempt to solve the continuous problem was performed later on by Euler, by using partial derivatives to solve the case of a vibrant string. This would generate a great deal of controversy, since at that time (until the demonstration in 1807 of Fourier's Theorem), Euler would not accept the fact that any arbitrary time-space function could be represented by the superposition of sinusoidal functions. It must be stated in this sense that Lagrange, who in 1759 analyzed the problem of a network of

point masses, did not accept the postulates proposed later on by Fourier.

In the XIX century, great deal of activity went on in pursuing knowledge of periodic systems. In 1830, Cauchy uses Newton's model to take into account dispersion of an optical wave. In 1841, Baden-Powell calculated the propagation velocity in an axis of a cubic lattice, as a function of the wavelength. In this analysis, however, frequency did not have a dependence with the wavelength, missing an important factor. This was taken into account in 1881 by Lord Kelvin, introducing a very important concept: the cut-off frequency. Later on, Lord Kelvin tried to obtain a dispersion theory using a more complex model than the initial one proposed by Baden-Powell, which introduces a new elastic constant in the system. This way, the amount of proper frequencies of the system is twice of those stated in the initial case.

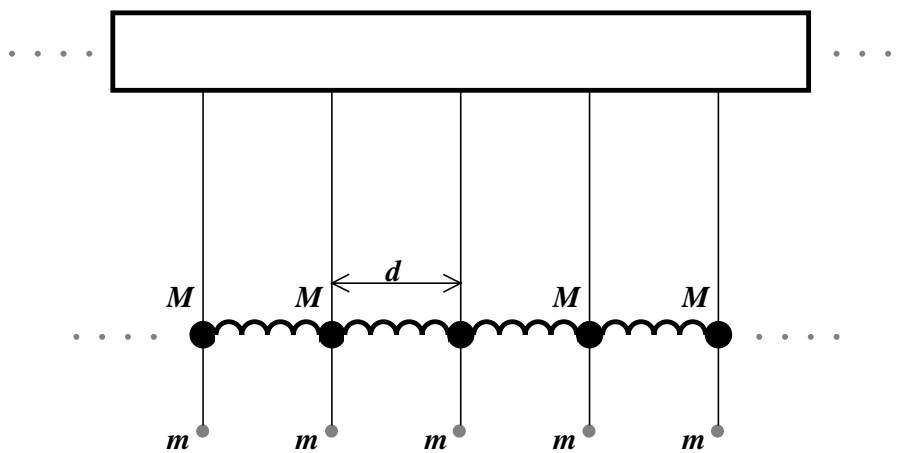


Fig. 1.2. Schematic of the mechanical system proposed by Vincent, based on Lord Kelvin's Model.

The first experimental filter was fabricated by Vincent, based on Lord Kelvin's Theory. It consists on a mechanical system of suspended masses, which are linked one another by springs. Another small mass is attached to the initial mass with the aid of another spring. The system, which is considered a mechanical filter, is schematically depicted in Fig. 1.2.

The first high pass filter was fabricated by Campbell in 1906, after synthesizing several band pass structures, analogous to those obtained by Vincent with the mechanical model. A schematic of the very well known lumped L-C implementation is shown in Fig. 1.3.

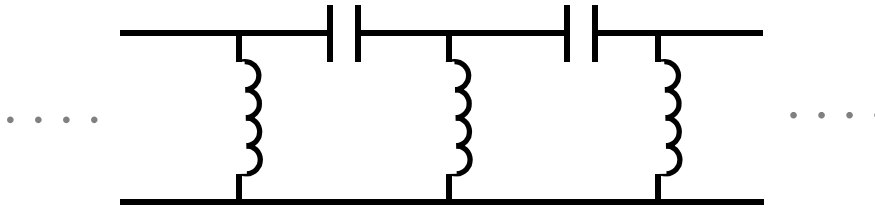


Fig. 1.3. Schematic of the High pass electrical filter implementation proposed by Campbell in 1906.

In 1912 Born investigates the propagation of waves in crystals, rediscovering the previous analysis performed by Lord Kelvin. As a consequence, two branches are clearly observed in the dispersion relation. Generally, the bottom branch is termed the acoustic branch, whereas the upper one is called the optical branch.

In the early 20<sup>th</sup> century, in the determination of blackbody thermal radiation, Planck came up with the following statement: any physical entity with one degree of freedom, whose coordinate is a sinusoidal function of time (i.e., performs simple harmonic oscillations), can only have total energies  $E$  that satisfy the following relation:

$$E = nh\nu \quad (1.2)$$

where  $n$  is a natural number,  $\nu$  is the frequency of oscillation and  $h$  is a universal constant called the Planck constant. Such a discovery led a quarter of a century later to the principles of quantum theory, which have revolutionized modern physics. Later on, in 1905, Einstein, based on Planck's research, proposed a quantum approach to the photoelectric effect, stating that radiating energy does so in quantized packets, which have come to be known as photons. Actually, the photon hypothesis is applied in all the EM spectrum.

In 1923 the corpuscular nature of radiation was confirmed with the experiments performed by Compton. Measuring scattered Bragg reflection from X-ray sources (the precursor of X-ray crystallography, as an extremely valuable tool to analyze the fine structure of matter, as well as the study of order disorder, among others [WARR 90]). In 1924 Louis de Broglie proposed the existence of waves in matter, which was experimentally validated in 1927 by G.P. Thomson.

## 1.2 The arrival of photonic crystals.

The advent of quantum physics gave rise to a great deal of practical devices. Among them, semiconductors have proved to be of extreme usefulness, as the control of electrons is the key of microelectronic components.

Semiconductors are responsible for the digital revolution. With the discovery of the diode and the transistor, integrated chips were just one step away. However, communication systems are everyday more demanding, requiring higher speeds. A few examples are D-WDM (dense wavelength division multiplex) optical transport systems, DXX (digital cross connect) intelligent core networks for mobile operators, optical computing, etc. The common factor is the need of optical sources in order to sustain the increase in bandwidth; also, optical transitions are much shorter than electronic ones, leading to much faster systems. Therefore, it would be appealing to achieve optical processors, based on optical diodes and transistors.

Such control of light, however, is not possible with materials readily available in nature. It is necessary, therefore, to artificially synthesize an optical equivalent of a semiconductor. In the late 1980's, Yablonovitch stated the advantages of a material that could inhibit spontaneous emission from laser sources, increasing quantum efficiency [YABL 87]. By doing so, communication links could be longer, due to the increase of stimulated radiation from the source. The motivation is to compare the propagation of EM waves in artificially created three-dimensional dielectric structures and the behavior of electrons in crystal structures found in nature. The reason is that a frequency band gap can appear where the propagation of EM waves is inhibited in all directions in space. In analogy to semiconductor physics, such frequency range is called a Photonic Bandgap (PBG). As stated earlier, the main purpose of such a medium is to limit spontaneous emission from light. This phenomenon is a key player in the following processes [YABL 93]:

- Spontaneous emission is a sink for the threshold current in a semiconductor laser, needing to be surpassed in order to initiate lasing.
- It determines the heterojunction bipolar transistor current gain in certain regions of its voltage current characteristic.
- It determines the maximum available output voltage in solar cells.
- It determines the degree of photon number state squeezing (it is known

that a decrease in the quantum efficiency for the lasing mode implies noise reduction in the squeezing process).

Control over spontaneous emission has been indirectly studied since the mid 40's, in the analysis of nuclear spin levels performed by Purcell. Later on, periodicity of a coaxial transmission line was also studied in that sense, as well as the Rydberg atom experiments described by Kleppner (performed with the aid of a couple of metal plates). The revolutionary step was taken several decades later, when the possibility of artificially synthesizing PBG structures was described [YABL 93] [YABL 93b], as well as the analysis of localized modes in PBG structures, with the straightforward mention of the phenomenon as "frozen light" [JOHN 87].

The main difficulty in the task of synthesizing PBG structures was that the resolution of the fabrication process had to be smaller than the operating wavelength of device. If the optical regime is considered, this implies microns or less. It is interesting to note, however, that the electromagnetic properties of PBG structures scale with frequency [JOAN 94]. Therefore, similar properties can be expected in dimensions of the structure are all up or downscaled. If the scale is made larger, the inhibited frequency range will be present at smaller values. The main advantage is that tolerances will be less critical, allowing better experimental validation of the devices. Therefore, prototypes of PBG structure in the optical regime can be tested in the microwave and millimeter wave range. This has another advantage, which is the possibility of developing novel devices in this lower frequency range. From this point on, great deal of research work has been performed in the microwave and millimeter wave range, coming to be of interest without the need of considering smaller wavelengths, some of which will be stated along this work.

### **1.3 A surprising effect: Extraordinary Optical Transmission (EOT)**

The first studies of transmission through apertures much smaller than the wavelength were carried out by Lord Rayleigh in the end of the 19<sup>th</sup> century. It was Bethe who finally developed an exact analytic expression for a small hole in an infinite metallic screen with infinite conductivity. Bethe showed that under normal incidence, transmittance is proportional to  $(r/\lambda)^4$ , where  $r$  is the hole radius. Later, Bouwkamp extended Bethe's analysis including higher order terms in the expression of the

transmission [BOUW 50], [BOUW 54].

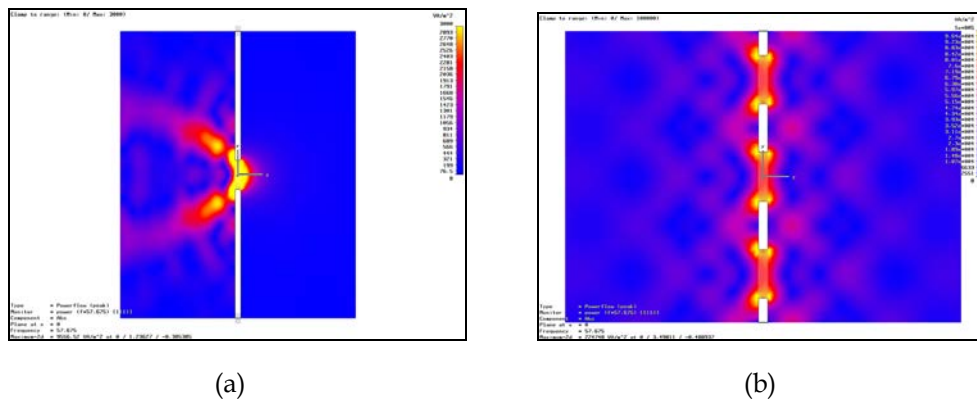


Fig. 1.4. Coupled power profile cross-section: through a sub-wavelength hole (a) and through an enhanced transmission structure (b). Note the different pattern in both cases.

Later on, in 1998 Ebbesen and co-workers reported an intriguing experimental result concerning silver plates perforated with periodic hole arrays [EBBE 98]. They observed an anomalous high transmission peak in the cut-off region of the holes that was about 4 or 5 times greater than the prediction expected following the classical Bethe-Bouwkamp theory. A graphical picture is given in Fig. 1.4. It has been simulated with the full-wave electromagnetic commercial solver *CST Microwave Studio™* the cases of single hole in an infinite perfectly conducting metallic screen (Fig. 1.4(a)) and the case of a structure similar to Ebbesen's (Fig. 1.4(b)). In both cases  $(r/\lambda) \approx 0.25$ . It is observed an improvement in transmission with the hole array compared to the single hole.

This phenomenon was called Extraordinary Optical Transmission (EOT), as the experiment was realized in the optical frequency range. Many theoretical as well as experimental studies were to follow this first result, and other structures were explored in order to observe anomalous transmittance peaks.

For instance, a research line studied the transmission across a narrow slit array on a metallic plane [TREA 99], [TREA 02]. The features observed in that structure were similar to the reported EOT, although the electromagnetic behavior of slits and holes is essentially different: slits always support a propagating mode, while holes have a cut-off frequency. However, an interesting path was opened when the slit array was replaced by a single slit on a texturized (corrugated) plane. A strong beaming and

transmission enhancement was observed [LEZE 02], [GARC 03].

All the experimental results were first obtained at optical wavelengths, and thus they were first identified as inherently linked to the metal behavior in optics, which is very different from a metal at, say, microwaves. Later on, similar experimental results were to appear at microwaves and millimeter waves frequencies.

## 1.4 Light can reverse Snell's law: Left-Handed Metamaterials (LHM)

Another research line that has been lead with great intensity is the search for metamaterial structures, i.e., materials which exhibit non-conventional electromagnetic properties.

In the late 60's, Veselago [VESE 68] studies the properties of a material with simultaneous negative dielectric permittivity as well as negative magnetic permeability. Surprising physical phenomena were predicted:

- Antiparallel phase and group velocities: when  $\epsilon, \mu < 0$  then it can be shown that vectors  $\mathbf{E}$ ,  $\mathbf{H}$  and  $\mathbf{k}$  form a left-handed triplet, instead of the conventional right-handed triplet of standard media. For this reason, this kind of media is usually referred to as Left-Handed Media or Left-Handed Metamaterials (LHM). This has been depicted schematically in Fig. 1.5. Notice that Poynting's vector  $\mathbf{S}$  always points in the same sense, since this is the sense of energy propagation.
- Negative refraction, or Snell's law inversion: in the interface between a standard RHM and a LHM metamaterial, the transmitted ray crosses the normal in an anomalous manner. This is due to the fact that the index of refraction  $n$  is negative; i.e.  $n = c/v_{phase}$ ;  $c$  is the velocity of light in vacuum which follows the right-hand rule. As  $v_{phase}$  is in the opposite sense, then  $n < 0$ . Applying now Snell's law,  $n_1 \sin(\theta_1) = n_2 \sin(\theta_2)$ , it is readily seen that if  $\text{sgn}(n_1) = -\text{sgn}(n_2)$  then  $\text{sgn}(\theta_1) = -\text{sgn}(\theta_2)$ . This is plotted in Fig. 1.6.
- Inversion of Doppler effect and inversion of Cerenkov radiation, see Fig. 1.7.

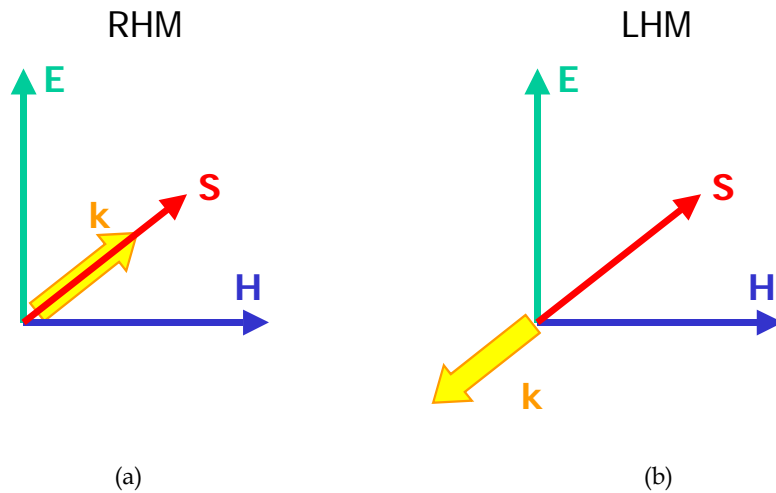


Fig. 1.5. (a) Electric field, magnetic field and wave vectors form a right-handed triplet in a standard media. (b) This triplet is left-handed in the media described by Veselago. Note that Poynting vector is always in the same direction.

Even though of great scientific interest, the lack of materials with  $\epsilon, \mu < 0$  in nature supposed a great drawback. The synthesis of a negative electric permittivity was feasible by that time, for example by means plasmas or a metal at optics frequencies. Negative values of magnetic permeability in contrast were not attainable. It was in 1999 when Pendry [PEND 99] proposes for the first time a particle which can give a negative magnetic response in a certain frequency range: the Split-Ring Resonator (SRR) depicted schematically in Fig. 5.2(a).

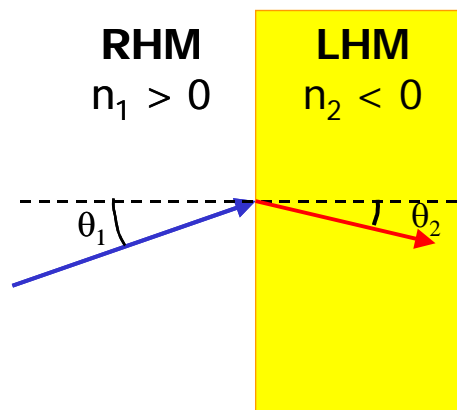


Fig. 1.6. Sketch of the Snell's law reversal in the interface between a standard medium and a left-handed medium. The transmitted ray crosses the normal.

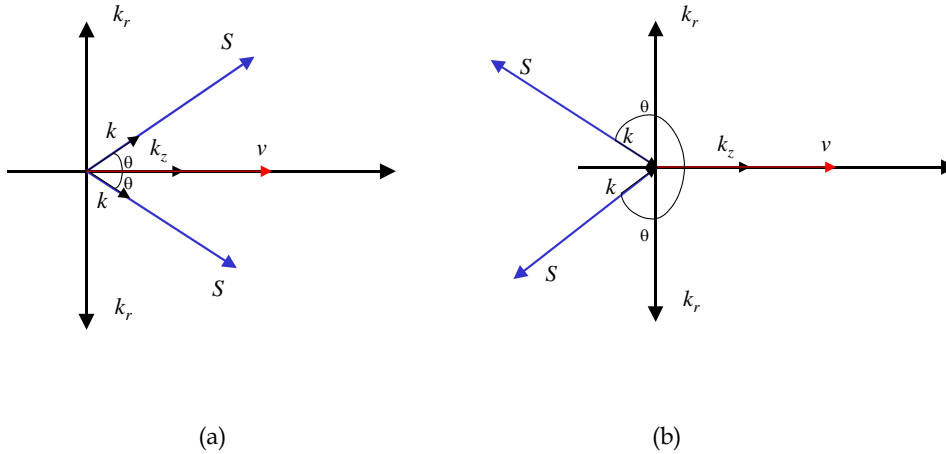


Fig. 1.7. Representation of the radiation of a particle in a RHM (a) and the same effect in an LHM (b).

The first medium showing simultaneously negative values of permittivity and permeability was developed in the next year by Smith et al. [SMITH 00] by using a mixture of metallic wires ( $\epsilon < 0$ ) and split-ring resonators ( $\mu < 0$ ). From that point on, a great number of publications has been devoted in the analysis of the properties of this type of medium, as well as practical implementations, in volumetric and in planar technology [FALC 05], taking advantage of the subwavelength scaling of these new structures in contrast with PBG's.

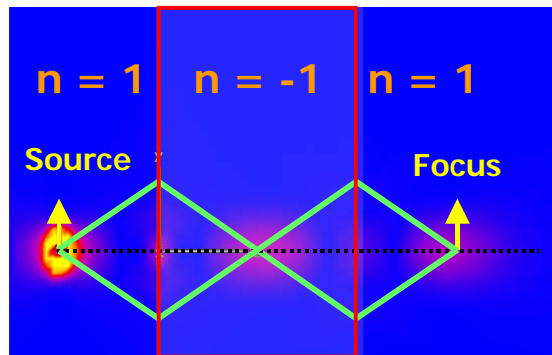


Fig. 1.8. Schematic of the focusing phenomenon when rays transverse a slab of LHM material. Due to the negative angle of refraction, rays tend to focus after passing through the RHM-LHM interface and the LHM-RHM interface. This holds true also for evanescent waves, where an amplification process also takes place. The ray tracing is superimposed to simulation results obtained with *CST Microwave Studio™*.

An interesting consequence of the negative refraction concept is the possibility to obtain a “perfect lens” by means of evanescent field amplification, as proposed by Pendry in 2000 [PEND 00]. This feature is schematically depicted in Fig. 1.8. As it has been stated previously, a negative value in the refractive index leads to bending of the propagating ray in a negative angle with respect to the RHM. This, of course holds true in an RHM-LHM interface and an LHM-RHM interface. Suppose that the red dot at the leftmost side is a point source, parting from a conventional RHM medium, for example vacuum. On its propagation path there is a LHM, with an index of refraction  $n_{LHM} = -1$ . If the media are impedance matched there will be no reflected ray, only transmission. The transmitted rays will be deflected corresponding to the change of sign in each one of the interfaces. The final result, depicted in Fig. 1.8, is that focusing is possible at the rightmost side of the system. Another important issue is that this type of “lens” is capable of sublambda focusing, since the evanescent field can be ideally recovered by virtue of the negative sign of the refractive index, which affects to all the spectral components, i.e. propagating as well as evanescent. As a consequence there is amplification of evanescent waves and perfect image reconstruction.

## 1.5 The pursuit of plasmonic circuits.

The development of electronics provided the ability to control the transport and storage of electrons, making possible the birth of microprocessors and personal computers. Nowadays ultrafast transistors are being used within a scale on the order of 50 nm. The production of transistors is a routinary task, but there is a major problem in the trasport of digital information from one point of a microprocessor to another that might be a few centimeters away. Traditionally, interconnections have been made by copper or gold wires. However the number of transistors in a chip grows exponentially and makes the interconnection increasingly complex. Moreover, unlike transistors for which performance improves with downscaling, the delay of interconnects increases and constitutes a major drawback in the speed of digital circuits [KOBR 04].

Fiber optic cables offer a great information speed and capacity more than a thousand times that of electronic interconnects. Unfortunately, their size is in the order of microns, i.e. approximately one thousand times larger than electronic components. This makes very difficult to integrate both technologies in the same circuit. The best solution would be a circuit with nanoscale features able to transport optical signal as

well as electric currents. This constitutes the core motivation of the *plasmonic circuit*. This nomenclature emerges from a special kind of surface wave called *plasmons*. These waves exist in the interface of a conductor at optics frequencies and a dielectric, say air. The interaction of light with matter in nanostructured metallic structures has led to a new branch of photonics: the plasmonics. Plasmonic circuits offer the potential to carry optical signals and electric currents along the same thin metal substrate, giving as a result the ability to combine the best qualities of photonics and electronics on the same chip [OZBA 06].

## 1.6 Quasioptical systems and gaussian beam propagation [GOLD 98].

Quasioptics deals with the propagation of a beam of radiation that is reasonably well collimated but has relatively small dimensions when measured in wavelengths, transverse to the axis of propagation. Quasioptics describes the situation between the two limiting cases of geometrical optics, where  $\lambda \rightarrow 0$ , and diffracting systems where  $\lambda \cong$  system dimensions. Within the geometrical optics formalism, propagation is described with a ray, representing a perfectly directed bundle of radiation. On the other hand, diffraction is the tendency for radiation from a source, to change its distribution as the distance from the source varies. Quasioptics permits the description of the intermediate situation and includes the case of a beam of radiation whose diameter is only moderately large in units of wavelength. Then, the theory of Gaussian beam modes and Gaussian beam propagation can be employed.

The systems used at radio and microwaves are usually monomode. The technologies utilized range from coaxial cables (TEM mode), metallic waveguides (usually in its fundamental mode operation), and 1D planar guides such as microstrip, stripline and coplanar waveguides (working in TEM or quasi-TEM modes). These systems employ metallic conductors and/or dielectric slabs to obtain the desired field configuration. A clear drawback of these technologies for its use at millimeter wave frequencies is that the power loss per unit length of dielectric materials generally increase at a rate at least as fast as proportional to the square of frequency. For a metallic waveguide loss increases as (frequency)<sup>1.5</sup>.

Therefore, losses limit the application of usual microwave technology in the scaling to millimeter waves. The essentially lossless nature of electromagnetic radiation

propagation in free space make this possibility very attractive in this range. However, in order to consider the system purely optical ( $\lambda \ll$  system dimensions) the size of the apertures and components must be extremely large, which turns out to be impractical. Quasioptical propagation using gaussian beam offers a solution to the problem of propagation radiation beams that are not large in their transverse dimension measured in units of wavelength.

## 1.7 Outline of this document.

The main aim along this Thesis has been to upscale intriguing experimental results obtained at optics wavelengths to the microwave and millimeter-wave wavelengths. The success in the obtained results has boosted the research in these ranges towards new structures and ideas that can possibly find the reverse way to exciting applications at optical wavelengths. With that aim in view, the following five chapters represent the central part of the text:

**Chapter 2** deals fundamentally with the experimental proof of Extraordinary Transmission through subwavelength hole arrays in the millimeter wave range. It was in this range where the systematic study of the structure size was first published. A short study of the phase response and of hole arrays on dielectric slabs are also presented.

**Chapter 3** is devoted to the experimental study of enhanced transmission through narrow slits on corrugated planes, in microwaves and in millimeter waves. Also, several flat antenna feeder prototypes based on the same phenomenon are described and measured.

**Chapter 4** tells what happens when several ET subwavelength hole arrays are stacked. It will be seen that LHM, PBG and ET can exist in a single structure. A variety of responses can be obtained by just tuning the stack period. Simulation as well as experimental results are given. A simplified equivalent circuit model is developed to explain the effects observed. Several simulation results bring forward experimental measurements that at present are in progress.

**Chapter 5** presents other works done in other hot topics of electromagnetics. Metasurfaces made of split-ring resonators and its complementary are analyzed, simulated and measured. Also, electroinductive waves in chains of resonators are

studied, and planar prototypes are constructed and measured. Possible connections with the results presented in the previous chapters are outlined.

Finally are presented the main **Conclusions** of the thesis and **Future work** opened and in progress.

# Chapter 2

## Extraordinary Transmission Through Perforated Metallic Plates.

---

*After the first report of Extraordinary Optical Transmission (EOT) in the cut-off region of perforated metallic plates given by Ebbesen, a great research interest was devoted to the subject. Big effort was in the elucidation of a plausible theory of the unexpected phenomenon.*

*Two fundamental lines were followed: the plasmonic hypothesis, where plasmons (a special kind of surface waves supported in the interface of a dielectric, say air, and a metal at optical frequencies) were given a prominent role in the high transmission observed; the other hypothesis ascribed the phenomenon mainly to the periodic structure, regardless of the metallic model used for the plate. Wood's anomalies were found to play an important role. This allowed for the replica of the phenomenon in other regions of the electromagnetic spectrum where plasmons are not supported. Furthermore it was claimed that Extraordinary Transmission (ET) could be attained with a most ideal and simple Perfect Electric Conductor (PEC) model.*

*In this chapter several experimental results of ET in the millimeter-wave range are presented. This constitutes a definitive proof of the hypothesis relating ET to Wood's anomalies. Moreover, it is advanced with the measurements the great significance on the transmittance of the number of illuminated holes. A comparison with other well-known structures is presented, and the differences are highlighted. Finally short comments about the phase of the transmission coefficient are given.*

## 2.1 Initial state-of-the-art: dichroic filters.

Dichroic filters or perforated plates can be considered as periodical structures fabricated of relatively close-packed waveguides drilled in a metallic substrate, see Fig. 2.1(a). The basic operation principle is described by Goldsmith [GOLD 98]: for a frequency below the cut-off frequency of the waveguide the power is essentially reflected, while above the cut-off frequency power is largely transmitted. The perforated plate was first analyzed in detail by Robinson [ROBI 60]. Chen presented the first paper [CHEN 73] dealing with the theory of microwave transmission through perforated plates of finite thickness. There he considered four different cases: circular and square openings in equilateral triangular and square lattices. He restricted the analysis to relatively big holes and dense arrays:  $a > 0.56d$  and  $d > 0.5\lambda$  for the case of circular openings in square lattices. Here  $a$  is the diameter of apertures and  $d$  is the spacing. The thickness of the plate  $w$  can be regarded as the length of a closed metallic waveguide. Transmission through arrays of holes has also been experimentally studied in other frequency ranges as in the far infrared [ULRI 67], mid infrared [RHOA 82] and infrared [KEIL 81] ranges.

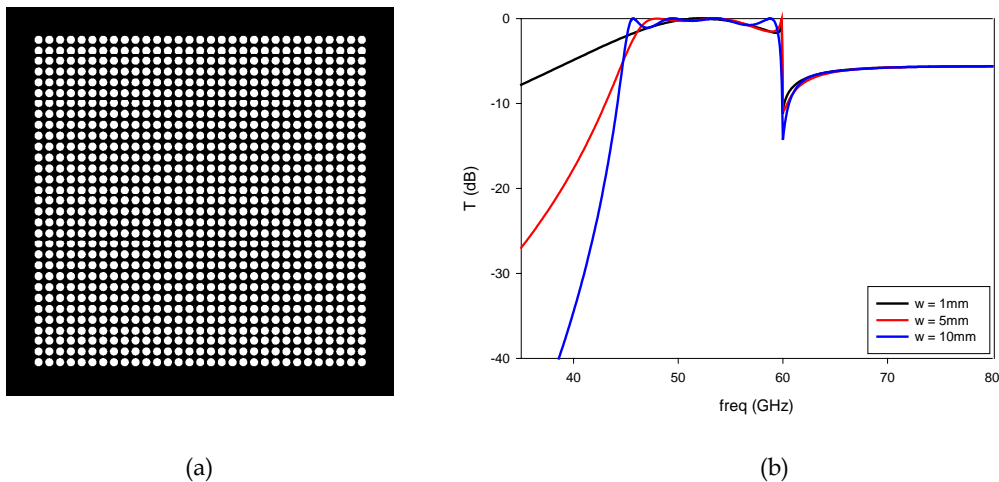


Fig. 2.1. Dichroic filter schematic (a) and frequency response for various waveguide lengths (b). The parameters of the structure are: hole diameter  $a = 4$  mm, lattice constant  $d = 5$  mm. As the thickness  $w$  increases, the slope of the lower band limit increases and also the ripple in the passband.

Dichroic filters are typically used as Frequency Selective Surfaces with a bandpass

response. Following the classical treatment, the low cut-off frequency is given by the hole electromagnetic cut-off, whereas the high cut-off frequency is due to the redistribution of energy caused by the periodic array when a new diffraction order becomes propagating, i.e. is determined by periodicity. A simplified model proposed by Goldsmith [GOLD 98] reduces the analysis to a transmission line problem. The waveguide is represented as a series admittance  $Y$  and the discontinuity between the guide and free space is modelled with a shunt admittance  $Y_s$  at each end of the perforated plate.

Under this formalism, the choice of the hole diameter, and thus the cut-off frequency, determines the basic form of the frequency response: transmission above the cut-off frequency is fairly close to unity with some response ripples in the pass band while below the cut-off frequency, the transmission drops sharply. Plate thickness has two major effects, see Fig. 2.1(b). First, the rate at which the transmission drops with frequency below the cut-off increases as the plate thickness increases. This may be very desirable for certain applications where a well-defined passband is required. Second, the period of the ripples in the pass band decreases as the plate thickness increases, as a result of increased electrical length between the guide - free space discontinuities.

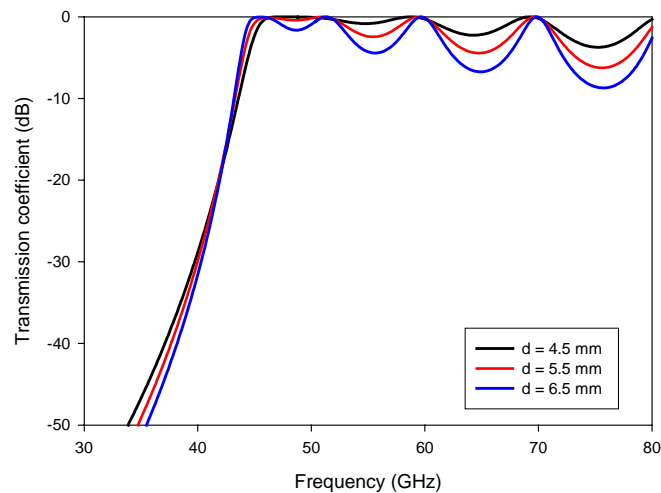


Fig. 2.2. Transmission coefficient of a perforated plate with with hole diameter  $a = 4$  mm, metal thickness  $w = 10$  mm and three periods:  $d = 4.5$  mm (black curve), 5.5 mm (red curve) and 6.5 mm (blue curve). The ripple in the band increases as the guide spacing is increased.

A very important parameter is the spacing of the waveguides, which affects the shunt reactance  $Y_s$ . The basic rule of thumb is given by Goldsmith [GOLD 98]: As the guide spacing is increased the magnitude of the shunt reactance increases which results in a greater discontinuity and more pronounced ripple responses, see Fig. 2.2 where the transmission coefficient for a perforated plate with hole diameter  $a = 4$  mm and metal thickness  $w = 10$  mm has been computed for three different periods:  $d = 4.5$  mm (black curve), 5.5 mm (red curve) and 6.5 mm (blue curve), using the simplified model given in [GOLD 98]. This is undesirable, and for this reason dichroic filters normally consist of very dense hole arrays. As Goldsmith points out, this approach inherently ignores diffraction which is only acceptable if the waveguide spacing is small enough relative to wavelength. In the next sections it will be seen that this restriction is of major importance in the description of extraordinary transmission phenomena. It will be shown that when diffraction is taken into account, this basic model is insufficient to compute the response of sparse hole arrays. Moreover, the upper cut-off frequency shown in Fig. 2.1(b) is intrinsically related with dynamical diffraction, and thus, it does not appear in Fig. 2.2 in which the simplified model has been used. It is the so called Rayleigh-Wood's anomaly [WOOD 02], [RAYL 07], which appears in every periodic structure and that for normal incidence emerges at  $\lambda = d$ . A discussion about the limitations of the simplified model proposed by Goldsmith is given in section 2.5.

## 2.2 Origin of the EOT phenomenon and controversy to explain it.

Back in 1998, Ebbesen and co-workers reported for the first time the existence of high transmittance peaks in the cut-off region of perforated silver plates [EBBE 98]. This phenomenon was called Extraordinary Optical Transmission (EOT), because the experiment was developed in the optical range. A metal in optics exhibits a plasma-like behavior, i.e. there are free-electron charges not bound to molecules which can be modelled as a plasma cloud in the same way as the constituent particles in a gas at high temperature. In electromagnetics, a plasma is characterized for having a permittivity with negative real part,  $Re\{\epsilon\} < 0$ . It is well known that the interface between a standard dielectric ( $Re\{\epsilon\} > 0$ ) and a plasma-like medium ( $Re\{\epsilon\} < 0$ ), supports a singular kind of surface wave, the so-called *surface plasmon* [ISHI 91] (For a full description see Appendix 2 at the end of the chapter). Therefore, in a first approach, Ebbesen's report gave surface plasmons a key role in the origin of EOT. In

his own words, “the experiments provide evidence that these unusual optical properties are due to the coupling of light with plasmons”. In a subsequent work [GHAE 98], the same team find more statements which seem to support the causative role of SPPs in the process of transmission enhancement: “the maxima are the result of a resonant excitation of surface plasmons (SP’s)”. Following the analysis of sub-wavelength hole arrays [KIM 99] that group mentions for the first time the relation of the phenomenon with Wood’s anomalies: the minima of transmission are identified with these anomalies due to diffraction. The transmission maxima are still related to surface plasmons.

The experiment was a catalyst for many theoretical and experimental studies. As early as in 1999, Treacy proposed a theoretical model related with dynamical diffraction [TREA 99]. He explained EOT in terms of Bloch waves and argued that propagating diffracted beams and surface plasmons are both part of the same dynamical scattering process. He restricted the two-dimensional hole array problem to the “equivalent” one-dimensional slit array which catches some of the physics of the hole array problem but not all. The reason is that there is a fundamental difference between slits and holes: a slit can always support a transverse electric and magnetic (TEM) wave with no cut-off, while in a hole waveguide there is a cut-off frequency. In 2000, Avrutsky and co-workers [AVRU 00] communicated the first theoretical model presenting quantitative results which, to some extent, can reproduce EOT. They interpreted the phenomenon as *plasmon-assisted light tunneling*. An interesting conclusion of this work is that it predicts extraordinary transmission even without the presence of holes, but only periodicity in the interface corrugation. In the same year Grupp et al. [GRUP 00] described what they interpret as an experimental evidence of the surface plasmon causative character in EOT: they observed that hole arrays in nickel supported relatively weak transmission anomalies, but when the substrate was coated with a relatively thin layer of silver on the top and bottom surfaces, the transmission anomalies increased significantly. Since only the surfaces were modified, it was reasoned that surface plasmons should be responsible.

By the end of the year Popov et al. communicated the first fully three-dimensional (3-D) theoretical study of EOT in hole arrays [POPO 00] and almost concurrently Martín-Moreno et al. presented another alternative 3-D model and contributed with an analytical minimal model [MART 01]. The conclusions of these two works were different: whereas in [POPO 00] EOT was assigned to an essentially propagating mode appearing in the hole array which exists only when a realistic dielectric constant

for the metal is considered, in [MART 01] EOT was ascribed to tunneling through surface plasmons formed on each metal-dielectric interface. This work was still connected with the surface plasmon formalism: EOT is attributed to the resonant coupling of the incident plane wave to surface plasmon polaritons (SPPs) thus establishing that "surface plasmons have the ability to transmit and focus light very efficiently". However, the model will be found to have more general application and to be able to extend EOT results to other frequency ranges where surface plasmons cannot exist (see section 2.3).

At the end of 2001, Vigoureux developed another interesting theoretical approach which interpreted Ebbesen's results under the formalism of evanescent short range diffraction [VIGO 01]. This manuscript established for the hole array case the first tentative basis of the approach initially drawn by Treacy for slit arrays. He argued that second order diffraction can reasonably explain the high transmittance seen in EOT experiments: Invoking reciprocity, if a propagating wave impinging a diffracting screen can be diffracted into evanescent waves the reciprocal must also be true. In other words, the incident wave is scattered in evanescent modes which can be converted into homogenous propagating waves when diffracted again. Almost immediately appeared a paper by Krishnan and co-workers (Ebbesen and Martín-Moreno amongst them) [KRIS 01] that studied the influence of the dielectric on either side of the perforated plate. They insisted on the interpretation of the phenomenon as plasmon assisted and obtained highest transmission when input and output dielectrics were matched. In the beginning of the next year, Cao and Lalanne threw the first caution about the actual role of plasmons [CAO 02]. They analyzed slit arrays and found that high transmittance was mainly due to waveguide mode resonance and diffraction. The more surprising conclusion was that the transmittance fell off to nearly zero for frequencies corresponding to surface plasmon excitation. This seemed to imply that surface plasmons actually played a negative role in the transmission. With the examination of the same slit array structure, Treacy presented later his paper [TREA 02] where he extended the initial ideas outlined in his former work [TREA 99] and reinforced in [VIGO 01] and [CAO 02]. He presented a unified explanation of *enhanced transmission phenomena* (generalised denomination of the original EOT) using diffraction concepts. He defended that surface plasmons do not play an independent causal role in EOT and rather they are an intrinsic component of the diffracted wave field. Anyway the aforementioned inconsistency between slit (no cut-off) and hole

arrays is still applicable. A further step in this direction was the work of Sarrazin et al. [SARR 03], where they attributed the enhanced transmission phenomena to the coupling between the incident plane wave and resonances supported by the perforated plate. These resonances are the so-called *resonant-Wood anomalies* [HESS 65], which may occur on any metal-dielectric plate that supports a slow wave when loaded by an appropriate grating. Notice that this interpretation implicitly recognizes the possibility to extend EOT to other frequency ranges. Soon after, Lomakin and co-workers extended the theoretical studies in a series of papers where they investigated in depth the finer details of the structures [LOMA 04], [LOMA 05]. An illuminating description of the hole array machinery was given in [BERU 05]: *The holes in the perforated plates have triple functionality. First, they support surface waves. This is easily recognized by considering a dense hole array, i.e one with  $d < \lambda$  where  $\lambda$  is the wavelength of the incident field. The fields on each face of the perforated plate approximately satisfy an inductive impedance boundary condition. Inductive impedance surfaces support TM surface waves; the same therefore holds true for the EOT perforated plate. Second, the holes provide a channel that allows for coupling between the two sides of the plate by means of evanescent hole fields. Third, the periodic grating formed by the holes allows the incident wave to be scattered into an infinite number of diffraction (Floquet) modes. Cross coupling between these modes gives rise to resonant- and Rayleigh-Wood anomalies.*

Finally, a closing observation about the different theoretical models should be done: although different in the approach, all of them implicitly incorporate elements of each other, and produce essentially identical predictions. Actually, one of the first of the aforementioned theoretical models which was proposed by Martín-Moreno and collaborators also predicts EOT even in the case of Perfect Conductor Metal. To verify this conjecture is the subject of the upcoming section.

## **2.3 Millimeter - wave enhanced transmission: Experimental validation of the perfect conductor model.**

The interpretation of the enhanced transmission phenomenon as mainly ascribed to the periodic array rather than to the substrate metal model has strong implications in the application to other frequency ranges where plasmons cannot exist. In this sense the experimental proof of enhanced transmission through sub-wavelength hole arrays

in the millimeter wave range, where metals admit a completely different description, is important in two aspects: First, it is a conclusive evidence of the perfect conductor hypothesis, thus giving a substantial evidence of the non-causative role of SPPs to obtain EOT; second, it paves the way to a rich variety of quasioptical devices such as Frequency Selective Surfaces, polarizers, antenna radomes, near-field imaging systems and so on, still unexplored in these frequency bands for the simple reason that nothing was expected beyond cut-off.

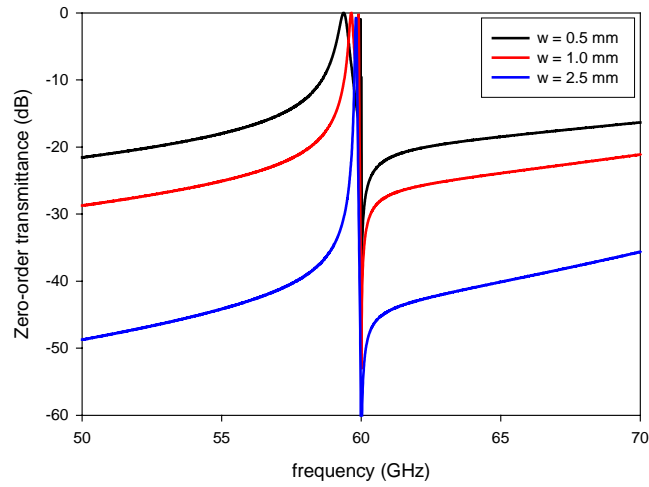
It is well known that a metal in the microwave and millimeter-wave range can be considered a good conductor, which can be defined as one that follows Ohm's law; displacement current is negligible compared to conduction current and the next relations can be admitted:

$$\mathbf{J} = \sigma \mathbf{E}$$

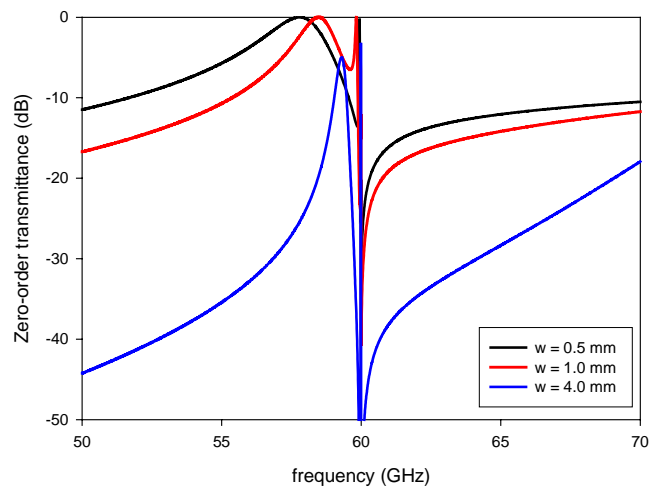
$$\varepsilon_r = 1 - j \frac{\sigma}{\omega \varepsilon_0}$$

where  $\mathbf{J}$  ( $\text{Am}^{-1}$ ) is the conduction current,  $\mathbf{E}$  ( $\text{Vm}^{-1}$ ) is the electric field and  $\sigma$  ( $\text{Sm}^{-1}$ ) is the conductivity of the metal. In these frequencies the conductivity can be considered a real constant (for the connection between the dispersive optics metal model and this real constant conductivity model see Appendix 2 at the end of this chapter). In the particular case of aluminum  $\sigma = 3.82 \cdot 10^7$ , which is a good approximation for Perfect Conductor ( $\sigma \rightarrow \infty$ ).

Applying the formalism described in [MART 01], and imposing perfect metal boundary conditions at all interfaces forming the structure the theoretical zeroth-order transmittance spectra of infinite arrays can be obtained. The results (shown in Fig. 2, *Article 2.1*) are very similar to those presented in Fig. 2.3 which have been obtained with the commercial full-wave electromagnetic solver *CST Microwave Studio™*. Two different hole diameters are considered:  $a = 2$  mm and  $a = 2.5$  mm with a lattice constant  $d = 5$  mm in all cases. Several metal thicknesses are used ranging from  $w = 0.5$  mm to  $w = 4$  mm. It can be seen that the simulation predicts the appearance of Extraordinary Transmission (ET) resonances under the condition of Perfect Conductor. Two different cases have been experimentally explored to confirm the calculations: Fresnel zone illumination and farfield illumination



(a)



(b)

Fig. 2.3. Simulated transmission coefficient spectra corresponding to infinite hole arrays with (a)  $a = 2.5$  mm and (b)  $a = 2$  mm and different metal thicknesses. The lattice constant is  $d = 5$  mm in all cases

### 2.3.1 Fresnel-zone illumination.

Several aluminum wafers with external diameter  $\varnothing = 62.4$  mm have been constructed for the experiment in Fresnel-zone illumination. A laser machine has been used for

drilling the holes. A small conical deviation from the theoretical cylindrical form is unavoidable because of the fabrication process, but the average diameter is preserved with a tolerance of  $\pm 50 \mu\text{m}$ . The hole array has a maximal dimension of  $11 \times 11$ . The rest of parameters are as aforementioned (see Fig. 2.4 for details and the picture of the prototypes).

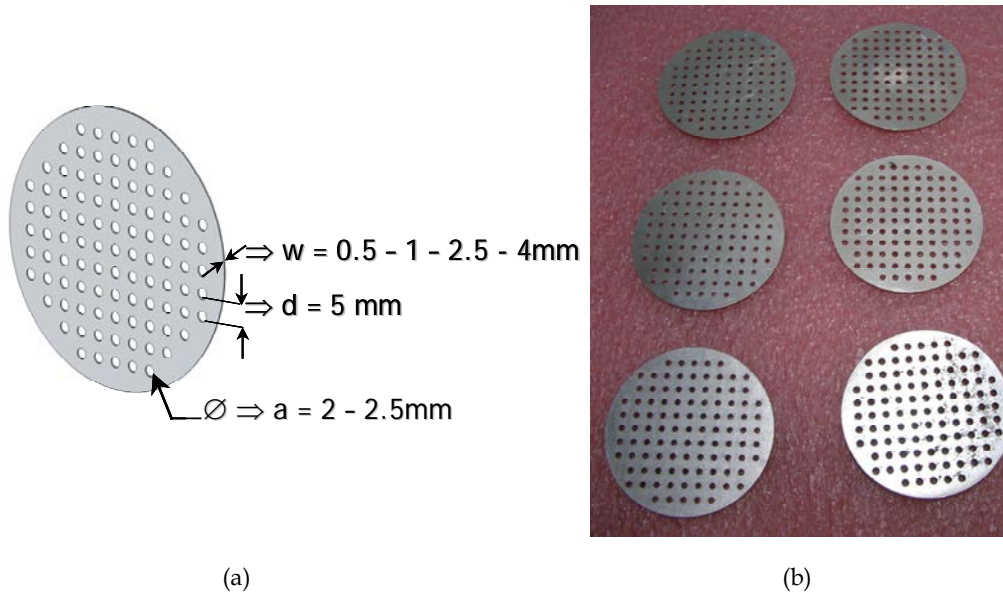


Fig. 2.4. (a) Schematic of the wafers used for Fresnel-zone illumination with the parameters shown. (b) Photograph of the six sub-wavelength hole array samples.

Transmission of light through these structures has been measured by using an advanced *AB-millimetre™* Quasioptical Vector Network Analyzer in the frequency range between 40 to 70 GHz (V-band). In Fig. 2.5 it is exposed the experimental set-up. The transmission through the samples is measured following the next procedure: A vertically polarized pure gaussian beam [ISHI 91] is generated by a corrugated horn antenna (Tx). This beam propagates up to a focusing pair of elliptical mirrors (A-B) designed to obtain an undistorted beam having its beam waist in the half of the distance, where the samples are located. Another identical pair of mirrors (C-D) focuses the transmitted beam into a corrugated horn antenna (Rx). The whole set-up can be considered as a beam waveguide [GOLD 98] and therefore, transmitted and reflected power can be easily measured. Importantly, due to finite size of the fixing system for the samples, the number of periods illuminated by the beamwaist is

restricted to  $6 \times 6$  holes.

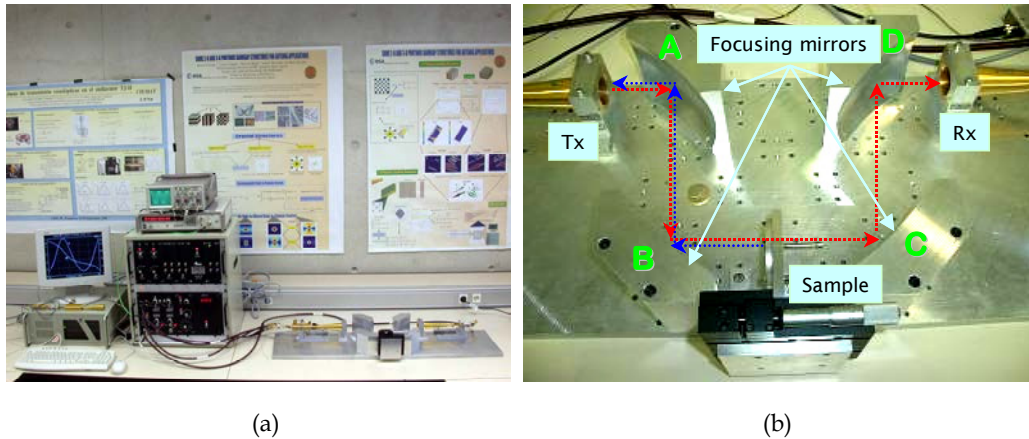
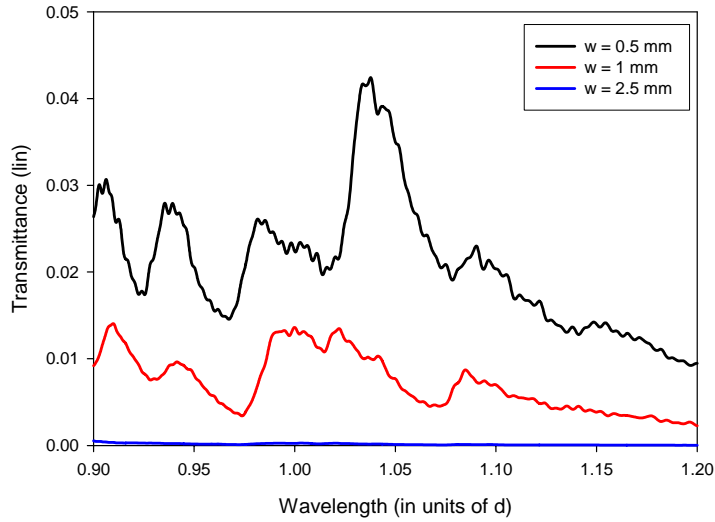


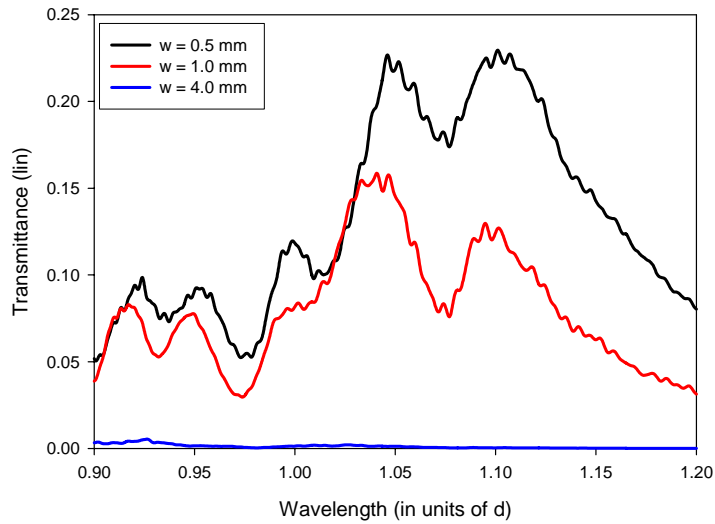
Fig. 2.5. (a) *AB-millimetre™* quasi-optical vector network analyzer and quasi-optical bench. (b) Detail of the Fresnel-zone illumination set-up. The whole system can be considered as a beam waveguide.

In Fig. 2.6 are plotted the experimental transmission spectra obtained for the different samples analyzed. In the three panels, it is represented the transmission power impinging the final antenna (normalized to the collected light when no sample is present in the system) as a function of the wavelength of the incident light in units of the period of the array,  $d = 5$  mm. In panels (a) and (b) (for  $a = 2$  mm and  $a = 2.5$  mm, respectively), it is clear the existence of a transmission resonance located near the condition  $\lambda = d$ . In both cases, we are working in the subwavelength regime, as the cutoff wavelength ( $\lambda_c$ ) for  $a = 2$  mm is  $\lambda_c = 0.52d$  and for  $a = 2.5$  mm is  $\lambda_c = 0.65d$ . and  $w = 4$  mm (blue). (c)  $a = 4$  mm and two  $w$ 's:  $w = 0.5$  mm (black curve) and  $w = 1$  mm (red). These spectra have strong similarities with the ones reported by Ebbesen et al. [EBBE 98] in the optical range and then it can be safely stated that ET also takes place in these samples under Fresnel-zone illumination. Interestingly, ET appears in the thinner films considered ( $w = 0.5$  mm and  $1.0$  mm) but not in the thicker films ( $w = 2.5$  mm in (a) and  $w = 4.0$  mm in (b)). For the sake of completeness, in Fig. 2.6(c) it has been plotted the transmission spectra obtained for two samples with  $a = 4$  mm: in this case  $\lambda_c = 1.3d$  and then, for all the wavelengths considered, there is a propagating mode inside the hole. As clearly seen in the figure, the dependence of the transmission with wavelength is quite different from panels (a) and (b). Samples with a very small diameter,  $a = 1$  mm, and two different thicknesses ( $w = 0.5$  mm and  $w = 1$  mm), have

been also constructed. In both cases, the transmission obtained is negligible (of the order of  $10^{-5}$  for  $w = 0.5$  mm and even much smaller for  $w = 1$  mm) and no signals of ET are present in the spectra.



(a)



(b)

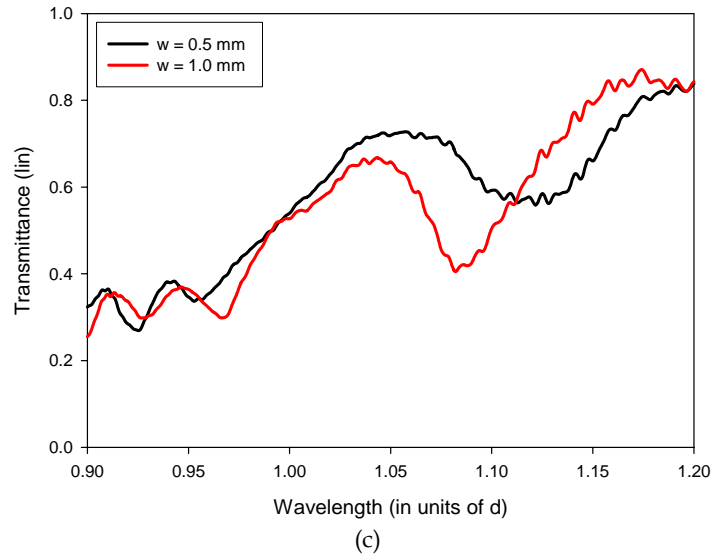


Fig. 2.6. Experimental transmittance spectra for (a)  $a = 2$  mm and three different and three different metal thicknesses:  $w = 0.5$  mm (black curve),  $w = 1$  mm (red) and  $w = 2.5$  mm (blue). (b)  $a = 2.5$  mm for also three different metal thicknesses  $w = 0.5$  mm (black curve),  $w = 1$  mm (red)

### 2.3.2 Farfield illumination.

For the case of farfield illumination other prototypes have been constructed with the aforementioned laser milling technique. They are square aluminum perforated plates with  $31 \times 31$  holes and the sub-wavelength diameters:  $a = 2$  mm,  $a = 2.5$  mm. The rest of the parameters are as in the Fresnel-zone case. In Fig. 2.7(a) it is shown the schematic of the farfield prototypes with the parameters and in Fig. 2.7(b) the photograph of two prototypes.

Transmission through the samples is measured by using the *AB-millimetre™* Quasioptical Vector Network Analyzer in the frequency range between 40 to 70 GHz (V-band). The experimental set-up in this configuration is schematically shown in Fig. 2.8(a) and the actual picture in Fig. 2.8(b). A vertically polarized pure Gaussian beam is generated by a corrugated horn antenna (Tx). This beam propagates to the sample (S) that is located at 166 cm from the antenna. The diameter of the beam waist at the sample location is approximately 50 cm at the wavelength range of interest. In this way the illumination of the hole array is rather uniform. The transmitted beam is finally collected into a horn antenna (Rx) that is placed 105 cm from the sample. The

samples are embedded into a sheet of millimeter-wave absorbing material such that any possible diffracted beam generated by the edges of the samples is absorbed by the sheet and not collected by the receiver antenna, Rx.

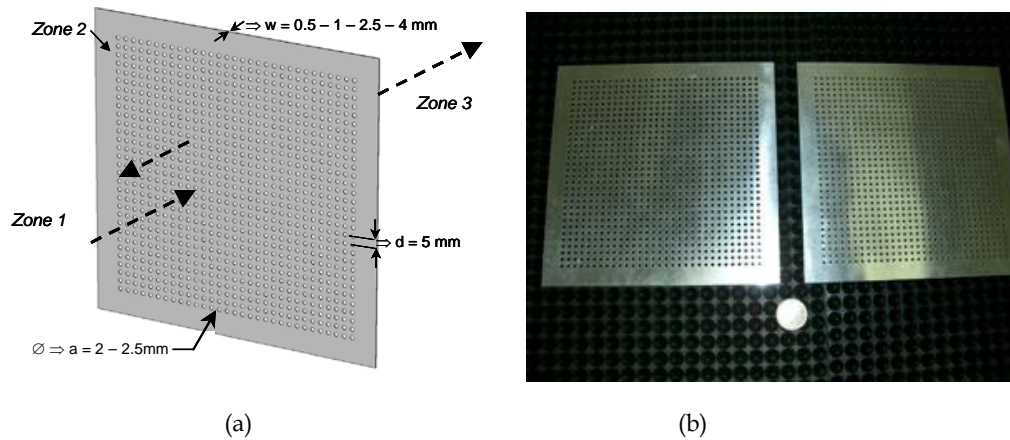
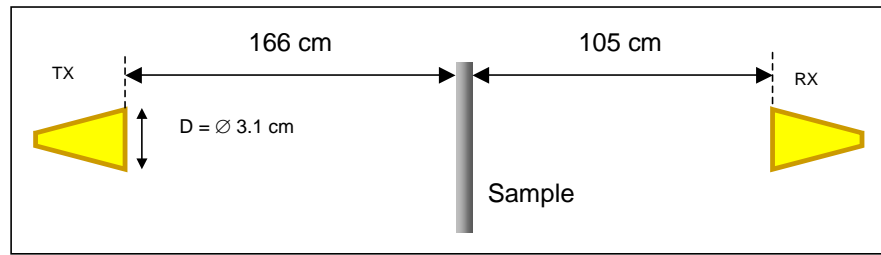


Fig. 2.7. (a) Schematic of the metallic plates used for farfield illumination with the parameters shown. (b) Photograph of two of the hole array samples.

The measured transmission spectra are plotted in Fig. 2.9 in decibel scale. The collected transmission power is normalized to the collected power when no sample is present and is represented as a function of the wavelength of the incident light in units of the period of the array,  $d = 5$  mm. The case of hole diameter  $a = 2$  mm is shown in Fig. 2.9(a) and  $a = 2.5$  mm in Fig. 2.9(b). In this last panel and for the case when  $w = 0.5$  mm (black curve) the transmission at resonance, located at around 57 GHz ( $\lambda = 5.26$  mm;  $\lambda$  slightly larger than  $d$ ) can be as large as 95% although the holes occupy only 20% of the unit cell. As the thickness of the plate grows,  $w = 1$  mm (red curve in Fig. 2.9(b)), the transmittance decreases, until the complete extinction of the peak when  $w = 4$  mm (blue curve). This is in agreement with the assumption of evanescent modes inside the holes. The transmission resonance is also present in the thinner samples  $w = 0.5$  mm and  $w = 1$  mm, see Fig. 2.9(a), of the  $a = 2$  mm hole arrays, but the associated transmittance peaks are much lower than the ones obtained for  $a = 2.5$  mm. Again, when the metal is thick  $w = 2.5$  mm, the collected power is extremely small and no fingerprints of transmission resonances are observed. As the measured transmission resonances appear in a frequency range in which the holes support only EM evanescent waves, it can be safely concluded that ET also takes place in the millimeter-wave range, as predicted by theory. In consequence, it has been proven the

Perfect Conductor Metal assumption. It is well established now that the origin of the Enhanced Transmission is the excitation of surface electromagnetic modes in the periodic metallic surface.



(a)

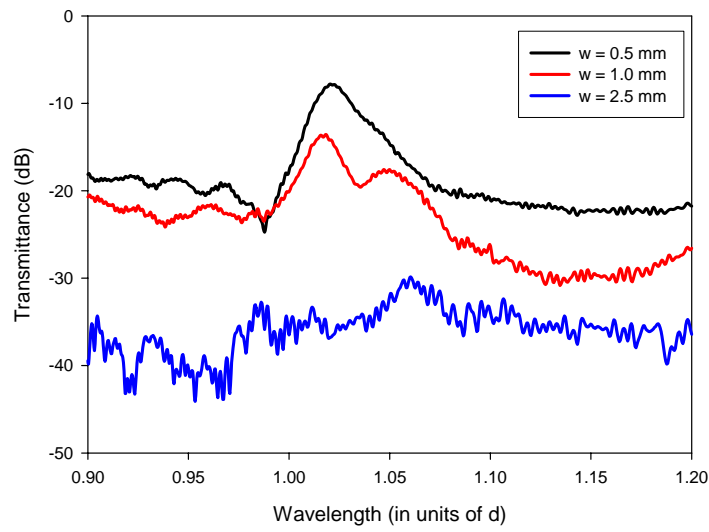


(b)

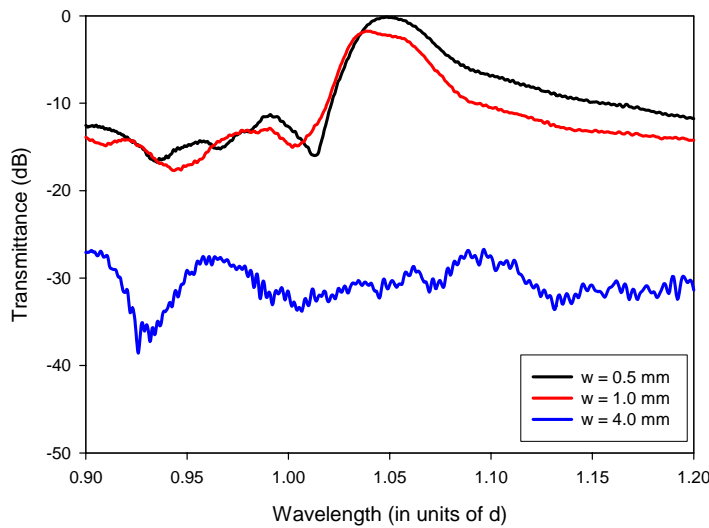
Fig. 2.8. (a) Schematic of the whole experimental setup. (b) Photograph of the source antenna (T) and the sample (S) covered with absorbing material to avoid diffraction. The receiving antenna is not shown.

Finally, the farfield set-up was employed to check the agreement between the infinite structure simulation and the experimental measurement in a larger bandwidth. The frequency span was extended from 40 GHz to 110 GHz. The structure with parameters  $a = 2.5$  mm and  $w = 0.5$  mm was used for the experiment. In Fig. 2.10, it is plotted the

measured spectrum in red and the simulation of the infinite structure in black.



(a)



(b)

Fig. 2.9. Experimental transmittance spectra for farfield illumination. (a)  $a = 2$  mm and three different  $w$ 's.  $w = 0.5$  mm (black),  $w = 1$  mm (red) and  $w = 2.5$  mm (blue). (b)  $a = 2.5$  mm and also three  $w$ 's.  $w = 0.5$  mm (black),  $w = 1$  mm (red) and  $w = 4$  mm (blue).

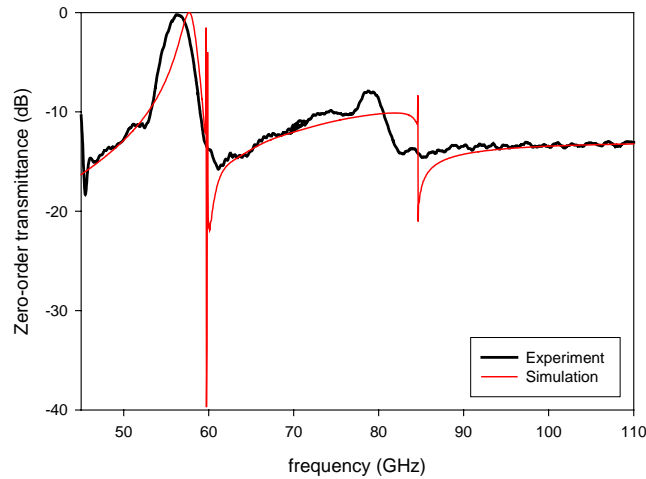


Fig. 2.10. Theoretical spectrum of the infinite structure (dashed) and experimental response of the  $31 \times 31$  hole array (solid) extended up to 110 GHz for parameters  $a = 2.5$  mm and  $w = 0.5$  mm.

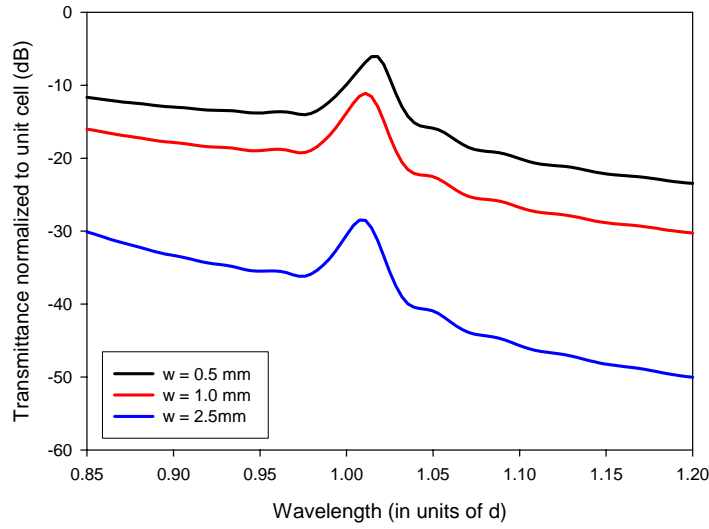
A good agreement is observed. Apart from very fine frequency details, the finite structure behaves qualitatively as the infinite one. Note the presence of Wood's anomaly around 60 GHz as expected and the second relative maximum with similar amplitude.

The results of the farfield illumination experiment were published in *Article 2.1* and more extensively developed in *Article 2.2*.

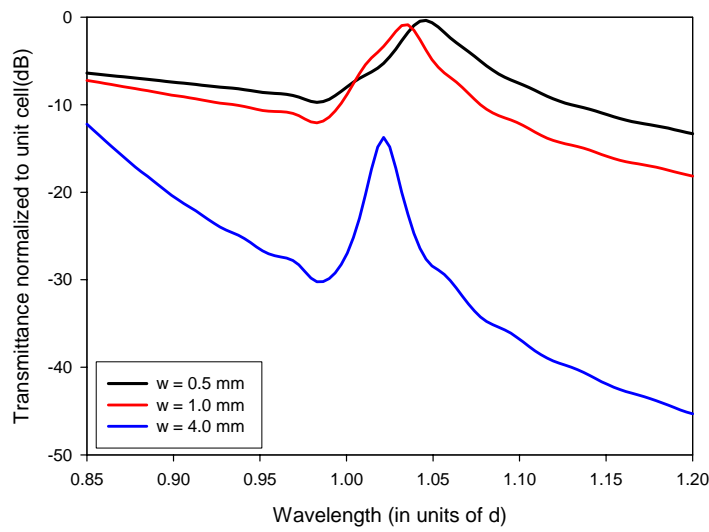
## 2.4 Finite structure effects.

It has not been explicitly stated, but it is obvious in the comparison of Fig. 2.3 (theoretical infinite structure), Fig. 2.6 (experimental Fresnel-zone illumination) and Fig. 2.9 (experimental farfield illumination) that the size of the structure is a critical parameter in the design of Enhanced Transmission hole arrays. For the case of Fresnel-zone illumination the effective number of illuminated holes is around  $9 \times 9$ , whereas in the farfield illumination this number increases up to  $31 \times 31$ . In the best case ( $a = 2.5$  mm;  $w = 0.5$  mm; black curve of Fig. 2.5(b)) the transmission level in Fresnel-zone illumination is around 23%, while in the farfield measurement it approaches the theoretical value of total (100%) transmission predicted for infinite structure. However, in all the remaining experimental curves the peak level falls

below the theoretical calculations. Also, the comparison between the simulation and experiment shown in Fig. 2.10 suggests that the size of structure is a critical parameter. A possible reason for this disagreement could be the intrinsically finite size of the arrays and thus, it is generically referred to as *finite structure effects*.



(a)



(b)

Fig. 2.11. Numerical simulation of finite size  $31 \times 31$  hole array zero-order transmittance for (a)  $a = 2$  mm and three different  $w$ 's.  $w = 0.5$  mm (black),  $w = 1$  mm (red) and  $w = 2.5$  mm (blue) and for (b)  $a = 2.5$  mm and three  $w$ 's.  $w = 0.5$  mm (black),  $w = 1$  mm (red) and  $w = 4$  mm (blue).

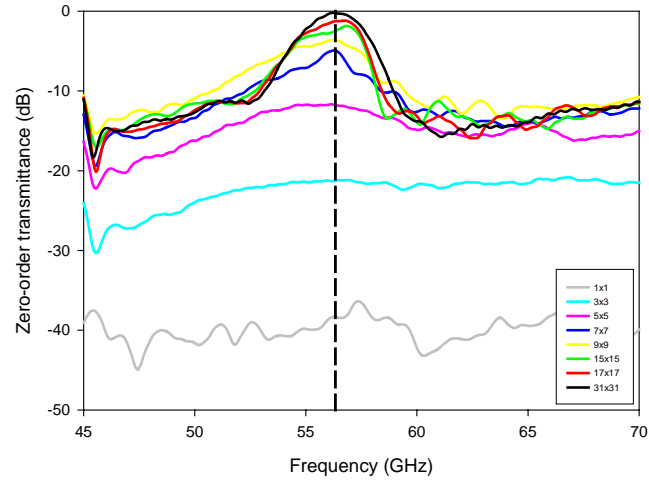
To explore this in more detail, Bravo-Abad and co-workers developed a new theoretical tool able to analyze the transmission properties of finite collections of holes drilled in a metallic film [BRAV 04]. The results particularized to the farfield illumination samples are shown in Fig. 2.11.

Notice that these results are in very good agreement with the measured farfield curves. Transmission always decreases as the thickness of the plate grows. The calculated curves predict almost total transmission for the structure with hole diameter  $a = 2.5$  mm and plate thickness  $w = 0.5$  mm as in the measurement. The plates with holes of diameter  $a = 2$  mm have a transmission peak of around  $-7$  dB for the best case ( $w = 0.5$  mm) both in the simulation and the experiment. Wood's anomaly is also present in these simulations, although it is not as clearly emphasized as in the measured curves. As typically happens in finite systems, it is slightly shifted towards higher frequencies [HESS 65].

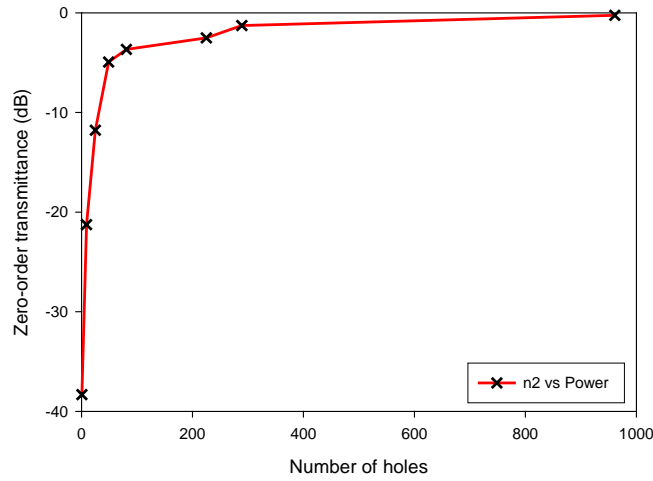
Attending to the mentioned results, it seems that making the sample finite implies coarse spectral resolution in the frequency response. This has two main consequences: the narrowest spectral details of the infinite structures are either lost or at least smoothed. As a consequence of this smoothing, the maximum of transmission falls dramatically for very narrow peaks, see for example the response when  $a = 2$  mm, Fig. 2.3(a) (infinite plate) and Fig. 2.9(a) (experimental). Additionally, in infinite structures Wood's anomaly appears as an abrupt fall of power within a very narrow frequency range and it is apparently softened in finite structures.

Following the aforementioned interpretation, in order to catch the finest details of the spectrum, the illumination should impinge on a larger effective area. This can be accomplished either by constructing larger samples maintaining the same hole diameter or by increasing the diameter of the holes maintaining the size of the array. This explains in a complementary point of view the high level of signal seen in Fig. 2.9(b) compared to the low level presented in Fig. 2.9(a).

A concluding experimental study that shows the significance of the hole array size was developed. The sample with  $a = 2.5$  mm and  $w = 0.5$  mm is initially covered with a silver foil layer. This film is gradually removed, allowing only illumination of the holes uncovered. Therefore, the incident beam impinges on a hole array window of progressively increasing dimension. In this experiment it is used the farfield configuration that shows the better experimental response



(a)



(b)

Fig. 2.11 (a) Experimental transmission spectra for  $d = 5$  mm,  $a = 2.5$  mm,  $w = 0.5$  mm for increasing number of holes. (b) Increase of power as a function of the number of illuminated holes for the resonance frequency.

The result of the measurements is sketched in Fig. 2.12(a). It has also been plotted in Fig. 2.12(b) the improvement at the resonance frequency (marked with black dashed line in Fig. 2.12(a)) as a function of the number of uncovered holes. It can be observed that for small array dimensions, the level of transmission increases abruptly as the window is enlarged. For a sufficiently large number of illuminated holes the growth is

more gradual, though it is seen enhancement without saturation. For  $31 \times 31$  holes the peak reaches 100%.

The initial communication of finite structure effects were presented in a primary approach in *Article 2.1*. The extended discussion was published in *Article 2.2*. The last results appeared in *Article 2.3*.

## 2.5 Dichroic filters and EOT structures.

Now that is clear that Enhanced Transmission also exists in the millimeter wave range, it is worth to explore the link between the classical dichroic filters and enhanced transmission hole arrays. Both consist of an array of holes drilled on a metallic plate. The main structural difference is the density of holes, i.e. the fraction of unit cell occupied by the hole, see Fig. 2.13. For a dichroic filter, the holes are located very close together because (as stated in section 2.1) “as the guide spacing is increased the magnitude of the shunt reactance increases which results in a greater discontinuity and more pronounced ripple responses” [GOLD 98]. In other words, the periodicity is usually chosen to be less than the cut-off wavelength of the packed waveguides,  $d < \lambda_c$ . The thickness of the metal plate also affects the response. To get a clean bandpass, this parameter must be neither too thin nor extremely thick. The bandpass of dichroic filters occurs above the cut-off of the holes. Therefore, the holes are acting as waveguides with a propagating mode inside them, and they collaborate together to couple power at the output face.

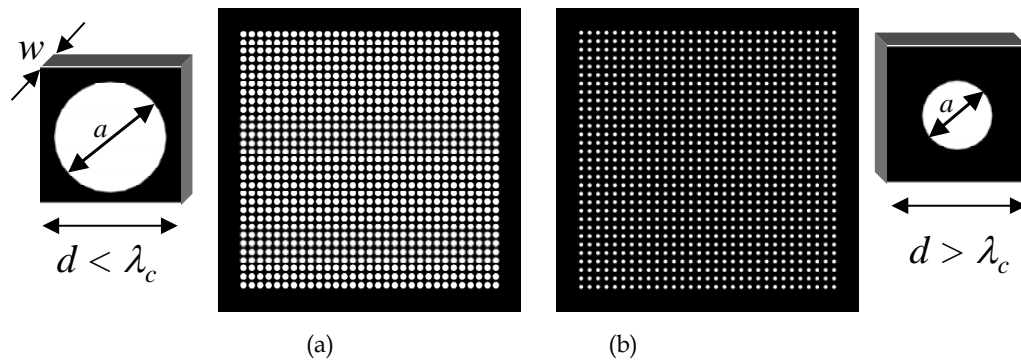
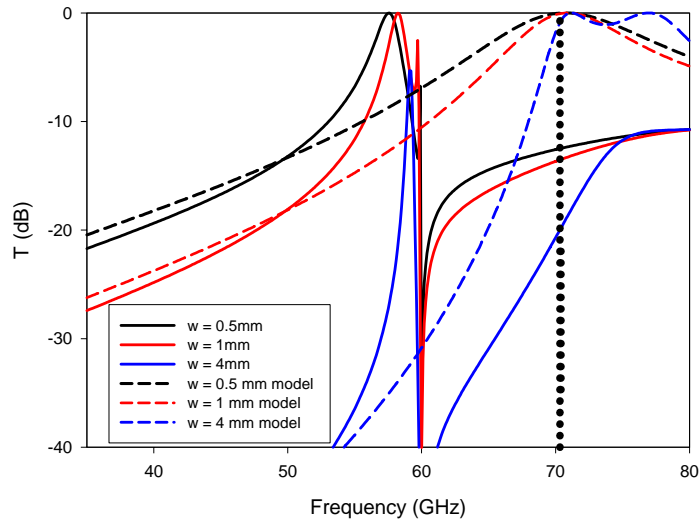
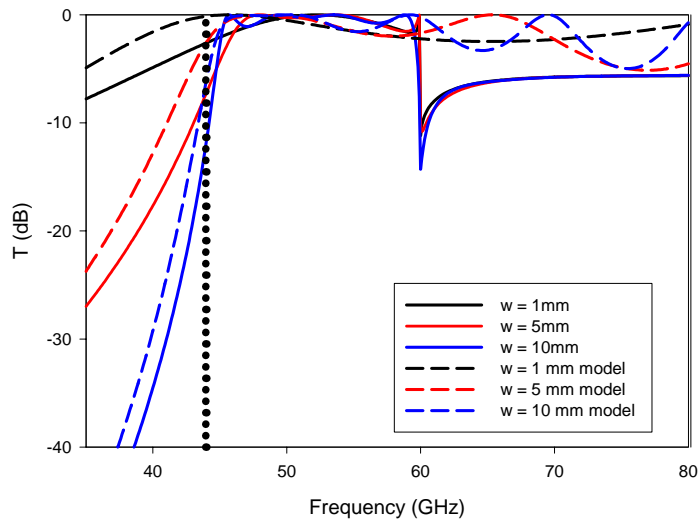


Fig. 2.13. (a) Dichroic filter schematic (b) Enhanced transmission structure schematic. The main structural difference is the fraction of unit cell occupied by the hole, i.e. the density of holes.



(a)



(b)

Fig. 2.14. Comparison between the transmission spectra calculated with the simplified equivalent circuit approach (dashed lines) and the simulation results (solid lines) for the cases  $a = 2.5$  mm and three  $w$ 's:  $w = 0.5$  mm (black),  $w = 1$  mm (red),  $w = 4$  mm (blue) (a) and  $a = 4$  mm and three  $w$ 's:  $w = 1$  mm (black),  $w = 5$  mm (red),  $w = 10$  mm (blue) (b)

To observe enhanced transmission, on the other hand, periodicity must be larger than the cut-off wavelength of the holes,  $d > \lambda_c$ . The bandpass is situated in the cut-off region, thus only evanescent modes exist inside the holes. Due to the exponential

decay characteristic of these modes, plates must be thin enough to ensure coupling to the output face.

This parameter range of values had not been studied before Ebbesen's experiment, may be due to the fact that nothing remarkable was expected for wavelengths beyond cut-off. In an unexpected way, the first experiments on EOT demonstrated that surface electromagnetic resonances were present in the corrugated metallic surface and allowed high transmission in the cut-off region of the holes. The comparison between dichroic filters and enhanced transmission structures was first presented in *Article 2.3*.

Recalling the simple model proposed by Goldsmith (see section 2.1), it is worth to note that it cannot reproduce the Enhanced Transmission peak. The reason of which is that it disregards diffraction, which is crucial in the description of Wood's anomalies (remind that in the elucidation proposed in [SARR 03] ET is accurately explained in terms of resonant-Wood's anomalies).

As a matter of fact, it is presented in Fig. 2.14 the comparison of the spectra calculated following the simplified equivalent circuit approach described in [GOLD 98] (dashed lines) and the spectra obtained with the simulator (solid lines), for hole arrays with the parameters:  $a = 2.5$  mm and three  $w$ 's:  $w = 0.5$  mm (black),  $w = 1$  mm (red),  $w = 4$  mm (blue) in panel (a) and  $a = 4$  mm and three  $w$ 's:  $w = 1$  mm (black),  $w = 5$  mm (red),  $w = 10$  mm (blue) in panel (b). The model works with reasonable accuracy in the low frequency region in all the analyzed structures.

For the propagating holes response shown in panel (b) the low frequency limit of the bandpass is quite appropriately outlined with a slight frequency shift towards lower frequencies. Also, the ripple in the band is predicted within a few percent error. The Wood's anomaly at 60 GHz is lost in the representation, since this feature is purely a dynamical diffraction effect. For the case of subwavelength holes shown in panel (a), the discrepancies are stronger. The only coincidence is at low frequencies. The ET peak is not present in this model. Rather, it predicts a bandpass with the low frequency cut-off at the hole wavelength cut-off (marked with black dotted line). Wood's anomaly is also lost in the spectra.

## 2.6 Phase response of cut-off metallic hole arrays.

Up to this point it is clear that ET also exists in microwaves and millimeter waves, and that is essentially different of previous studies of similar structures in these ranges. Experimental as well as theoretical studies have been presented and the parametric dependance of the magnitude response has been exhaustively described but nothing has been said about the phase. The understanding of the transmission coefficient phase behavior is important in applications ranging from the construction of microwave filters to mode converters and a variety of quasi-optical structures. This section is devoted to this study.

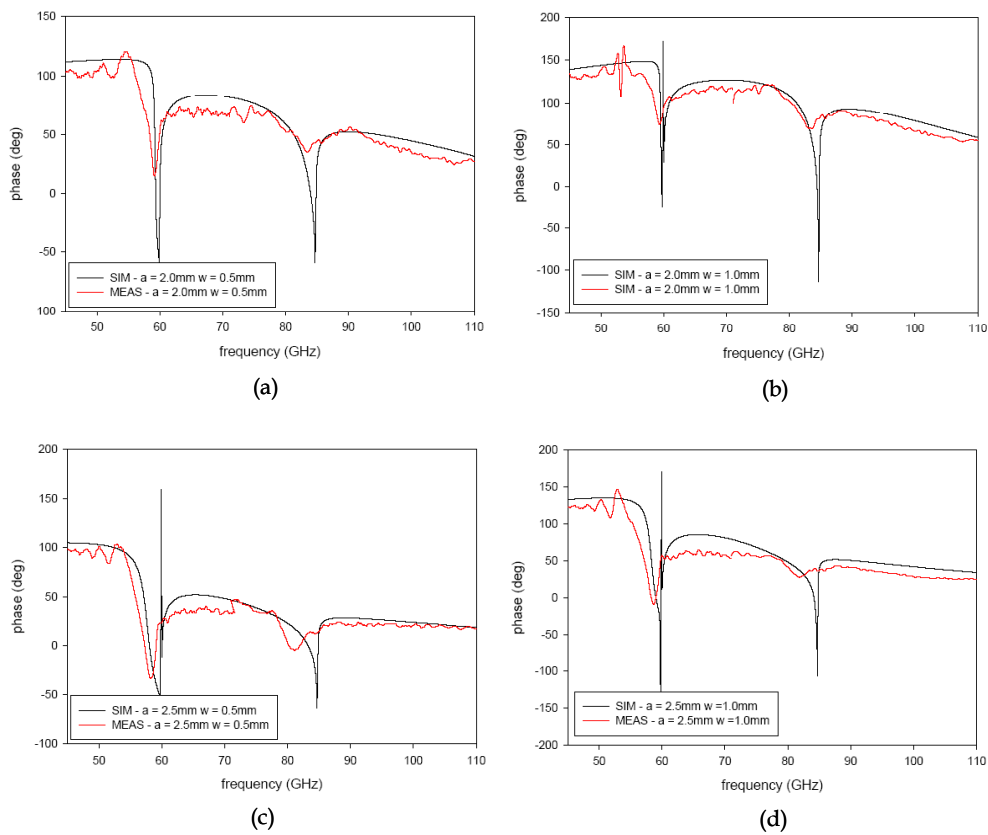


Fig. 2.15 Simulated (black) and measured (red) phase response for the structures with (a)  $a = 2.0$  mm,  $w = 0.5$  mm (b)  $a = 2.0$  mm,  $w = 1.0$  mm (c)  $a = 2.5$  mm,  $w = 0.5$  mm and (d)  $a = 2.5$  mm,  $w = 1.0$  mm. Theoretical curves are for infinitely periodic structures.

At this point, phenomena of extraordinary transmission through perforated plates are viewed as manifestations of so-called Wood anomalies [RAYL 07], [HESS 65], i.e. rapid variations of the frequency or angular dependence of the magnitude and/or phase of scattering coefficients of a periodic structure that occur when specific conditions are met. The resonant and Rayleigh Wood anomalies are associated with complex poles and (square root) branch points characterizing the transmission coefficient, respectively. The poles characterize resonances supported by the perforated plate. They lead to rapid variations of  $\pi$  in the transmission coefficient phase. The branch points determine the condition under which an additional Floquet mode appears/disappears as the frequency of the normally illuminating plane wave is scanned. They result in unboundedly rapid variations of the transmission coefficient phase.

Note that in the symmetrical case, when the perforated plate is sandwiched between two identical dielectric slabs, the resonant and Rayleigh Wood anomalies almost coincide. Numerical results of infinite hole arrays with the parameters  $a = 2$  mm,  $2.5$  mm,  $d = 5$  mm,  $w = 0.5$  mm,  $1$  mm were obtained via the modal approach detailed in [CHEN 71] assuming that the structure is infinitely periodic. The black line representing the numerical result in Fig. 2.15 shows rapid variations of the transmission coefficient phase for  $f \approx 60$  GHz,  $80$  GHz. For the experiment, the farfield prototypes were used, section 2.3.2. The measured results are given in the red curves of Fig. 2.15. It is observed that the experimental phase behavior matches well that obtained numerically for infinitely periodic structures, for instance it exhibits rapid variations for the same frequency ranges. The discrepancies in the measured and calculated results are mainly due to the finite size of the measured structures.

## 2.7 Double periodicity structures on dielectric slabs.

Taking as a starting point the works by Lomakin *et al.* [LOMA 04], [LOMA 05], a double periodicity structure sandwiched between two dielectric slabs has been designed and measured. With the double periodicity the hole array can be designed to present ET for only one polarization. Moreover, the introduction of a shorter periodicity in  $d_x$  makes the array more compact (more holes per unit area) than in standard hole arrays, thus increasing the effective illuminated area for the same

structure size. Therefore, in finite structures it is expected a better level of measured transmission with the new topology. The introduction of dielectric slabs, apart from implications such as giving support for grounded-slab surface waves, discussed extensively in [LOMA 05] also has consequences in the size of the structure. For instance, compare in Fig. 2.16 the simulated response of two subwavelength hole arrays of the same dimension, one of them sandwiched between two dielectric slabs of thickness  $h = 0.49$  mm and relative dielectric permittivity  $\epsilon_r = 2.43$  (red curve) and the other one in air (blue curve). Clearly, when the hole array is inserted between a dielectric sandwich the ET peak is shifted to lower frequencies, in the present case from 73 GHz to 60 GHz, and then the structure is effectively bigger in units of wavelength. Putting the hole array in a dielectric sandwich contributes to a better illumination since more holes per wavelength can be effectively illuminated. As a result, the structure considered in this section allows for a very efficient hole illumination via two mechanisms: double periodicity increases the density of holes per unit cell, and the introduction of dielectric slabs forces the ET resonance to lower frequencies making possible illuminate more holes per wavelength.

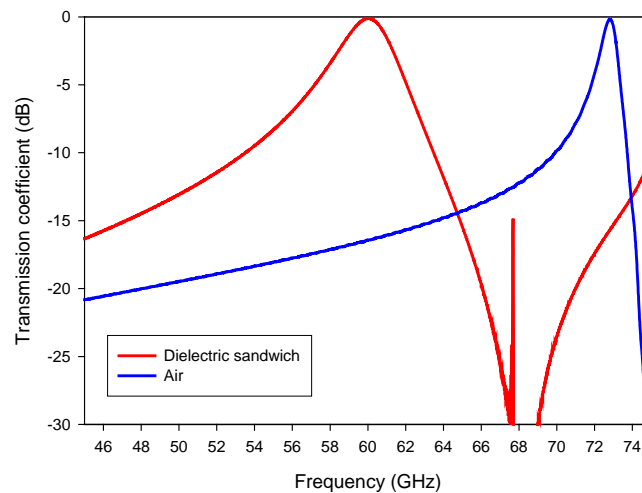


Fig. 2.16. Simulated transmission coefficient magnitude comparing two double periodicity hole arrays, one immersed in air (blue curve) and the other one sandwiched between two dielectric slabs of thickness  $h = 0.49$  mm and relative dielectric permittivity  $\epsilon_r = 2.43$  (red curve). The hole array parameters are: hole diameter  $a = 1.2$  mm, periodicity in  $x$  dimension  $d_x = 1.5$  mm, periodicity in  $y$  dimension  $d_y = 4$  mm, copper metallic plate of thickness  $t = 35$  microns.

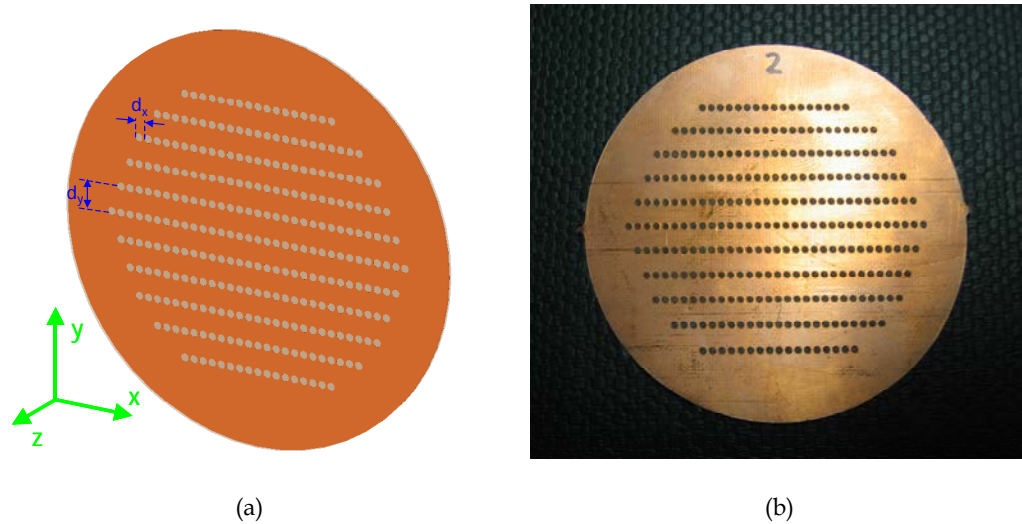
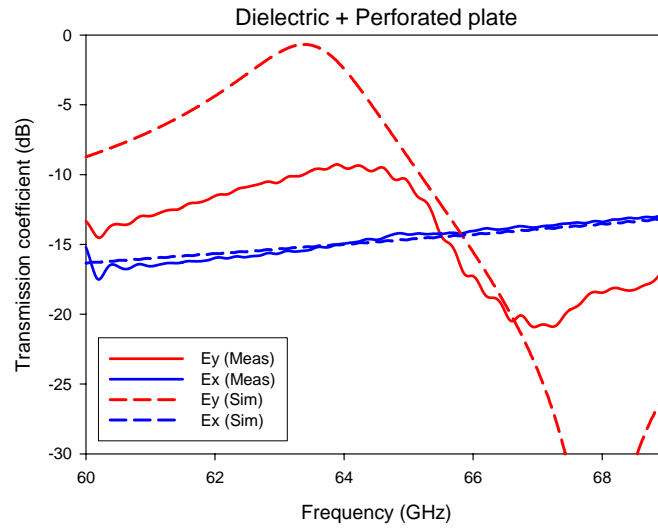


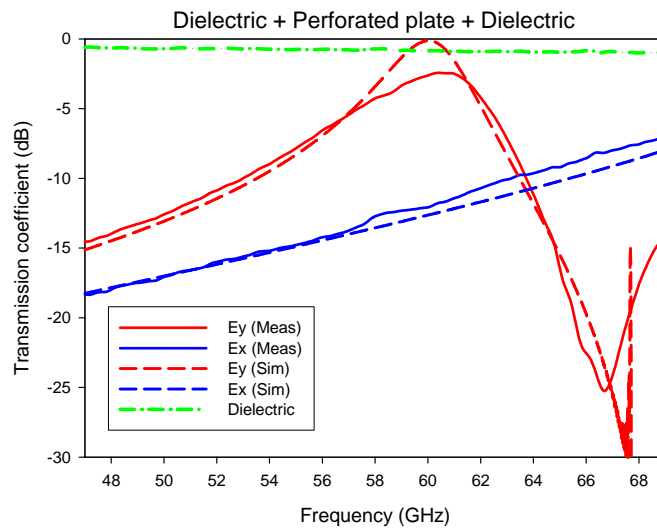
Fig. 2.17. (a) Schematic of the double periodicity hole array sandwiched between two dielectrics. (b) Photograph of the hole array etched on a commercial printed circuit substrate.

These ideas are tested both in simulation and in experiment. The schematic is shown in Fig. 2.17. It consists of circular wafer of diameter  $\varnothing = 62.4$  mm etched with a double periodicity hole array with transversal periods  $d_x = 1.5$  mm,  $d_y = 4$  mm and hole diameter  $a = 1.2$  mm. The array is etched by numerical control machining on the  $t = 35$  microns copper metallization layer of a commercial printed circuit dielectric substrate, and sandwiched with an identical dielectric layer of nominal characteristics: relative permittivity  $\epsilon_r = 2.43$  and dielectric thickness  $h = 0.49$  mm. The fractional area of the hole, defined as the ratio of hole to unit cell area, is approximately  $F = 0.2$ . The prototype is measured by using the *AB-millimetre*<sup>TM</sup> Quasioptical Vector Network Analyzer in the frequency range between 40 to 70 GHz (V-band), with the quasioptical or Fresnel zone illumination set-up, see Fig. 2.5.

The transmission coefficient under normal incidence was measured for electric field along  $x$  (see axis orientation in Fig. 2.17(a)) and electric field along  $y$  (see axis orientation in Fig. 2.17(a)) polarizations. Measurement results of the asymmetric *dielectric + perforated plate* as well as the symmetric *dielectric + perforated plate + dielectric* configurations were taken. The results are shown in Fig. 2.18, together with the simulations made with *CST Microwave Studio*<sup>TM</sup>.



(a)



(b)

Fig. 2.18. Simulation (dashed curves) and measurement (solid curves) results for a dielectric + perforated plate structure (a) and a dielectric + perforated plate + dielectric structure (b). Red lines are for electric field polarized along  $y$  and blue lines are for electric field polarized along  $x$ . Green line is the transmission measurement of a single dielectric slab.

It is observed that the structure presents a ET resonance only when the electric field is polarized along the larger periodicity, i.e. when the polarization is in the direction where the density of holes is smaller. For the other polarization no traces of

resonances are detected, and the level at 60 GHz is -11.6 dB. It is noticeable the good agreement seen between simulation and measurement for the sandwich configuration, panel (b). The measured peak level is -2.46 dB, below the simulation prediction of 0 dB, and (as usual in ET hole arrays) the finest frequency details are lost in the measurement. A possible cause of the smaller level in the measurement can be due to losses.

For a rough estimation of dielectric losses, a single dielectric slab was measured (green line in Fig. 2.18(b)). The measurement gives a loss of 0.9 dB in the passband. As the sandwich has two twin dielectric slabs, the total losses due to dielectrics are (roughly) 1.8 dB. This gives as a result that the perforated plate losses are 0.66 dB. Notice that the measurements are taken by using the Fresnel-zone illumination set-up and that, accordingly, the actual illuminated area has a diameter approximately equal to gaussian beamwaist, i.e. 27.9 mm, and still the measured transmission is quite high.

The effective number of illuminated holes is  $19 \times 8$ , which corresponds to an area (normalized to the EOT wavelength)  $S / \lambda^2 = 24.45$ . Compare the response obtained with that shown in section 2.3.1, for single periodicity samples embedded in air. In the best case of  $a = 2.5$  mm,  $d = 5$  mm and  $w = 0.5$  mm the measured power level was -7 dB (see Fig. 2.6(b)) and for the smaller hole diameter  $a = 2$  mm it was -13 dB, i.e. 10.5 and 4.5 dB below the current double period hole array. The fractional hole area is  $F = 0.12$  and  $0.2$  for  $a = 2$  and  $2.5$  mm respectively.

The effective number of illuminated holes in the single period samples was  $6 \times 6$ , much lower than the experimentally found  $31 \times 31$  holes for near total transmission in Fraunhofer illumination, as shown in Fig. 2.11. This hole array size corresponds to an area of  $S / \lambda^2 = 900$ , i.e. 36 times greater than in the double periodic hole array between dielectric slabs.

The agreement in the asymmetrical case shown in panel (a) is worse. In this case the measurement falls to -9 dB while the simulation predicts a value of -0.6 dB. This disagreement can be due to the fact that one face is backed by air and the electric field concentration there is weaker. This makes a difference with the sandwich case in which both faces present the same matching and, more important, a stronger electric field concentration due to the presence of dielectrics.

## 2.8 Concluding remarks.

It has been demonstrated in this chapter that the phenomenon of extraordinary transmission through arrays of subwavelength holes is also present in the millimeter-wave range. Since in this wavelength regime plasmons do not exist, this results gives evidence of the periodic structure-based explanation of the phenomenon.

Moreover, it has also been shown by comparing Fresnel zone measurements and Farfield measurements that one of the key parameters to observe this phenomenon is the number of periods of the array. A systematic experimental study of the dependence on the number of holes has also been presented and the number of  $31 \times 31$  holes seems to be sufficient.

A comparison of ET structures with similar structures in microwaves and millimeter waves has been presented and their differences highlighted. The failure of classical equivalent circuit approaches to show ET results has also been checked, being the cause the neglect of diffraction effects.

A preliminary study of the phase response has been advanced, as well as some other experimental results of double periodicity structures on dielectric slabs. It has been shown that ET is mainly governed by one of the transversal periodicities, the one in the direction of the electric field (under normal incidence). Also, the presence of dielectrics can produce a great field confinement and therefore, a more efficient illumination of holes.

## Appendix 2

### Dispersive model of metals

The dielectric constant of any material is in general dependent on frequency, and it can be considered constant only within a narrow frequency band. This dependence on frequency is called dispersion. In general for a dielectric material, its frequency response can be computed following a simplified model of molecules with electrons bound elastically to the heavy nuclei. The equation of motion of an electron is then,

$$m \frac{d^2 \mathbf{r}}{dt^2} = -m\omega_0^2 \mathbf{r} - m\nu \frac{d\mathbf{r}}{dt} + \mathbf{F} \quad (\text{A.1})$$

where  $m$  is the mass of the electron,  $\mathbf{r}$  is the displacement of the electron,  $-m\omega_0^2 \mathbf{r}$  is the elastic restoring force  $-m\nu d\mathbf{r}/dt$  is the damping force,  $\nu$  is the collision frequency, and  $\mathbf{F}$  the Lorentz force acting on the electron. The restoring force is assumed to be proportional to the displacement of the electron, and the constant  $\omega_0$  is equal to the frequency of the free oscillations of the electron under the influence of the restoring force alone. The Lorentz force is given by:

$$\mathbf{F} = e(\mathbf{E}' + \mathbf{v} \times \mathbf{B}') \quad (\text{A.2})$$

where  $e$  is the charge of an electron,  $\mathbf{E}'$  and  $\mathbf{B}'$  the local field, and  $\mathbf{v}$  the velocity of the electron. Since  $|\mathbf{B}'|$  is on the order of  $(1/c)|\mathbf{E}'|$ , if it is assumed  $|\mathbf{v}| \ll c$ , then the second term is negligible compared with the first term.

The local field  $\mathbf{E}'$  can be expressed in terms of the applied field and the polarization vector as,

$$\mathbf{E}' = \mathbf{E} + \frac{\mathbf{P}}{3\epsilon_0} \quad (\text{A.3})$$

Assuming now that there are  $N$  bound electrons per unit volume, the polarization vector can be written as:

$$\mathbf{P} = Ne\mathbf{r} \quad (\text{A.4})$$

If a time-harmonic dependence is assumed, Eq. (A.1) can be written as:

$$m\omega^2 \mathbf{r} = -m\omega_0^2 \mathbf{r} - j\omega m \nu \mathbf{r} + e \left( \mathbf{E} + \frac{Ne\mathbf{r}}{3\epsilon_0} \right) \quad (\text{A.5})$$

Noting that  $\mathbf{D} = \epsilon_0 \epsilon_r \mathbf{E} = \epsilon_0 \mathbf{E} + \mathbf{P}$ , the relative dielectric constant can be written as a function of frequency.

$$\epsilon_r = 1 + \frac{Ne^2}{m\epsilon_0(\omega_1^2 - \omega^2 + j\omega\nu)} \quad (\text{A.6})$$

where  $\omega_1^2 = \omega_0^2 - Ne^2/3\epsilon_0 m$ . The previous equation is the general expression for the frequency dependence of the dielectric permittivity when there is only one resonance. For the more general case of more than one resonance see [ISHI 91].

In the particular case of a conductor, there are free electrons not bound to molecules, and therefore, the restoring force  $-m\omega_0^2 \mathbf{r}$  is absent. Also, the interaction between molecules can be neglected and the local field is equal to the applied field. Equation (A.6) is then,

$$\epsilon_r = 1 + \frac{\omega_p^2}{-\omega^2 + j\omega\nu} \quad (\text{A.7})$$

where  $\omega_p = (Ne^2/m\epsilon_0)^{0.5}$  is called the plasma frequency.  $N$  is the number of free electrons per unit volume and is called the electron density. The damping is caused by the collisions between the electron and other molecules, and  $\nu$  is called the collision frequency.

The expression of the permittivity of a lossy conductor is [ISHI 91]:

$$\epsilon_r = 1 - j \frac{\sigma}{\omega\epsilon_0} \quad (\text{A.8})$$

Combining (A.7) and (A.8) the frequency dependence of the conductivity is extracted:

$$\sigma = \epsilon_0 \frac{\omega_p^2}{\nu + j\omega} \quad (\text{A.9})$$

When  $\omega \ll \nu$  the conductivity is almost constant. In general, however it is a function of frequency.

## Plasmons

It is clear that a metal in optics has a dispersive behavior, and that in general the dielectric permittivity has a frequency dependence in the form of (A.7). If losses are neglected, ( $\nu = 0$ ) it is seen that in the region below the plasma frequency  $\omega_p$  the dielectric permittivity is negative and above is positive. In general, when losses are taken into account, the real part of the dielectric permittivity of a metal is negative ( $\text{Re}\{\epsilon_1\} < 0$ ) within a frequency range below the plasma frequency.

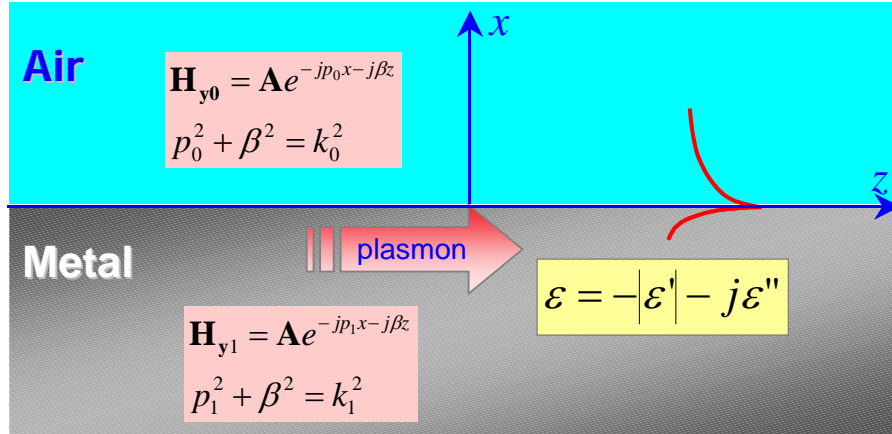


Fig. A.1. Schematic picture of a wave propagating in the interface of air and a metal at optics frequencies ( $\text{Re}\{\epsilon_1\} < 0$ )

Consider now a TM wave at the interface between a standard dielectric, say air ( $\epsilon_0$ ) and a metal at a frequency where  $\text{Re}\{\epsilon_1\} < 0$ , see Fig. A.1. The wave in air ( $x > 0$ ) can be expressed as

$$H_{y0} = A e^{-jp_0 x} e^{-j\beta z} \quad (\text{A.10})$$

where  $p_0^2 + \beta^2 = k_0^2$ . In the metal ( $x < 0$ ) the magnetic field is written as,

$$H_{y1} = A e^{-jp_1 x} e^{-j\beta z} \quad (\text{A.11})$$

where  $p_1^2 + \beta^2 = k_1^2 = \epsilon_1 k_0^2$ . The continuity of  $H_y$  in the interface ( $x = 0$ ) implies that,

$$\beta_1 = \beta \quad (\text{A.12})$$

From  $H_y$  the components of the electric field are readily obtained making use of

Maxwell's equations. In particular the z- component has the form:

$$E_{z0} = -\frac{H_{y0}}{\omega\epsilon_0} p_0 \quad (\text{A.13})$$

$$E_{z1} = -\frac{H_{y1}}{\omega\epsilon_0\epsilon_1} p_1 \quad (\text{A.14})$$

Applying the continuity of the tangential component of the electric field at the interface ( $x = 0$ ) is obtained:

$$p_1 = \epsilon_1 p_0 \quad (\text{A.15})$$

After some algebra it can be shown that:

$$\beta = k_0 \sqrt{\frac{\epsilon_1}{1 + \epsilon_1}} \quad (\text{A.16})$$

$$p_0 = \frac{k_0}{\sqrt{1 + \epsilon_1}} \quad (\text{A.17})$$

$$p_1 = \frac{\epsilon_1 k_0}{\sqrt{1 + \epsilon_1}} \quad (\text{A.18})$$

Now, if losses are neglected and at a working frequency below the plasma frequency, dielectric permittivity is purely real and negative ( $\epsilon_1 = -|\epsilon_1|$ ) and the previous relations become:

$$\beta = k_0 \sqrt{\frac{|\epsilon_1|}{|\epsilon_1| - 1}} \quad (\text{A.19})$$

$$p_0 = \frac{k_0}{\sqrt{1 - |\epsilon_1|}} = j\alpha_0 \quad (\text{A.20})$$

$$p_1 = \frac{-|\epsilon_1| k_0}{\sqrt{1 - |\epsilon_1|}} = -j\alpha_1 \quad (\text{A.21})$$

For the particular case when  $|\epsilon_1| > 1$ , then it is obtained a propagating wave in the z

direction (in the interface) and evanescently decaying (from the interface to the respective media) in  $x$  direction. This kind of wave is the plasma wave. When losses are taken into account ( $\varepsilon'' > 0$ ) the resulting wave has complex values of  $\beta$ ,  $p_0$  and  $p_1$ , i.e. it has propagating and evanescent components in  $x$  and  $z$  directions. Anyway, if losses are low ( $\varepsilon'' \ll |\varepsilon_1|$ ) then the wave is essentially propagating in  $z$  and essentially evanescent in  $x$ . These waves are called plasmons and can exist in the interface of media of  $\text{Re}\{\varepsilon_1\} < 0$  and  $\text{Re}\{\varepsilon_0\} > 0$ .



# Chapter 3

## Enhanced Transmission Through Slits In Corrugated Metallic Planes: Slit + Grooves Structures.

---

---

*After the first report of Extraordinary Optical Transmission (EOT) through two-dimensional subwavelength hole arrays, a great research effort was developed, both from the theoretical and the experimental point of view.*

*In this chapter, first, it is given a brief historical description of the evolution from the hole array case to the single aperture on texturized metallic plane. The similarities and differences with the hole array are highlighted.*

*Then, the slit + grooves structure is compared with alike structures well-known in the microwave and millimeter wave range, and the main differences are pointed.*

*Later, the translation of the results obtained by other authors in the optical regime is experimentally proven in microwaves and millimeter waves. The mechanisms of the transmission enhancement are experimentally studied in detail. Also, the beaming capability of the structure is checked.*

*Finally, a technological advance is given by presenting several low-profile and all-metallic antenna prototypes based on these phenomena. Simulation as well as experimental results are obtained that show the feasibility of the proposed prototypes for applications in different wireless systems, like base station, WLAN in millimeter waves, and radiofrequency links.*

### 3.1 Evolution from Ebbesen's experiment towards the understanding of metallic structured surfaces.

After the first report of Extraordinary Optical Transmission (EOT) through sub-wavelength hole arrays [EBBE 98], many other works were boosted, both theoretically and experimentally. As it has been detailed in the previous chapter, the first attempts to explain the phenomenon identified the high transmittance with the coupling of light to surface plasmons. Under this assumption, some works explored structured surfaces to augment the transmission through a single subwavelength hole. The strategy proposed was: first, coupling light to plasmons by means of the appropriate surface structure and then converting plasmons in photons radiated through a small aperture. Besides - and simultaneously with other approaches - it was developed the study of EOT by simplifying the analysis to the easier 1D equivalent, the array of slits. This path was worked out in parallel with the aforementioned *small aperture + structured surface* method, and has the historic value to have been essential in the diffraction description of the phenomenon. In the following it will be presented in chronological order the different milestones leading towards enhanced transmission through slits in grooved metallic planes.

In 1999, Grupp et. al [GRUP 99] investigated the transmittance through a metallic surface drilled with holes and structured with dimples (circular indentations). They found an improvement of transmission when holes were surrounded by the structured surface. The reasoning made was that the dimples can give the support for the plasmon excitation that contributes to the enhancement. Also in 1999, Treacy proposed the first attempt of EOT elucidation based on slit arrays and obtained [TREA 99] good theoretical results in terms of dynamical diffraction, thus opening a new line of analysis different from the surface plasmon formalism. Almost simultaneously Porto et al. [PORT 99] studied slit arrays under the plasmonic point of view and identified two different mechanisms for the transfer of light from the input to the output face, namely: excitation of coupled surface plasmon polaritons on both surfaces and the coupling of incident light to slit waveguide resonances.

Later on, Avrutsky and co-workers [AVRU 00] published an attempt to explain EOT following the same surface plasmon approach. Importantly, they found that EOT can

exist by only imposing some periodicity in the interface corrugation, a conclusion that supports in some manner the results obtained in [GRUP 99]. Went et al. experimentally examined the transmission properties of metallic slit arrays and gave a simple explanation in terms of Fabry-Pérot cavities [WENT 00]. In the same path, Takakura [TAKA 01] studied the transmission of a single slot on a thick metallic plate and concluded with the same argument of Fabry-Pérot-like resonance (the experimental case was explored later by Yang and Sambles in [YANG 02]). Takakura suggested that the same analysis with arrayed slots could be used to clarify EOT mechanism. Shortly after, Went and Sambles presented measured reflectivity results on grooved gratings at microwave frequencies and found that the spectrum was strongly wavelength dependent [WENT 01]. The frequency details were attributed to the resonant excitation of self-coupled surface plasmon polaritons in the cavities of the samples, despite of the fact that surface plasmons do not exist in metals at microwave frequencies. In [HIBB 01] it was prolonged the experimental analysis of slit arrays in the microwave regime. The enhanced transmission was attributed to the excitation of resonant waves in the cavity and to the coupling of surface-plasmons at the entrance face.

By the end of 2001, Thio and collaborators [THIO 01] presented a paper continuing the master line introduced in [GRUP 99]: they sought enhancement of transmission through a single aperture. With this purpose, two different cases of subwavelength opening on structured metallic surface were experimentally explored: *hole + dimples array* and *hole + concentric circular grooves*. With the latter (optimal) geometry a transmission enhancement of a factor of 3, compared to the single hole case, was observed. They interpreted the enhancement as an effect of surface plasmon coupling to the incident light. The work was complemented with the technological investigation published in [THIO 02]. Later on, the paper by Cao and Lalanne [CAO 02] came to declare that surface plasmons actually could be playing a negative role in the transmittance of slit arrays. They found that high transmittance is mainly due to waveguide mode resonance and diffraction and that in the frequencies of surface plasmons excitation transmittance falls off to nearly zero. Meanwhile, Lezec et al. published an influential paper [LEZE 02] where the enhancement of transmission with a grooved surface was presented in detail. Concentric rings, as well as parallel strips grooves, were examined and a clear enhancement was observed. A strong angular dependence in the transmission was reported both theoretically and experimentally.

By the end of 2002, Treacy insisted in the dynamical diffraction theory to explain EOT in slit arrays [TREA 02], recognizing implicitly the possibility to extend the results to other frequency regimes where plasmons do not exist.

In 2003, Sarrazin et al. presented a work [SARR 03] where EOT was attributed to resonant Wood anomalies, which are intrinsically related to periodic structures. Later on, García-Vidal and co-workers [GARC 03] gave the theoretical explanation of the results presented in [LEZE 02]. They identified three mechanisms to enhance transmission through a slit on a textured metallic surface: groove cavity mode excitation or cavity resonance, in-phase groove reemission which depends directly on the periodicity and slit waveguide mode or, in other words, the aforementioned Fabry-Pérot cavity resonance noticed by Takakura [TAKA 01]. In this work, the authors talked only about geometrical parameters and did not give plasmons a fundamental role in the enhancement, contrary to what was said in the former work [LEZE 02]. Thus, they explicitly opened the way to the exploration of these results in other regimes like microwaves and millimeter waves. As an alternative approach Oliner and Jackson [OLIN 03] and Zhao et al. [ZHAO 03] modelled these phenomena as a leaky mode excitation, which in optics is a leaky plasmon mode, while in microwaves and millimeter waves is a standard leaky wave excited by the periodic corrugation.

### **3.2 Antecedents in microwaves: corrugated planes.**

Corrugated planes have been extensively used in microwaves in many applications and prominently in the antenna community. Travelling wave antennas normally use corrugated planes as support for guidance of TM waves. Depending essentially on the periodicity these antennas are classified in two groups: Surface-wave antennas, based on slow waves and with end-fire radiation and leaky-wave antennas, based on fast waves and with frequency dependent angle of radiation [COLL 69]. In travelling wave antennas the radiating aperture and the feeding structure are intimately contiguous [ELLI 03]. In Fig. 3.1(a) the schematic of a flare feed for a corrugated plane is shown. The guided wave is gradually matched to the corrugated plane which gives the necessary reactance to support a TM wave. Once it has been coupled to the surface mode it can be radiated via a slow wave, or a fast wave. Usually, the periodicity is

chosen to ensure many teeth per wavelength,  $d \ll \lambda$ . The width of the teeth  $L$  is narrow compared with the air section,  $L \ll d-L$ . Under these conditions TEM waves can be excited inside the indentations, which results in the inductive reactance necessary to couple impinging TM waves to guided surface waves. Note that this parameter set is essentially different from those chosen in the enhanced transmission based “*slit+grooves*” structures (here after referred as S+G structures), where periodicity is usually chosen comparable to the wavelength,  $d \approx \lambda$  [see Fig. 3.2 and Eq. (3.3)]

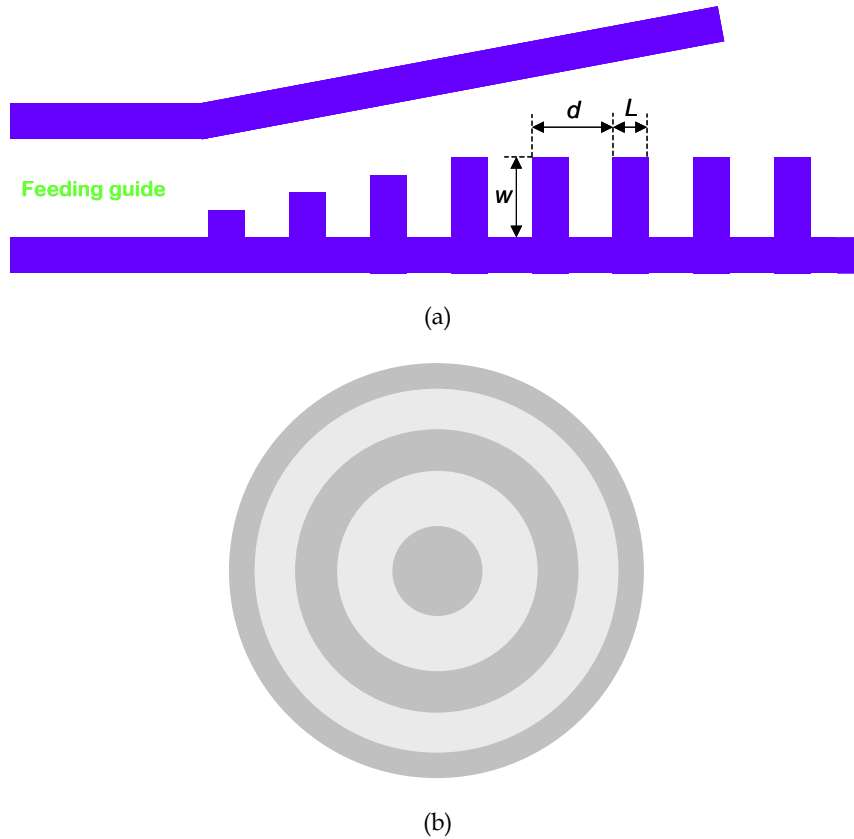


Fig. 3.1. (a) Flared feed for a corrugated surface and structural parameters. (b) Schematic of a Fresnel reflector.

Dielectric corrugated planes have also found application as reflectors in Fresnel Antennas, see a simple schematic in Fig. 3.1(b) [HRIS 00]. The principle of operation is basically the same as in Fresnel lenses but for a opaque structure. It is well known that a standard lens modifies the optical path for the multiple rays of a wave in order to

compensate the phase difference acquired during the propagation. In a Fresnel reflector the grooves provide a phase shift between adjacent zones which under the proper design conditions permits focallization. Fresnel reflectors are usually used as a planar alternative to paraboloid reflectors. Design of Fresnel reflectors take as input parameters the two focii distances, object and image. From these are obtained the diameters of the various zones, with an increment between adjacent zones that is not constant in general. This constitutes a dissimilarity with the S+G structures, where the radius increment, or period, between metal corrugations is constant.

Other important difference is that S+G structures are used in transmission. Fresnel formulas can also be used to construct Fresnel lenses. The phase difference between adjacent zones is usually achieved by using dielectric materials with different dielectric constant. Other approach due to Soret consists of shielding even (or odd) zones with a metallic leaving opened the odd (or even) zones. In contrast S+G structures present only a tiny central aperture and enhances transmission with the corrugations.

### 3.3 Microwave range enhanced transmission and beaming.

The remarkable results presented by Lezec et al. [LEZE 02] showing in the optical range strong beaming and high transmission through small apertures on a textured metallic plane and the theoretical discussion developed in [GARC 03] showing that geometrical parameters are sufficient to obtain the aforementioned features, opened the path for a new application of corrugated planes in the microwave range. In this range it had already been tested the transmission through a slit surrounded by two grooves [HIBB 02]. It remained still the study of enhancement with a grating.

$$a \ll \lambda \quad (3.1)$$

$$w \approx \frac{(2n+1)\lambda}{4} \quad (3.2)$$

$$d \approx \lambda \quad (3.3)$$

$$h \approx \frac{n\lambda}{2} \quad (3.4)$$

In order to check this possibility, the structure of Fig. 3.2 was constructed by using numerical control workshop in an aluminum plate of thickness  $h = 8$  mm. It consists of a narrow central slit of width  $a = 2$  mm flanked by a finite number of grooves of the same width and depth  $w = 3$  mm, 15 grooves on either side, with periodicity  $d = 20$  mm on a metallic plane. The analysis of this S+G structure is given in [GARC 03] assuming perfect electric conductor boundary conditions at the metal and a modal expansion of the electromagnetic fields inside the grooves and in the central slit. To excite the grooves' resonance the impinging wave must be TM, i.e.  $\mathbf{H}$  directed along  $y$ . The set of parameters that optimizes the transmittance is given in [GARC 03] and reproduced here (Eqs. (3.1)-(3.4)). With this structure two different experiments were carried out: transmission and beaming measurements.

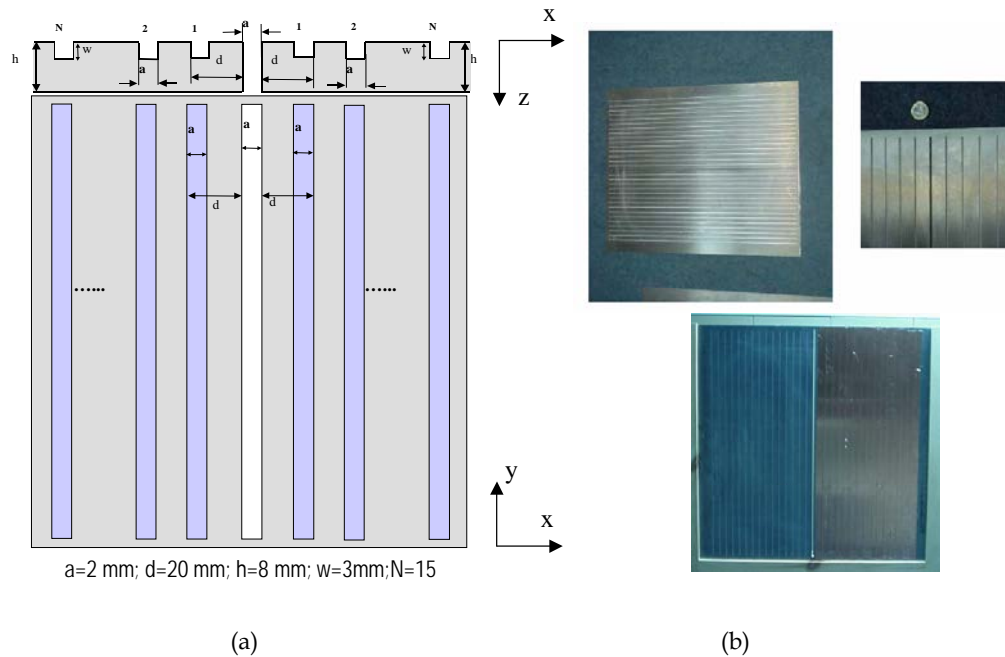


Fig. 3.2. Schematic of the slit + grooves structure for measurement in the microwave range with the numerical value of the parameters (a) and photograph of the fabricated prototype placed on the support (b)

### 3.3.1 Transmission results.

The measurement of the structure is made by means of an antenna test range and a HP8510C Vector Network Analyzer (45 MHz–26 GHz). The frequency span extends

from 10 to 18 GHz. In this frequency range, the slit-aperture to wavelength ratio is around 0.1 (0.12 at 18 GHz). A photograph and schematic of the experimental setup is shown in Fig. 3.3. It consists of an emitting horn antenna placed at a fixed distance of 50 cm rear the sample, and a receiving horn antenna moving along a vertical mast from 25 to 275 cm with a step of 25 cm. It can be seen that the metallic plate is surrounded by absorbing material in order to avoid spurious effects due to diffraction. Two different cases have been tested: Corrugations at the input face or input corrugation (IC) and corrugations at the output face or output corrugation (OC).

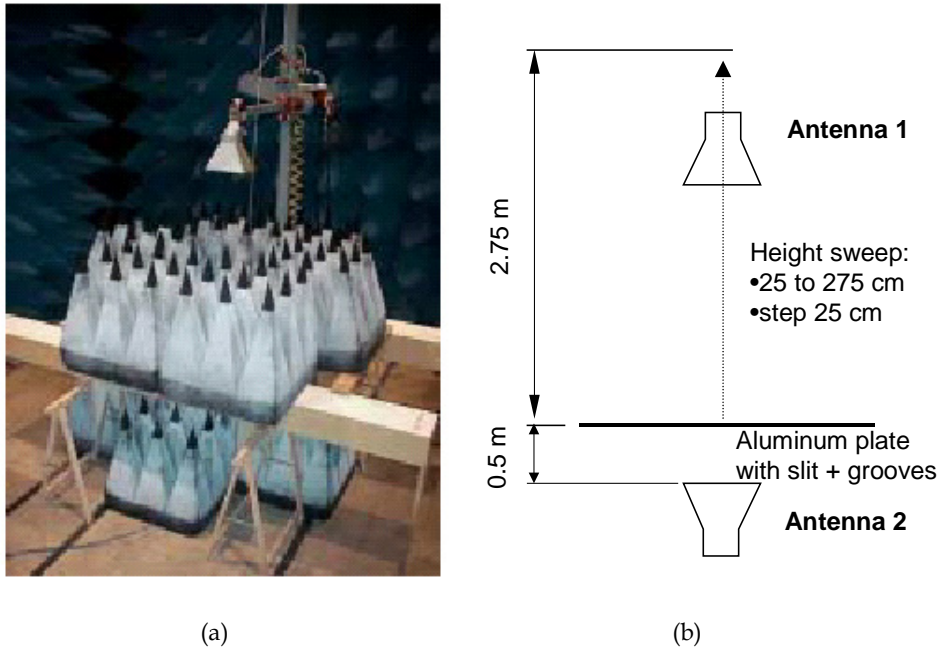


Fig. 3.3. Photograph of the experimental set-up (a) and schematic with the relevant parameters (b) for the transmission measurements of the slit+ grooves structure.

The experimental results are shown in Fig. 3.4. In panel (a) it is shown the transmission for the IC case and selected distances of the receiving antenna. It can readily be seen a clear resonance around 13.5 GHz, the design frequency, followed by a minimum of transmission at 14.5 GHz corresponding to the Rayleigh-Wood anomaly. For an infinite structure and under normal incidence, Rayleigh-Wood anomaly should occur at  $\lambda = d$ , that is, at  $f = 15$  GHz. In this case it is shifted towards lower frequencies, as usually happens in finite systems. It is also observed that the spectrum is basically uniform for all the distances. The power level decreases as the

distance is increased, thus accounting for propagation losses in free space. A sharp ripple with decreasing level as the receiver distance is increased appears. This ripple is most likely related with a Fabry-Perot like resonance in the cavity formed by the metallic sample and the receiving antenna.

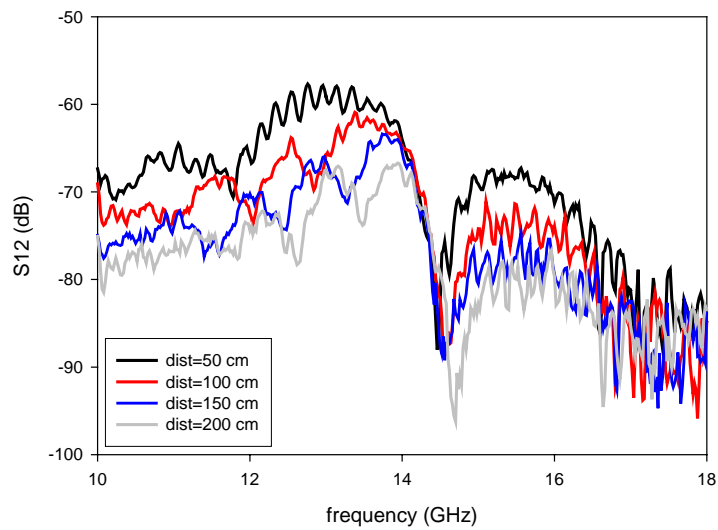
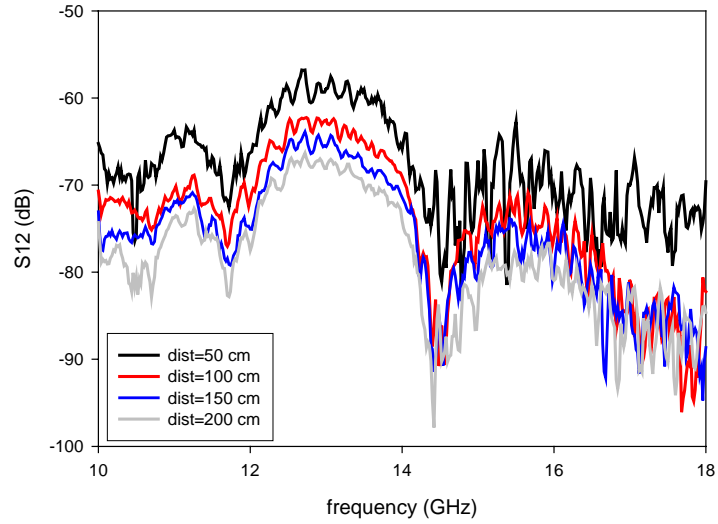
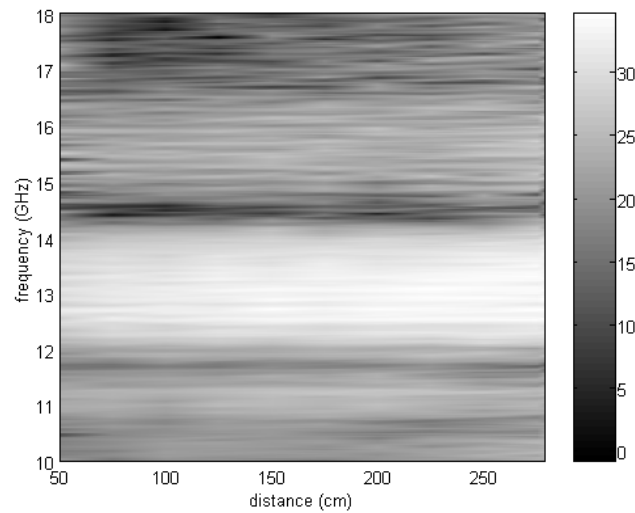
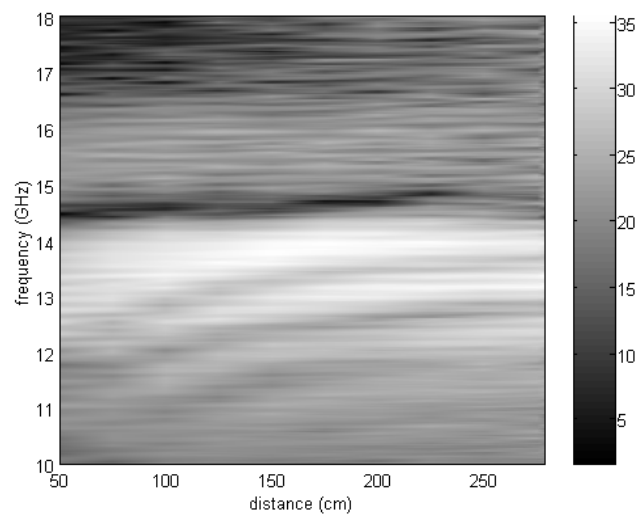


Fig. 3.4. Measured transmission spectra for various distances of the receiving antenna for corrugations facing the emitter (input corrugation, IC) (a) and corrugations facing the receiver (output corrugation, OC) (b).

Panel (b) displays the measurement for the OC case and the same receiver distances. Here a clear resonance around 13.5 GHz is also noticed. However, in this instance the shape of the spectrum depends on the distance. All along the spectrum the power level decreases with increasing distance, but the resonance is sharper and better defined as the distance is incremented. Again a ripple due to Fabry-Pérot resonance is observed, being more pronounced for short distances.



(a)



(b)

Fig. 3.5. Post-processed measured power corrected by the subtraction of free-space propagation loss for the IC case (a) and OC case (b).

The reason for this dissimilar behavior in the IC and OC cases is pointed out in [GARC 03]. Corrugations facing the emitter optimize the amount of collected power, while corrugations facing the receiver focus the power in singular angular directions. Thus, under IC illumination the collection of power is the same regardless the distance of the receiver, as the path transmitter - sample remains unaltered. The power collected is coupled to the output face across the central slit and is isotropically radiated (actually a cylindrical wave), like a long and narrow slot on a metallic plane. In this way, the measured spectra show the same shape for all the receiver distances and only a power decay related with the propagation loss of the cylindrical wave is observed. This can be plainly observed if propagation-loss is subtracted from the experimental data, see Fig. 3.5(a): the spectra present essentially the same features and the resonance is insensitive of the receiver location.

On the other hand, the results for the OC illumination differ for the several receiver distances. Now a tiny fraction of power is coupled through the slit. This power is re-radiated by the periodic structure of the output face, which contributes to the field radiated by the slit alone. At a sufficiently large distance the near field features do not appear (farfield is recovered) and the general shape of the spectrum does not depend on the distance, showing a peak in the zone of enhancement. Attending to Fig. 3.5(b) it is immediately seen that in the OC configuration the resonance is much more clearly defined for larger distances.

The same could have been observed for the IC configuration if the transmitter - sample distance had been increased. It is important to note that the design of the structure is made assuming plane wave, or in-phase, excitation. Under that condition, the resonance of the structure is sharp and well defined. Invoking reciprocity, the results obtained in Fig. 3.4(b) can be interpreted in the reverse way, assuming that the transmitter is moving and the receiver remains still. In that case, as the transmitter is taken away from the structure, the illumination of the grooves is more uniform and approximately in-phase. The overall response is a well-defined resonance for large distances. Anyway, the best situation would be one in which both the transmitter and the receiver would be at a sufficiently distant from the structure in order to have approximately plane wave excitation from the transmitting side and farfield recovering from the receiving side.

The structure in OC illumination has been simulated with *CST microwave studio™*.

Taking advantage of the existing symmetries it has been made infinite in the  $y$  dimension. Excitation of the structure is achieved by means of a plane wave impinging normally. Using an electric field probe located at a distance of 50 cm the electric field is recorded. The result is shown in Fig. 3.6. It has been compared with the measurement at that distance, after normalizing both simulation and measurement to their respective maxima. It is noticeable the good agreement observed.

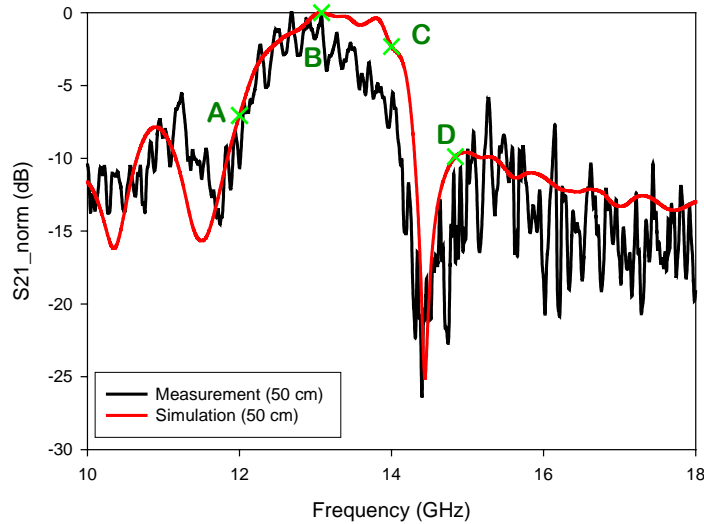


Fig. 3.6. Simulated (red) and measured (black) spectrum for the OC configuration at a receiver distance of 50 cm.

### 3.3.2 Beaming results

It has been mentioned that one of the most remarkable features presented in the work by Lezec et al. [LEZE 02] is the strong beaming observed for this structures, in OC configuration. In other words, it can be said that the high transmission in this configuration is a consequence of the angular power concentration.

To measure the beaming capability the experimental set-up shown in Fig. 3.7 was implemented. It consists of a rotary platform supporting an emitting horn antenna illuminating with vertical polarization the sample, with both, the slot and the corrugations, normal to the incident E-field vector. The receiving horn is fixed at 300 cm from the sample. The angular response of the structure is measured with a step of 1 deg.

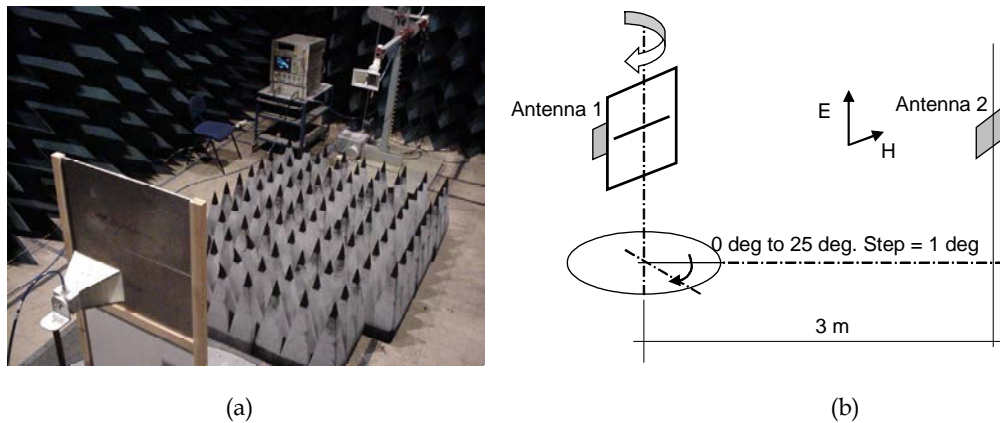
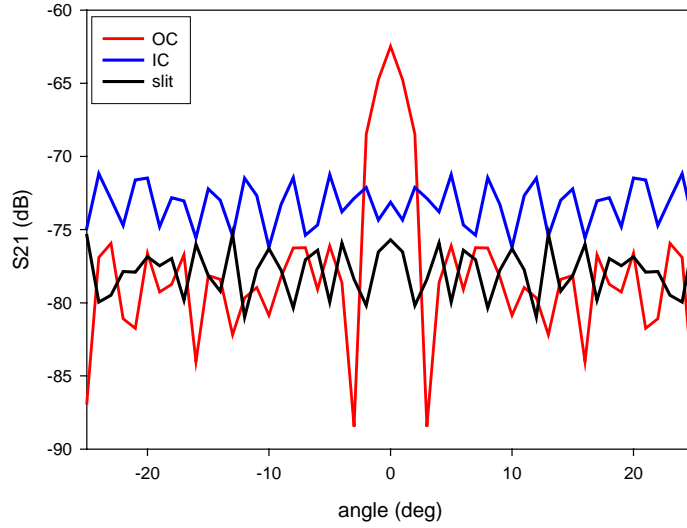


Fig. 3.7. Photograph of the experimental set-up for the farfield measurements (a) and schematic with the constituent parameters (b)

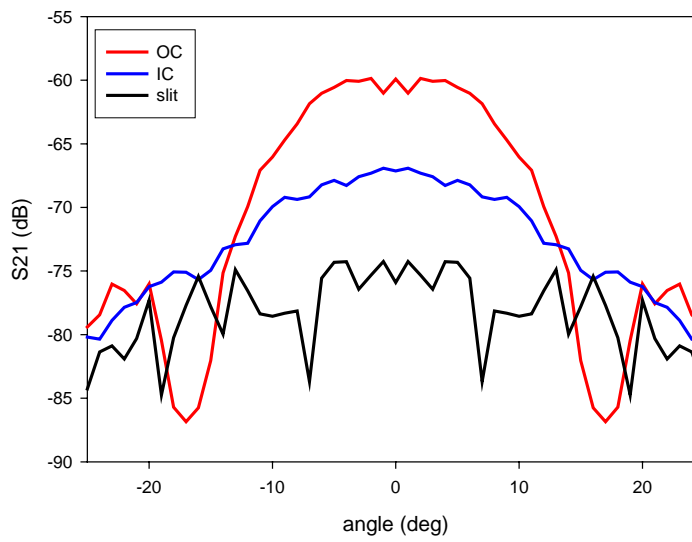
The results of the beaming measurements are given in Fig. 3.8. for the E-plane in panel (a) and the H-plane in panel (b). Three cases have been investigated: single slit (black), OC (red) and IC (blue). It is seen that in the H-plane no beaming is observed, but only the effect of the finite metallic plane on the radiation of the central slot. On the contrary, in the E-plane case the features observed are much more interesting. First, for a single slit a uniform level of power oscillating around  $-78$  dB is seen for all directions. For the IC case, the efficient collection of power achieved when the corrugations face the emitter produces an improvement of about 5 dB with no privileged directions. Things change radically when corrugations are faced to the receiver. In the OC case, the power is strongly focused in the normal direction and undergoes an enhancement of 13 dB within a very narrow angular range. For any other direction, the level of signal is very similar to that of the single slit. The  $-3$  dB angular aperture in this case is  $\pm 3$  deg.

A nice graphical picture of the near-field behavior of the OC structure is obtained with *CST Microwave Studio*<sup>TM</sup>. It has been plotted in Fig. 3.9 the power profile in the  $x$ - $z$  plane at the frequency points highlighted in Fig. 3.6. It is apparent that the S+G topology in the OC configuration acts as an angular scanner as the frequency is swept. This is in good agreement with the leaky wave formalism [OLIN 03] [ZHAO 03]. The radiation angle in leaky wave antennas can be tuned with frequency. In the particular case of S+G, the corrugations at each side of the central slit radiate at the same angle but in opposite  $x$  direction, a fact that is clearly shown in Fig. 3.9(c) and (d). The

contribution of both sides is optimal in near-broadside radiation (Fig. 3.9.(b)) producing a narrow main lobe around 0 deg. Besides, the grooves and central slit resonances have also been tuned to that frequency, resulting in a maximum of radiation for the design frequency.



(a)



(b)

Fig. 3.8. Angular pattern in the farfield measurements and three different cases: single slit (black), OC (red) and IC (blue). (a) E-cutting plane (b) H-cutting plane.

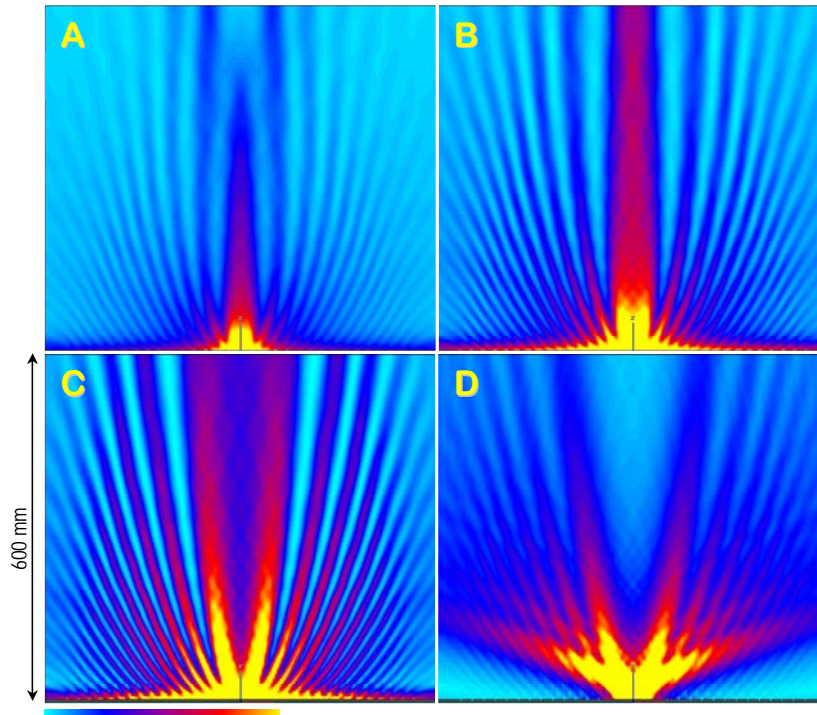


Fig. 3.9. Power profile in the  $x$ - $z$  plane for the OC configuration and four different frequencies: (a) 12 GHz, (b) 13 GHz, (c) 14 GHz and (d) 14.84 GHz. The parameters of the structure are as given in Fig. 3.2.

A major part of the results shown in this section have been published in *Article 3.1*. Subsequent experimental results in the microwave range appear in [SENA 05].

### 3.4 Millimeter-wave enhanced transmittance and reflectance: quasioptical illumination

In this section, the results of the *slit + grooves* structure are extrapolated to the millimeter wave frequency range. Five aluminum samples were fabricated by means of micromachining milling technique. The schematic and the photograph of the prototypes are shown in Fig. 3.10. All the aluminum wafers have an external diameter of 62.4 mm, with parameters, following the notation of the figure:  $a = 0.6$  mm,  $d = 3$  mm,  $w = 0.48$  mm, and  $N = 5$ . To evaluate the enhancement obtained when the metal is textured, plates with only central slit and plates with one face grooved were constructed. Two different metal thicknesses were used:  $h = 1$  mm,  $h = 1.5$  mm. An

extra sample with grooves on both faces and  $h = 1.5$  mm was also constructed and measured.

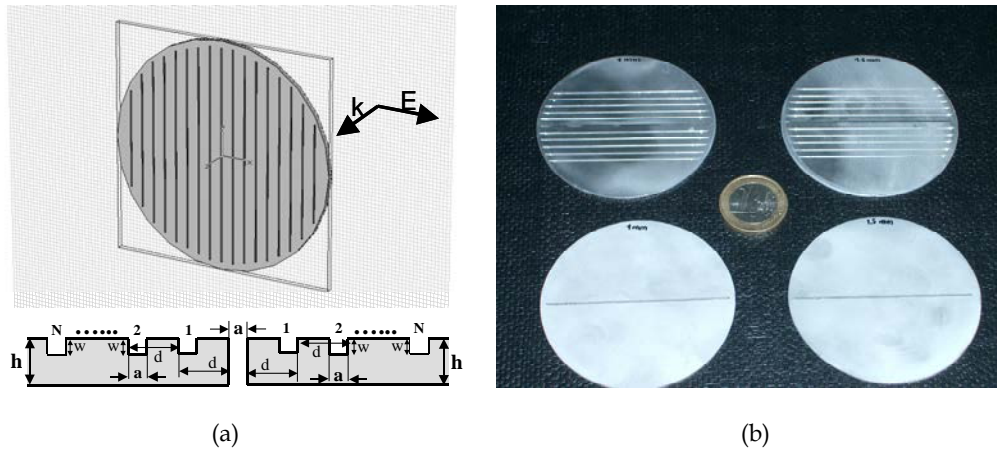


Fig. 3.10. (a) Schematic of the slit + grooves structure for measurement in the microwave range. The electromagnetic wave impinges normally to the structure the electric field polarized along  $x$ . (b) Photographs of four samples analyzed in the experiments with:  $a = 0.6$  mm,  $w = 0.48$  mm,  $d = 20$  mm,  $h = 1$  mm and  $1.5$  mm. Not shown the prototype with grooves on both faces.

The measurement of the prototypes was made by using an *AB-millimetre™ Millimeter Wave Vector Analyzer* with capability to make measurements in the frequency range from 40 to 260 GHz. In this case, the span was restricted to the W-band which extends from 70 to 110 GHz. The experimental set-up makes use of the quasioptical illumination described in the section 2.3.1. A graphical picture of the whole experimental set-up is shown in Fig. 2.5.

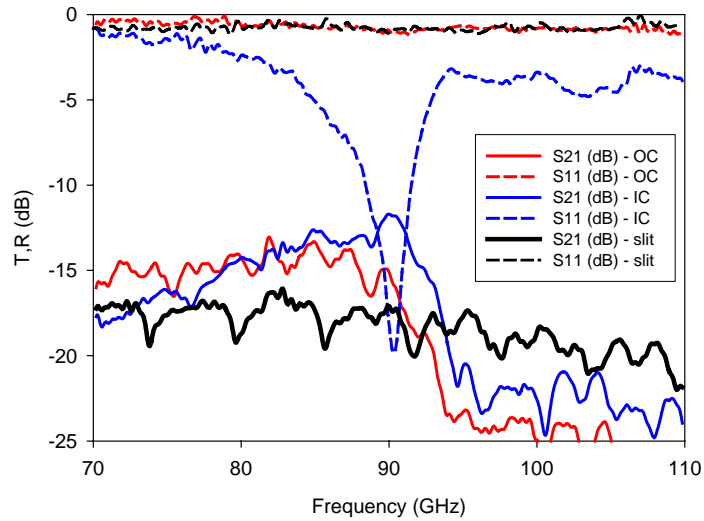
For the transmission and reflection measurements the abovementioned cases were explored: single slit, input corrugation (IC) and output corrugation (OC). In addition, the combined effect of input and output corrugations (IOC) was tested with the double face grooved sample.

The results are plotted in Fig. 3.11, where the reflection coefficients are represented with dashed traces and the transmission coefficients with solid lines. The single slit case is drawn in black, the OC one in red and the IC in blue.

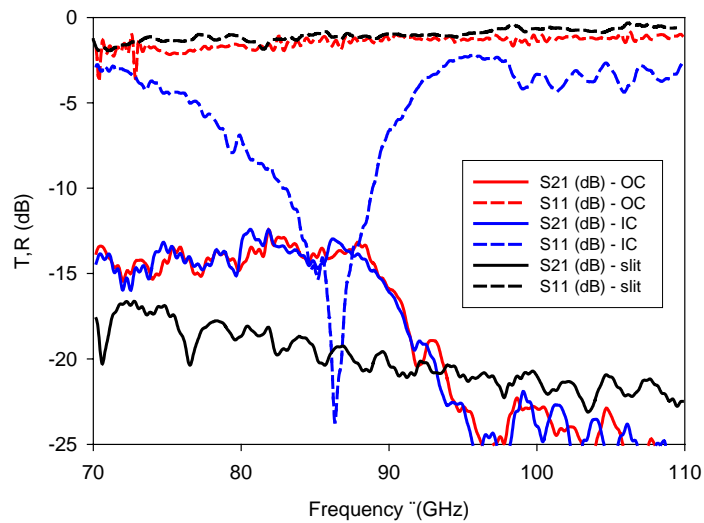
In panels (a) and (b) are shown the results of the wafers of thickness  $h = 1$  mm and  $h = 1.5$  mm respectively. The IOC ( $h = 1.5$  mm) is in panel (c). It is readily seen that the transmittance around 90 GHz is enhanced when the metallic plane surrounding the

slit is grooved in any of the configurations measured.

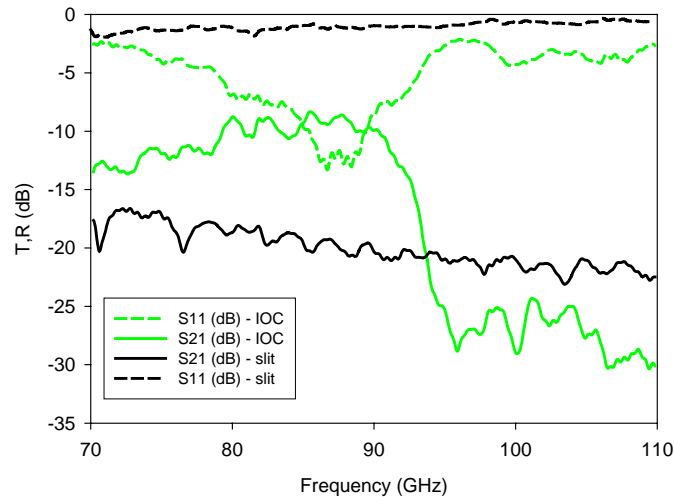
Comparing panels (a) and (b) it is observed that the best transmittance is achieved when  $h = 1.5$  mm. In this case the transmission in IC and OC is essentially the same, whereas for  $h = 1$  mm, the transmission is better in the IC configuration. Attending to the reflection coefficient, a sharp resonance is detected for the IC case. In the OC case the measurement is very similar to the single slit situation.



(a)



(b)



(c)

Fig. 3.11. Experimental transmittance spectra for (a) structure with only one face corrugated and plate thickness  $h = 1$  mm; (b) the same with  $h = 1.5$  mm; and (c) structure with grooves on both faces. Notation: dashed line represents reflection coefficient; solid line represents transmission coefficient; black curve is the single slit response; red lines are for the OC case (grooves facing the receiver); blue lines are for the IC case (grooves facing the emitter); green lines are for the IOC case.

Notice that this results back up in an alternative way the proposition made in [GARC 03] for the enhancement in these structures. With IC configuration, the improvement is a consequence of the efficient collection of power achieved with the grooves, which is manifested in a sharp dip in the reflection coefficient and a growth in the transmission. The enhancement in the OC configuration is accomplished by means of in-phase groove re-emission. In this case only the transmission is raised up, and the reflection coefficient does not present any notable feature, resembling that of the single slit.

Furthermore, a comparison between panel (c) and panels (a) and (b) shows that transmittance is clearly enhanced when grooves are milled on both faces (IOC configuration) with an improvement of around 3 dB with respect to IC and OC configurations and up to 9 dB with respect to the single slit. This is the result of the combination of both effects: efficient power collection on the input face (IC) and efficient beaming on the output face (OC). It should be noted, however, that full

transmission is not available because the incident circular symmetric Gaussian beam is broken in the slit and the transmitted quasi-cylindrical beam is not well matched to the last pair of mirrors. The reflection coefficient is apparently noisy, with two distinct adjacent peaks. The reason for this could be an inaccurate matching of the grooves on both faces due to fabrication tolerances.

The results shown in this section are developed in *Article 3.2*.

### 3.5 Application to all-metallic low-profile antenna feeder prototypes based on “slit + grooves” structures.

It has been proven that narrow apertures on a textured metallic plane also presents enhancement of transmission in the microwave and millimeter wave range, as happened in optics. Apart from the obvious interest in replicating the results obtained in optics, several features make these structures interesting from the engineering point of view:

- **All metallic:** This is desirable in applications where dielectrics can be a major drawback. For instance, in space applications dielectrics may harm a communication system due to the dependence of their electrical parameters on temperature. The cosmic radiation can severely degrade the dielectric's performance.
- **Low profile:** The structure consists of a flat metallic plane with no special profile, which makes it useful and handy. A flat plane is much easier to fit than a paraboloid for example.
- **Low cost design:** The design is easy and immediate, with no intricate corners or curves.
- **Strong beaming in broadside:** This characteristic is very valuable in the design of directive antennas.

Up to this point, these structures have been used as a special kind of metallic lenses: an emitting antenna illuminates from the rear the metallic plane which in turn re-emits power to the receiver. It would be very profitable having all the radiating system in a single device, and not only as a radome. A possible option is to connect a

coaxial-to-waveguide transition as the feeding of a slit on corrugated metallic plane. To avoid leakage and mismatch, the central slit is transformed into a slot, i.e. the lateral walls are brought closer, see Fig. 3.12.

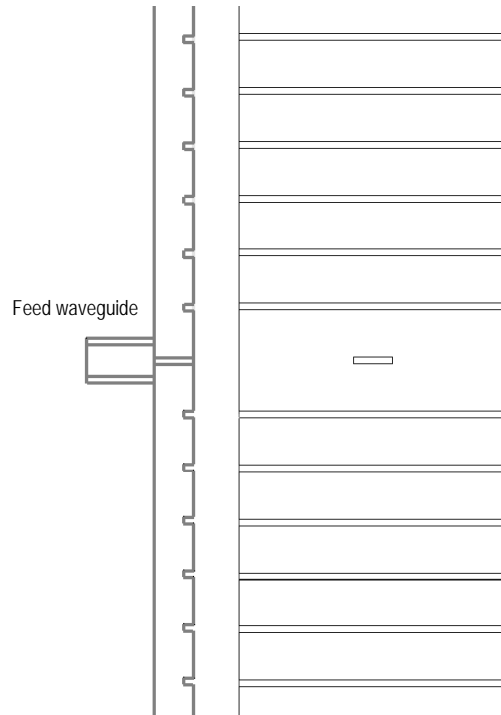


Fig. 3.12. Schematic of the waveguide feeding arrangement and the replacement of the infinite slit by a practical slot.

With these two ingredients a single piece radiator can be designed. The first objective to accomplish is ensuring a good level of coupling through the central slot. This can be achieved by exciting a resonance inside the cavity. For infinite slits, the standard procedure has been to use the longitudinal dimension (the metal thickness) to excite a longitudinal resonance. But having a finite slot, the lateral dimension can also be used to excite a transversal resonance. This approach has many advantages as will be apparent in what follows. Once the slot is in resonance and coupling power to the output face, the radiation performance is molded with the grooves, i.e. the structure is working in the OC configuration. This results in a rich variety of all-metallic and low profile antennas.

Metallic antennas have been developed in *Article 3.3*, *Article 3.4* and *Article 3.5*

### 3.5.1 High gain and low profile "Slot + 12 grooves" antenna.

The first antenna prototype implemented with this technique is the "Slot + 12 grooves" antenna shown in Fig. 3.13. This antenna is a direct extension of the S+G structure shown in sections 3.3 and 3.4. The feeding is realized by means of a coaxial-to-waveguide transition and the lateral dimension of the slot is reduced. The horizontal dimension of the metallic plate has also been reduced since the slot is finite.

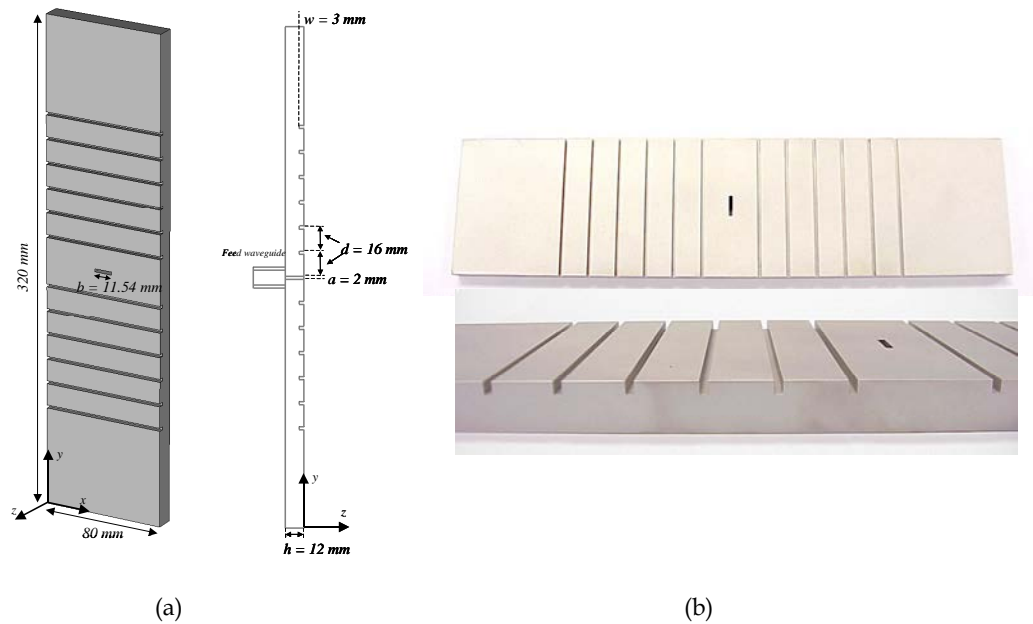
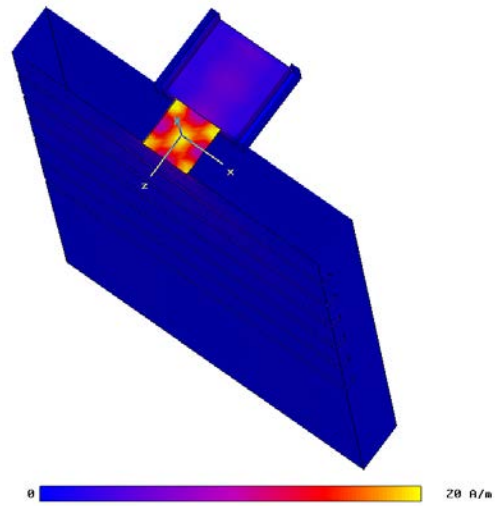
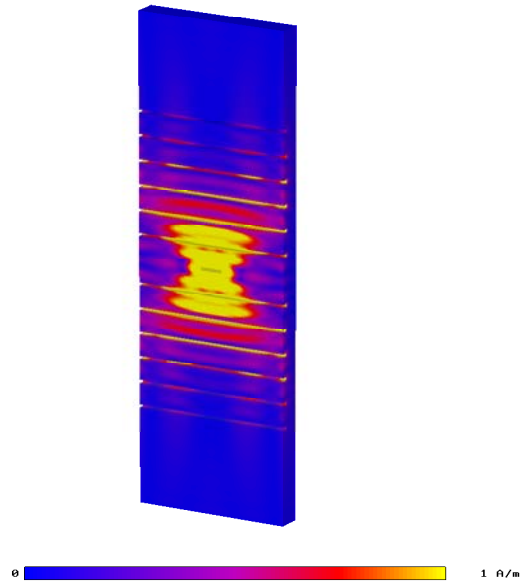


Fig. 3.13. Schematic with the antenna dimensions (a) and photographs of the "slot + 12 grooves" structure (b)

In Fig. 3.14 it is plotted the magnitude of the total surface current distribution of the antenna at the longitudinal resonance frequency. In panel (a) is the current inside the slot and in panel (b) the distribution on the output surface. The grooves' depth has been tuned to resonate at the working frequency. This resonance is accompanied by a power leakage or radiation which makes the current be more intense in the grooves near the slot. From a leaky-wave point of view, this resonance is not necessary, since only a periodic structure is needed. Anyway, making the grooves resonant helps in coupling power to radiation. Due to this resonance, the power is efficiently radiated with a reasonable small number of grooves which is important in designing short enough structures.



(a)



(b)

Fig. 3.14. Simulation result of the surface current distribution inside the central slit in its longitudinal resonance (a) and on the output surface (b)

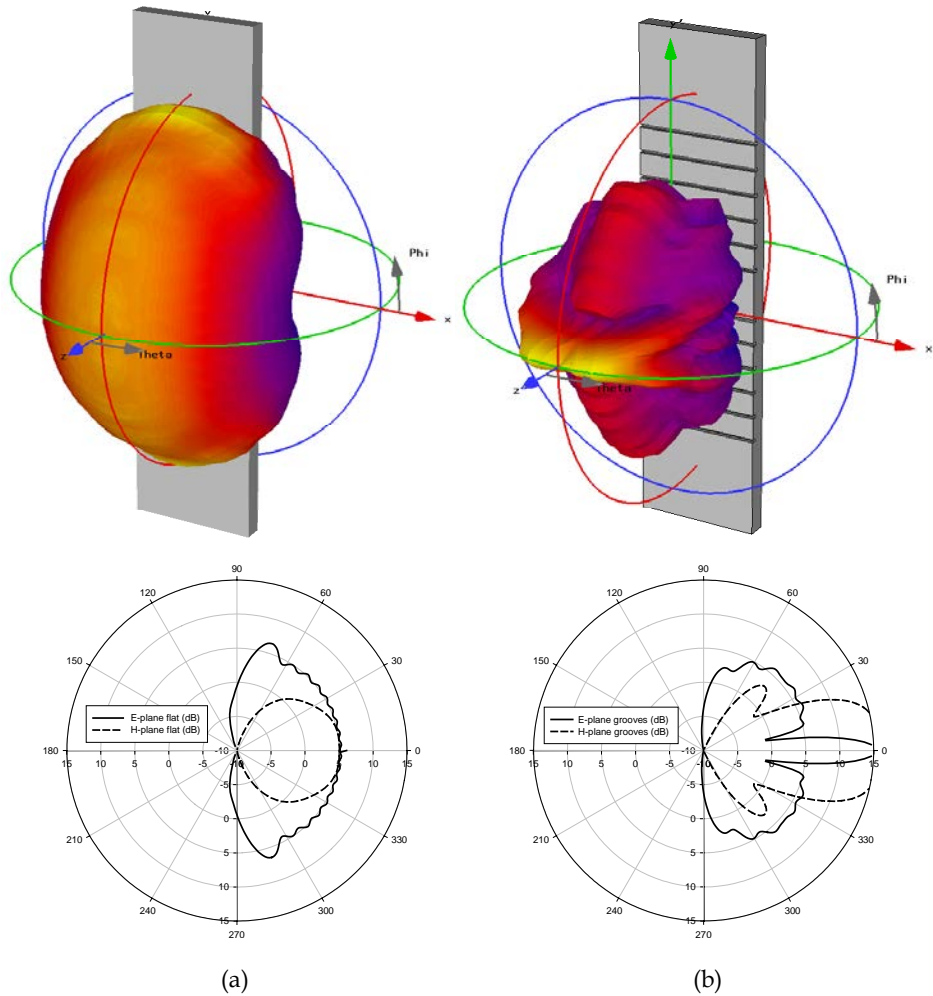


Fig. 3.15. Simulation results for the 3-D farfield diagram (above) and polar diagram (below) for single slot on a finite perfectly conducting flat plane (a) and for the "Slot + 12 grooves" antenna (b).

To observe the improvement introduced by introducing grooves in the plane, it is shown in Fig. 3.15 the farfield radiation patterns obtained with *CST Microwave Studio™* for a finite slot on a finite perfectly conducting flat plane, panel (a), and for the antenna prototype at the working frequency of 16.5 GHz. Both the three-dimensional farfield pattern and the polar E- and H-planes are plotted. For the flat plane case a gain of more than 6 dB is predicted with an almost isotropic diagram. When corrugations are included in the metallic plane the gain is boosted up to 15.4

dB, more than 8.9 dB than for a flat metallic plane. It is clear in the polar plot the enhanced directivity in E-plane.

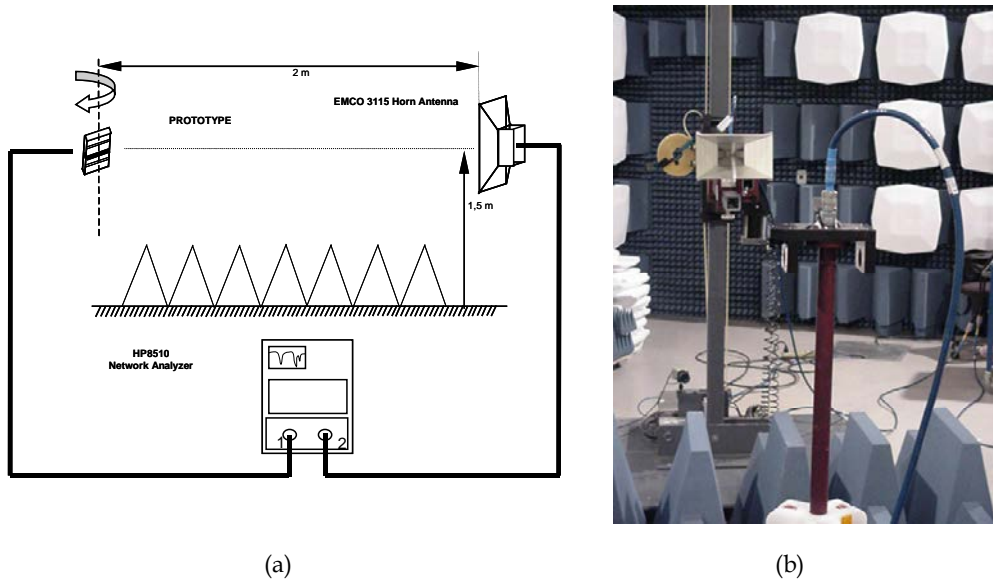


Fig. 3.16. (a) Schematic of the experimental set-up for the measurement of the antenna prototypes based on enhanced transmission "slit + grooves" structures. (b) Photograph of the experimental set-up in the anechoic chamber.

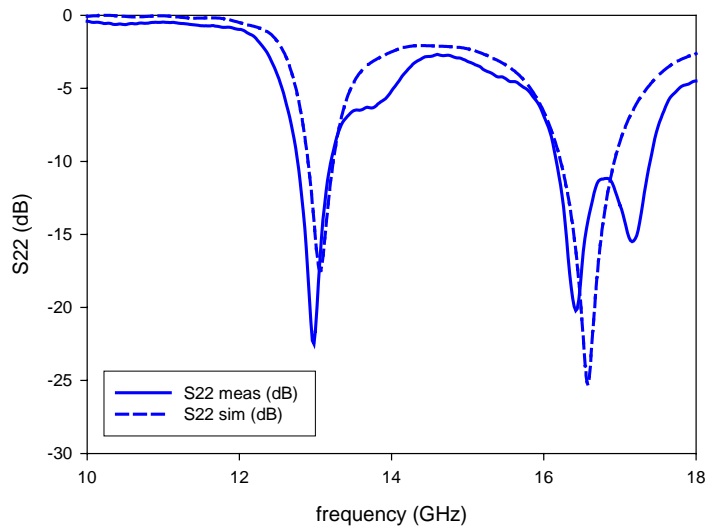


Fig. 3.17. Reflection coefficient: measurement (solid line) and simulation (dashed line). Some discrepancies are detected at the 16 GHz resonance, probably due to meshing effects in the simulation or tolerances in the fabrication.

The prototype shown in Fig. 3.13(b) was constructed by numerical control machining. By inspection of the photograph it is seen that relatively thin antennas are feasible. The frequency response as well as the farfield characteristics were measured by means of the LABEIN antenna test range and an *HP 8510C* Vector Network Analyzer (45 MHz–26 GHz), in the frequency range of 10 - 18 GHz where the slit-aperture to wavelength ratio is around 0.1.

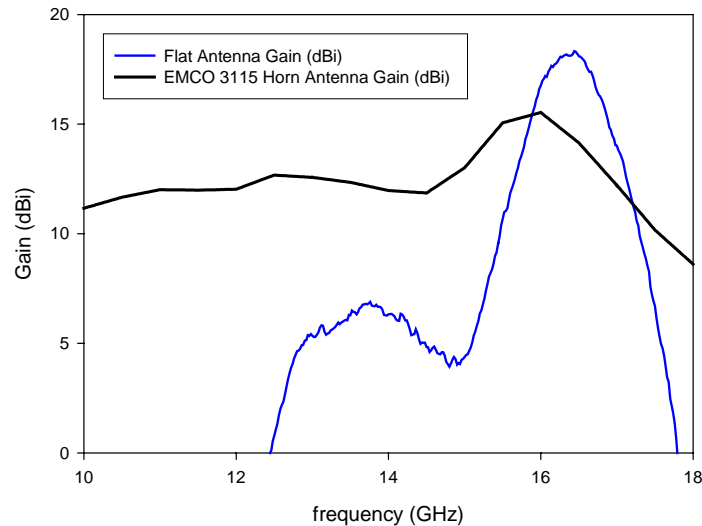


Fig. 3.18. Spectral gain in the band from 10 to 18 GHz for the “Slot+12 grooves” Antenna (blue curve) and an EMCO 3115 Horn Antenna (black line)

A calibrated standard test horn antenna was placed opposite to the antenna under test at a distance of 2 m. Both antennas were placed 1.5 m above the ground, and this floor was properly covered with absorbing material to obtain full anechoic conditions. The prototype under test was located on a rotary platform to measure its farfield radiation pattern. The experimental set-up is depicted in Fig. 3.16 with a picture of the actual experiment.

The experimental reflection coefficient is given in Fig. 3.17 along with the simulation result. Two resonances are detected, one around 13 GHz and the other around 16 GHz, corresponding respectively to transversal slot resonance and longitudinal slot resonance. Some discrepancies are observed in the upper resonance probably due to non perfect meshing and/or tolerances of fabrication. Notice also that the metal thickness is  $h = 12$  mm which is not the  $\lambda/2$  resonance for 16.5 GHz in a closed cavity, which is around 9.1 mm. The reason is that the slot is bounded by a waveguide on one

side and the free-space on the other, which is essentially different of a perfect reflector boundary. The final value of the metal thickness is tuned to resonate at the desired frequency with the help of the simulator.

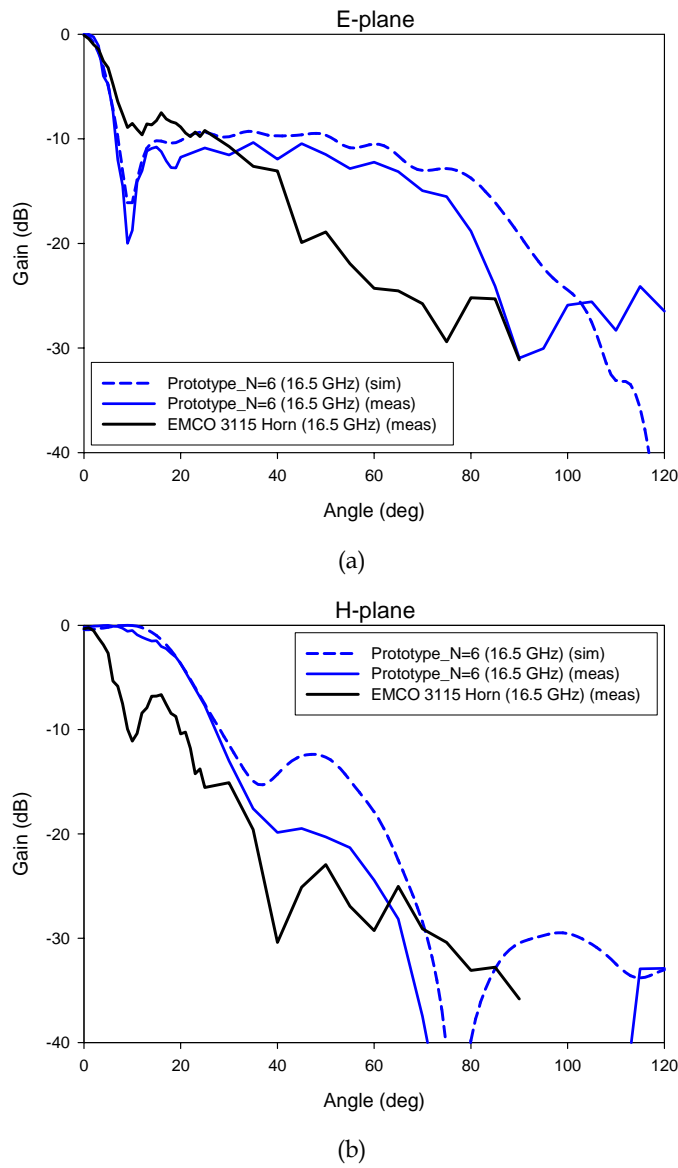


Fig. 3.19. Farfield diagrams in cartesian coordinates normalized to the maximum power for the measured “Slot+12 grooves” Antenna (solid blue curve) and an EMCO 3115 Horn Antenna (solid black line). Also shown the simulation results in dashed blue line. The better directivity is seen in the E-plane (panel (a)) whereas in the H-plane the antenna is less directive (panel (b)).

By means of the *gain-transfer (gain-comparison)* method, the antenna gain is measured [IEEE 79]. An 18 dB value at the design frequency is obtained, see Fig. 3.18. Note that the standard horn antenna has a gain of 12 dB at the same frequency. By inspection of Fig. 3.17 it can be concluded that the proposed antenna works well at the design frequency, presenting a peak of gain 6 dB higher than that of the standard horn antenna. The angular behavior of the antenna is also tested in the range from 0 to 120 degrees. The results are given in Fig. 3.19 in cartesian coordinates and normalized to the maximum power. The simulation results and the diagram of a standard horn antenna are also included. Reasonable agreement with simulation can be observed for the E- and H-planes (correspondingly panel (a) and panel (b)). The measured farfield shows nice features in directivity with a -3 dB angular width of 12 degrees in the E-plane and 30 degrees in the H-plane. As expected, the directivity is better in the E-plane, as happens in these structures where the current density is distributed preferently along the vertical (E-field) direction.

### 3.5.2 Isotropic enhanced “Slot + 2 grooves” antenna.

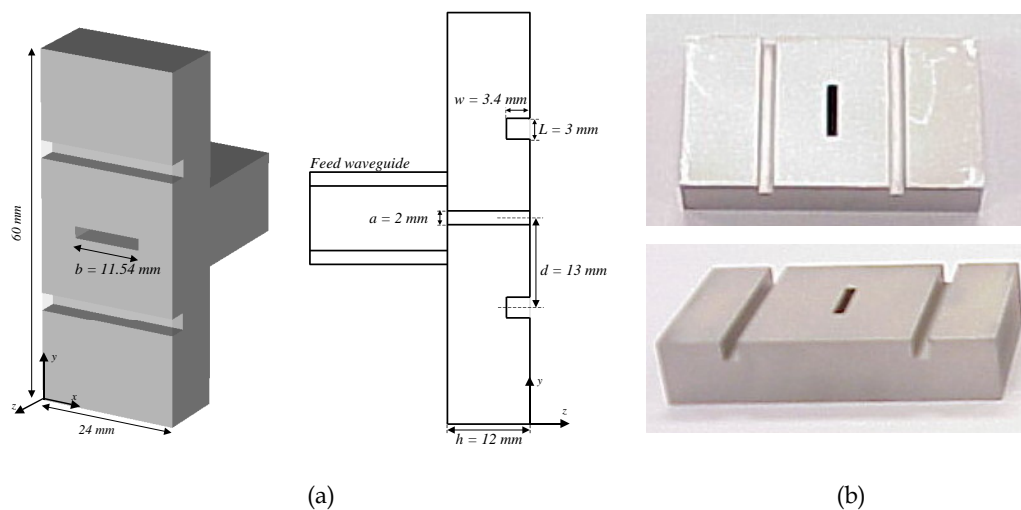


Fig. 3.20. Schematic with the antenna dimensions (a) and photographs of the “Slot + 2 grooves” structure (b)

It has been seen in the previous section that the gain of a slot on a metallic plane can be enhanced by just drilling grooves on the plane. Ideally the gain can be improved by increasing the number of grooves. This would logically result into a more directive

farfield pattern. However, more grooves implies a bigger structure, which can turn out to be impractical for some applications. In this section a miniaturized version of the aforementioned design is presented. It is the “Slot + 2 grooves” antenna, see Fig. 3.20, that shares many features in common with the previous one and will be explained in less detail.

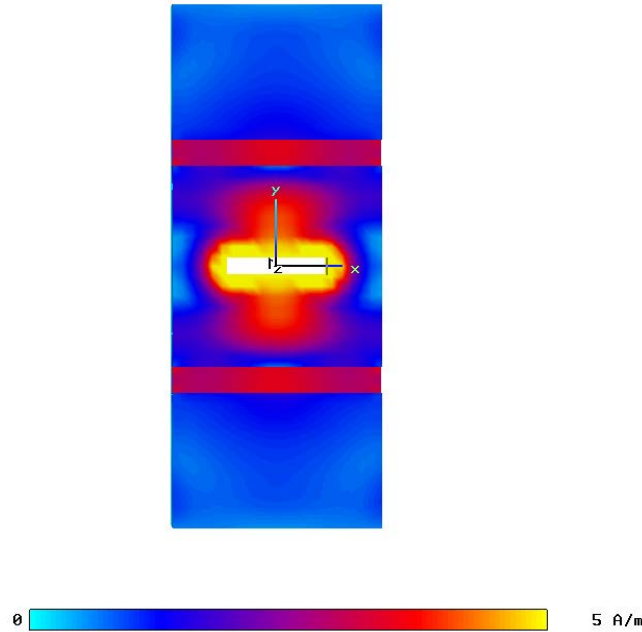


Fig. 3.21. Surface current distribution on the output surface. At the working frequency there is a clear grooves’ resonance.

The prototype consists of a narrow slot flanked by two grooves on a metallic plane and fed by means of a coaxial-to-waveguide transition. It can be seen that the parameters of the antenna have been slightly modified compared to the previous case. The distance between the grooves and the central slot is now  $d = 13$  mm with a groove length  $L = 3$  mm. This set of parameters seems to be optimal. The deviation from the analytical formulas given in [GARC 03] may be due to the finiteness of the present structure (with only one groove on each side). Recall that the analytical approach is developed for an infinite slit flanked by a relatively large number of grooves.

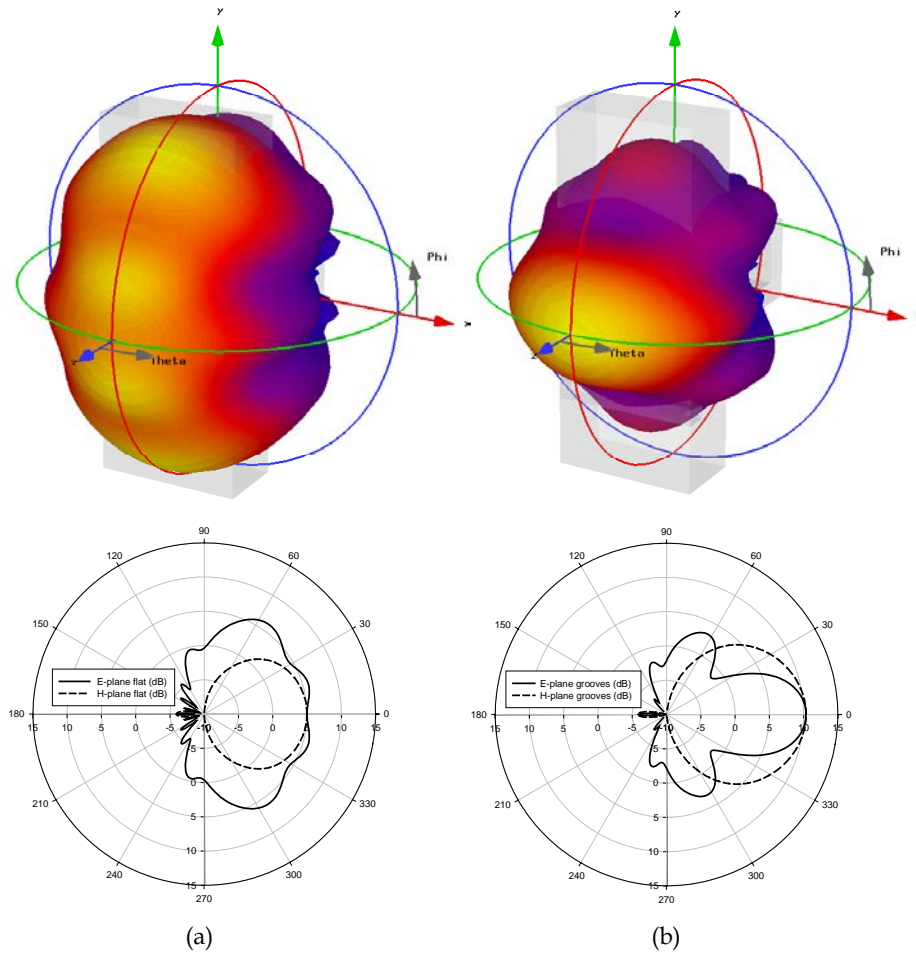


Fig. 3.22. Simulation results for the 3-D farfield diagram (above) and polar diagram (below) for single slot on a finite perfectly conducting flat plane (a) and for the "Slot + 2 grooves" antenna (b)

The simulation results obtained with *CST Microwave Studio™* shows a surface current distribution with a clear resonance in the grooves at the working frequency, see Fig. 3.21. Farfield results are also obtained, see Fig. 3.22. It is shown the three-dimensional farfield diagram and the polar E-plane for the present prototype (panel (b)) jointly with the flat plane case (panel (a)). It can readily be seen a gain enhancement of 4.3 dB when two grooves are etched on the metallic plane. The flat plane diagram is nearly isotropic with a maximum gain of 6 dB whereas the "Slot + 2 grooves" antenna prototype presents a gain of 10.34 dB at the working frequency. Notice that the diagram for the flat plane case is different from the one presented in Fig. 3.15(a). The reason for this is that the metal plate in that case was larger and this affects to the

angular distribution of the power radiated by the slot [KRAU 02].

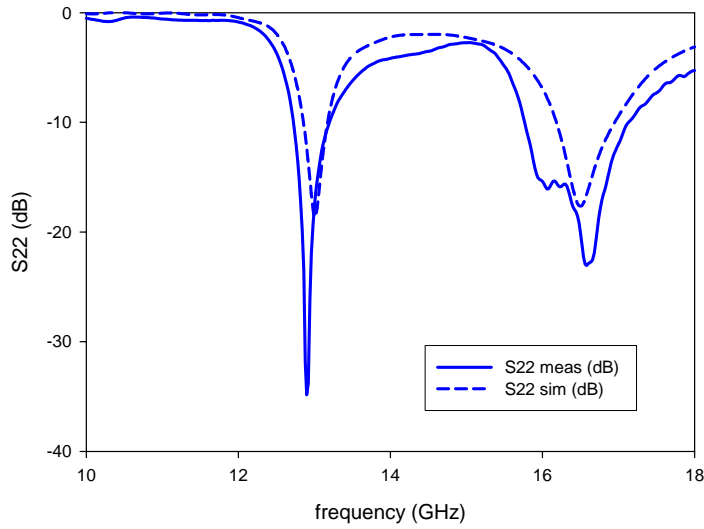


Fig. 3.23. Reflection coefficient: measured (solid line) and simulated (dashed line). A good agreement is observed.

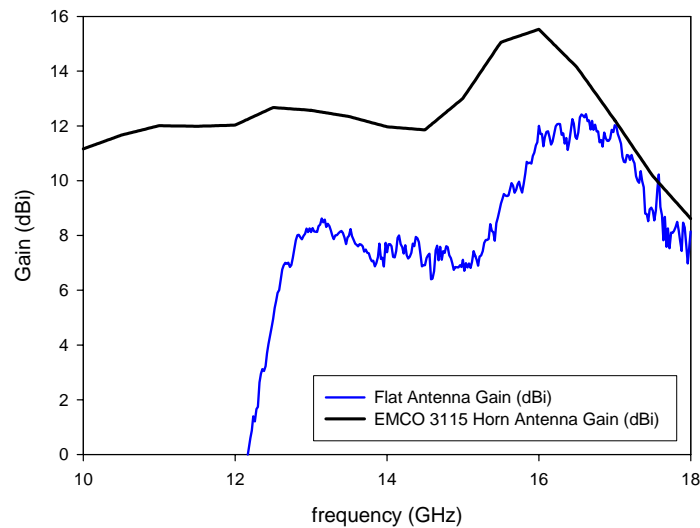


Fig. 3.24. Spectral gain in the band from 10 to 18 GHz for the “Slot+2 Grooves” Antenna (blue curve) and the reference EMCO 3115 Horn Antenna (black line).

The prototype shown in Fig. 3.20(b) was measured in the frequency range from 10 to 18 GHz by using the experimental set-up of Fig. 3.16. The reflection coefficient is plotted in Fig. 3.23 with the simulation. A good agreement is observed. The *gain-*

*transfer (gain-comparison)* method is again used to measure the antenna gain [IEEE 79]. It gives a 10 dB value at the design frequency (Fig. 3.24). Note that the standard horn antenna has a gain of 12 dB at the same frequency.

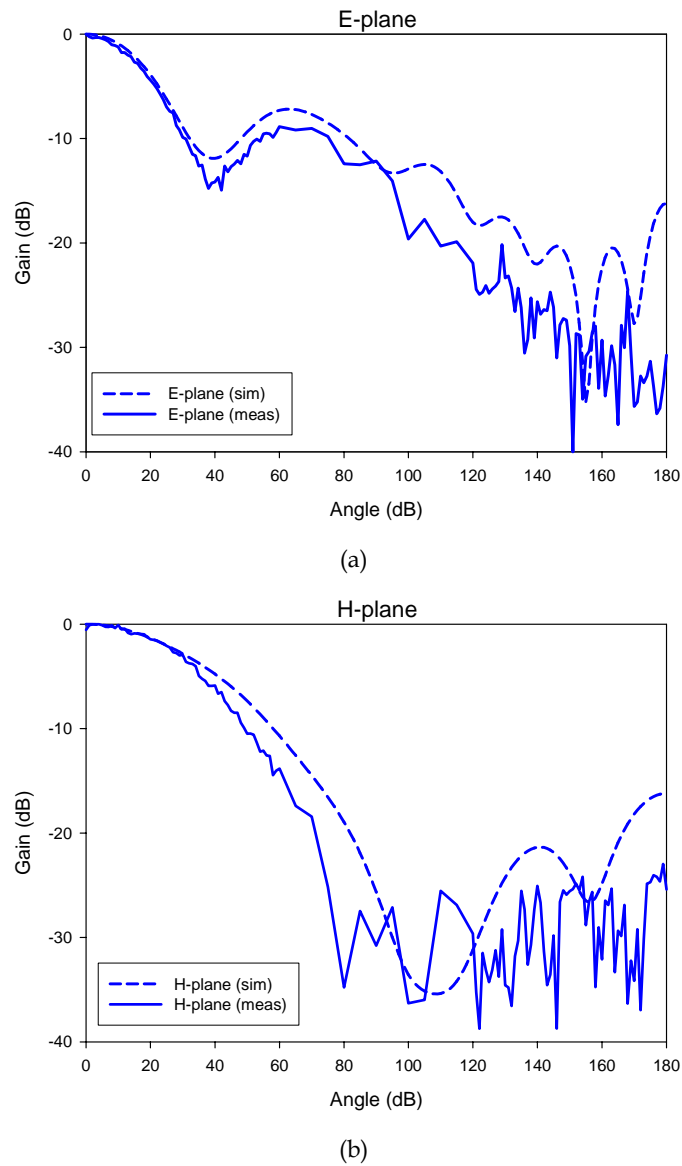


Fig. 3.25. Farfield diagrams in cartesian coordinates normalized to the maximum power for the measured "Slot+2 Grooves" Antenna (solid blue curve). Also shown the simulation results in dashed blue line. Again the better directivity is seen in the E-plane (panel (a)) where the currents are dominant.

The angular distribution is measured from 0 to 180 degrees. The results in cartesian coordinates are shown in Fig. 3.25 in panel (a) for the E-plane and in panel (b) for the H-plane, normalized in both cases for the maximum transmission. Also included are the simulated predictions, which show a very good agreement with the experiments. The measurement shows a -3 dB angular width of 34 deg in E-plane and 60 deg in H-plane.

Attending to the characteristics of the prototype it can be described as weakly directive antenna with broadside gain enhancement of 4.3 dB compared to a single slot on a metallic plane. The structure is flat, light, easy to fabricate and easy to fit.

### 3.5.3 Towards a thinner metallic antenna.

Up to now, the antenna prototypes seen have used the longitudinal slot resonance to couple the power to radiation. It could be used as well the transversal slot resonance. This approach has a clear advantage: the longitudinal resonance is directly dependent on the metal thickness, while the transversal resonance depends strictly on the horizontal slot dimension. Using the latter, the condition on the metal thickness can be relaxed providing the possibility to design very thin prototypes. This has a direct consequence on the weight and profile of the antennas, making them easy to handle. In this approach, the only restriction on the metal thickness is governed by the grooves' depth.

The proposed prototype is shown in Fig. 3.26. Notice that the parameters have been modified to tune the grooves' contribution to the transversal resonant frequency, 13 GHz. Most of the magnitudes have been enlarged with respect to the antenna shown in the last section, which was optimized at 16.5 GHz. However, the metal thickness has been reduced due to the fact that it is no longer necessary to preserve a slot longitude to excite a resonance. Note that in order to design a longitudinal resonance at 13 GHz the metal thickness should have been of around  $h = 15$  mm. With the current *transversal resonance* antenna this parameter has been divided exactly by a factor of three,  $h = 5$  mm. The constraint for the thickness now is to provide mechanical resistance in the section where the grooves are etched. Here a margin of 1.2 mm has been safeguarded.

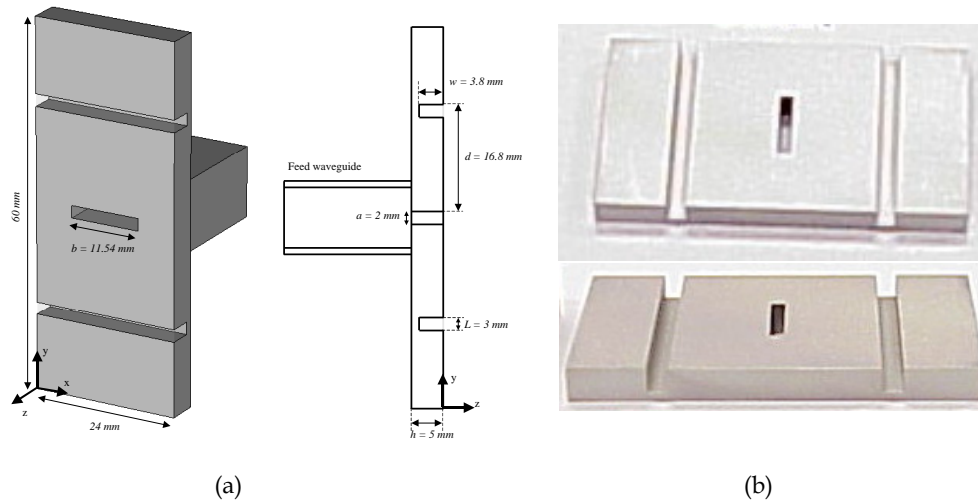
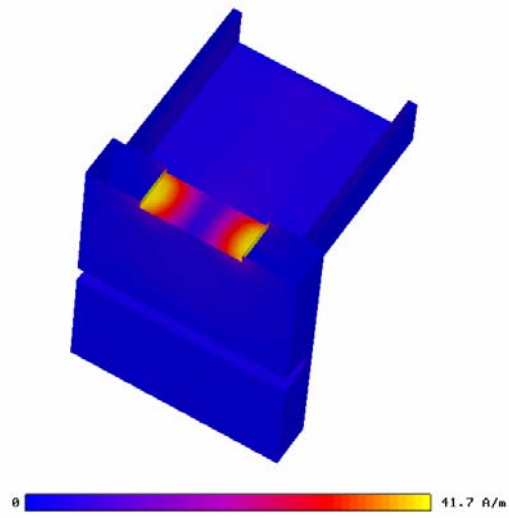


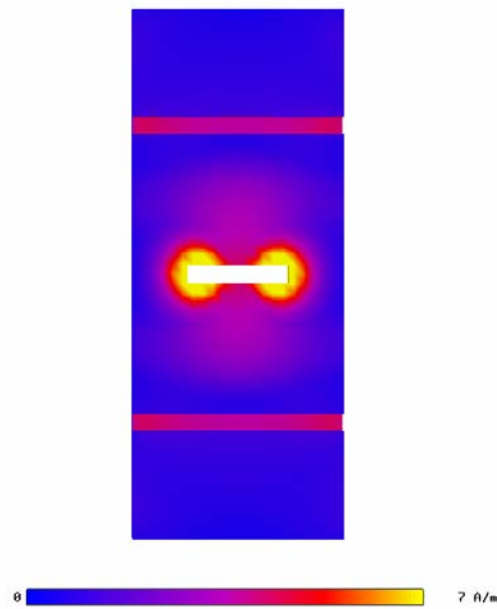
Fig. 3.26. Schematic of the thin antenna working at 13 GHz (a) and photographs of the constructed prototype (b)

Attending now to the simulated current distribution plotted in Fig. 3.27 the feasibility to obtain a good farfield response by using the transversal resonance is proven. Perceive the clear resonance excited inside the central slot (panel (a)) which is essentially different from the pattern in the longitudinal resonance, see Fig. 3.14(a). Although different in nature and in field configuration, this current distribution is also capable to excite the grooves resonance, as shown in Fig. 3.27(b). The next simulation results (Fig. 3.28) show clearly that the transversal resonance works like the longitudinal one in terms of the farfield. There is an enhancement in the gain of around 4 dB, the slot on a flat plane has a gain of 6 dB, panel (a), and with corrugations 10 dB, panel (b).

The antenna was measured in the range from 10 to 18 GHz by using the procedure described in the previous sections, see Fig. 3.16. It is interesting to observe the reflection coefficient shown in Fig. 3.29. With the present *compact antenna* prototype both simulation and measurement show a single resonance around 13 GHz ( $\lambda = 23$  mm), which matches with the transversal slot  $\lambda/2$  resonance (lateral dimension  $b = 11.54$  mm). The longitudinal resonance has disappeared from the measurement range and has been translated towards higher frequencies. The gain curve has also been measured and computed by the *gain transfer* method. It is shown in Fig. 3.30. A maximum gain of 10 dB is obtained at the working frequency. Notice that the reference horn antenna presents there a gain of 12.5 dB.



(a)



(b)

Fig. 3.27. Surface current distribution inside the central slit at its transversal resonance (a) and on the output surface (b). Notice that the grooves can be excited with this new resonance.

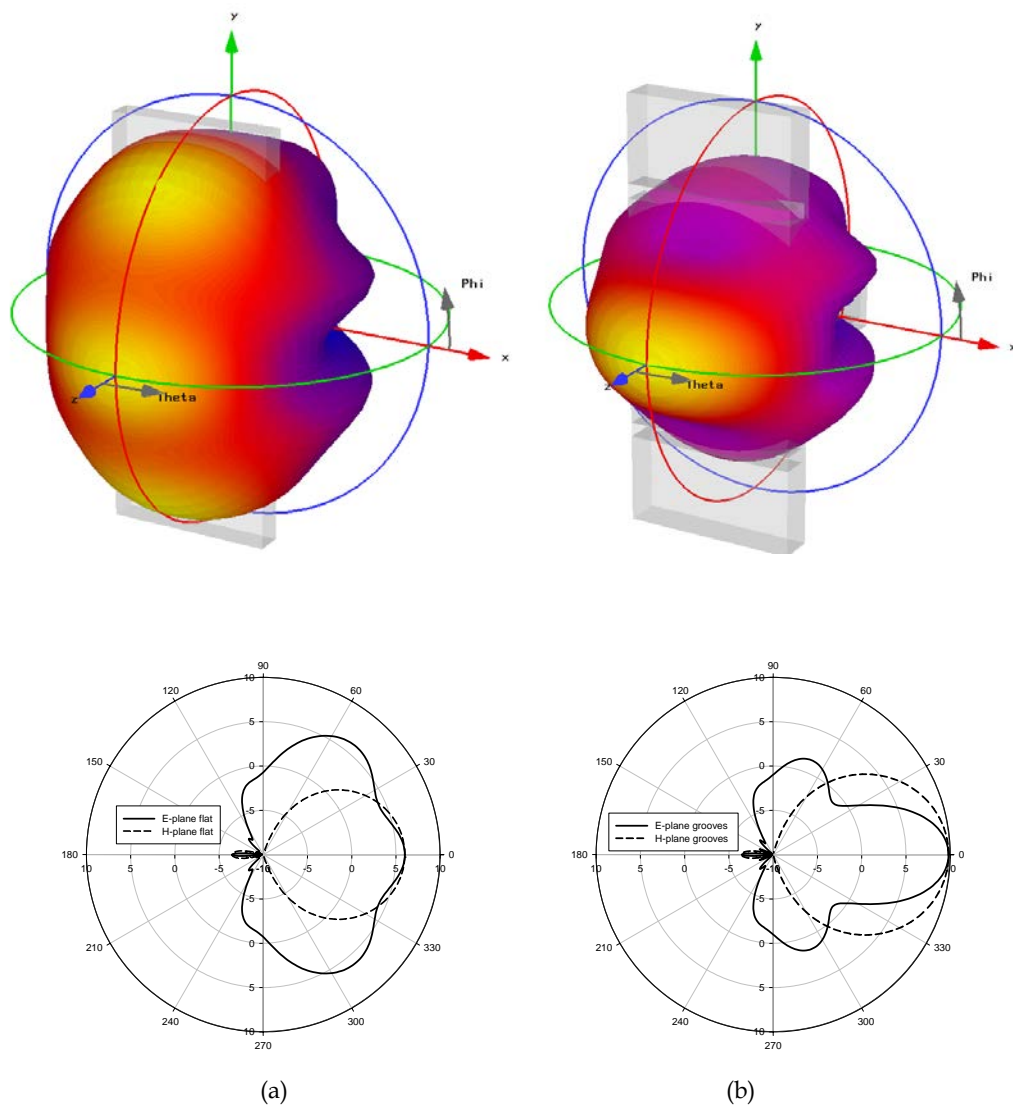


Fig. 3.28. Simulation results for the 3-D farfield diagram (above) and polar diagram (below) for single slot on a finite perfectly conducting flat plane (a) and for the "Compact Slot+2 grooves" antenna(b)

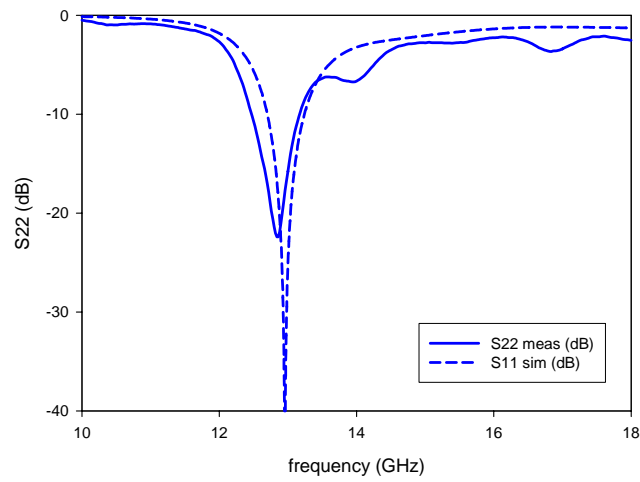


Fig. 3.29. Reflection coefficient: measured (solid line) and simulated (dashed line). A good agreement is seen.

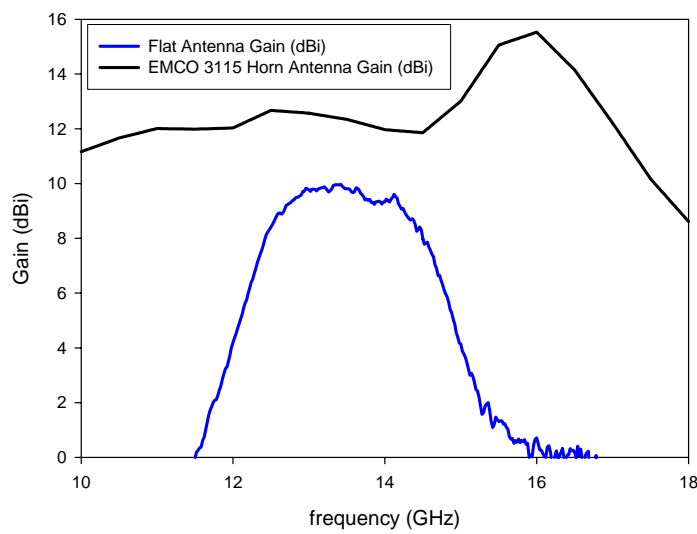
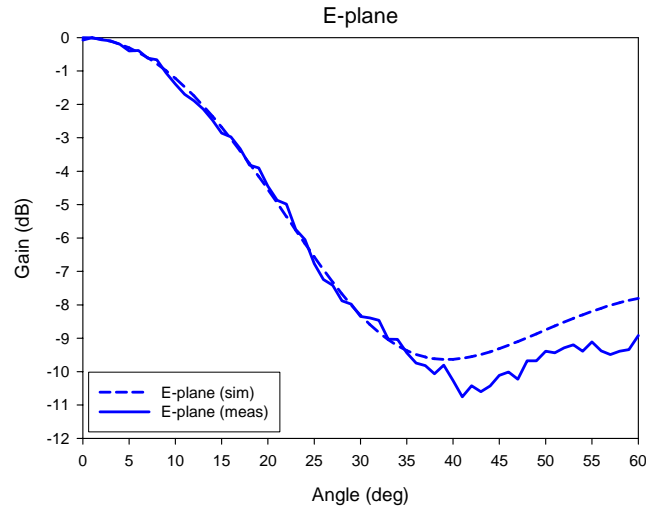
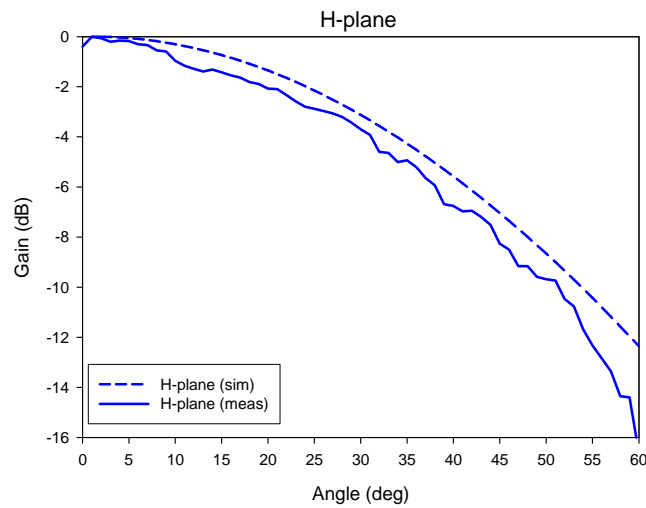


Fig. 3.30. Spectral gain in the band from 10 to 18 GHz for the “Compact Slot+2 grooves” antenna (blue curve) and the reference EMCO 3115 Horn Antenna (black line)



(a)



(b)

Fig. 3.31. Farfield diagrams in cartesian coordinates normalized to the maximum power for the measured “Compact Slot+2 grooves” Antenna working in the slot transversal resonance regime (solid blue curve). Also shown the simulation results in dashed blue line.

Finally, the angular distribution from 0 to 60 degrees at the resonance frequency is measured. The results are given in Fig. 3.31 normalized to the maximum in cartesian coordinates and compared with the simulation results. A good agreement is seen between simulation and measurement. The experiment shows a  $-3$  dB angular width

of 32 degrees in E-plane and 56 degrees in H-plane. Again the directivity is better in the E-plane. Thus, with the transversal resonance, the current density is mainly distributed along the vertical (E-field) direction, as happens with the longitudinal one.

### 3.5.4 Dual-band antenna.

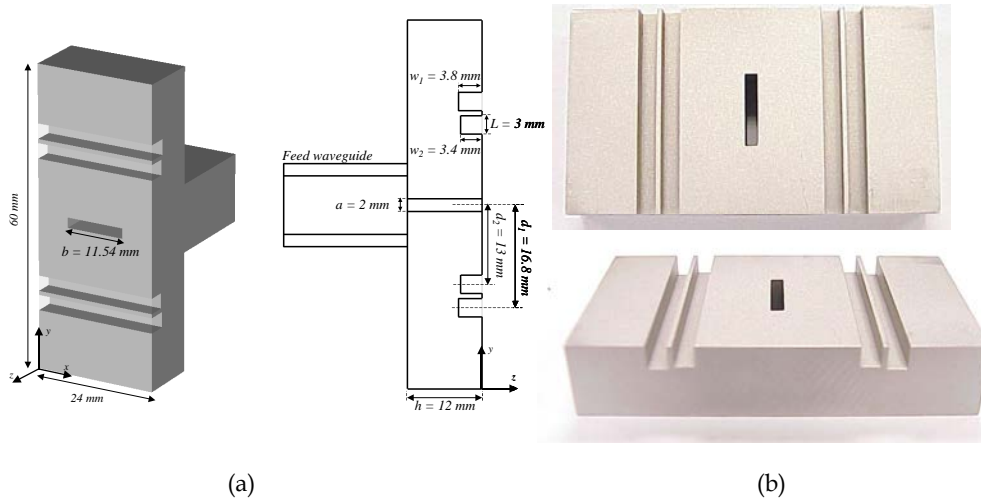


Fig. 3.32. Schematic with the dual antenna working at 13 GHz and 16.5 GHz (a) and photographs of the constructed prototype (b)

In the preceding sections two small and low profile metallic antennas have been exposed. It has been shown that by using both longitudinal and transversal slot resonances and by etching grooves on the metallic plate radiation is enhanced. Due to the fact that some wireless applications demand the capability of dual-operating-frequency band, it has been explored the possibility to extend the current design for that desired dualband operation. It is clear that the two slot resonances can be independently tuned. Attending to the design rules (Eqs. (3.1)-(3.4)) and to the results shown in sections 3.4.2 and 3.4.3, it is seen that all the antenna parameters are frequency dependent. In principle, grooves' distance and depth can be accurately tuned to work at a single frequency.

The dual antenna is shown in Fig. 3.32. In panel (a) is shown the antenna schematic with the parameters. The working frequencies proposed for the prototype are those utilized in the previous sections. The lateral dimension of the slot ( $b = 11.54$  mm) is tuned to resonate at  $f_1 = 13$  GHz (transversal resonance) and the metal thickness

chosen ( $l = 12$  mm) is resonant at  $f_2 = 16.5$  GHz. Notice that the grooves' parameters are tuned as in the preceding sections without modifications.

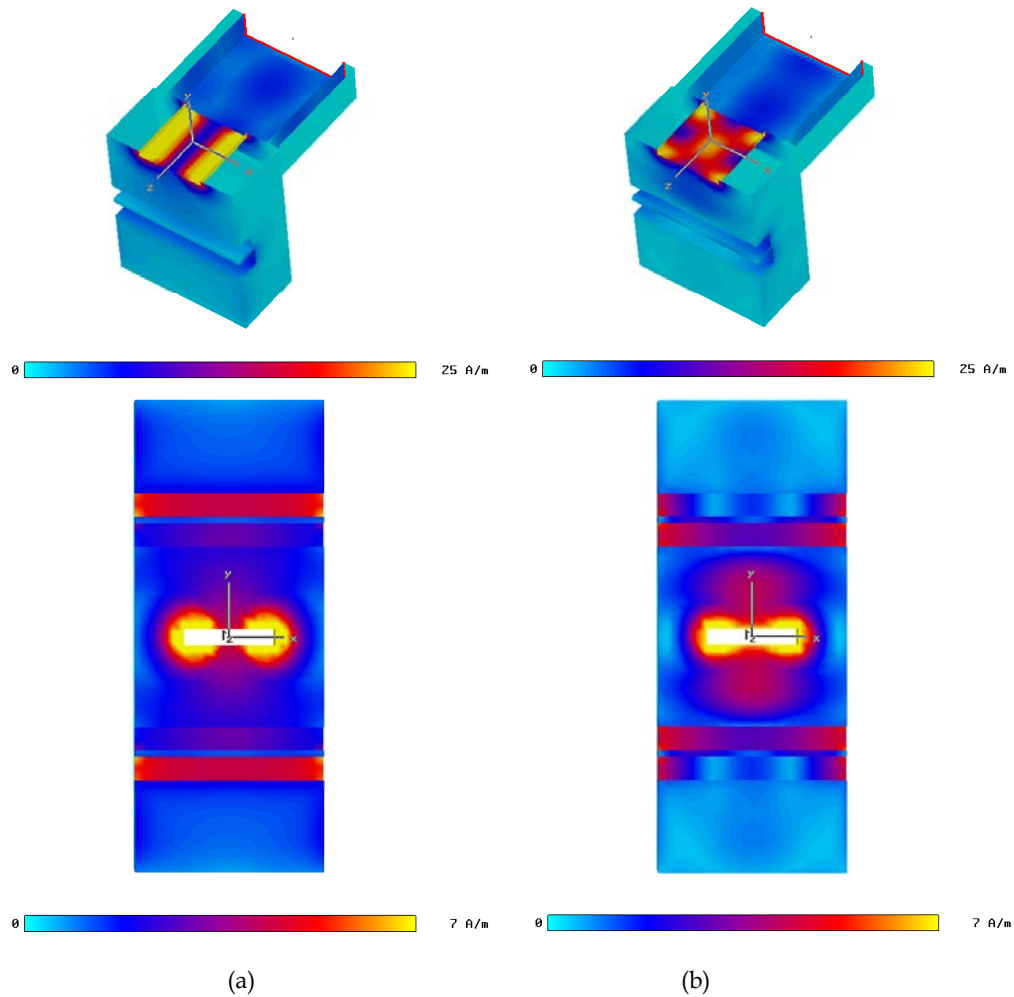
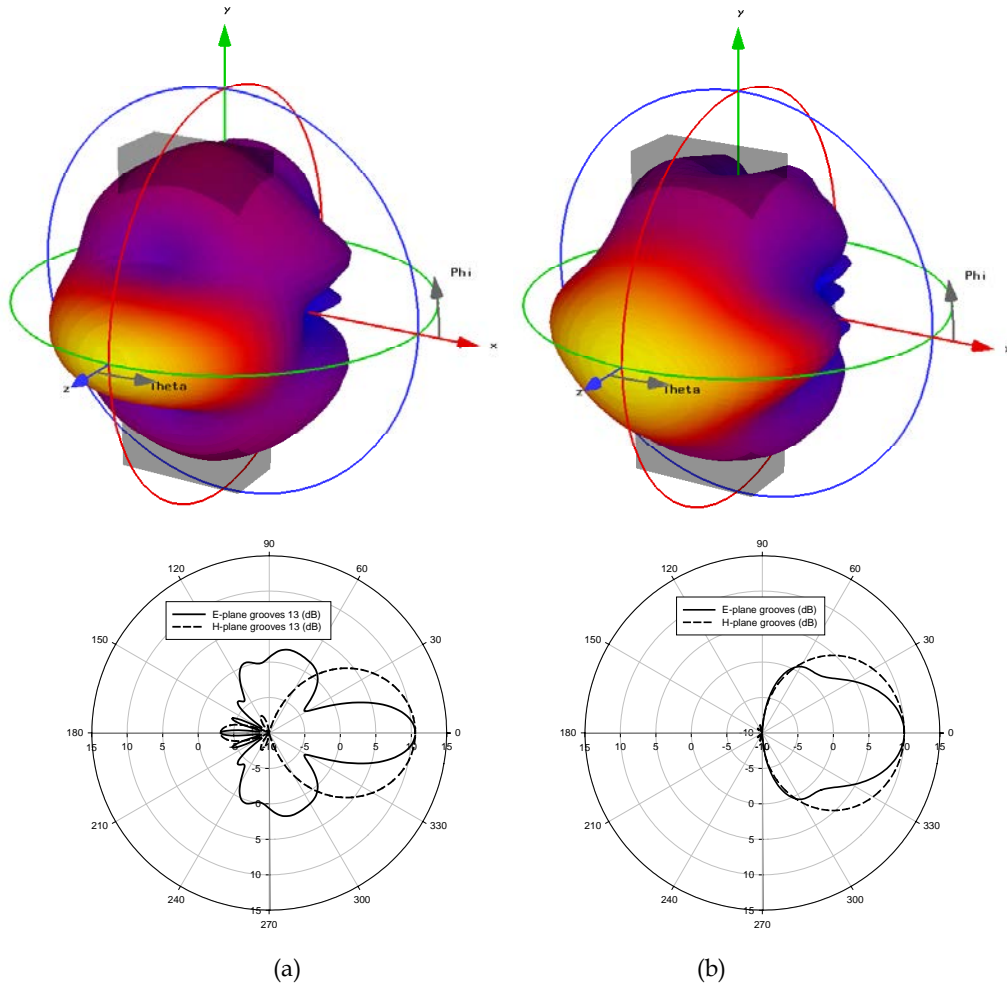


Fig. 3.33. Surface current distribution at 13 GHz (a) and 16.5 GHz (b). Above is shown the central slit resonance, which is transversal in (a) and longitudinal in (b). Below is the current at the output surface. Notice that the grooves are only excited at the design frequency and remain almost transparent for the other frequency band.



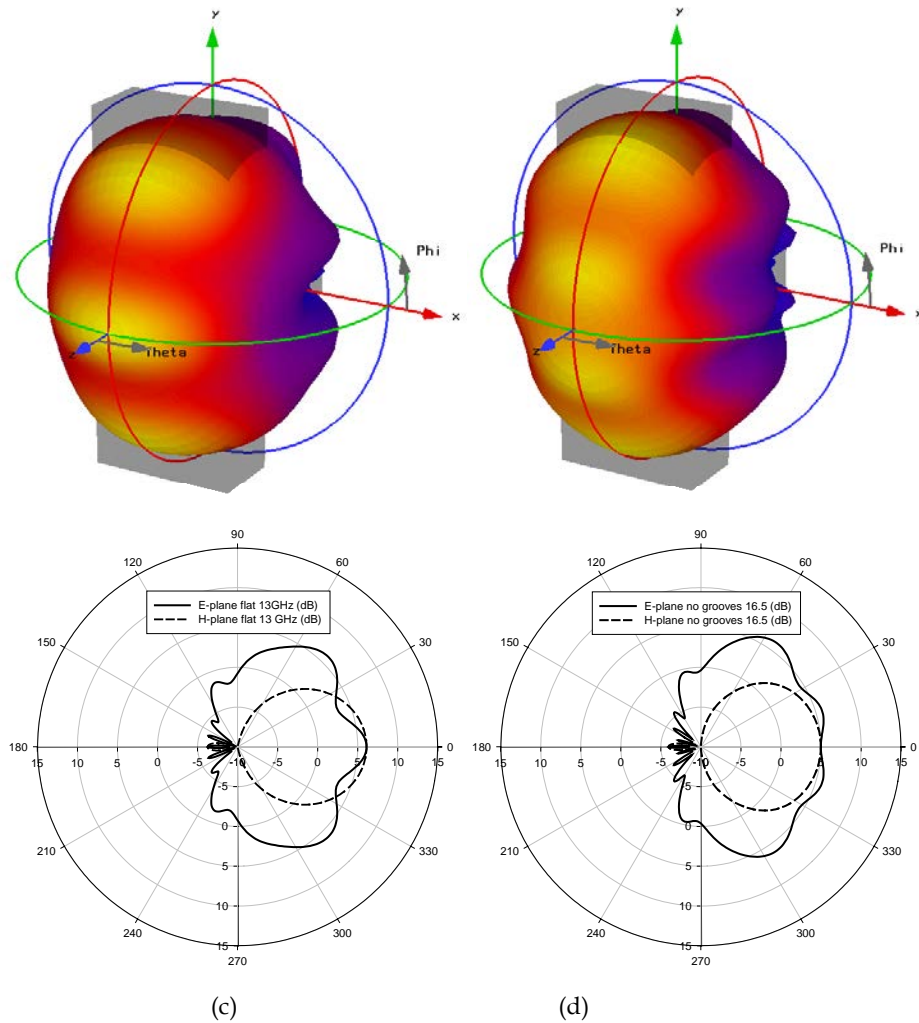


Fig. 3.34. Simulation results for the 3-D farfield diagram and polar diagram for the *Dual Antenna* in the transversal resonance (a) and the longitudinal resonance (b). The same for a flat metallic plane at the same frequencies, (c) and (d)

The simulation of the surface current distribution shows clearly that the design of the two operating bands can be made independently, see Fig. 3.33. The grooves are operating only at their resonant frequency being practically transparent in the other band. The slot also works independently in both frequency bands. The farfield characteristics are shown in Fig. 3.34. Both bands have been represented with the three-dimensional diagram and the polar E-plane diagram. The farfield at 13 GHz is in panel (a), and at 16.5 GHz in panel (b). For comparison purposes also are shown the

farfield diagrams for flat metallic plane at both frequencies, 13 GHz in panel (c) and 16.5 GHz in panel (d). A clear improvement in the gain of the antenna of around 4 dB is seen for both frequencies.

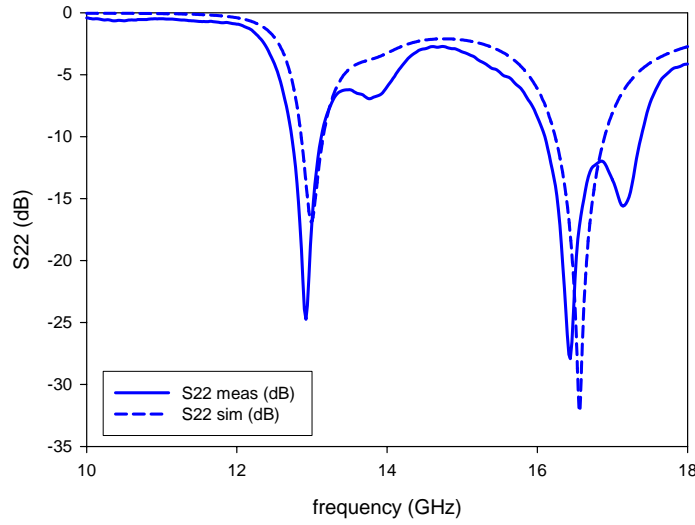


Fig. 3.35. Reflection coefficient: measured (solid line) and simulated (dashed line). A good agreement is seen with two clear resonances at 13 GHz and 16.5 GHz.

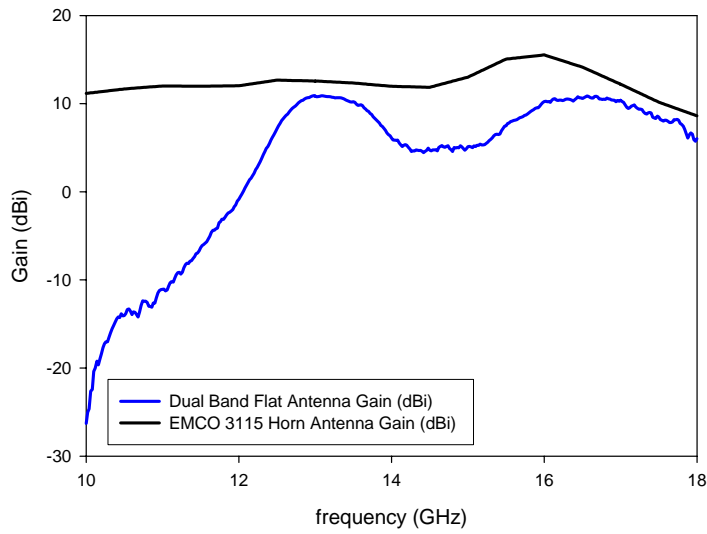


Fig. 3.36. Spectral gain in the band from 10 to 18 GHz for the *Dual Band* Antenna (blue curve) and the reference EMCO 3115 Horn Antenna (black line).

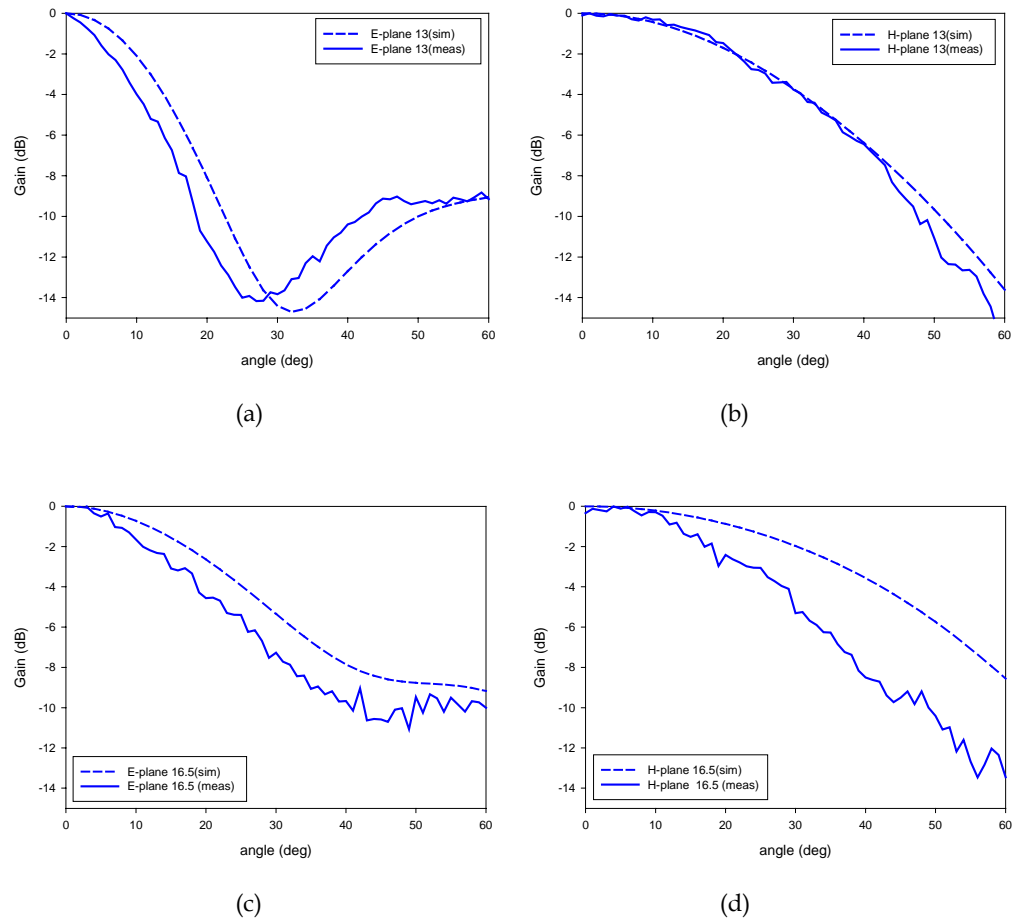


Fig. 3.37. Measured farfield diagrams in cartesian coordinates normalized to the maximum power for the measured *Dual Band Antenna*. (a) E-plane in the slot transversal resonance regime. (b) H-plane at the same frequency. (c) E-plane in the slot longitudinal resonance. (d) H-plane at the same frequency.

The antenna shown in Fig. 3.32(b) was measured in the band between 10 GHz and 18 GHz with the technique described in the preceding sections. The results of the reflection coefficient show plainly the two resonances excited in the central slot, see Fig. 3.35. Simulation and measurement curves agree well, with some discrepancies in the longitudinal resonance, probably due to insufficient mesh in the simulation or to tolerances in the fabrication process. The broadband gain behavior is also obtained by using the *gain transfer* method [IEEE 79] and is compared to the gain of a reference

horn antenna, see Fig. 3.36. Two clear peaks of transmission are detected corresponding each one to the two design frequencies. At the frequency of 13 GHz a peak of 10.4 dB is measured whereas at 16.5 GHz it is around 9 dB.

In a similar way as in the previous sections, the farfield diagram is measured. The results in cartesian coordinates and normalized to the maximum are shown in Fig. 3.37. In panels (a) and (b) are shown the E- and H-plane at 13 GHz respectively. In panels (c) and (d) are plotted the E- and H-plane polar diagrams at 16.5 GHz. A good agreement can be seen between simulation and measurement. The measured -3 dB angular width is of 20 degrees in the E-plane (Fig. 3.37(a)) and 50 degrees in the H-plane (Fig. 3.37(b)) at 13 GHz, whereas these value change for 16.5 GHz into 30 degrees in the E-plane (Fig. 3.37(c)) and 40 degrees in the H-plane (Fig. 3.37(d)).

### 3.5.5 High gain "Bull's-Eye" antenna.

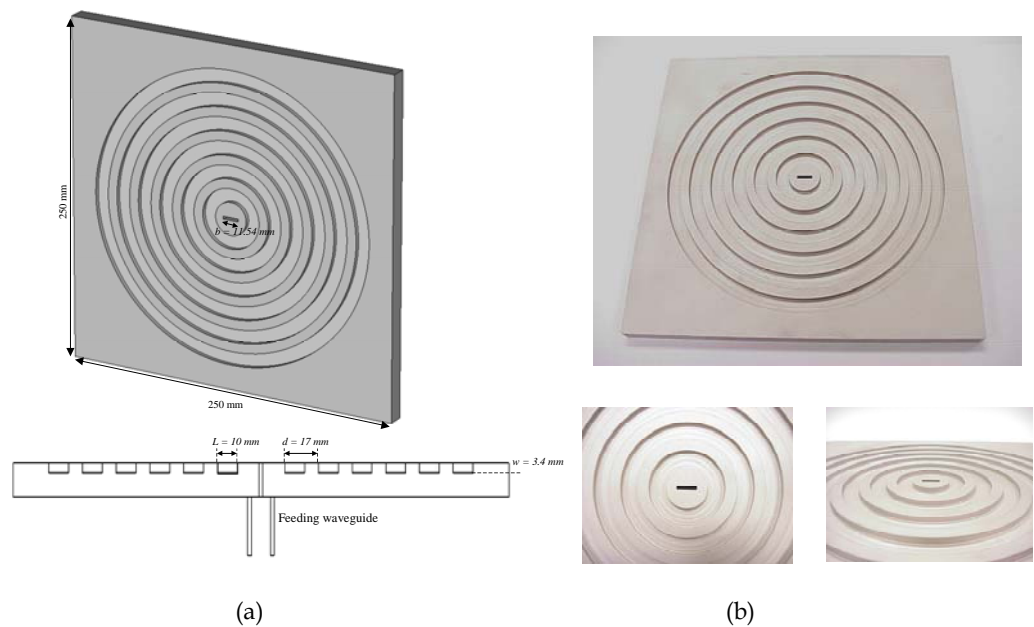
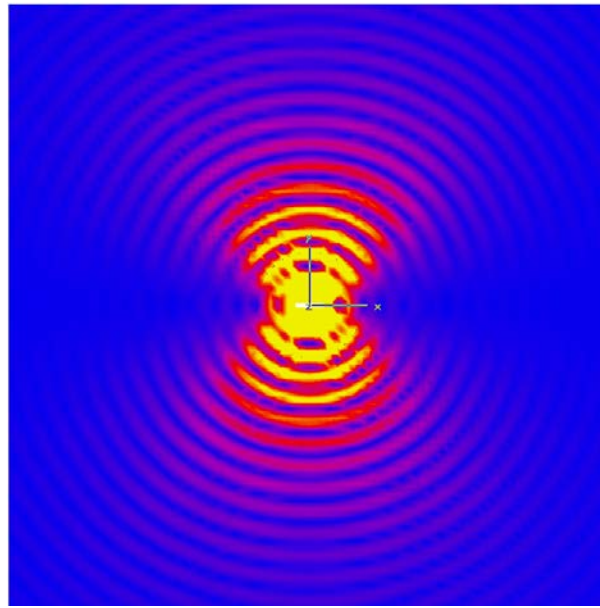
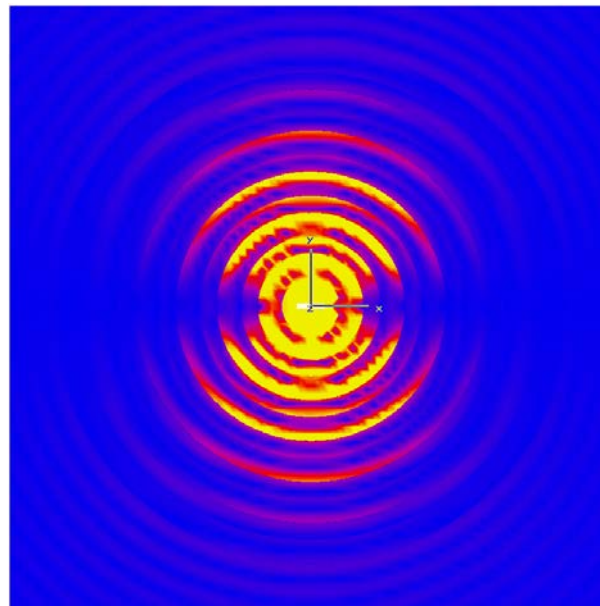


Fig. 3.38. Schematic with the "Bull's-Eye" antenna (a) and photographs of the constructed prototype (b).

Up to the present section, all the prototypes taken into account are framed in the "slit + grooves" structure. All of them consist of a narrow aperture surrounded by straight corrugations. In this section the grooves are given revolution symmetry, see Fig. 3.38.



(a)



(b)

Fig. 3.39. Simulated surface current on the output metallic plane for a single slot on a flat metallic surface (a) and for the "Bull's-Eye" antenna prototype (b).

Due to its characteristic shape, this structure is named “*Bull’s-Eye*” antenna and is a modified version of the presented in [LEZE 02]. In that work, the “*Bull’s-Eye*” was used as a planar metallic lens. It was illuminated with a plane wave by the rear and the power was collected at a long enough distance where the outgoing plane wave could be considered completely recovered. The power was coupled through a sub-wavelength hole in the center and transmission enhancement was ascribed to the metal texturization. The same procedure has been applied in experiments realized in microwaves [LOCK 05], [CAGL 06] using the “*Bull’s-Eye*” as a lens.

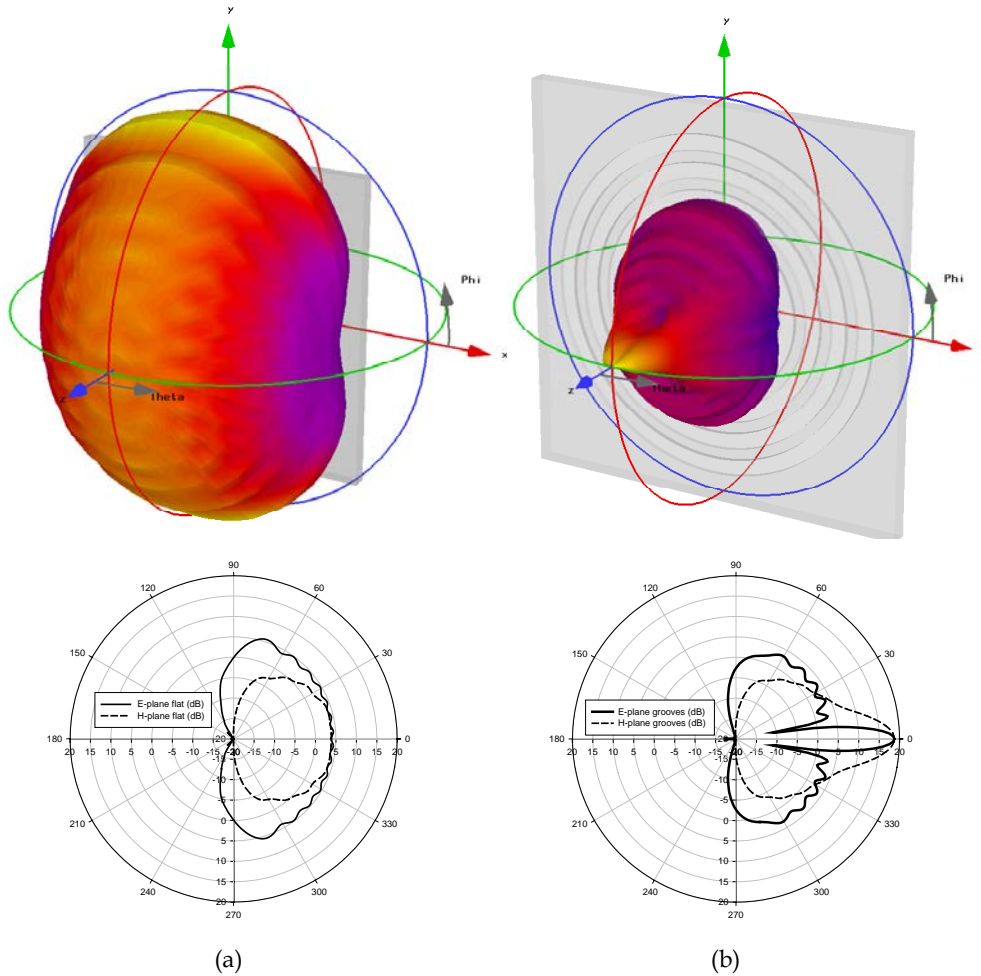


Fig. 3.40. Simulation results for the 3-D farfield diagram (above) and polar diagram (below) for single slot on a finite perfectly conducting flat plane (a) and for the “*Bull’s-Eye*” antenna (b)

In the present antenna, the central sub-wavelength aperture has been replaced by the slot presented in the precedent sections. It has been done this way in order to ensure a good level of coupling. Second, the excitation is made by means of the aforementioned coaxial-to-waveguide transition. The design procedure is the same as in the precedent sections. A final tuning with the simulator is needed to optimize the antenna gain in the working frequency. The final parameters are given in Fig. 3.38(a) and several photographs of the prototype are shown in Fig. 3.38(b)

Watching the simulated surface current on the output metallic surface for the flat plane case, Fig. 3.39(a), it is clear that a good geometrical choice for the grooves is the annular shape. After adjusting the construction parameters a good resonance can be excited inside the corrugations, see Fig. 3.39(b), which is essential to improve the farfield characteristics.

The farfield behavior in the simulation results of Fig. 3.40 establishes clearly that giving rotational symmetry to the corrugations boosts the gain. There is an improvement in radiation of more than 13 dB for the "Bull's-Eye" antenna compared to a flat metallic plane. The prototype presents a simulated gain at broadside of 18.35 dB at the working frequency, whereas for a metallic plane is situated around 5 dB.

As usual, the antenna was constructed by numerical milling machining and measured by the LBEIN antenna test range in the frequency band from 10 to 18 GHz. The reflection coefficient shown in Fig. 3.41 shows the two aforementioned resonances. The agreement between simulation and experiment is good with a slight deviation in the resonance around 16.5 GHz probably due to tolerances in the fabrication process. They have a positive effect since the resonance is intensified. The measured gain (Fig. 3.42) has a peak in the design frequency with a maximum value of 21 dB. Note that this is higher than the simulation prediction. It seems that this increment in gain is related to the enhancement of resonance ascribed to the tolerances.

The angular distribution measurement is presented in Fig. 3.43 in cartesian coordinates and normalized to the maximum power. In this case, also the cross-polarization was measured. There is evidence of the strong beaming obtained for the E-plane (panel (a)) and the low cross-polarization level, more than 30 dB. A narrow -3 dB angular width of 6 degrees is measured. The side lobe suppression level is better than -15 dB. For the H-plane the cross-polarization level is near 25 dB. The strong beaming seen in E-plane can be explained by considering the surface current

distribution of Fig. 3.39(b), where the current density is higher in vertical direction that corresponds to E-plane.

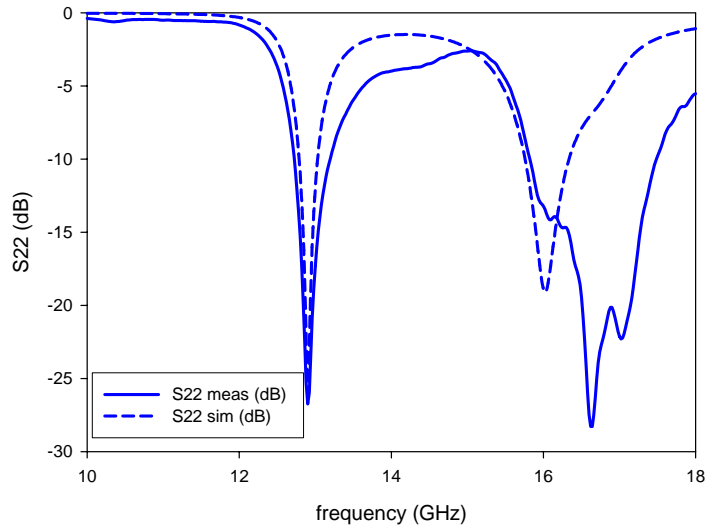


Fig. 3.41. Reflection coefficient: measured (solid line) and simulated (dashed line). A good agreement is seen, with a deviation in the higher resonance. The measurement in this case presents a deeper reflection coefficient resonance.

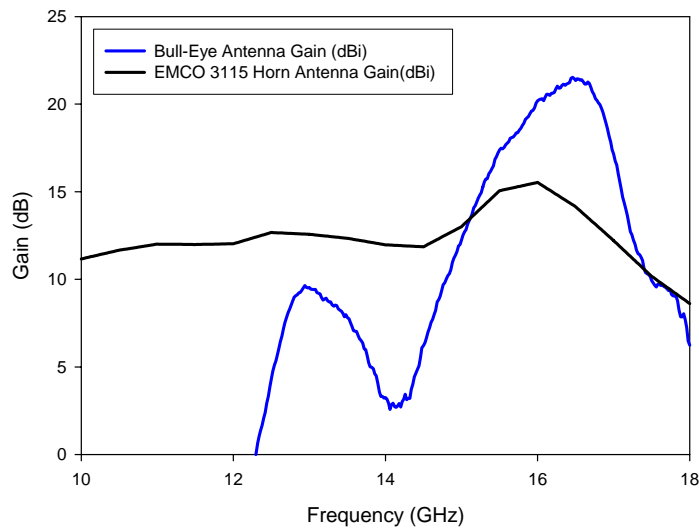
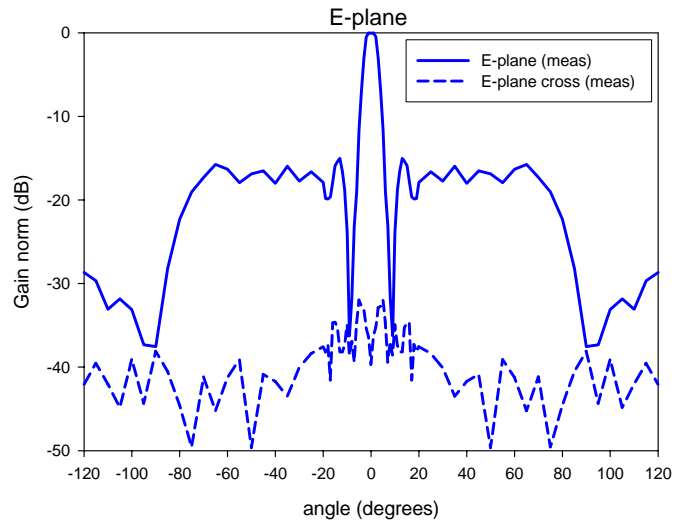
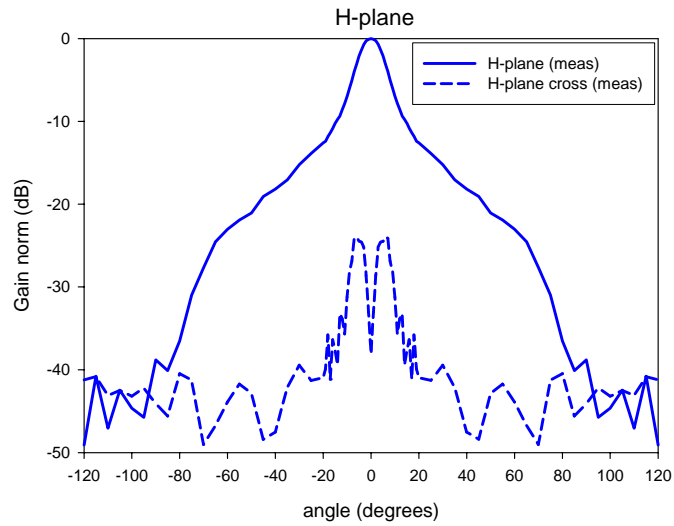


Fig. 3.42. Spectral gain in the band from 10 to 18 GHz for the “Bull’s-Eye” Antenna (blue curve) and the reference EMCO 3115 Horn Antenna (black line).



(a)



(b)

Fig. 3.43. Measured farfield diagrams in cartesian coordinates normalized to the maximum power for the measured "Bull's-Eye" Antenna (solid blue curve). Also shown the cross-polarization components in both planes.

### 3.5.6 Dielectric loaded antenna.

A further improvement in the antenna prototype is presented in this section. The aim here is to reduce the thickness of the antenna as much as possible. Recalling the procedure hitherto given, first the thickness has been reduced by using the transversal slot resonance, instead of the longitudinal one. Thus, the thickness is no longer limited by this dimension, but still remains a minimum groove depth to maintain. Here the groove depth is reduced by the introduction of a dielectric material with relative permittivity  $\epsilon > 1$ . In particular it has been chosen  $\epsilon = 4$  in order to simplify the design. With this value of permittivity in a rough approximation the groove depth is reduced in a half. The prototype is shown in Fig 3.44. Notice in the schematic the reduction of the metal thickness to  $h = 4$  mm. Shown in the photograph of the final prototype is the dielectric inserted in the grooves.

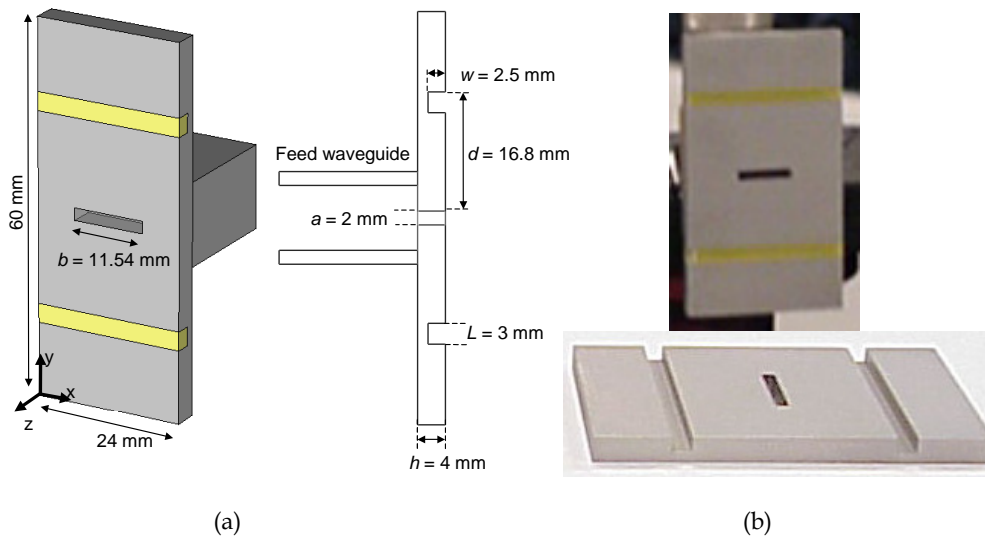


Fig. 3.44. Schematic with the “dielectric-filled” antenna (a) and photographs of the constructed prototype (b). Notice the reduction in the metal thickness and the inclusion of dielectric material (glass fiber) inside the grooves.

The simulated surface current shows clearly a good resonance excited inside the grooves at the working frequency when the dielectric (glass fiber,  $\epsilon = 4$ ) is inserted in the grooves, see Fig. 3.45(b). For comparison purposes it is also shown in panel (a) the surface current for the same architecture with the grooves filled with air ( $\epsilon = 1$ ). It is clear that the resonance in this case is not optimum.

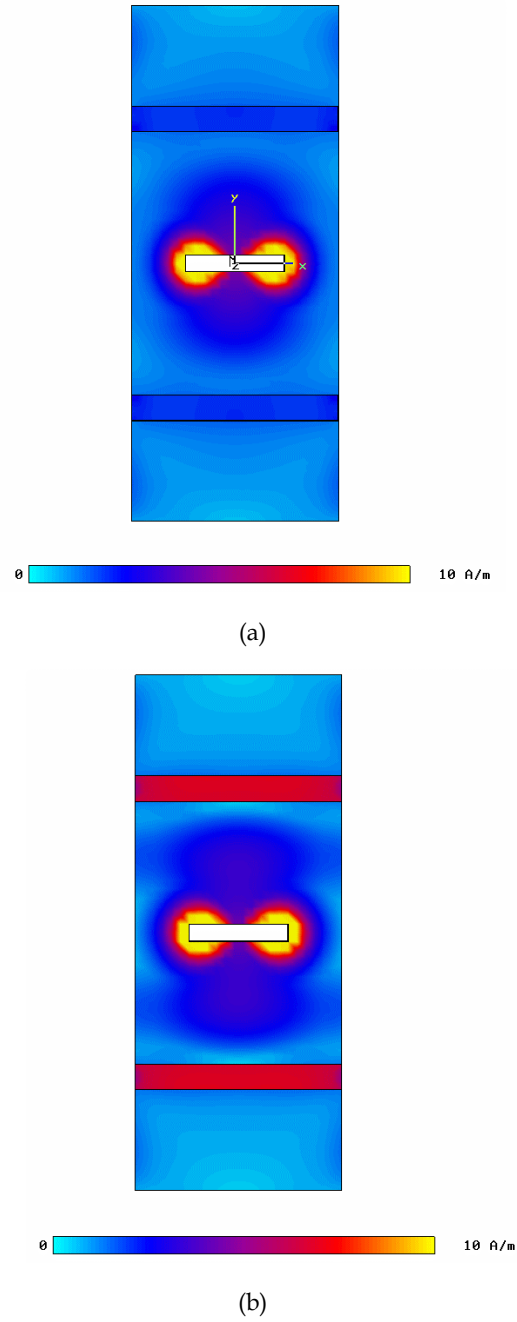


Fig. 3.45. Simulated surface current on the output face for the antenna with air-filled grooves antenna (a) and for the same antenna with dielectric-filled grooves (b). Notice the stronger grooves' resonance in the latter case.

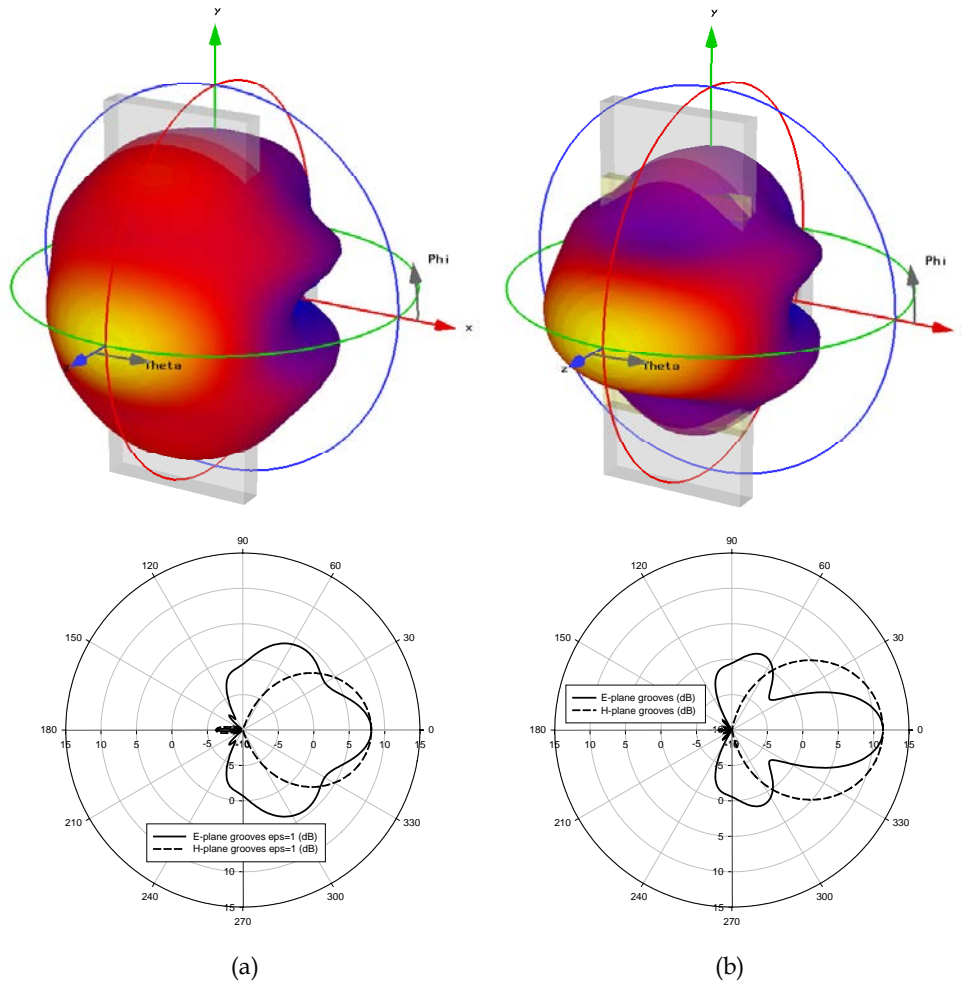


Fig. 3.46. Simulation results for the 3-D farfield diagram (above) and polar diagram (below) for the antenna with air-filled grooves (a) and for the same antenna with grooves filled with dielectric ( $\epsilon_r = 4$ ) (b)

In Fig. 3.46 are shown the simulated farfield diagrams. In panel (b) it is seen the farfield pattern of the current antenna, with the grooves filled with a dielectric of  $\epsilon_r = 4$ . There is a clear improvement in the radiation pattern with a gain of 11.3 dB, more than 5 dB larger than that of a flat metallic plane, see Fig. 3.22(a). The importance of the choice for the dielectric inside the grooves is plotted. In panel (a) the grooves are filled with air,  $\epsilon_r = 1$ . The gain now is 8.1 dB, i.e. 2 dB better than a flat plane but 3.2 dB lower than the optimum. In this last case, the grooves are collaborating to the radiation, but are too shallow to support an efficient resonance.

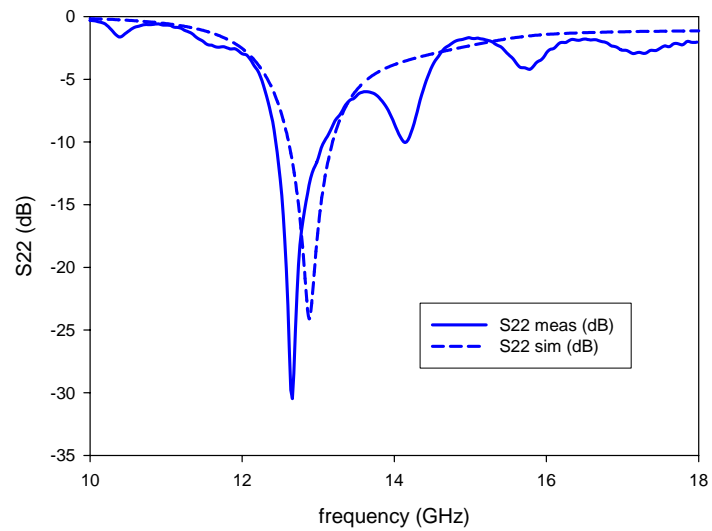


Fig. 3.47. Reflection coefficient: measured (solid line) and simulated (dashed line). Notice that only one resonance is seen, corresponding to the transversal slot resonance. The measurement shows a ripple, probably due to fabrication tolerances.

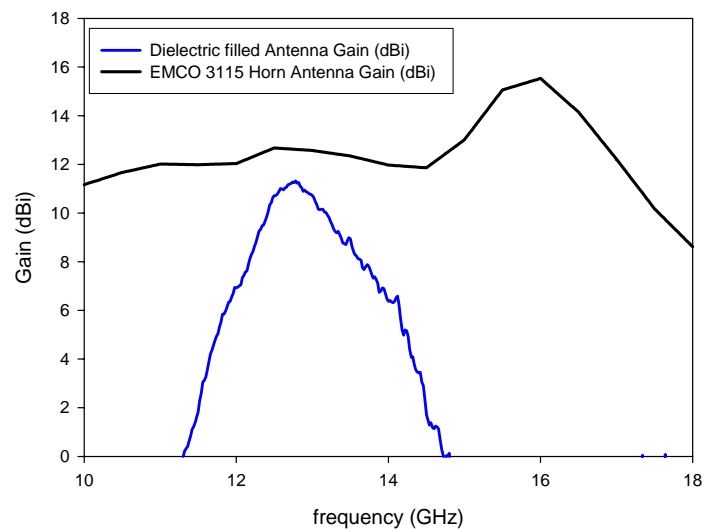


Fig. 3.48. Spectral gain in the band from 10 to 18 GHz for the “Dielectric-filled Antenna” (blue curve) and the reference EMCO 3115 Horn Antenna (black line).

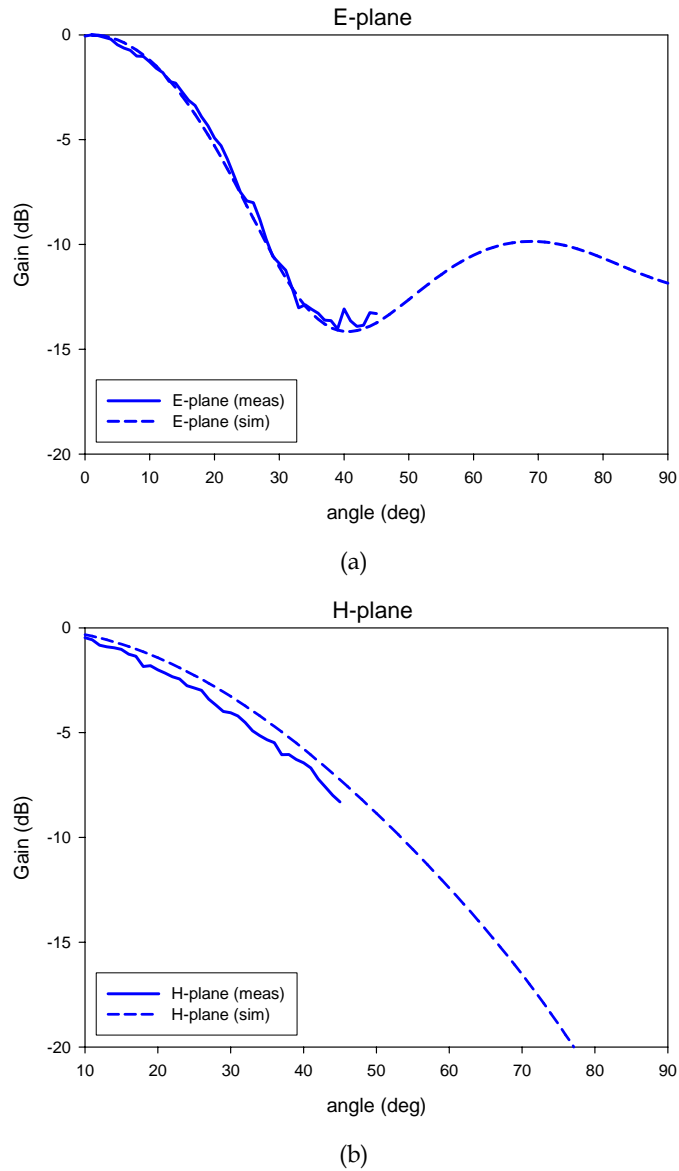


Fig. 3.49. Measured farfield diagrams in cartesian coordinates normalized to the maximum power for the measured “Dielectric-filled Antenna” (solid blue curve). Also shown the simulation results in dashed blue line.

The antenna was constructed and measured with the usual set-up. The measurement results for the reflection coefficient and the broadband gain are presented in Fig. 3.47 and Fig 3.48 respectively. A good agreement is seen between simulation and measurement in the reflection coefficient, although a ripple is present in the

experiment, probably due to fabrication tolerances. Also, notice that only one resonance is observed, corresponding to the transversal slot resonance. With the given metal thickness the longitudinal slot resonance has been translated to higher frequencies. With respect to the broadband gain shown in panel (b) a clear enhancement around the design frequency is observed. A peak of 11.3 dB appears at approximately 13 GHz with a much lower gain in the rest of the spectrum. The horn antenna at that frequency has a gain of 12.6 dB.

The next measurement results are the farfield angular distributions. It is plotted in Fig. 3.49(a) for the E-plane and in Fig. 3.49(b) for the H-plane, with the gain normalized to the maximum and in cartesian coordinates. A very good agreement is seen in both panels. The measured  $-3$  dB angular width for E-plane is 30 degrees and for H-plane is 52 degrees.

### 3.5.7 Further improvements: sinusoidal profiles.

In this section it is presented the latest result obtained in the optimization of the antennas. The usual square profile of a "Bull's-Eye" has been substituted by a sinusoidal one, obtaining the shape of Fig. 3.50(a).

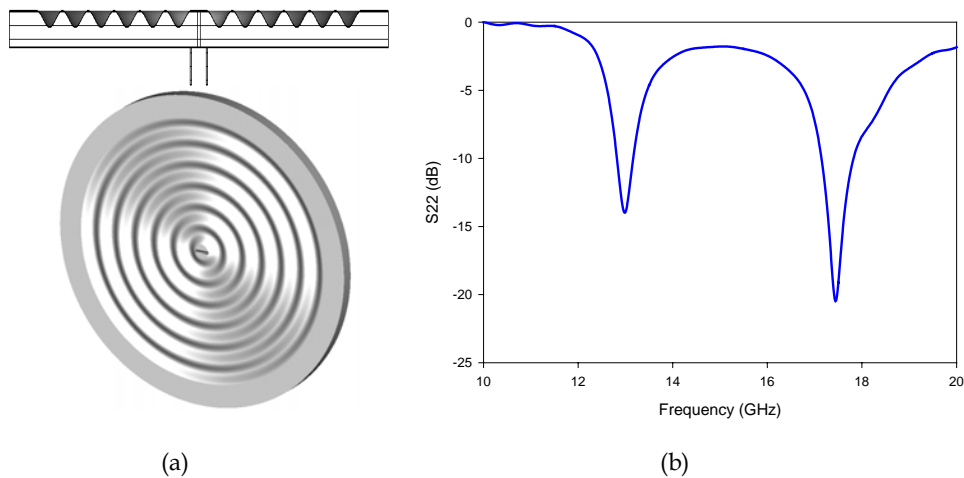


Fig. 3.50. (a) Schematic of the sinusoidal profile Bull's-Eye Antenna. The design parameters are: Period,  $d = 17$  mm, sinus amplitude,  $w = 2.21$  mm, metal thickness,  $h = 10$  mm, number of periods:  $N = 6$ . (b) Simulated reflection coefficient magnitude.

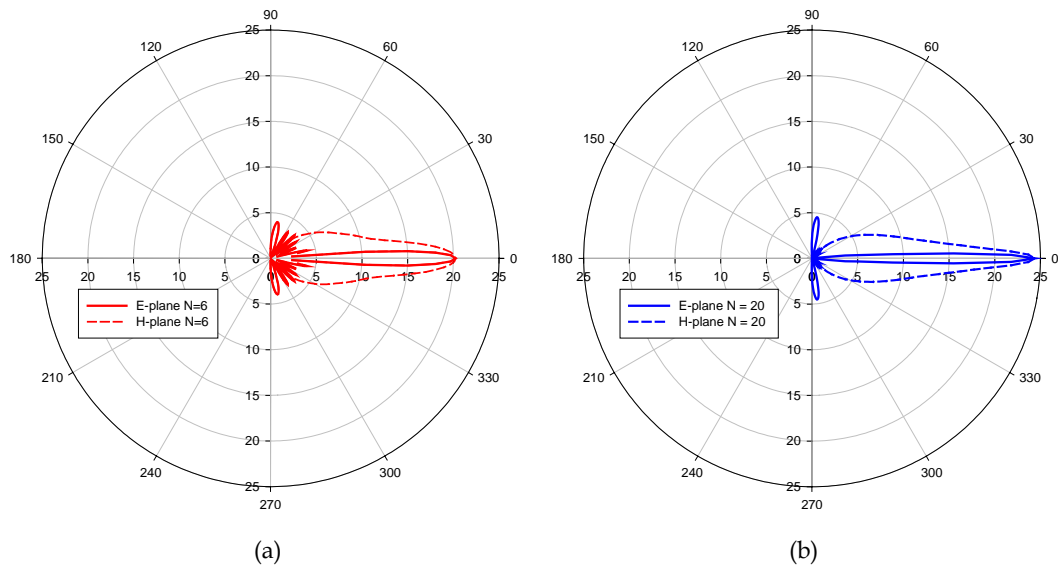


Fig. 3.51. Polar plot diagram of sinusoidal profile Bull's-Eye antenna with  $N = 6$  periods (a) and  $N = 20$  periods (b). E-plane is represented with solid line and H-plane with dashed line.

The antenna has been simulated with *CST Microwave Studio™*. The reflection coefficient obtained is shown in Fig. 3.50(b). Note that the upper resonance is shifted to 17.5 GHz, while in the standard Bull's-Eye was located at 16 GHz, see Fig. 3.41. In fact, the value obtained here is more accurately related to the leaky wave formalism [OLIN 63], which predicts radiation through the spacial harmonic  $n = -1$  at an angle near broadside when the wavelength is close to the period, or in frequency,  $f \approx 17.64$  GHz. Therefore, the rest of parameters need to be tuned to give a good level of radiated power. The metal thickness is modified to translate the longitudinal resonance to the broadside radiation frequency and the sinus amplitude is also adjusted to give good resonance at that frequency.

The simulated farfield characteristics for sinusoidal antennas are shown in Fig. 3.51, for six periods in panel (a) and twenty periods in panel (b). With six periods the simulated broadside gain is 20.3 dB, 2 dB better than the gain obtained with a square profile. The sidelobe suppression is 16.2 dB, 1.3 dB above the square profile. The  $-3$  dB angular width is 4.5 deg, 1.7 deg narrower than the square profile. When the number of periods is increased to twenty, the farfield characteristics improve. The gain is now 24.4 dB, with a sidelobe level suppression of 21.4 dB and a very narrow  $-3$  dB angular

width of 2 deg.

A final comparison is given in Fig. 3.52. It is depicted in panel (a) the gain curve and in panel (b) the sidelobe suppression of the square profile Bull's-Eye with six periods (black), the sinusoidal profile Bull's-Eye with six periods (red) and the sinusoidal profile Bull's-Eye with twenty periods. It is noticeable the enhancement achieved by changing the corrugation profile.

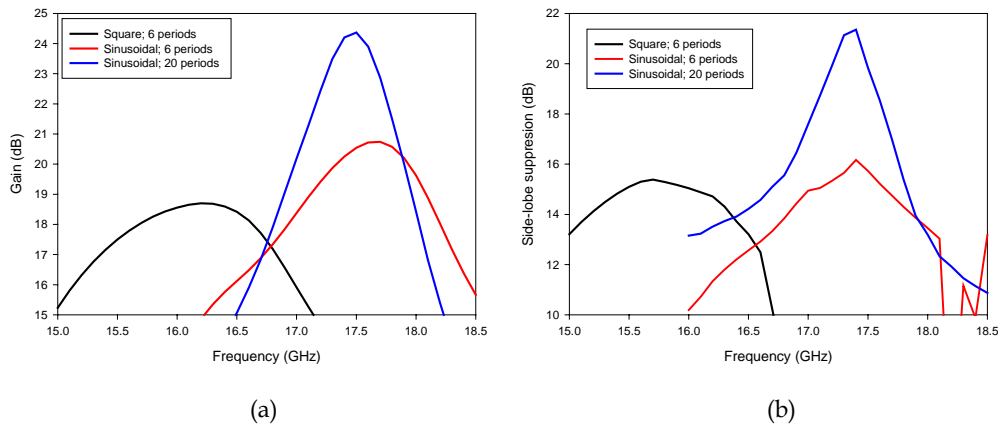


Fig. 3.52. Comparison between the farfield characteristics of Bull's-Eye antennas with a square profile and six periods (black curve), sinusoidal profile and six periods (red curve) and sinusoidal profile and twenty periods (blue curve). (a) Gain curve (b) Side-lobe suppression curve.

### 3.6 Concluding remarks.

In this chapter the enhancement of transmission through a narrow slot on a metallic plane achieved by corrugating the metallic plane has been experimentally proven in the range of microwaves and millimeter waves. This fact corroborates the theoretical approach that found the origin of the enhancement on the periodic structure, regardless of the model used to describe the metal.

It has been checked the ability to enhance directivity by using these structures in the output corrugation configuration. This result has been extended to the practical implementation of several low-profile and all-metallic antennas in the microwave range. The feeding is made by means of a waveguide. By changing the central (ideally) infinite slit to a finite slot several improvements can be done, fundamentally

the thickness of the antenna can be reduced and a dual-band operation can be achieved. It has been seen that a great variety of farfield characteristics can be obtained by changing the number of corrugations.

High gain antennas can be attained by using annular corrugations, the so-called Bull's-Eye antenna. Further improvements deal with the insertion of dielectric inside the corrugations and with changes in the shape of the corrugations.

These results show that light, compact and flat antennas for applications in different wireless systems, like base station, WLAN in millimeter waves, and radiofrequency links are feasible.

# Chapter 4

## Stacked Hole Arrays: Merging Photonic Crystals, Enhanced Transmission And Metamaterials In A Single Structure.

---

---

*In this chapter it is shown how a left-handed metamaterial can be achieved by the periodic stacking of sub-wavelength hole array plates to form a photonic band-gap structure. First, a preliminary analytical study of the transmission through stacked structures is developed by using an artificial waveguide approach. This initial model is checked with the commercial simulator. Later is presented the measurement results in the millimeter wave regime of a prototype built by stacking subwavelength hole arrays. It is experimentally shown that extraordinary transmission (ET) and electromagnetic band-gap (EBG) can be tuned independently, and that, under some conditions, a left-handed behaviour (LHM) in the frequency band where extraordinary transmission happens can be observed as well, even for very small longitudinal periods. An equivalent circuit approach based on the inverse transmission line concept is worked out to explain this surprising effect. It will be shown that by modifying the periodicity of the stack a rich variety of responses can be obtained and that by positioning the bandgap over the ET band, LHM is inhibited and transformed into a pair of right-handed bands. Further study is developed by simulating and measuring stacks with different periodicities. Special attention will be given to the periodicity where the transition from LHM to RHM arises. By exploiting the LHM character of the stack, metamaterial prisms and parabolic lenses with anomalous features are designed. A final simulation discussion of the necessary ingredients to obtain LHM is presented.*

## 4.1 Introduction.

Three discoveries have altered the state of the art of electromagnetic radiation research over the last years. First, the concept and realisation of photonic band-gap (PBG) structures have opened up new original approaches for the control of light flow and confinement with great technological consequences [YABL 87], [JOHN 87], [JOAN 97], [NODA 00]. Photonic Crystals (Ph. C.) are artificial structures which fundamentally inhibit propagation of electromagnetic waves for certain directions and wavelengths [YABL 87], [JOAN 97], so-called photonic band-gap (PBG). Artificially introduced defects permit light control and localization [JOHN 87], [NODA 00], and for this reason they have been proposed as the photonic counterpart of electronic semiconductors [YABL 87].

Second, the demonstration of extraordinary optical transmission (EOT) through sub-wavelength hole arrays and other structures has provided the basis for using subwavelength apertures for a variety of potential applications [EBBE 98], [LEZE 02], [MART 01], [BARN 03] [PEND 04], [OZBA 06]. In the optical range EOT has been explained as a diffraction effect, assisted by the enhanced fields associated with surface plasmon polaritons [BARN 03b]. Surface plasmons provide the possibility of localization and the guiding of light in subwavelength metallic structures [MART 01], [BARN 03] [PEND 04], which can be tailored for the creation of plasmonic circuits with the potential ability to merge photonics and electronics [OZBA 06].

Third, the concept of negative refraction index (NRI) has refreshed the classical electrodynamics field by introducing highly unconventional properties –so-called left-handed metamaterials (LHM)– that can lead to a new class of devices [VESE 68], [PEND 00], [PEND 96], [PEND 99], [SHEL 01], [SMIT 05], [SMIT 05b]. Foremost among these properties is the opposite Snell’s refraction law at the interface between a standard and a NRI medium. For NRI to happen, both the permittivity and permeability must be negative simultaneously [VESE 68]. Pendry claimed that those NRI materials could act as perfect lenses [PEND 00]. Pendry’s group had previously shown the feasibility to fabricate an artificial material with negative permittivity using a lattice of thin metal wires [PEND 96], and they had also reported how to obtain a negative magnetic response from a lattice of “split rings resonators” [PEND 99]. Smith et al. built a structure with simultaneous negative  $\epsilon$  and  $\mu$  showing negative refraction for the first time [SMIT 00]. Since then left-handed metamaterials have been achieved

for frequencies in the microwave range [PEND 05], [SMIT 05] from split-ring resonators components [PEND 99] and their complementary [FALC 04]. Only very recently a media with negative permeability at optical frequencies has been reported [GRIG 05], thus paving the way for NRI materials at visible frequencies [SAMB 05].

Up to now, relations of photonic crystals and negative refraction have been shown [NOTO 02], [CUBU 03] as well as of photonic crystals and sub-wavelength hole arrays [YE 05], [QIU 05] and, moreover, evanescent growth and tunnelling effects have been predicted in paired complementary metamaterials [ALU 03], [ALU 05]. Finally, it has also been suggested that negative refraction and extraordinary transmission through hole arrays are probably different manifestations of the same physical behaviour of surface modes [GOME 03].

## 4.2 Artificial waveguide approach to the hole array problem.

### 4.2.1 Formulation of the problem.

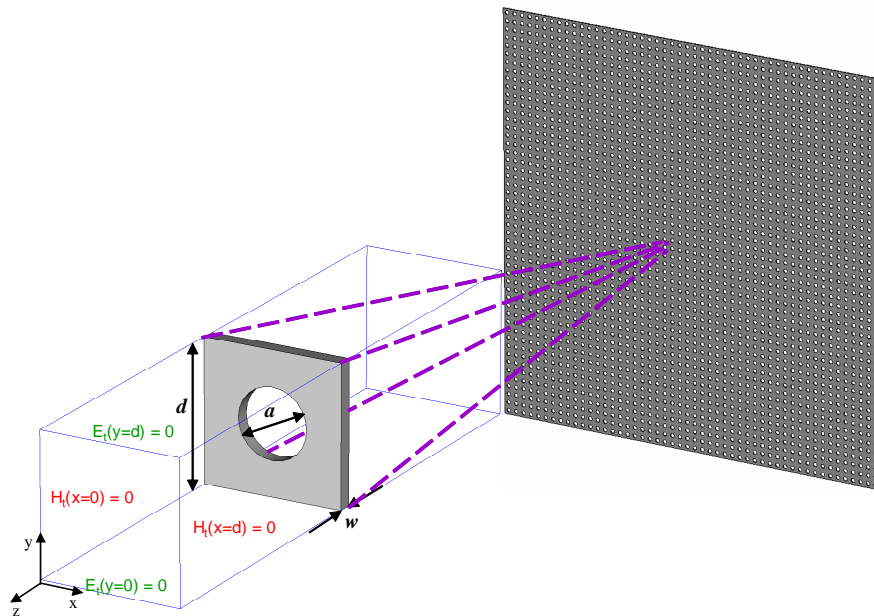


Fig. 4.1. Unit cell of a single hole array and the planes defining the boundary conditions of the artificial waveguide.

Prior to the description of the phenomena related with the stacking of hole arrays, is presented in this section an *ab-initio* analysis of the single plate hole array. The analysis is based on the method given in [KATS 60], [KATS 98]. This analysis considers that the diffraction problem by a periodic surface can be reduced from the three dimensional case to a rectangular waveguide problem provided that a plane wave impinges normally to the periodic surface. Following the procedure, two sets of planes perpendicular to the surface are added and proper electric and magnetic wall boundary conditions are imposed on these planes. In this situation, the incident plane wave becomes the fundamental mode of the artificial square waveguide (of side identical to  $d$ , being  $d$  the period of the hole array) defined with these planes.

The reflection and transmission coefficients are the desired parameters of the problem as well as the power distribution of the high-order mode spectrum. Several non-evanescent higher diffraction orders, similar to those appearing in the spectrum of a diffraction grating, emerge if  $kd > \pi$  [KATS 60], [KATS 98].

In order to form the square artificial waveguide are drawn perpendicularly to the hole array surface two sets of artificial parallel planes, i.e.  $x = n.d$  and  $y = q.d$ , (being  $\dots -2, -1, 0 = n, q = +1, +2, \dots$ ) in such a way that each hole remains just in the middle between two pairs of planes,  $x = \text{constant}$ ,  $y = \text{constant}$ , see Fig. 4.1. The proper boundary conditions are fixed for the tangential field components on the artificial planes defined above, i.e.,

$$E_t = E_x = E_z = 0 \text{ on the planes } y = \text{constant} \quad (4.1)$$

$$H_t = H_y = H_z = 0 \text{ on the planes } x = \text{constant} \quad (4.2)$$

Note that the artificially defined planes do not disturb the propagation of the  $y$ -polarized plane wave incident normally to the hole array surface, that is, they act as electric and magnetic walls. Therefore, the fundamental mode of this artificial squared waveguide is the incident plane wave, a transversal electric and magnetic (TEM) mode with no cut-off frequency.

$$E_y = E_0 \exp(-jkz) = \eta \quad H_x = \eta H_0 \exp(-jkz) \quad (4.3)$$

These component values remain unchanged for a uniform waveguide, i.e., a waveguide without discontinuities or obstacles [KATS 98]. As the fundamental mode (the plane wave) of the artificially defined waveguide is incident on the discontinuity, placed in  $z = 0$ , and defined as the individual hole of diameter  $a$  drilled in a metallic

squared wall of side  $d$  (the period of the hole array), the reflected fundamental mode is excited together with a set of high-order reflected modes for  $z < 0$ . A similar situation occurs for the transmitted fundamental mode (the plane wave) and another set of high-order transmitted modes. Most of these reflected or transmitted modes are evanescent but some of them become propagating if  $kd > \pi$ .

The above mentioned scattered fields are symmetrical along two of these planes because the impinging plane wave and the discontinuity share the same symmetry planes. A set of infinite squared waveguides dividing the hole array, see Fig. 4.1, can be introduced to divide the hole array in a two-dimensional array of elementary cells and, due to the imposed boundary conditions (electric and magnetic walls), the electromagnetic fields on a pair of opposed waveguide walls are identically equal. In other words, the fields on a pair of such opposite waveguides walls are exactly the same and, therefore, the electromagnetic field in all the artificial waveguides is continuous on the walls.

Following the above described procedure, the various electromagnetic fields of this waveguide are the solution of the scattering problem of the periodic hole array surface, when a plane wave is normally incident. The reflected fundamental mode amplitude in the waveguide is equivalent to the reflection coefficient from the hole array surface and the modulus of the remaining angular spectrum are identical to the modulus of the artificial waveguide higher order modes [RAMO 94].

Provided that waves have a time harmonic dependence varying along the time and the space as  $\exp(j\omega t \pm \gamma z)$ , where the minus sign describes forward modes and the plus sign backwards modes respectively; and provided that the total electric charge density is zero and conduction currents are included in the complex permittivity, then we can take advantage of the Helmholtz wave equations for the electric and magnetic three-dimensional vector fields, following the well known approach in electrical engineering, see [COLL 91],

$$\nabla^2 \mathbf{E} + k^2 \mathbf{E} = 0 \quad (4.4)$$

$$\nabla^2 \mathbf{H} + k^2 \mathbf{H} = 0 \quad (4.5)$$

If the three-dimensional operator is separated in its transversal and longitudinal components, then we have,

$$\nabla^2 \mathbf{E} = \nabla_t^2 \mathbf{E} + \frac{\partial^2 \mathbf{E}}{\partial z^2} = \nabla_t^2 \mathbf{E} + \gamma^2 \mathbf{E} \quad (4.6)$$

Resulting in the well known eigenvalue problem equations,

$$\nabla_t^2 \mathbf{E} = -k_c^2 \mathbf{E} \quad (4.7)$$

$$\nabla_t^2 \mathbf{H} = -k_c^2 \mathbf{H} \quad (4.8)$$

where the fields are the eigenfunctions and the eigenvalues are  $k_c^2 = \gamma^2 + k^2$ . Therefore, it is possible to simplify the resolution of the problem in terms of the longitudinal field components.

Using vector calculus operations on the Maxwell equations, the transversal electromagnetic field components can be expressed in terms of the longitudinal ones,

$$E_x = -\frac{1}{k_c^2} \left( \gamma \frac{\partial E_z}{\partial x} + j\omega\mu \frac{\partial H_z}{\partial y} \right) \quad (4.9)$$

$$E_y = \frac{1}{k_c^2} \left( -\gamma \frac{\partial E_z}{\partial y} + j\omega\mu \frac{\partial H_z}{\partial x} \right) \quad (4.10)$$

$$H_x = \frac{1}{k_c^2} \left( j\omega\varepsilon \frac{\partial E_z}{\partial y} - \gamma \frac{\partial H_z}{\partial x} \right) \quad (4.11)$$

$$H_y = -\frac{1}{k_c^2} \left( j\omega\varepsilon \frac{\partial E_z}{\partial x} + \gamma \frac{\partial H_z}{\partial y} \right) \quad (4.12)$$

From Eqs. (4.9)-(4.12), it follows that transverse electromagnetic waves, TEM (plane waves), are obtained in the case of  $E_z = H_z = 0$ . Under these conditions, the transversal components are also zero, unless  $\gamma^2 + k^2 = 0$ , which implies that  $\gamma_{TEM} = \pm j k$ . In other words, the wave propagates with the velocity of light in the medium, see [KATS 60].

Moreover, in the above described artificial waveguide, a set of modes, TE (with  $E_z = 0$ ) and TM (with  $H_z = 0$ ) can be obtained from the above transversal eigenfunctions  $H_z$  for the TE modes, and  $E_z$  for the TM modes, respectively, satisfying the proper boundary conditions,

$$E_z(x, y) = 0 \text{ and } \frac{\partial H_z}{\partial y} = 0, \text{ for } y = 0 \text{ and } y = d \quad (4.13)$$

$$H_z(x, y) = 0 \text{ and } \frac{\partial E_z}{\partial x} = 0, \text{ for } x = 0 \text{ and } x = d \quad (4.14)$$

This requires that the eigenfunctions have to be,

$$H_z(x, y) = N^{nq} \sin(n\pi x / d) \cos(q\pi y / d) \quad (4.15)$$

for  $n = 2, 4, 6, \dots$  and  $q = 0, 2, 4, \dots$

$$E_z(x, y) = M^{nq} \cos(n\pi x / d) \sin(q\pi y / d) \quad (4.16)$$

for  $n = 0, 2, 4, \dots$  and  $q = 2, 4, 6, \dots$

being  $n\pi/d$  and  $q\pi/d$  the eigenvalues  $k_{cx}$  and  $k_{cy}$  respectively of the problem satisfying,

$$k_c^2 = \gamma^2 + k^2 = \left(\frac{n\pi}{d}\right)^2 + \left(\frac{q\pi}{d}\right)^2 \quad (4.17)$$

The symmetry of the problem forces to allow only for even  $n$  and  $q$ , and the case  $n = q = 0$  can be seen as the particular TEM plane wave.

As usual, when the mode is in propagation the convention  $\gamma = j\beta$  is used. The fields for a mode under cut-off are evanescent, and  $\gamma = \alpha$  represents a reactive attenuation without power dissipation nor radiation. Moreover, the terms  $N^{nq}$  and  $M^{nq}$  are power normalization factors that can be determined imposing the specific value of the power transported by a given mode [KATS 98], [RAMO 94]

Employing (4.9)-(4.12), (4.15), (4.16) the electric and magnetic field transversal components can be derived. Firstly, for the case of  $TE_{nq}$  modes, and assuming the  $z$  dependence as  $\exp(\pm \gamma z)$ , it is obtained,

$$E_x(x, y) = \frac{j\omega\mu q\pi}{k_c^2 d} N^{nq} \sin(n\pi x / d) \sin(q\pi y / d) \quad (4.18)$$

$$E_y(x, y) = \frac{j\omega\mu n\pi}{k_c^2 d} N^{nq} \cos(n\pi x / d) \cos(q\pi y / d) \quad (4.19)$$

$$H_x(x, y) = \frac{-m\pi}{k_c^2 d} N^{nq} \cos(n\pi x / d) \cos(q\pi y / d) \quad (4.20)$$

$$H_y(x, y) = \frac{\gamma q \pi}{k_c^2 d} N^{nq} \sin(n\pi x / d) \sin(q\pi y / d) \quad (4.21)$$

and, for the  $TM_{nq}$  modes,

$$E_x(x, y) = \frac{m\pi}{k_c^2 d} M^{nq} \sin(n\pi x / d) \sin(q\pi y / d) \quad (4.22)$$

$$E_y(x, y) = \frac{-\gamma q \pi}{k_c^2 d} M^{nq} \cos(n\pi x / d) \cos(q\pi y / d) \quad (4.23)$$

$$H_x(x, y) = \frac{j\omega \epsilon q \pi}{k_c^2 d} M^{nq} \cos(n\pi x / d) \cos(q\pi y / d) \quad (4.24)$$

$$H_y(x, y) = \frac{j\omega \epsilon n \pi}{k_c^2 d} N^{nq} \sin(n\pi x / d) \sin(q\pi y / d) \quad (4.25)$$

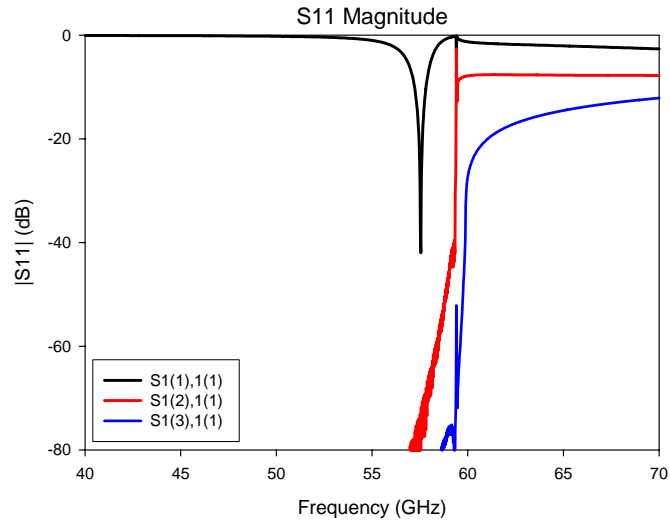
Note that to get a complete system of modes, the TEM plane wave needs to be added to the previously introduced TE and TM modes.

Several approaches can be found in the literature in order to determine the complex reflection and transmission coefficients for the fundamental mode, i.e., the plane wave, as well as for the high-order modes. For instance, one approach is based upon the coupling coefficients [KATS 98]: a system of coupled-wave equations describes the evolution of the power of the modes along the nonuniform waveguide and allows to compute the power exchange between the modes. This method was intensively used by Schelkunoff in the fifties of last century, see the discussion given in [KATS 98]. Another semi-analytical method, developed in parallel to the previous one is that of Mode Matching Technique, see [RIEN 01].

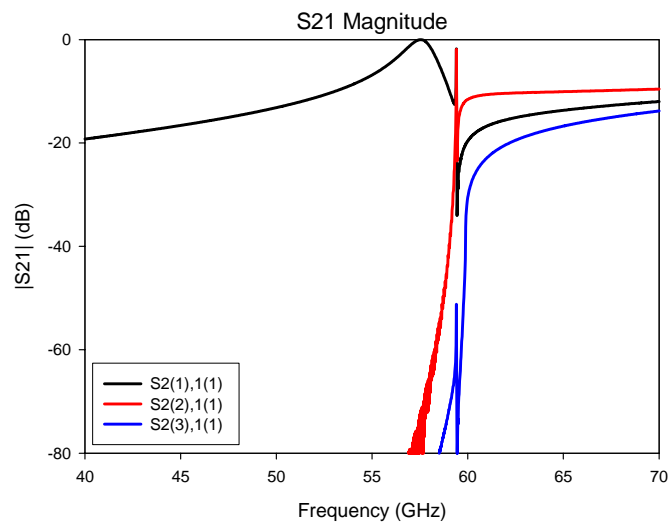
#### 4.2.2 Simulation results.

Having the problem formulated, now the commercial code *CST Microwave Studio*<sup>TM</sup>, based upon the Finite Integration Time Domain Method will be used. This software allows to define the proper boundary conditions to get the artificial waveguide described above. Therefore, the diffraction problem can be solved under the basis of

the determination of the mode amplitudes distribution caused by the hole drilled on a perfect conductor sheet placed inside the artificial waveguide.



(a)



(b)

Fig. 4.2. Equivalent waveguide multimode S-parameters for the case of  $a = 2.5$  mm,  $d = 5$  mm and  $w = 0.5$  mm, S11 (a), S21 (b). In black is represented the response of the fundamental TEM mode (or plane wave), in red is the response of the  $TM_{02}$  mode under plane wave excitation and in blue the response of the  $TE_{20}$  mode under plane wave excitation

In Fig. 4.2 it is depicted the frequency response of a hole array structure with hole

diameter  $a = 2.5$  mm, lattice constant  $d = 5$  mm and thickness  $w = 0.5$  mm. Extraordinary Transmission appears as a narrow peak which tops 100% of transmission in the hole cut-off region. As it can be deduced from the observation of the modal transmission and reflection scattering matrix representation of Fig. 4.2, there are only two relevant modes contributing to the enhanced transmission near 60 GHz. One is a  $TM_{02}$  mode having its cut-off frequency just at 60 GHz, and the other one is its degenerated mode  $TE_{20}$  with the same cut-off frequency. This can be easily proven by inspection of Eqs. (4.18)-(4.25). As the frequency increases, the  $TM_{22}$  and  $TE_{22}$  modes begin to play a role in the electromagnetic field. The cut-off frequency of these modes is at 84.85 GHz, the location of the second minimum of transmission, see Fig. 2.10.

In order to simplify the discussion that follows, the  $z$ -component of the electric field for the  $TM_{02}$  mode and the  $z$ -component of the magnetic field for the  $TE_{20}$  mode are represented in Fig. 4.3. As it can be expected, the  $TM_{02}$  mode has only functional variations along the vertical  $y$ -axis being constant with  $x$ . Moreover, this mode does not present  $x$ -component of the electric field nor  $y$ -component of the magnetic field as it can be easily derived from Eq. (4.22) and Eq. (4.25). Similarly, the  $TE_{20}$  mode has only functional variations along the horizontal  $x$ -axis being constant with  $y$ . Also, this mode does not present  $x$ -component of the electric field nor  $y$ -component of the magnetic field as follows from Eq. (4.18) and Eq. (4.21).

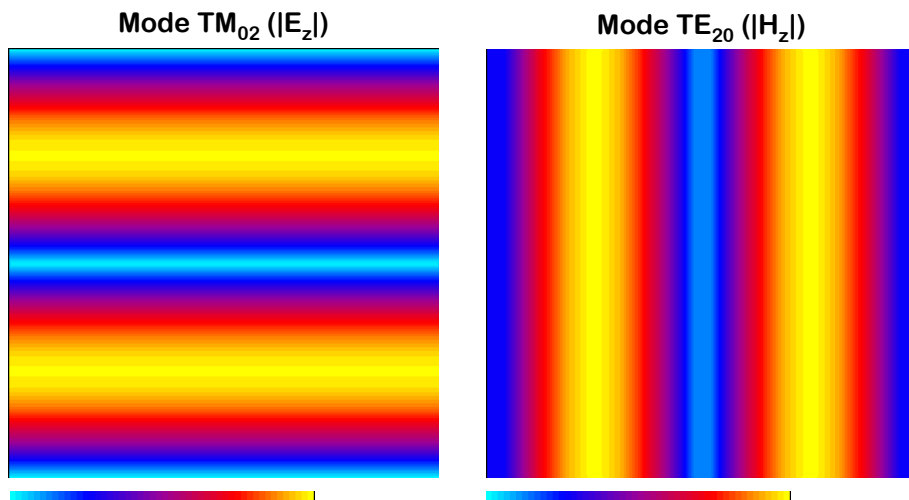


Fig. 4.3. Profile of the  $E_z$  field magnitude of the  $TM_{02}$  and the  $H_z$  field magnitude of the  $TE_{20}$  modes

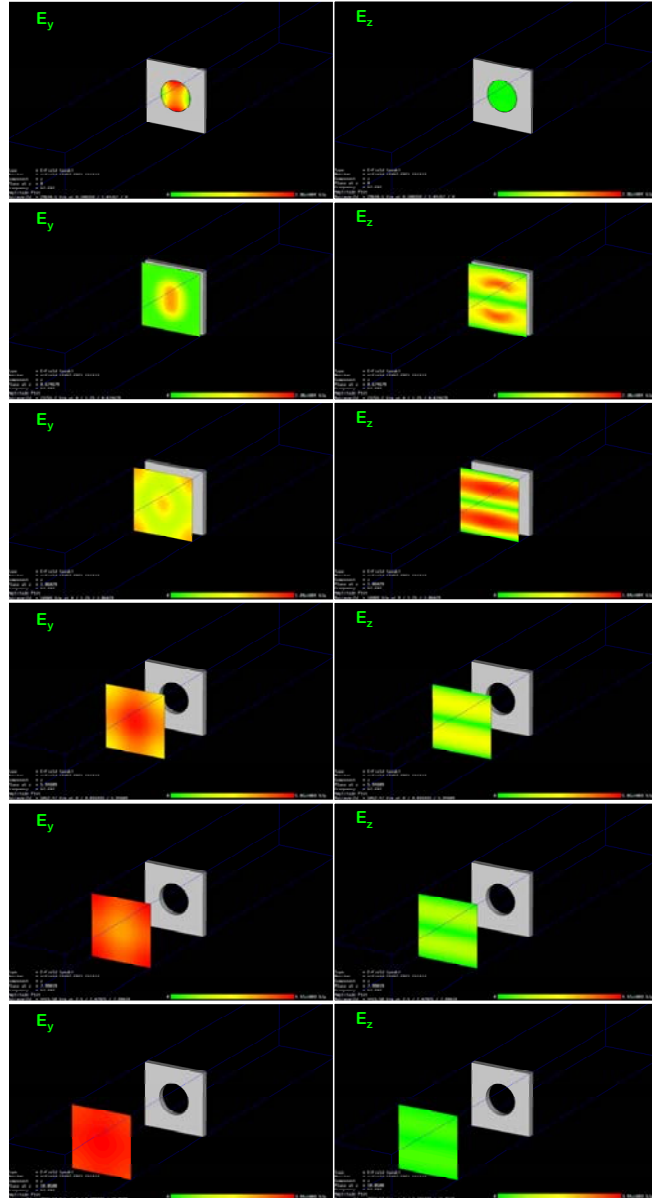


Fig. 4.4. The evolution along the artificial waveguide of the  $y$ - and  $z$ -components of the electric field ( $TM_{02}$  mode) in cut-planes parallel to the hole at 57 GHz.

In Fig. 4.4, it is represented the evolution along the artificial waveguide of the  $y$ - and  $z$ -components of the electric field in cuts parallel to the hole at 57 GHz, the frequency where the peak of enhanced transmission is maximum. And the  $x$ - and  $z$ -components of the magnetic field are given in Fig. 4.5. For this very particular case, due to the fact

that there is not reflected wave, it suffices to plot the output side of the waveguide. The input side is totally identical. This situation disappears as the reflected waves become relevant.

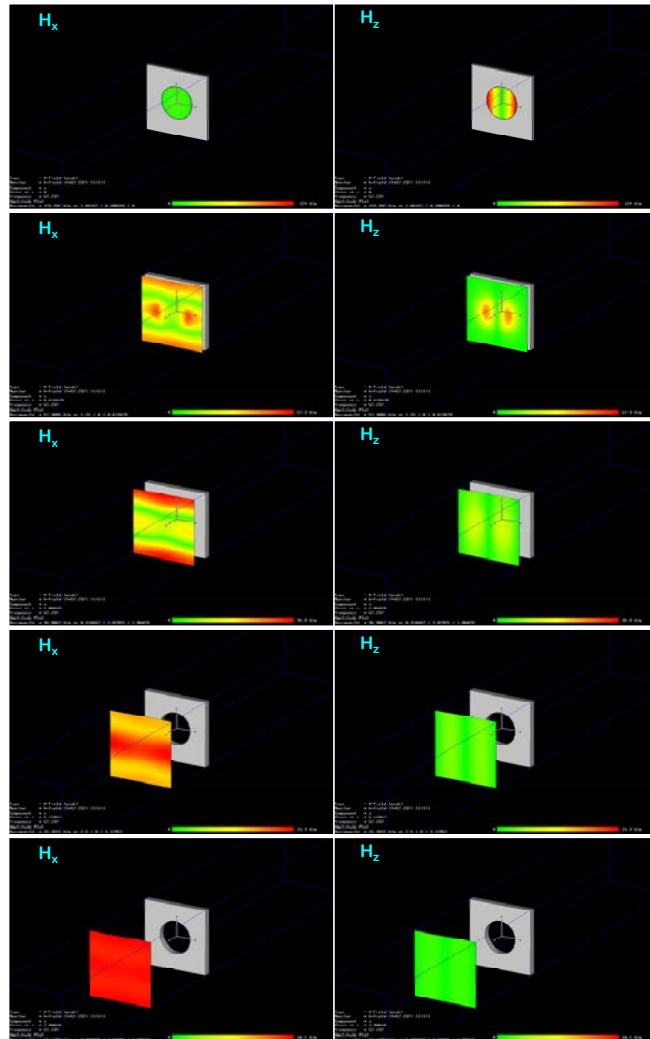


Fig. 4.5. The evolution along the artificial waveguide of the  $x$ - and  $z$ -components of the magnetic field ( $TE_{20}$  mode) in cut-planes parallel to the hole at 57 GHz.

Due to the fact that the  $TM_{02}$  and  $TE_{20}$  modes are evanescent at this frequency, the *fundamental mode* (plane wave)  $y$ -polarized electric field is recovered as one moves away from the nearby hole array surface. This fact will play a key role in the effects described in the next section.

Also, it must be remembered that the individual hole cut-off is around 70 GHz, for the lowest mode of the circular waveguide ( $TE_{11}$ ), see Figs. 4.4 and 4.5, when the cut-plane is located on the hole. This mode is also evanescent but it exhibits a magnetic field component along z-axis that cannot be compensated by the plane wave nor by the  $TM_{02}$  mode, and then the presence of the degenerated  $TE_{20}$  mode can be understood. As the operating frequency is increased, more modes enter in propagation and, consequently, the electromagnetic field structure becomes more complicated.

The Wood's anomaly [WOOD 02], [HESS 65] can be explained within the framework of this model as the perturbation that produces the entrance into propagation of the  $TM_{02}$  and  $TE_{20}$  modes of the artificial waveguide. The cut-off of these higher order modes is related to the so-called Rayleigh-Wood's anomaly, and in the hole array results in a null of transmission. From the classical point of view this kind of anomaly can be linked to branch point singularities occurring in a periodic structures at the Rayleigh wavelengths, i.e. at wavelengths where a new spectral order (a high order mode in the equivalent waveguide approach) passes from evanescent to propagating [HESS 65]. When this happens, rapid variations in the amplitude of the different spectral orders (waveguide modes) take place.

Resonant Wood anomalies, on the other hand, are related to forced resonances of the periodic structure. A perforated plate supports (complex) waves, which can be resonantly excited when the incident wavenumber matches the real part of the surface wave complex wavenumber, i.e. a spectral order is resonantly excited [SARR 03], [LOMA 05]. The additional effect of the resonance is to redistribute the energy among the other spectral orders, and, in particular among the observable propagating ones. Following the discussion of [HESS 65], the resonant spectral order is always evanescent. The holes provided a channel that allows for coupling between the two sides of the plate by means of evanescent hole fields. The periodic grating formed by the holes allows the incident wave to be scattered into an infinite number of diffraction (Floquet) modes. Cross coupling between these modes gives rise to resonant- and Rayleigh-Wood anomalies.

Therefore, extraordinary transmission has been explained in terms of the artificial waveguide model which is equivalent to the diffraction problem of a plane wave impinging normally to the hole array. From the experimental results, this model needs to be corrected in the sense that total transmission is only possible provided a

reasonably high number of holes are illuminated by the impinging plane wave, i.e., a minimal size of the structure is necessary, see Fig. 2.11. Notice that the aforementioned boundary conditions implicitly entail infinite replica of the unit cell.

The description of the subwavelength hole array problem as an equivalent artificial waveguide has been submitted to revision in the form of *Article 4.3*.

### 4.3 Left-handed propagation in the enhanced transmission band by stacking hole arrays.

In this section it is presented the surprising result of a left-handed propagation inside the structure constructed by stacking subwavelength hole arrays. First, the dispersion diagram of the structure is obtained taking advantage of the commercial simulator *CST Microwave Studio™*. It is compared with the dispersion diagram of stacked dense hole arrays plates. A graphical picture of the evolution of the fields is given as well. Then, the experimental results confirming the simulation predictions are shown. The results given here have been published in *Article 4.1*.

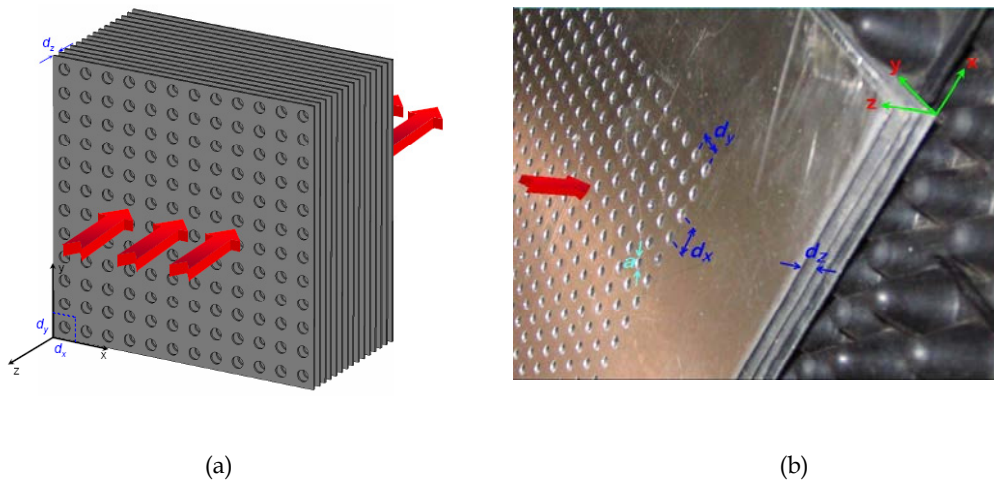


Fig. 4.6. (a) Schematic of the stacked hole array structure. (b) Photograph of the prototype. Parameters: hole diameter  $a = 2.5$  mm, transversal lattice constants  $d_x = d_y = d = 5$  mm and metal thickness  $w = 0.5$  mm. The longitudinal periodicity  $d_z$  can be conveniently tuned.

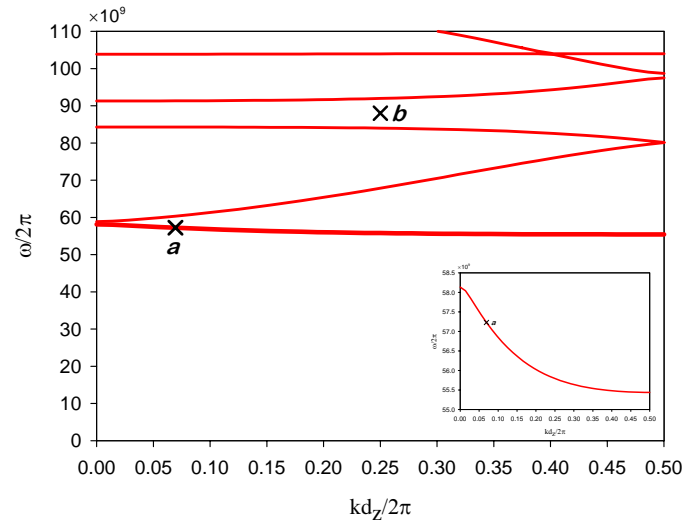
### 4.3.1 Dispersion diagrams: antiparallel phase and group velocities.

Once the single sub-wavelength hole array has been analyzed, one can explore the effects on the electromagnetic wave propagation along a stacked structure made of sub-wavelength hole arrays as it appears in Fig. 4.6. The proposed configuration is a particular case of a periodic structure that presents an electromagnetic band gap along the  $z$  direction.

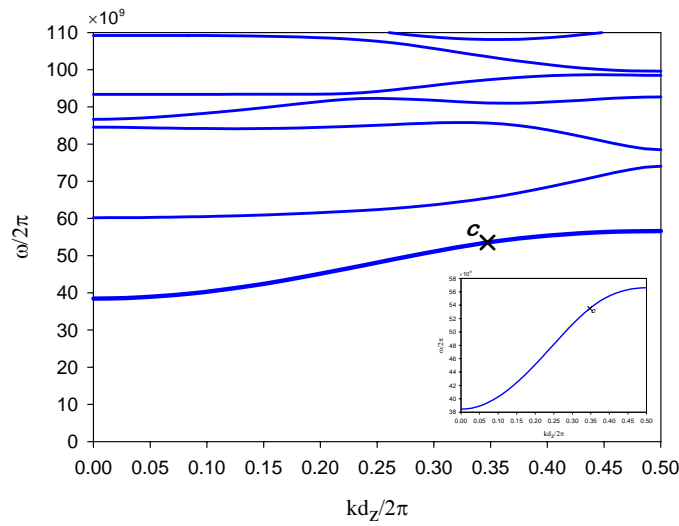
The longitudinal lattice  $d_z$  between each hole array can be conveniently adjusted in order to select the band gap position of the photonic crystal structure, which is located around a wavelength two times the inter-plate air cavity length. For this study, it was selected  $d_z = 2.25$  mm, i.e. cavity length  $d_z - w = 1.75$  mm, which corresponds to a band-gap centred at 86 GHz ( $\lambda = 3.41$  mm). Therefore, the band gap has been placed far away over the frequency band where ET appears.

Taking advantage of the eigenmode solver provided by the *CST Microwave Studio™* commercial code, it is possible to determine the dispersion diagram of the structure (alternatively, a similar approach based upon mode matching and generalized scattering matrix, see [RIEN 01], can be used to compute such dispersion diagram). In Fig. 4.7(a) is plotted the dispersion diagram of a subwavelength hole array stack with the next parameters: hole diameter  $a = 2.5$  mm, transversal lattice constants  $d_x = d_y = d = 5$  mm, cut-off wavelength  $\lambda_c = 4.3$  mm ( $\lambda_c = 0.85d$ ), and metal thickness  $w = 0.5$  mm. For comparison purposes, it has been depicted in panel (b) the dispersion diagram of a stack of dichroic filters (i.e. plates perforated with a dense hole array). The parameters of this last structure are:  $a = 4.0$  mm, cut-off at 40 GHz ( $\lambda_c = 7.5$  mm, being  $\lambda_c = 1.5d$ ), with the same lattice constants and metal thickness. The longitudinal periodicity is  $d_z = 2.25$  mm, as mentioned above.

The ET band for the subwavelength hole array photonic crystal structure corresponds to the first band of Fig. 4.7(a). Notice that this band shows a negative slope (see inset in Fig. 4.7(a)), which accounts for phase velocity opposite to the group velocity, or, in other words, phase and group velocities are antiparallel. This kind of propagation in which phase evolves in the opposite sense of the energy propagation is usually referred as left-handed propagation and has found many interest in the field of metamaterials [VESE 68], [SHEL 01], [PEND 00], [SMIT 05b]. Thus it can be said that by just stacking subwavelength hole arrays a Left-Handed Metamaterial (LHM) can be obtained.



(a)



(b)

Fig. 4.7. Simulated dispersion diagrams for photonic crystals with longitudinal periodicity  $d_z = 2.25$  mm, made by stacking (a) sub-wavelength hole arrays with parameters  $a = 2.5$  mm,  $d = 5$  mm,  $w = 0.5$  mm (b) propagating hole arrays with  $a = 4$  mm and the same lattice constant and metal thickness.

This behavior is qualitatively different to what happens when dichroic filters are stacked. Recall that for dichroic filters ET was not obtained. Note that the first band in Fig. 4.7(b) begins at the cut-off of the holes. Looking at the inset of the figure, it is seen

that the first band shows a positive slope, that is, phase and group velocities are parallel. Employing the mentioned terminology, this corresponds to conventional right-handed propagation or Right-Handed material (RHM).

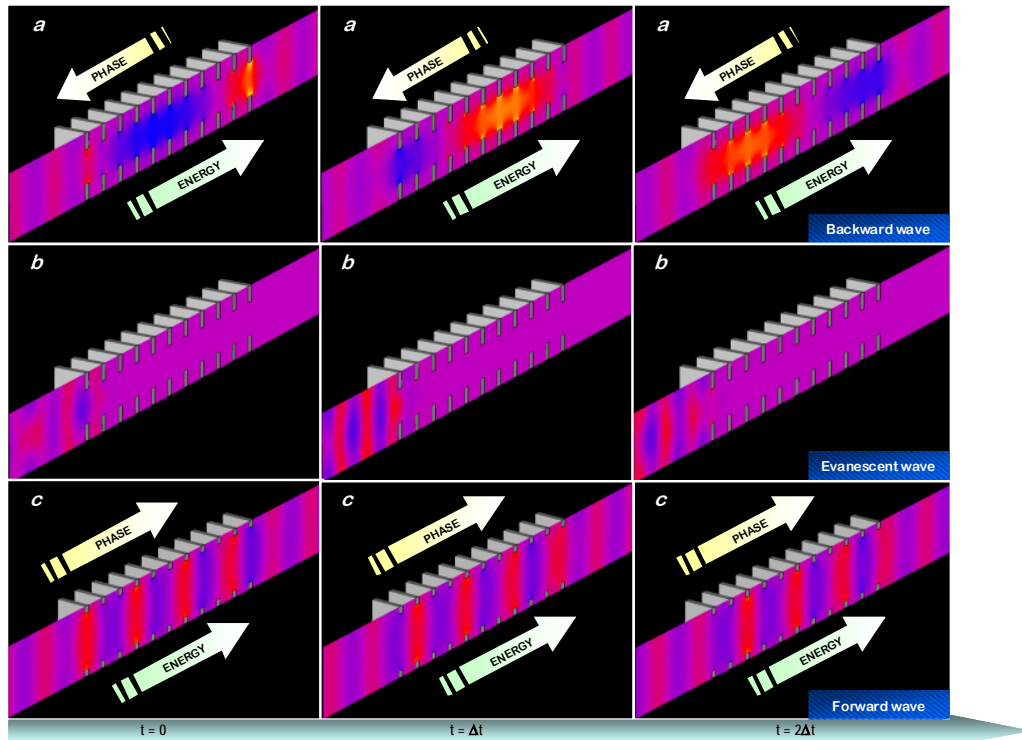


Fig. 4.8. Simulated vertical electric field of a plane wave impinging normally to the lossless structure. Simulations for the cases of sub-wavelength hole array structure (a) in the first band (ET band) at 57.3 GHz and (b) inside the band gap at 88 GHz. Simulations for propagating hole array structure (c) in its first band, at 53.5 GHz.

Notice that the band gaps are placed at 86 GHz ( $\lambda = 3.41$  mm) in both cases due to the same inter-plate cavity. It can be observed that the band-gap in the sub-wavelength case is broader than in the propagating one. Moreover, a previous band-gap is present around 60 GHz ( $\lambda = 5$  mm) due to the transversal periodicity related to Wood anomalies. Conversely, this band-gap is narrower in the subwavelength case.

A graphical picture of the electric field evolution inside the metamaterial when a plane wave impinges normally to the plates is shown in Fig. 4.8. Each panel correspond to the highlighted points (a, b, and c) in Fig. 4.7: panels (a) and (b) correspond to the first band and band-gap of the metamaterial made of sub-

wavelength hole arrays (points  $a$  and  $b$  in Fig. 4.7(a), respectively), whereas panel (c) correspond to the first band of the photonic crystal made of propagating hole arrays (point  $c$  in Fig. 4.7(b)). Notice that – following the formulation of the problem given in section 4.1 - the structure is infinite in the  $x$  and  $y$  dimensions and only the unit cell is shown.

In Fig. 4.8(a) the electrical field evolution is visualised for a particular frequency inside the band, say the frequency of maximum transmission with a single plate, 57.3GHz (point  $a$  in Fig. 4.7(a),  $\lambda = 5.23$  mm). The phase fronts inside the structure are reversed with respect to the incident and emergent plane wave phase fronts, proving the existence of a backward wave there. In other words, anti-parallel phase and group velocities inside the stacked hole array result in a left-handed metamaterial.

For the sub-wavelength structure it is also given the electric field evolution at the band gap, specifically at 88 GHz (point  $b$  in Fig. 4.7(a),  $\lambda = 3.41$  mm), see Fig. 4.8(b). Note the stationary wave pattern at the face where the plane wave is impinging.

For propagating holes working in its first band, at 53.5 GHz (point  $c$  in Fig. 4.7(b),  $\lambda = 5.61$  mm), it is readily seen (Fig. 4.8(c)) that phase and group velocities travel parallel inside the structure, giving evidence of standard, right-handed behaviour.

Finally, the electric field evolution at the band-gap of the propagating hole structure is not given since it shows a similar behaviour as that of Fig. 4.8(b).

### 4.3.2 Experimental results: LHM.

The possibility to obtain a metamaterial by stacking hole arrays is experimentally tested in this section. The structure of Fig. 4.6 was constructed by means of laser drilling machining. The parameters of the structure are as mentioned in the previous section, and the size of the array is  $54 \times 54$  holes.

By means of an *AB Millimetre™* quasioptical vector network analyzer, the amplitude and phase of the transmission coefficient have been measured in the frequency range of 45 up to 110 GHz (2.73 mm up to 6.67 mm), employing the set-up shown in Fig. 4.9. The emitter and receiver have been located at a distance of 950 mm from the sample. The beam waist diameter impinging on the structure has a maximal dimension of approximately 326 mm (at 40 GHz), that is comparable to the side length of the structure. To avoid perturbing diffraction effects the bench is covered with absorbing

material. The results of the measurements when the longitudinal periodicity is fixed in  $d_z = 2.25$  mm are given in Fig. 4.10.

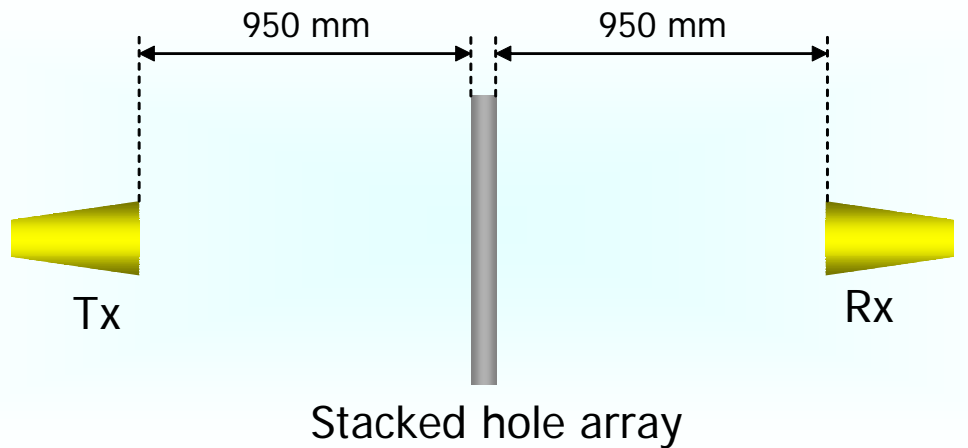
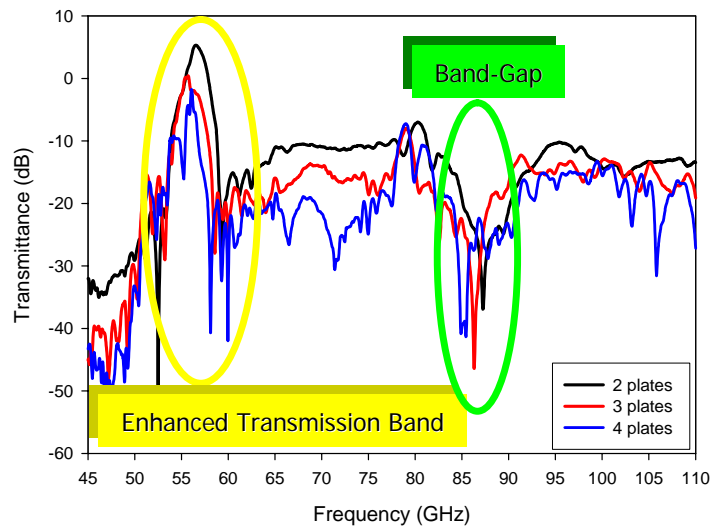


Fig. 4.9. Schematic of the experimental set-up used for the transmission measurement of stacked hole array structures.

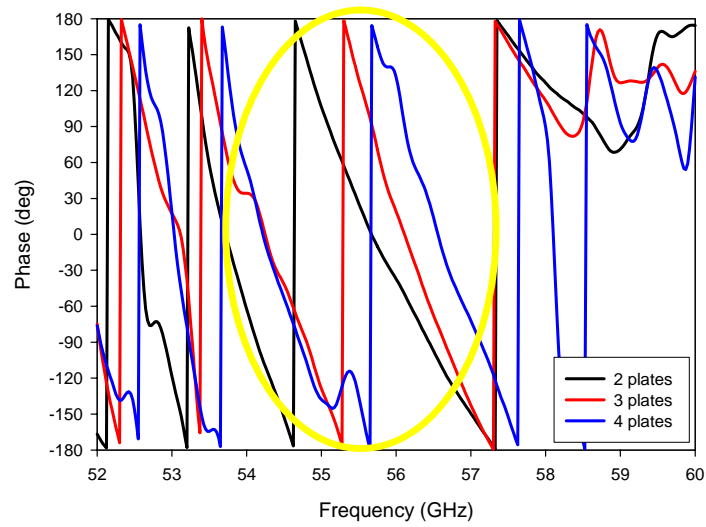
Looking at the experimental results for the amplitude (panel (a)), it can be seen that a selective transmission band is obtained for different number of plates, thus showing enhanced transmission that can be used in novel filters. The level of signal diminishes somewhat as the number of stacked plates increases. However, in all the cases the level of signals is at a reasonable level. Moreover, for 2 plates the received power is above 0 dB, though the structure is passive. This may be due to a possible increase of the emergent beamwaist compared with that of the incident gaussian beam. Also notice in the magnitude response the clear presence of a band-gap around 88 GHz, as predicted in the dispersion diagram of Fig. 4.7(a).

Fixing the attention on Fig. 4.10(b), in the band where the transmission reaches its maximum, the phase surprisingly increases with the number of structure periods. Note that the phase for two plates (black line) is lower than for three plates (red line) and these two lower than for four plates (blue line) in the ET frequency range, whereas out of this range the phase behaves normally, i.e. it decreases as the number of plates increases, see panel (c). This result shows experimentally that the phase velocity and power flow are in opposite directions and, therefore, left-handed

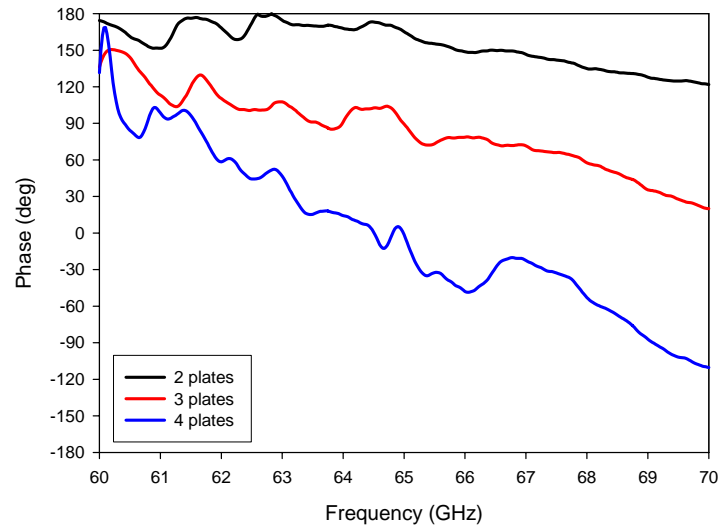
propagation effects appear inside the structure.



(a)



(b)



(c)

Fig. 4.10. (a) Measured logarithmic transmission coefficient magnitude for  $N = 2$  (black),  $N = 3$  (red), and  $N = 4$  (blue) stacked plates, (b) measured phase varying the number of sub-wavelength hole array plates,  $N = 2$  (black),  $N = 3$  (red), and  $N = 4$  (blue) in the LHM band, and (c) the same as in (b) in the RHM band.

## 4.4 EBG over ET band: RHM.

In this section it is seen that by just modifying the longitudinal period, the left-handed character of the stacked structure can be converted to right-handed. These results are currently under revision in the form of *Article 4.2*.

### 4.4.1 Simulation results: tuning RHM or LHM with the EBG.

The band of Extraordinary Transmission depends fundamentally on the vertical hole array lattice constant,  $d_y$ . In contrast, the Electromagnetic Band Gap position of the structure is engineered by choosing the longitudinal lattice  $d_z$  between each hole-array in such a way that it is located around a wavelength two times the inter-plate air cavity length. Therefore, it is deduced that both phenomena can be controlled independently. This leads to the possibility of placing the EBG just over the ET band. Selecting  $d_z = 2.75$  mm, i.e. cavity length  $d_z - w = 2.25$  mm, and taking into account the phase introduced by the imperfect mirrors that bound the cavity, the band-gap is centred at 57 GHz, just over the frequency band where LHM-ET appeared. The result

of this is seen in the dispersion diagram depicted in Fig. 4.11

Note that a band gap is opened just over the band where previously appeared joint ET and left-handed effects (see Fig. 4.7(a)). The first band in Fig. 4.11 (shown in detail in the inset) is shifted towards lower frequencies (longer wavelengths) and exhibits a positive slope, i.e. phase velocity parallel to the group velocity. In other words, right-handed propagation exists inside the structure.

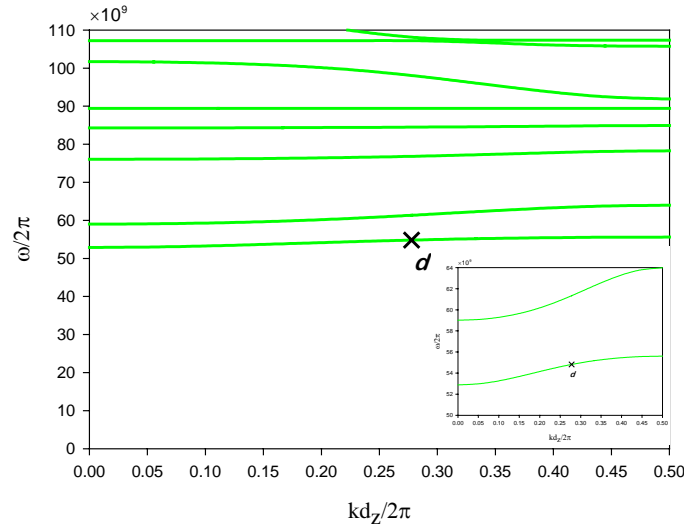


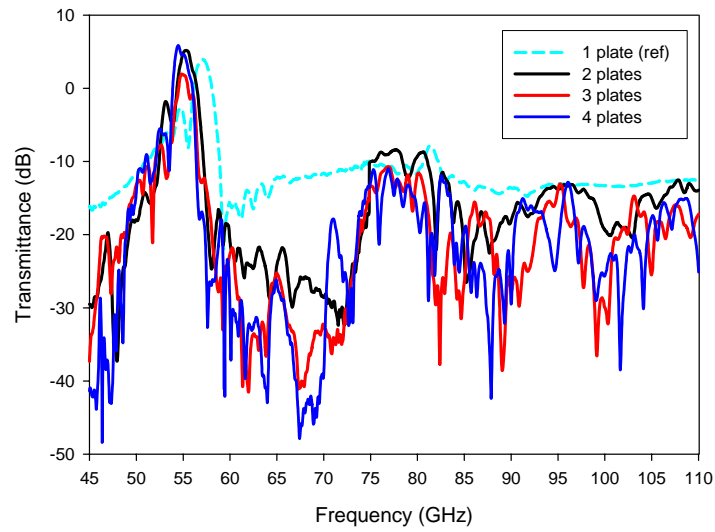
Fig. 4.11. Simulated dispersion diagram for a stack of sub-wavelength hole arrays with parameters  $a = 2.5$  mm,  $d = 5$  mm,  $w = 0.5$  mm and longitudinal periodicity  $d_z = 2.75$  mm.

The physical origin of the band gap, where wave propagation is not allowed, is caused by interferences of multiple waves in the periodic structure [JOAN 95]. In this case, propagation is forbidden along the longitudinal direction in certain frequencies, and the longitudinal lattice allows us to select the gap position. Putting the EBG just over the ET band, inhibits LHM-ET propagation and provokes the emergence of a pair of shifted right handed propagation bands surrounding the band gap. Hence, it is apparent that tuning the EBG position LHM or RHM propagation can be selected. An intuitive explanation for this fact will be given later in section 4.5.

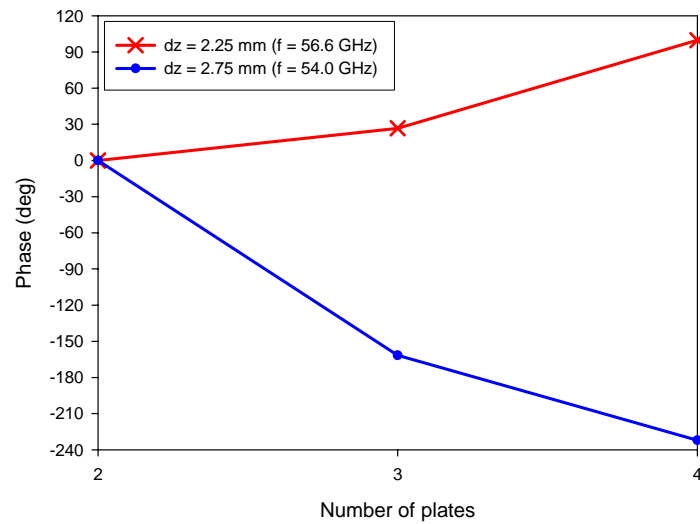
#### 4.4.2 Experimental results: RHM.

With the prototype shown in Fig. 4.6, and selecting a longitudinal period of  $d_z = 2.75$

mm, measurements are carried out in the millimeter wave range by using our *AB Millimetre<sup>TM</sup>* quasi-optical vector network analyzer and using the experimental set-up depicted schematically in Fig 4.9.



(a)



(b)

Fig. 4.12. Experimental amplitude transmission spectra in the case of RHM-ET,  $d_z = 2.75$  mm, as the number of stacked subwavelength hole arrays increase (a) and a comparison of the measured phase response for increasing number of stacked subwavelength hole arrays for LHM-ET (red) and RHM-ET (blue).

The transmission coefficient magnitude measured in the frequency range of 45 up to 110 GHz is shown in Fig. 4.12(a), for an increasing number of plates,  $N$ . The peaks appearing for  $N > 1$  are notably shifted towards lower frequencies as compared with the case of  $N = 1$  (single subwavelength hole array, displayed as reference). However, this phenomenon is more than just a frequency shift. It actually comprises the mixture of two related singularities: EOT is inhibited from its frequency range, the band at 57 GHz vanishes, and a new right-handed band emerges at 54 GHz. Note also that several minima of transmission are clearly identified, as the band diagram of Fig. 4.11 predicted.

Moreover, the phase response for the case of ET measured at 54 GHz (see blue trace of Fig. 4.12(b)) decreases with the number of structure periods, i.e. the phase behaves normally as in an ordinary Right-Handed structure. Conversely, for the case where band gap is away from the ET band ( $d_z = 2.25$  mm), the phase inside the first band (56.6 GHz) increases with the number of periods of the structure, which accounts for an anomalous phase behavior. This result suggests that the left-handed propagation effects have been inhibited due to the electromagnetic band gap of the periodic structure. The measurement results demonstrate our simulation predictions. The results presented in this section have been submitted for publication in a paper which is currently under revision, *Article 4.2*.

## 4.5 LHM- and RHM-ET: an intuitive explanation.

It has been shown that in stacked subwavelength hole arrays left-handed and right-handed propagation can be obtained by simply modifying the longitudinal periodicity. Here, an intuitive engineering-based explanation is developed to clarify in some extent the phenomenon.

Since the times of radar development, it is well known that a sub-wavelength hole in a conducting plate can be considered as a self-inductive element, being the self-inductance larger as the hole diameter decreases. Conversely, a capacitive response is obtained when the hole diameter increases [SCHW 68]. Therefore a subwavelength hole array in a conducting plate can be considered as an array of self-inductance elements,  $L_{hole}$ . The hole array plate stacking brings about a mutual capacitance,  $C_{plates}$  between the plates in such a way that a structure of shunt  $L_{hole}$  and series  $C_{plates}$

elements respectively is created. Additionally, the free space between the plates behaves as a transmission line with a distributed series inductance  $L_{line}$  and a distributed shunt capacitance  $C_{line}$  that permits wave propagation [RAMO 94]. For a fixed periodicity within the plate plane, as the hole diameter decreases the fractional area of metal is enlarged and the capacitance  $C_{plates}$  between the plates increases. At the same time,  $C_{plates}$  is augmented as the plates are stacked closer.

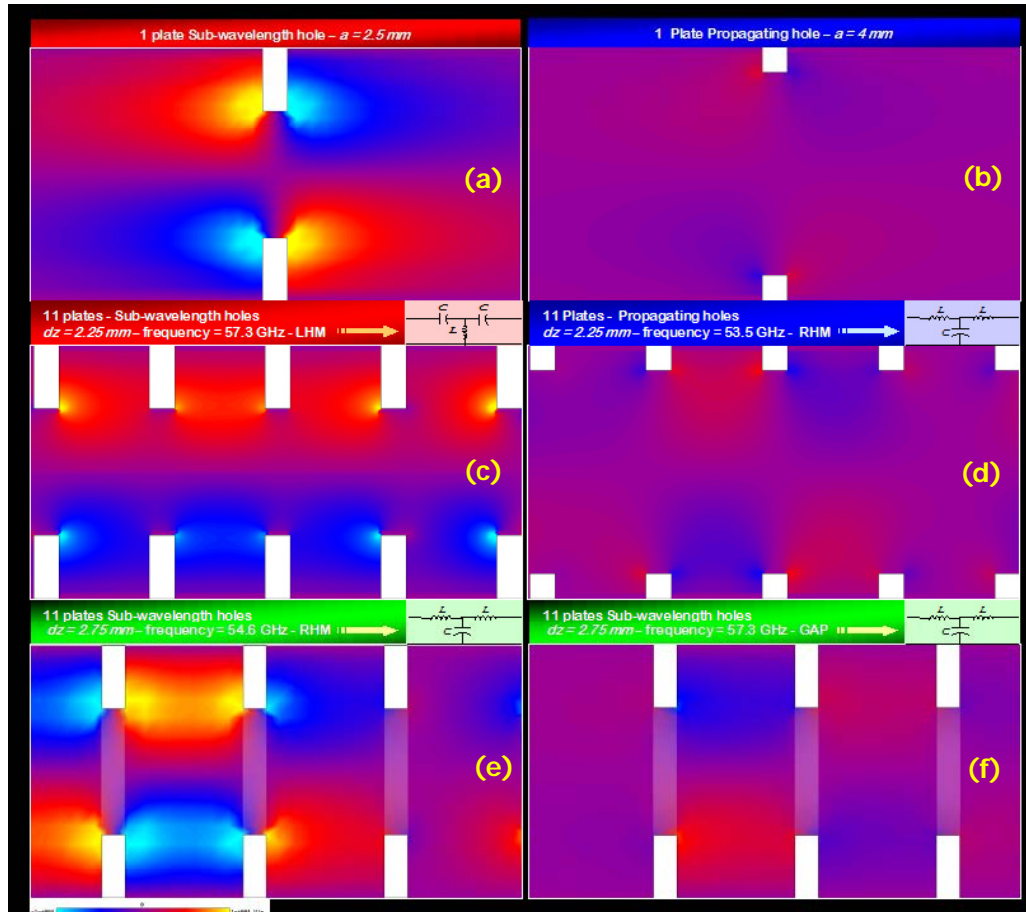


Fig. 4.13. Simulations for the cases of single sub-wavelength hole array structure (a) in the first band (EOT band) at 57.3 GHz. Single propagating hole array structure (b) at 53.5 GHz. Sub-wavelength hole array structure with 11 stacked plates spaced  $d_z = 2.25$  mm (c) at 57.3 GHz. Propagating hole array structure with 11 stacked plates spaced  $d_z = 2.25$  mm (d) at 53.5 GHz. Sub-wavelength hole array structure with 11 stacked plates spaced  $d_z = 2.75$  mm (e) at 54.6 GHz and (f) inside the band gap at 57.3 GHz.

Due to the complex electromagnetic field distribution governing this problem it will be followed a simplified approach in order to identify the kind of propagating waves present in these structures. It has been considered the evolution of the  $z$ -component of the electric field (i.e. perpendicular to the plates) along the  $y - z$  cutting plane. Under the modal formalism approach outlined in section 4.1, the evanescent electric field  $E_z$  can be attributed to the  $z$ -component of the  $TM_{02}$  mode. It is shown in Fig. 4.13(a) and Fig. 4.13(b) the  $E_z$  field for a single plate of subwavelength and propagating hole arrays respectively. It is clear that  $E_z$  for subwavelength holes is much more intense than for propagating ones at the edge of each hole. Moreover, the field out of the subwavelength hole array plate extends over a longer distance perpendicular to the plate. Figures 4.13(c) to 4.13(f) show  $E_z$  for different stacked structures: subwavelength hole array plates stacked with periodicities  $d_z = 2.25$  mm in the LHM-ET band (Fig. 4.13(c)) and  $d_z = 2.75$  mm in the RHM-ET band (Fig. 4.13(e)) and inside the bandgap (Fig. 4.13(f)), as well as propagating hole array plates stacked with periodicity  $d_z = 2.25$  mm, Fig. 4.13(d). From this figure it is clear that the electric field along  $z$  behaves similarly for all the cases of subwavelength or propagating stacked hole arrays (Figs. 4.13(d), (e), and (f)) where usual RHM wave propagation has been observed (note that a RHM-ET is also present in Fig. 4.13(e)). In these cases, the fields are not able to change the total series inductance and the total shunt capacitance and, therefore, the waves are propagating in the usual RHM way. This is also in agreement with the dispersion diagrams of Fig. 4.7 and Fig. 4.11.

However, for the case of LHM-ET, the field is very different compared with the remaining cases, see Fig. 4.13(c). It suggests that the inter-plate series capacitance  $C_{plates}$  and the subwavelength hole shunt inductance  $L_{holes}$  become dominant. Therefore, a dual transmission line [RAMO 94], consisting of dominant shunt inductances and series capacitances, is formed. The key property of this simplified and idealized dual transmission line model is that it supports waves where energy and phase fronts are travelling in opposite ways, which implies that LHM propagation is present. It can be consequently stated that a left-handed metamaterial can be obtained by ET through a photonic crystal structure of metallic plates with subwavelength hole arrays whenever the longitudinal periodicity of the structure is short enough to allow for an intense coupling between the subwavelength hole array plates. Conversely, a right-handed propagation is obtained for spaced subwavelength hole arrays and for arrays of propagating holes. These results provide direct evidence to the statement that the

extraordinary transmission, negative refraction, and photonic band-gap are connected phenomena [GOME 03].

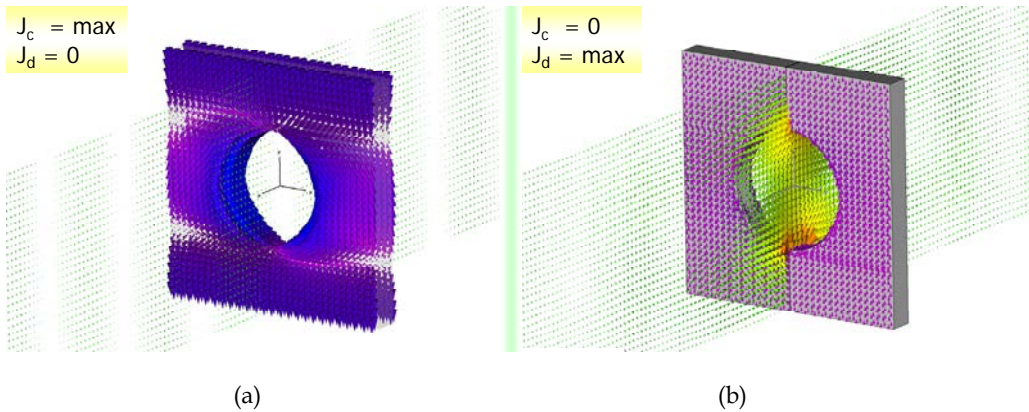


Fig. 4.14. Simulation results of a single hole array. The surface current on the plate and the electric field on a cutting plane representation are overlaid. It is shown that in ET operation, the hole array can be described by a LC-tank circuit: when the conduction current is maximum, the displacement current is nearly zero (a) and when the displacement current is maximum, the conduction current is nearly zero (b).

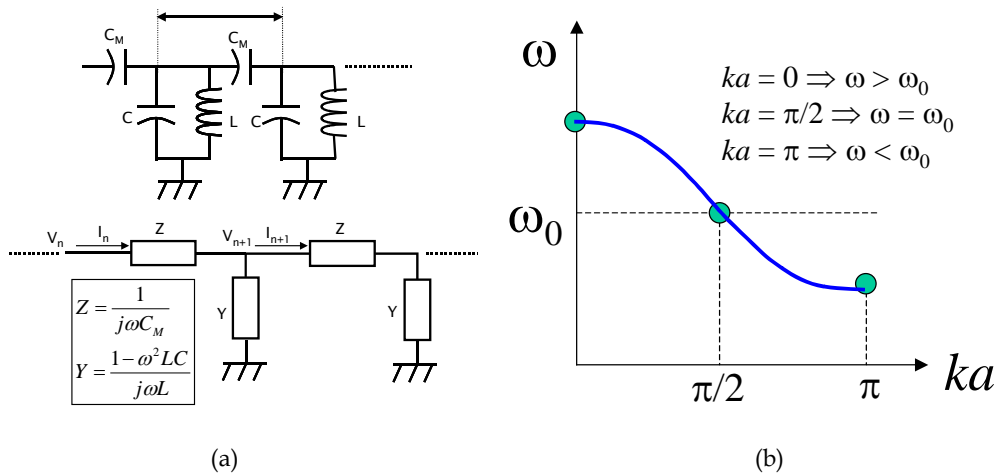


Fig. 4.15. (a) Schematic of a chain of electrically coupled resonators. (b) Generic curve obtained for the first band of the depicted structure.

Finally, note that the modellization of a small hole as an inductance is an advantageous simplification for the rough analysis given here. However, a more correct model for each hole array in its ET band would be a shunt LC-resonator. To

observe this, it has been depicted in Fig. 4.14 the simulated surface current on a single plate hole array overlaid to the electric field in a cutting plane at two different instants. It is observed that when the surface current (conduction current) reaches a peak, the electric field (displacement current) is nearly zero, see panel (a). Conversely, as shown in panel (b), when the electric field reaches a peak the surface current is nearly zero. Thus, in the first half of the period the energy is contained in the conduction current, directly related with the magnetic field and in the other half it is contained in the displacement current, directly related with the electric field. Thus the hole array in the regime of ET can be appropriately modelled by a LC-tank.

It is shown here that provided there is an electric coupling between resonators, LHM propagation is found. The schematic of the structure is depicted in Fig. 4.15(a). From the circuit, the dispersion relation can be obtained (see details in section 5.3):

$$\omega = \frac{\omega_0}{\sqrt{1 - \frac{2C_M}{C + 2C_M} \cos(ka)}} \quad (4.26)$$

where  $\omega_0 = [L(C + 2C_M)]^{-1/2}$ ,  $L$  is the inductance and  $C$  is the capacitance to ground of the each resonator and  $C_M$  is the mutual capacitance between adjacent resonators.

Particularizing the argument of the cosine to  $0, \pi/2, \pi$ , the general shape of the first band is obtained. As it can be observed in Fig. 4.15(b) it presents a negative slope, accounting for the left-handed propagation. Thus, any chain of electrically coupled resonators is LHM in its first band.

## 4.6 Transition from RH to LH (zero group velocity) and other results.

Up to now it has been seen that by stacking hole arrays and modifying the stack period, LHM and RHM response can be obtained. A natural question arises about the point where the transition from the LH to RH regime is effectively done. It is depicted in Fig. 4.16 the first band for different longitudinal periodicities of hole arrays with the usual parameters, see Fig. 4.6.

As it is readily observed, for the curves  $d_z = 1.25$  mm (black), 1.75 mm (yellow) and 2.25 mm (red), the first band has a left-handed characteristic. It is worth to note that

even for very small periods the band is LH (in the case  $d_z = 1.25$  mm the relation to wavelength is  $d_z/\lambda = 0.24$ ). This fact allows to consider the stacked hole array as an effective metamaterial in the longitudinal direction, without any explicit reference to the operating wavelength.

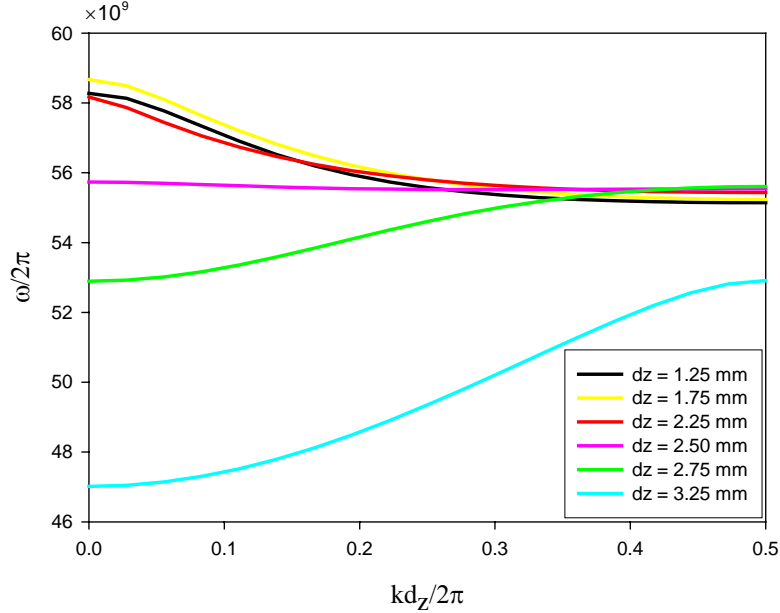


Fig. 4.16. Simulated first band of stacked hole arrays with different longitudinal periodicity:  $d_z = 1.25$  mm (black), 1.75 mm (yellow) and 2.25 mm (red) show left-handed character,  $d_z = 2.50$  mm (pink) is the transition from LH to RH propagation,  $d_z = 2.75$  mm (green) puts the bandgap over ET band and a RH band appears just below and  $d_z = 3.25$  mm (cyan) presents a first RH band due to resonant F-P cavity.

On the other hand, for large periods, say  $d_z = 3.25$  mm, the first band is certainly RH and appears at a frequency below ET. The origin of this band is clearly a F-P cavity mode resonance of the inter-plate spacing. Note that as the period is enlarged, the cavity resonance wavelength is also enlarged. Therefore the holes are relatively smaller in terms of resonance wavelength, giving as a result a cavity of length equal to the thickness of the air slab ( $d_z - w = 3.25 - 0.5 = 2.75$  mm) bounded by a couple of imperfect reflectors. Transmission of power through the holes is allowed by a tunnel-like mechanism, when the resonance condition of the cavity, corrected by the phase introduced by the imperfect reflectors, is accomplished.

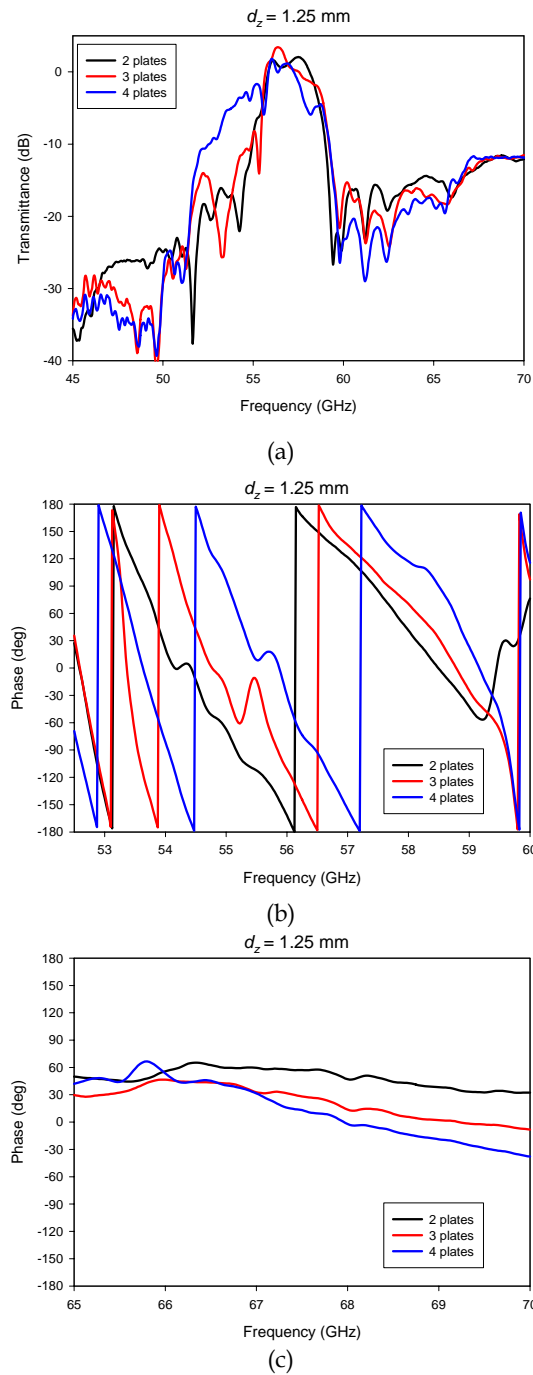


Fig. 4.17. Measured transmission coefficient results when  $d_z = 1.25$  mm for two (black), three (red) and four (blue) plates. (a) Magnitude from 45 to 70 GHz. (b) Phase from 52.5 to 60 GHz: anomalous behavior in the ET band. (c) Phase between 65 and 70 GHz: normal behavior.

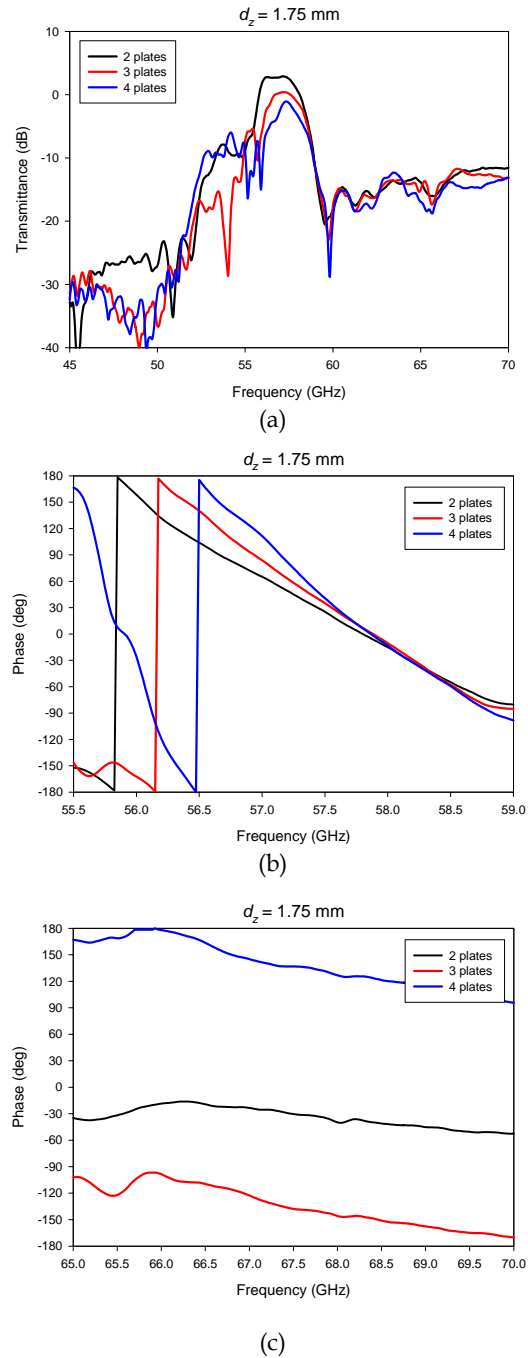
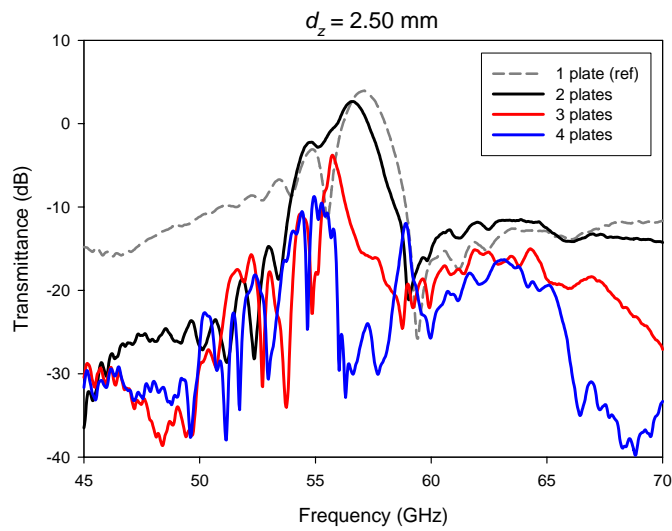
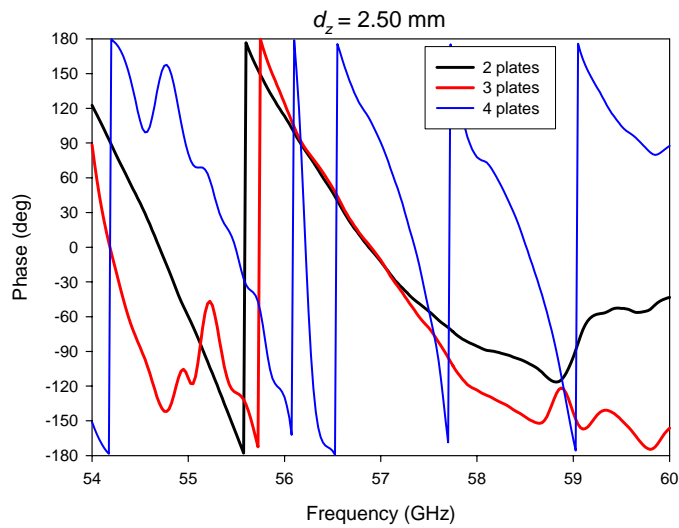


Fig. 4.18. Measured transmission coefficient results when  $d_z = 1.75$  mm for two (black), three (red) and four (blue) plates. (a) Magnitude from 45 to 70 GHz. (b) Phase from 55.5 to 59 GHz: anomalous behavior in the ET band. (c) Phase between 65 and 70 GHz: normal behavior.



(a)



(b)

Fig. 4.19. Measured transmission coefficient results when  $d_z = 2.5$  mm for two (black), three (red) and four (blue) plates. (a) Magnitude from 45 to 70 GHz. For comparison purposes it has been included the trace of a single plate (dashed gray). (b) Phase from 54 to 60 GHz.

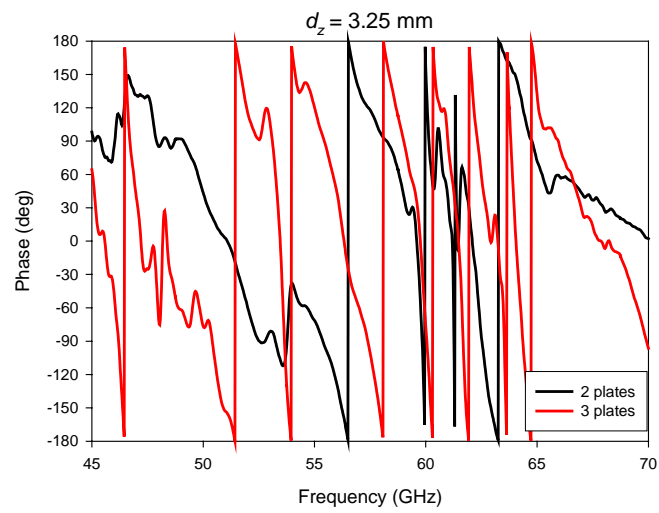
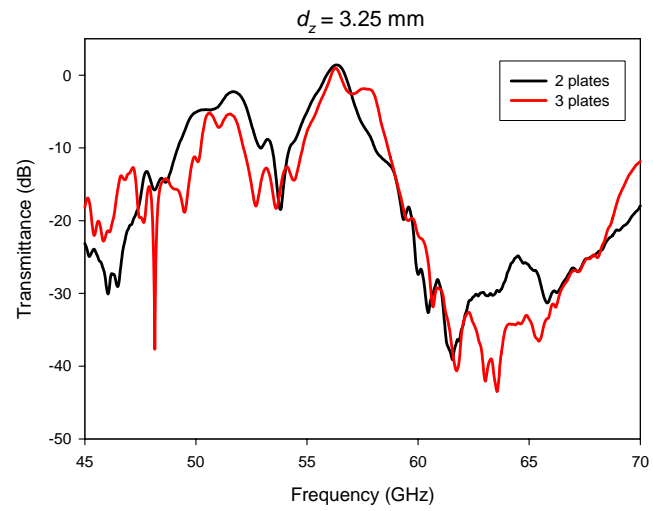


Fig. 4.20. Measured transmission coefficient results when  $d_z = 3.25$  mm for two (black) and three (red) plates. (a) Magnitude from 45 to 70 GHz. (b) Phase from 45 to 70 GHz. In the first band around 50 GHz the phase presents a normal behavior.

Finally and very interestingly, the limit between LH and RH propagation is the case  $d_z = 2.50$  mm where the curve obtained presents a slope approximately equal to zero, i.e. zero group velocity. This fact suggests that with this periodicity and at that particular frequency, a frozen mode - a mode with very low group velocity - can exist inside the stacked structure. This frozen mode regime as well as a revision of the left-handed and right-handed propagation in stacked subwavelength hole arrays has been submitted to revision in the form of *Article 4.3*.

All these cases have been experimentally studied. It is shown in Fig. 4.17(a) the transmission coefficient magnitude when  $d_z = 1.25$  mm, for two (black), three (red) and four (blue) plates. As it is readily seen, the measured transmitted power level in the ET band is reasonably high in all the cases shown, and is effectively above 0 dB probably due to a lens effect produced when the structure is inserted. It can also be identified the presence of the Wood's anomaly at around 60 GHz.

The phase in the ET band is shown in panel (b). It is clearly seen that in this range the phase for two plates goes below the phase of three plates and this two below the phase of four plates, accounting for a LHM behavior. Finally is shown in panel (c) the phase behavior out of the ET band. Now the phase obeys a RH behavior decreasing with an increasing structure.

When the periodicity is  $d_z = 1.75$  mm the results are quite similar. The magnitude response (Fig. 4.18(a)) has also a high level in the ET band, and also the peak for two plates is more than 0 dB. The Wood's anomaly is clearly shown in then measurements. The phase response in the ET band (panel (b)) accounts for the LH behavior, with phase increasing as the structure grows in thickness. Out of the ET band (panel (c)) the phase behaves normally, with that of two plates above the one three plates, and these two above that of four plates, though in the figure it has suffered of a 180 degrees wrap and is apparently above the other curves.

The case of  $d_z = 2.25$  mm has been explained in detail in section 4.3 and the measurement results are shown in Fig. 4.10. The study continues with  $d_z = 2.50$  mm, the periodicity where the transition from LH to RH propagation takes place. In Fig. 4.19(a) is depicted the transmission coefficient magnitude for this case. Watching the dispersion diagram, it is expected that only a narrow peak at approximately 55.8 GHz should be detected. For two plates this is quite not the case. Rather a wide band is obtained in the range of ET.

This suggests that the effect is a dynamic one and we should at least construct a three plates stack in order to have the minimum necessary periodic structure. In fact when three plates are stacked the transmission is strongly affected and only a narrow peak with a level of  $-5$  dB in the vicinity of 55.1 GHz remains. The transmission with four plates shows a deep rejected band precisely in the ET frequency range (it has been included in dashed gray the response of a single plate), with a weak trace of a peak at 55 GHz and other at 59 GHz, related to the second band (not shown in Fig. 4.19). Therefore, it seems that losses as well as finite structure effects cancel the emergence of the very narrow peak of transmission around 55 - 56GHz.

Importantly enough, the phase measurement plotted in panel (b) shows no signs of LH behavior in the band, except in the narrow frequency range of 55.5 to 56.2 GHz between two and three plates. However, as it has been mentioned before, the rejection of the band needs at least three plates to be effective, accounting for a dynamical nature of the effect, in contrast with the LHM behavior which manifests itself for only two plates.

When the periodicity is  $d_z = 2.75$  mm, the ET band is splitted into two RH bands. This has been explained in detail in section 4.4 and the measurement results are in Fig. 4.12. The case  $d_z = 3.25$  mm is the last one to be studied. In this case only the measurement results for two and three plates have been included in Fig. 4.20, in order to make it more readable. In the magnitude plot of panel (a) the first band around 50 GHz is clearly detected. This is followed by a second band centered at 56 GHz, with a deep rejection band between them. The phase measurement of panel (b) shows unambiguously the RH character of the first band, with the phase of two plates above that of three plates.

## 4.7 Gaussian beam compression: beaming.

Watching the experimental results obtained, it is noticed that for some configurations a transmission level above 0 dB is detected. This is a notable effect and deserves some attention. By putting the farfield measurement set-up with the  $54 \times 54$  subwavelength hole array located at 950 mm of the antennas a peak of transmission between 3 - 4 dB is obtained at the ET frequency, see Fig 4.21(b). This means that the structure enhances in some manner the power collected by the receiver antenna in comparison to the free-space propagation calibration.

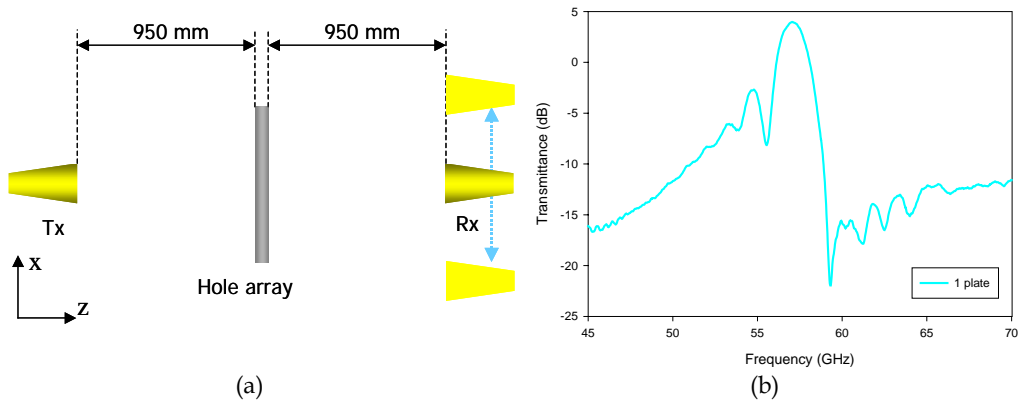


Fig. 4.21. (a) Schematic of the experimental set-up to measure the gaussian beam waist compression. (b) Transmittance coefficient magnitude of a  $54 \times 54$  subwavelength hole array.

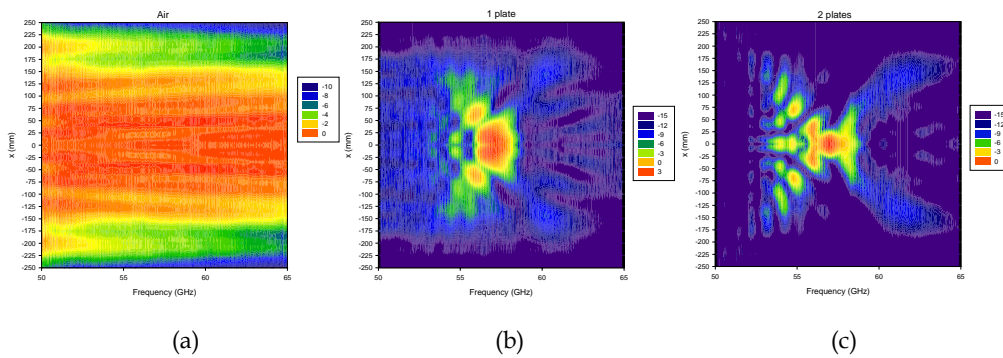


Fig. 4.22. E-plane measurement. Contour plot of the received power level as a function of the frequency (abscissa) and the lateral shift (ordinate). The frequency span extends from 50 to 65 GHz and the lateral shift excursion from -250 to 250 mm. (a) Bench support without hole array. (b) Bench support and hole array. (c) Bench support and two stacked hole array plates with  $d_z = 1.25$  mm.

This phenomenon has been experimentally investigated in more detail, performing a measurement of the gaussian beam waist in the plane of the receiver. The set-up is depicted schematically in Fig. 4.21 (a). The transmitting antenna is located at a fixed position at 950 mm of the sample, and the receiving antenna is moved, with a step  $\Delta x = 5$  mm, along the  $x$  axis in the plane located at 950 mm from the sample. The measured spectrum is registered at every position with the *AB Millimetre™* Vector Network Analyzer in the band between 50 and 65 GHz. The experiment is done for

both E-plane and H-plane. In the case of E-plane the receiver is moved along the line in the direction of the electric field vector, whereas in the H-plane case is moved in the orthogonal direction. The procedure is made for three configurations: bench support without hole array, bench with the hole array inserted and bench with two stacked hole arrays, with longitudinal period  $d_z = 1.25$  mm. The results are depicted in Fig. 4.22 for E-plane and in Fig. 4.23 for H-plane. The received power level is represented with a color scale in function of the frequency (abscisa) and the lateral shift (ordinate).

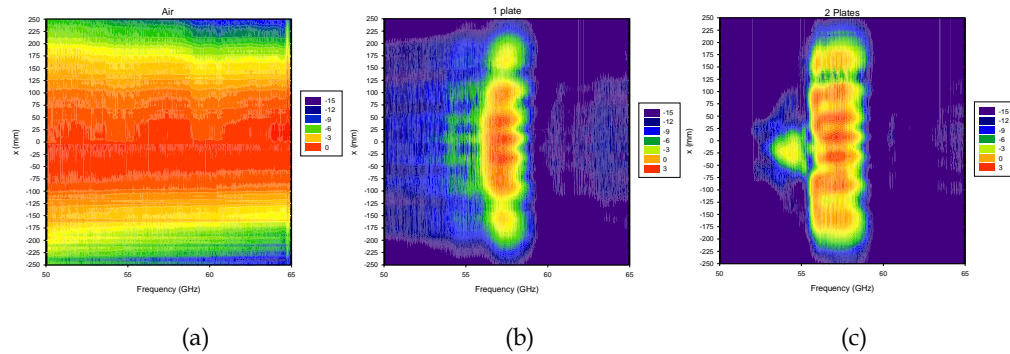


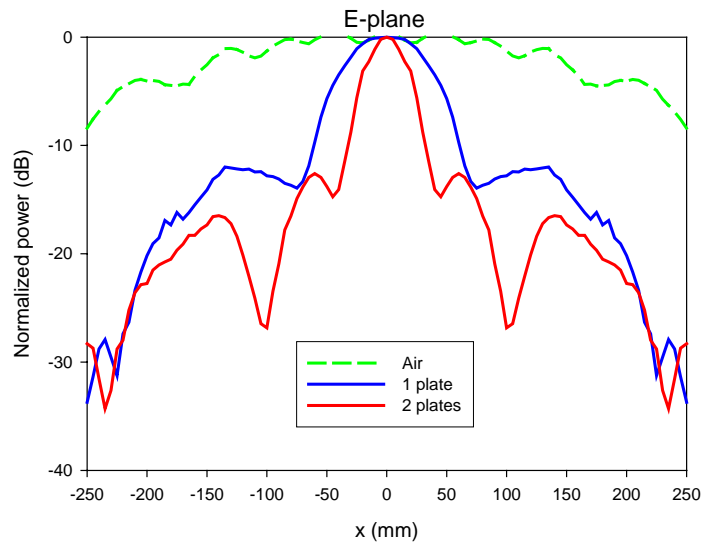
Fig. 4.23. H-plane measurement. Contour plot of the received power level as a function of the frequency (abscisa) and the lateral shift (ordinate). The frequency span extends from 50 to 65 GHz and the lateral shift excursion from  $-250$  to  $250$  mm. (a) Bench support without hole array. (b) Bench support and hole array. (c) Bench support and two stacked hole array plates with  $d_z = 1.25$  mm.

In panel (a) of Figs. 4.22 and 4.23 are the results when only the bench support is inserted in the path. It can be seen that the structure is transparent in both cutting planes. Also, the gaussian beam is narrower for higher frequencies, as expected from theory [GOLD 98].

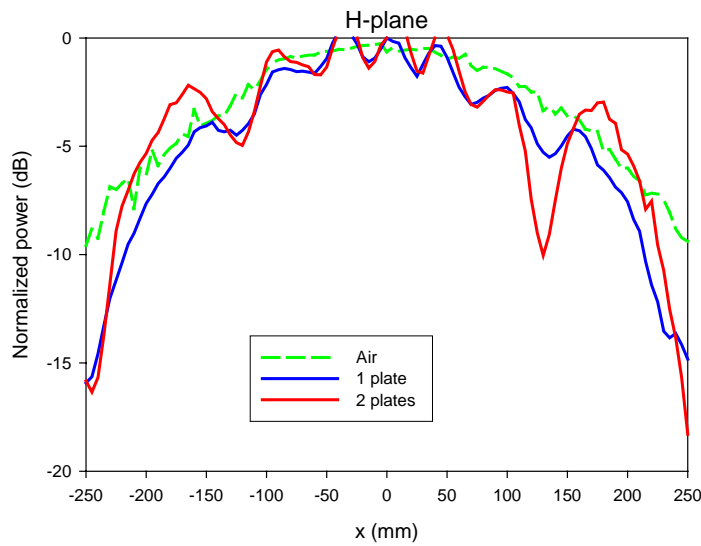
When the hole array is introduced in the path, see panel (b), a clear frequency filtering is observed around the ET frequency of 57 GHz. Also, a strong beaming is obtained in the E-plane. The gaussian beam is also narrower in the H-plane, but is not so clearly noted. Finally, it is noticed an enhancement in the maximum measured power, that goes up to 3 dB at the ET frequency.

In the last panel of both figures it has been depicted the case of two perforated plates stacked with a longitudinal period  $d_z = 1.25$  mm. The frequency filtering is observed again in both cutting planes. Moreover, for the E-plane case the beaming is reinforced

and for the H-plane, the effect is not so strong.



(a)



(b)

Fig. 4.24. Measured beam waist at the position of the receiver ( $z = 1900$  mm) for the free-space propagation (dashed green curve), single hole array case (solid blue curve) and two stacked plates with period  $d_z = 1.25$  mm. E-cutting plane (a) and H-cutting plane (b).

To observe these results more clearly, it has been plotted in Fig. 4.24 the power level as a function of the lateral shift particularized at the frequency of Extraordinary Transmission. In panel (a) is shown the E-cutting plane and in panel (b) the H-cutting plane. The power has been normalized to the value measured at the position  $x = 0$ . Due to the unavoidable ripple the value maximum value is above 0 dB in some cases, being this an experimental artifact.

It is readily observed that the inclusion of a hole array is accompanied by a gaussian beam compression, being more remarkable in the E-cutting plane. The beam radius is defined as the distance to the axis where the power has been reduced by a factor  $e^{-2}$ , or in dB:  $P_{\text{beam-waist}} = 20\log(e^{-1}) = -8.68$  dB [GOLD 98]. With this definition, the measured beam radius for the free-space case is slightly larger than 250 mm,  $\varpi_{\text{free-space}} \approx 250$  mm. When the hole array plate is inserted (blue curve), the beam radius is markedly reduced,  $\varpi_{\text{hole\_array}} \approx 55$  mm. Thus, it can be concluded that the hole array provides a reduction of the gaussian beam diffraction, which is accompanied by a gain. This effect is similar to that seen in chapter 3 for “slit + grooves” structures in the OC illumination, see for instance Fig. 3.8(a). Finally, when two plates are stacked, the beaming is enhanced, and the beam waist is reduced to a value of  $\varpi_{\text{2plates}} \approx 30$  mm.

In the H-cutting plane, the effect is weaker. The beam waist radius in free-space propagation is  $\varpi_{\text{free-space}} \approx 240$  mm. For the single hole array case is  $\varpi_{\text{hole\_array}} \approx 205$  mm and for two stacked plates  $\varpi_{\text{2plates}} \approx 225$  mm. This result can also be related to that presented in Fig. 3.8(b) and, in general, with all the radiation diagrams presented for the metallic antennas shown in section 3.5. In all those cases, the beaming in the E-cutting plane was stronger than the beaming in the H-cutting plane. The argument given there, relating the beaming to the direction where the currents are excited, is also applicable to the hole array.

## 4.8 Superprism or anomalous collimation.

The achievement and control of a LHM made by stacking subwavelength hole arrays opens up the way to a new class of practical devices both in the microwave and in the optical range. One possible realization is related to superprism effects or anomalous collimation.

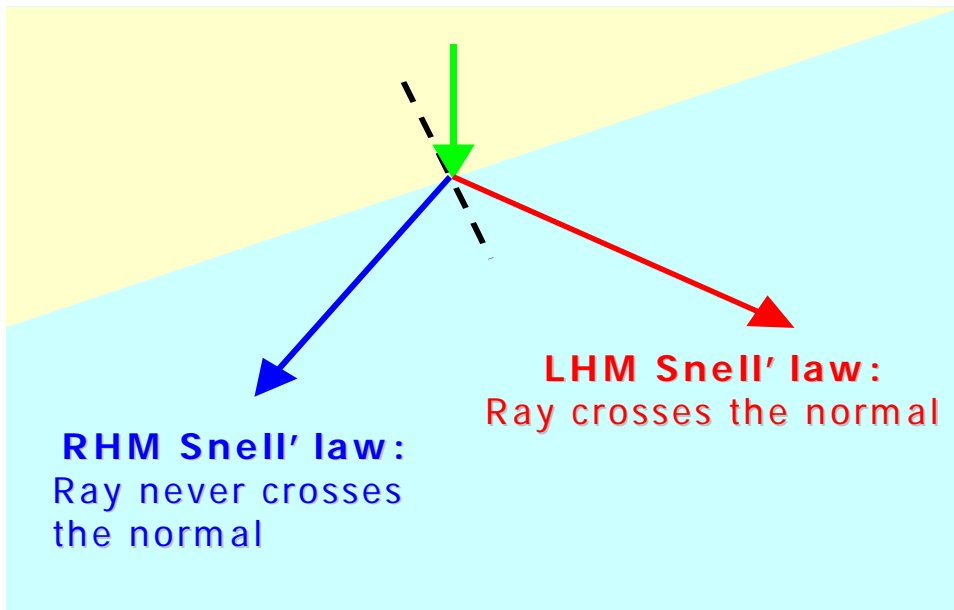


Fig. 4.25. Graphical ray illustration of Snell's law in the interface between a RHM and other RHM with different refractive index (blue arrow) and in the interface between a RHM and a LHM (red arrow). The incident ray is represented with a green arrow.

As it has been explained, one of the more surprising features of LHMs is that Snell's law is reversed in the interface of a standard RHM and a LHM, see Fig. 4.25. This atypical effect can be tested with the commercial simulator *CST Microwave Studio*<sup>TM</sup> by constructing a prism. First it is shown the behavior of a prism made of a normal dielectric. In Fig. 4.26 is depicted the electric field contour - panel (a) - and the power flow - panel (b) - for the case of a prism made of a dielectric material of permittivity  $\epsilon_r = 2$  ( $n = 2^{0.5}$ ) surrounded by air. As it can be seen, some reflected power exists at the input, and the transmitted ray goes away from the normal, as Snell's law asserts. In the opposite case, a prism of air surrounded by a dielectric with  $\epsilon_r = 2$ , shown in panels (c) and (d), the ray approaches the normal but does not cross it. Conversely, for the case of a homogenous metamaterial with negative refractive index, the transmitted ray crosses the normal, see panels (e) and (f). In the figure is depicted the case of  $\epsilon_r = \mu_r = -1$  and then perfect matching is seen with no reflected power. According to Snell's law the transmitted angle is equal to the angle of incidence but with opposite sign.

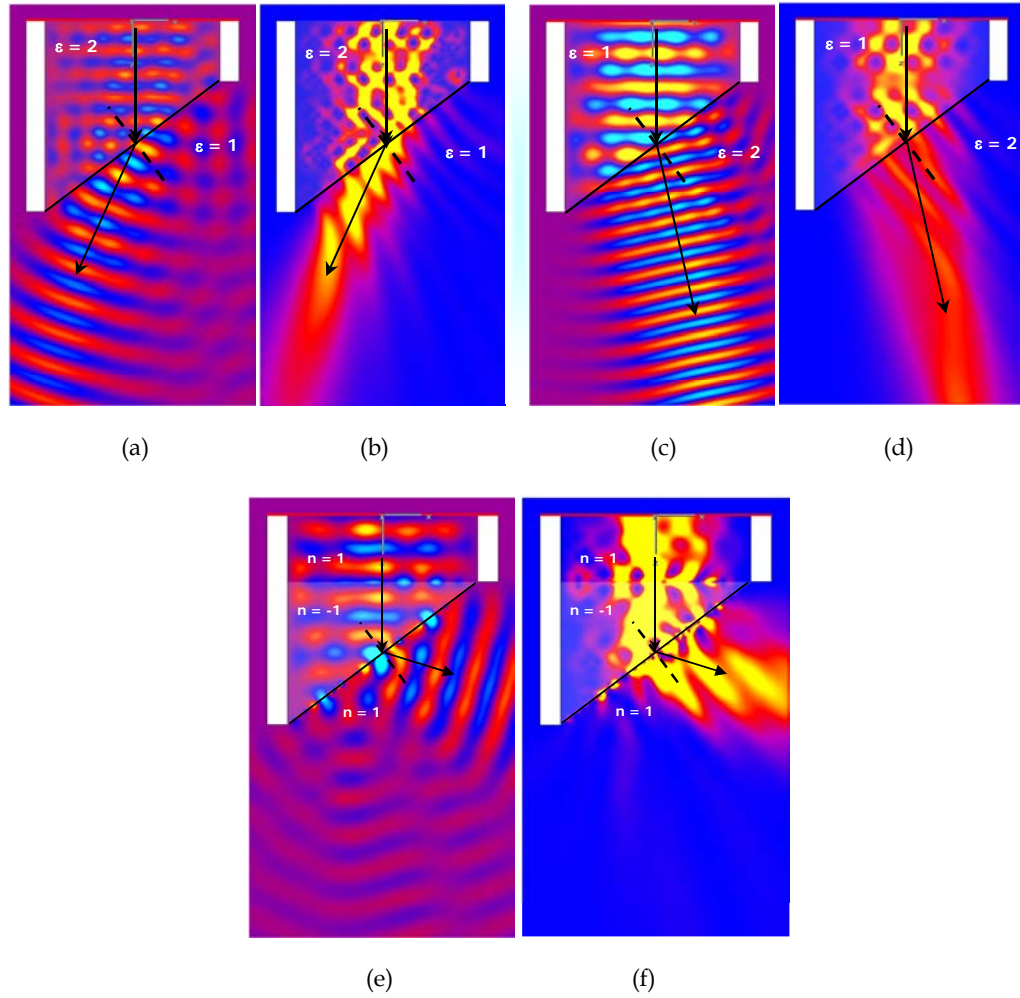


Fig. 4.26. Simulated contour of the vertical component of the electric field (a) and power flow magnitude (b) for a prism with  $\epsilon = 2$  inserted in air  $\epsilon = 1$ . The transmitted ray goes away from the normal. Vertical electric field (c) and power flow magnitude (d) in the case of a prism of air inserted in a medium with  $\epsilon = 2$ . The transmitted ray approaches the normal but does not cross it. Vertical electric field (e) and power flow magnitude (f) in the case of a metamaterial with  $n = -1$  inserted in air ( $n = 1$ ).

This is the visual illustration of Snell's law reversal, and for the particular case of prisms this phenomenon is called *superprism effect*. The concept of superprism is applied when the refractive index of the prism presents exotic values, i.e.  $n < 1$ . Superprism effects have been described in Ph.C. structures [KOSA 98], [ENOC 03] and in LHMs [SHEL 01], [SMIT 04].

#### 4.8.1 Prism in microwaves.

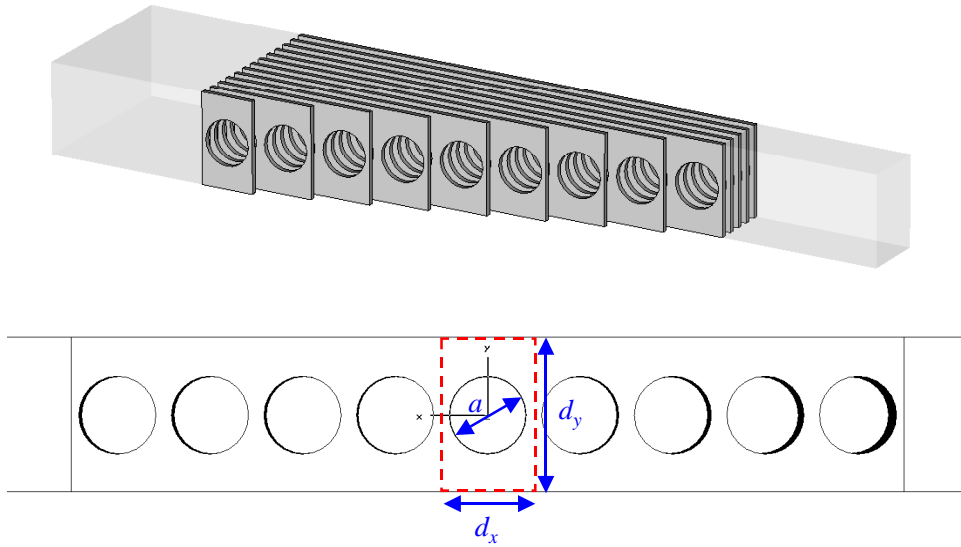
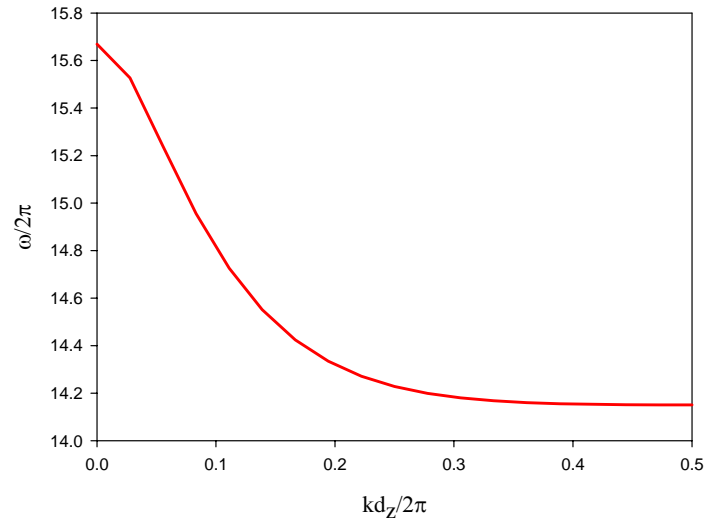
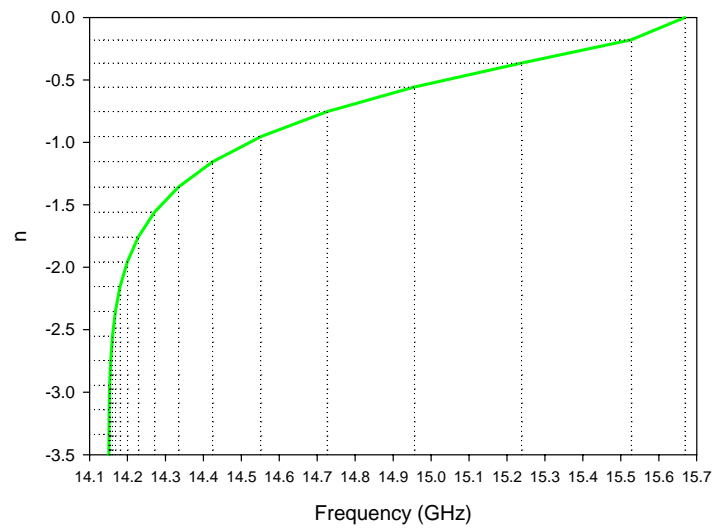


Fig. 4.27. Schematic of the prism designed by stacking hole arrays. Parameters:  $a = 9.25$  mm,  $w = 1$  mm,  $d_x = 11$  mm,  $d_y = 18.5$  mm,  $d_z = 3$  mm. With the given dimensions the ET band is in the microwave range.

With the stacked hole array, a prism is designed by progressively removing columns of holes, see Fig. 4.27. In the figure it is shown only one period, but in the simulation the boundary conditions extend the structure infinitely in the vertical dimension. The parameters of the structure are:  $a = 9.25$  mm,  $w = 1$  mm,  $d_x = 11$  mm,  $d_y = 18.5$  mm,  $d_z = 3$  mm. With these dimensions, the ET band is located in the microwave range, around 15 GHz. At this frequency the longitudinal periodicity is  $0.15\lambda$ , thus in this dimension the long wavelength limit can be considered, i.e. a homogeneous description is valid. The metal thickness is also small, about  $1/20$  the wavelength, which is optimum for ET. It can be noticed that the  $x$  and  $y$  periodicities are not equal. This is due to the fact that ET essentially depends on the periodicity  $d_y$  (the larger periodicity) [LOMA 05]. Recall that the phenomenon can be explained in terms of resonant-Wood's anomalies [SARRA 03], [HESS 65], which is directly related to periodic structures. Thus, it can be chosen this configuration in order to have the ET resonance and also a good level of signal due to the fact that the density of holes is larger.



(a)



(b)

Fig. 4.28. (a) Dispersion diagram for the stacked hole array with parameters  $a = 9.25$  mm,  $w = 1$  mm,  $d_x = 11$  mm,  $d_y = 18.5$  mm,  $d_z = 3$  mm. (b) Calculated refractive index.

The dispersion diagram for a stacked hole array with the aforementioned dimensions has been computed with the electromagnetic simulator. It is shown in Fig. 4.28(a) where the graphic is restricted to the first band. It is obviously LHM and extends from 14.2 GHz to 15.7 GHz. From the data, it can be calculated the equivalent refractive

index by a simple procedure:  $n = c/v_{phase} = ck/\omega$ . Notice that the sign of the phase velocity is negative and, therefore, the refractive index must be negative, as it is depicted in Fig. 4.28(b). At around 14.5 GHz the refractive index is approximately  $n = -1$ . The electric field and power profile at this frequency are shown in Fig. 4.29 in panels (a) and (b) respectively. It is readily seen that the simulation predicts a transmitted angle equal to the incidence angle but with opposite sign in agreement with the predicted reversal of Snell's law for LHMs. This demonstrates the left-handed prism effect of the stacked hole array structure.

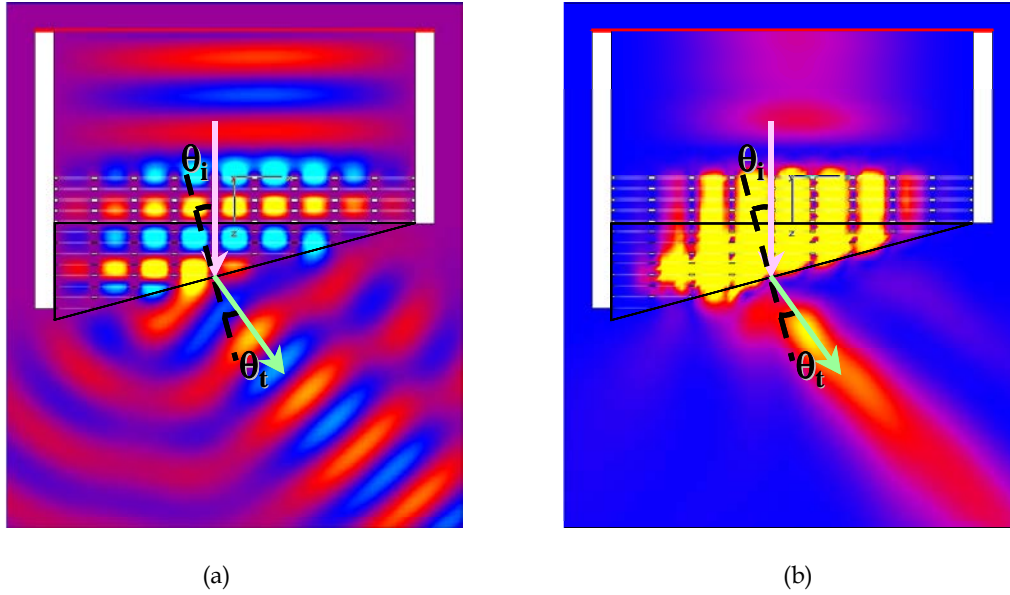


Fig. 4.29. Contour plot of the  $y$ -component of the electric field (a) and the magnitude of the power flow (b) at 14.5 GHz for the simulated prism made with stacked hole arrays in microwaves. At this frequency  $n = -1$ , and according to Snell's law  $\theta_t = -\theta_i$  as it happens.

#### 4.8.2 Prism in millimeter waves.

The results in microwaves are scaled now to the millimeter wave range. This range is less optimal for the design of prisms, due to the fact that things are further from ideality. The minimal available standard aluminum thickness is 0.5 mm which limits the thickness to wavelength ratio to around 1/10 (at 60 GHz). Also the longitudinal stack periodicity cannot be extremely reduced, and the misalignments between correlative plates are hard to control.

With all this limitations in mind, it has been chosen the double periodicity topology and plates very close, see the proposed prototype in Fig. 4.30.

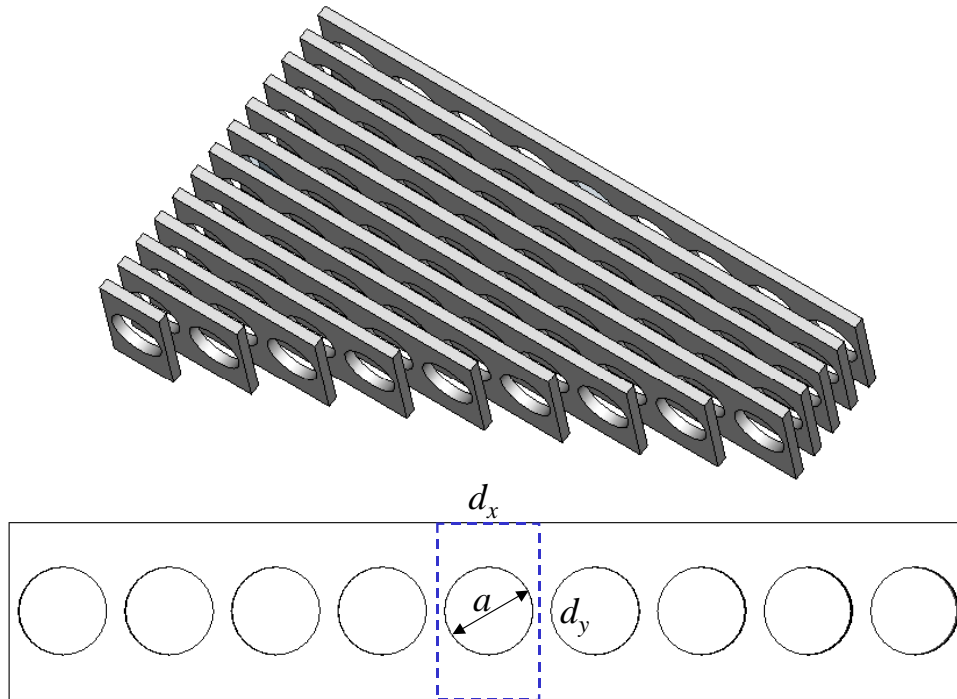
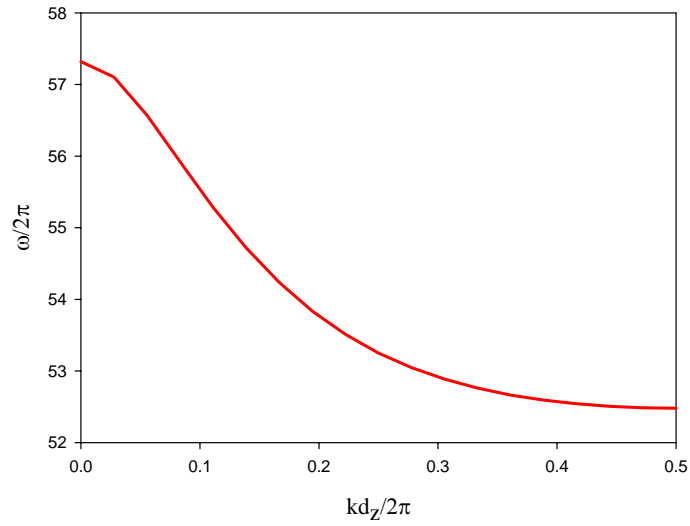
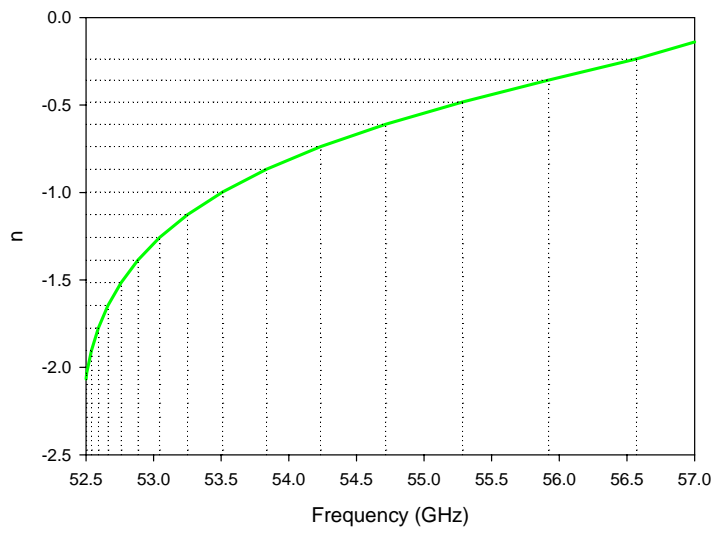


Fig. 4.30. Schematic of the prism in millimeter waves range. Parameters:  $a = 2.5$  mm,  $w = 0.5$  mm,  $d_x = 3$  mm,  $d_y = 5$  mm,  $d_z = 1.25$  mm.

Repeating the mentioned procedure, it has been computed the dispersion diagram for the first band of the structure. It is shown in Fig. 4.31(a). The first band is left-handed and extends from 52.5 GHz to 57.3 GHz. From the data is extracted the equivalent refractive index. It is shown in Fig. 4.31(b). It ranges from  $n = -2$  to  $n = 0$ . It reaches the value  $n = -1$  at about 53.5 GHz. The electric field and power profile at this frequency are shown in Fig. 4.32 in panels (a) and (b) respectively. The simulation predicts a transmitted angle equal to the incidence angle but with opposite sign in agreement with the predicted reversal of Snell's law for LHMs. This demonstrates the left-handed prism effect of the stacked hole array structure also in the millimeter wave range.



(a)



(b)

Fig. 4.31. (a) Dispersion diagram for the stacked hole array with parameters  $a = 9.25$  mm,  $w = 1$  mm,  $d_x = 11$  mm,  $d_y = 18.5$  mm,  $d_z = 3$  mm. (b) Calculated refractive index.

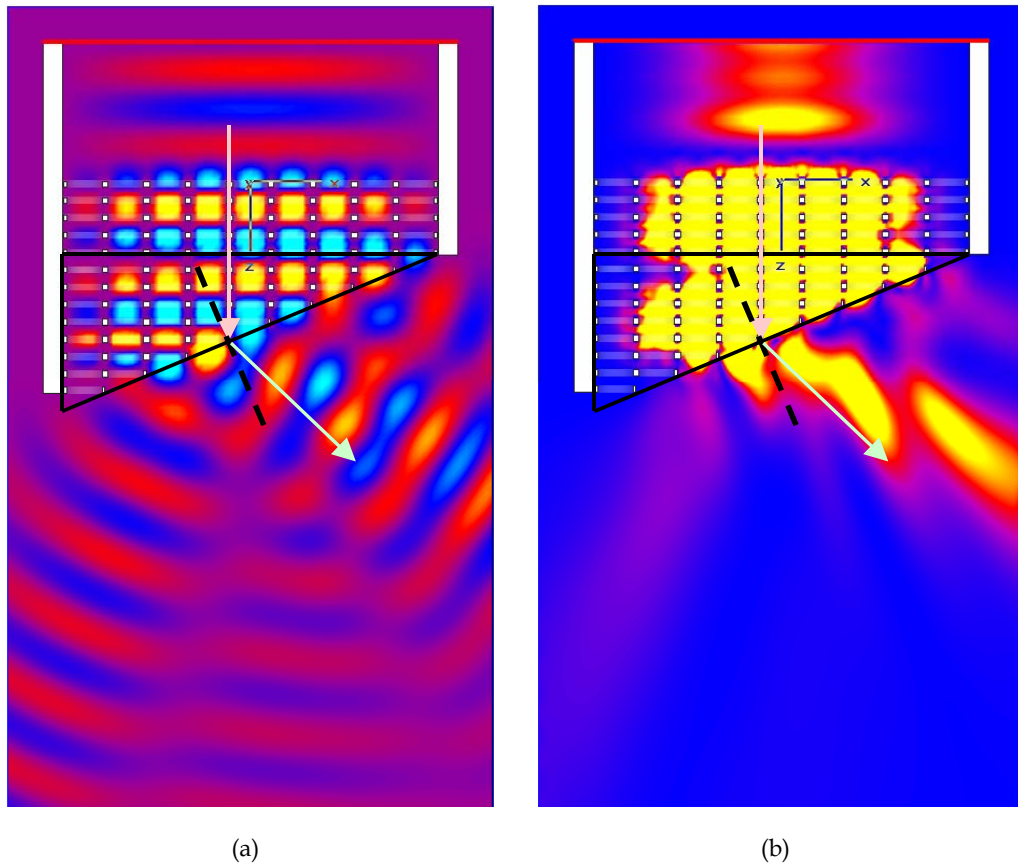


Fig. 4.32. Contour plot of the  $y$ -component of the electric field (a) and the magnitude of the power flow (b) at 53.5 GHz for the simulated prism made with stacked hole arrays in millimeter waves. At this frequency  $n = -1$ , and according to Snell's law  $\theta_t = -\theta_i$  as it happens.

## 4.9 Parabolic lens.

In the same sense that a prism made of negative refractive index material shows unconventional properties, other geometries based on metamaterials can be tried. They also show atypical and exotic features. One of the most immediate architectures is the parabolic geometry.

As it is well known, a parabolic-shaped mirror has the property of focusing all the incident parallel rays on a point called focus of the parabola, see Fig. 4.33(a). Reciprocally, also all the rays emitted by a point source located on the focus are reflected by the paraboloid mirror in a set of parallel rays.

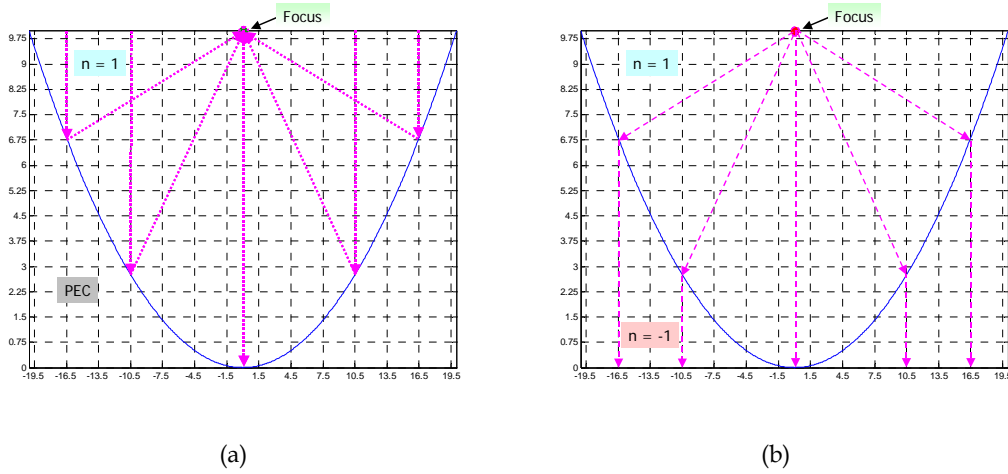


Fig. 4.33. Ray tracing of the operation of a parabolic mirror, where parallel rays are reflected to the focus (or reciprocally all the rays emerging from the focus are reflected as parallel rays) (a) and ray tracing when the interface between a standard RHM medium with  $n = 1$  and a metamaterial with  $n = -1$  is parabolic. The rays travel parallel in the LHM medium. If there is impedance matching there is not reflection.

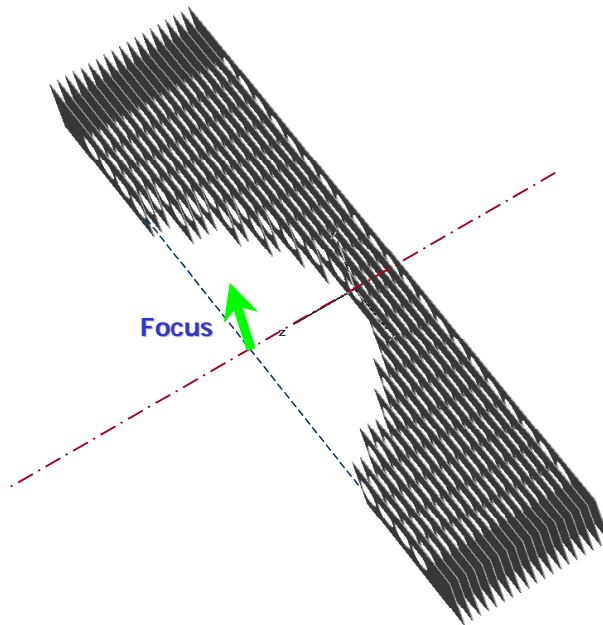
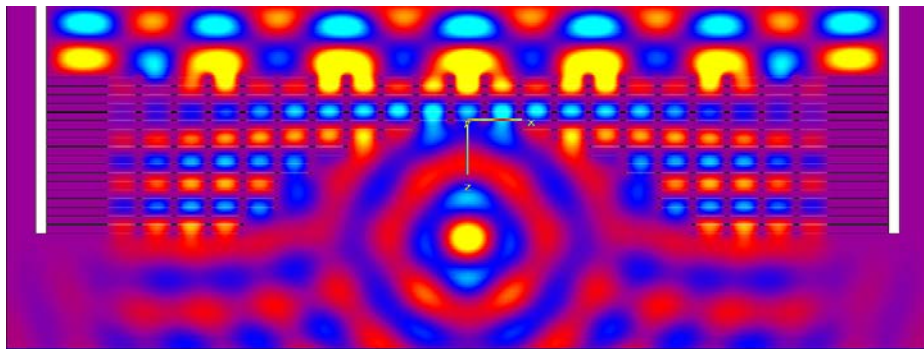
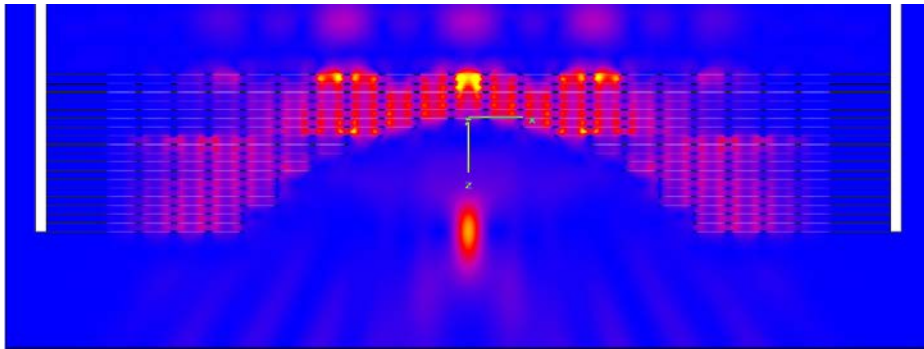


Fig. 4.34. Schematic of the parabola constructed by stacking subwavelength hole arrays. The parameters of the structure are, following the usual notation:  $a = 2.5$  mm,  $w = 0.1$  mm,  $d_x = 3$  mm,  $d_y = 5$  mm,  $d_z = 0.75$  mm.

Following the usual formalism of geometrical optics, the reflection is usually described as being a material with refractive index  $n = -1$  [CORN 94]. This is an advantageous interpretation in order to study reflection as the equivalent refraction on a idealized material, a mere mathematical tool. But with the incoming of the metamaterials formalism this abstract idea can be seen to take a real form. In fact, when shaping with a parabola the interface of a standard RHM medium, say air with  $n = 1$ , and a LHM medium with  $n = -1$ , and using as a emitter a point source on the focus of the parabola waves, the situation depicted in Fig. 4.33(b) arises. The rays that emerge from the source diverge as spherical waves until they reach the interface. Then, applying Snell's law, the rays propagate parallel in the metamaterial. In the particular case when there is impedance matching between the two media the waves can traverse the surface without reflection.



(a)



(b)

Fig. 4.35. Top view of the simulated vertical electric field component (a) and power flow magnitude (b) of the parabola constructed by stacking hole arrays. The structure is excited by a plane wave impinging from the back. A clear concentration of power is observed in the focus.

A metamaterial paraboloid can be constructed with stacked hole arrays by using the same procedure as for the prism. The design proposed is shown in Fig. 4.34. A parabolic shape is roughly constructed by carefully removing rows of holes. This result in a staircase approximation of the ideal parabola. The parameters of the design are, following the usual notation:  $a = 2.5$  mm,  $w = 0.1$  mm,  $d_x = 3$  mm,  $d_y = 5$  mm,  $d_z = 0.75$  mm. The structure is excited by a plane wave impinging on the back and by using the appropriate boundary conditions is made infinite in the vertical dimension. The results for the electric field and the power flow are depicted in Fig. 4.35 in panels (a) and (b) respectively.

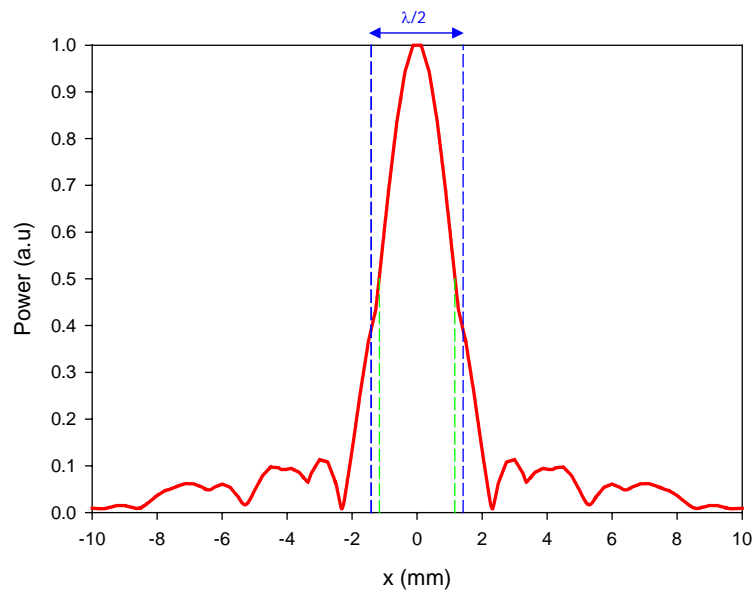


Fig. 4.36. Normalized power along  $x$  on the focus cross-plane. It has been represented with green dashed lines the points where the power is half the maximum and with blue dashed lines the half a wavelength distance.

Notice the clear concentration of field and power observed on the focus of the parabola. As it can be seen in the power plot (panel (b)) the focus is very narrow in the  $x$  direction but more extended in the  $z$  direction. It has been plotted in Fig. 4.36 the normalized power on the focus cross-plane along the  $x$  direction. It is seen that the distance of the half power (green dashed lines) is smaller than half a wavelength (blue dashed lines).

## 4.10 Equivalent circuit discussion.

In this section it is intended to grasp a little more in the equivalent circuit approach outlined before. The main aim here is to show in some extent the validity of this approach by taking some selected simulation results.

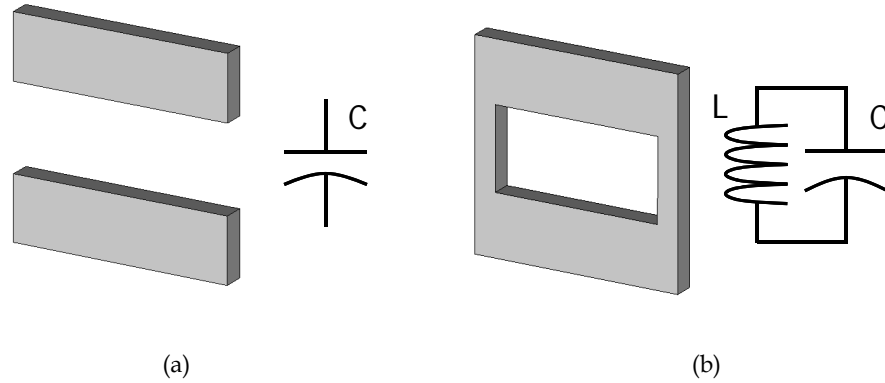
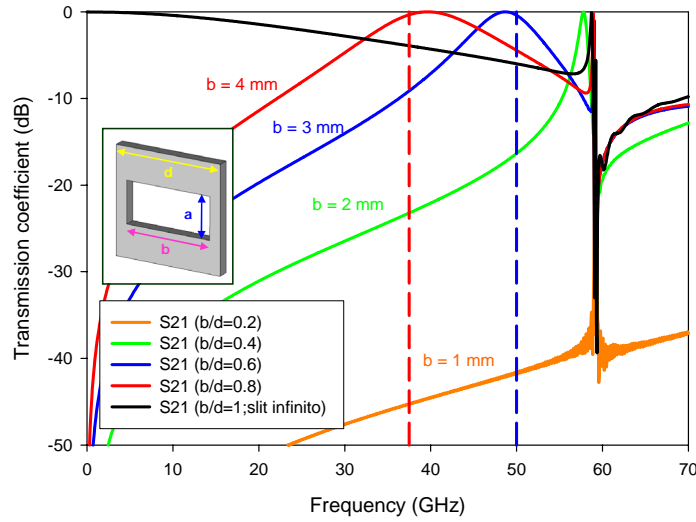


Fig. 4.37. Unit cell and equivalent circuit for an infinite slit array (a) and an infinite slot array (b). The unit cell is infinitely replicated by inserting electric walls in the upper and lower planes and magnetic walls in the lateral planes.

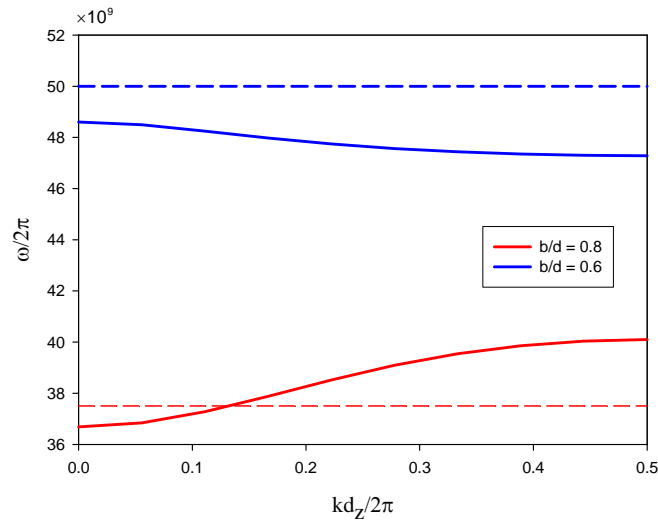
As it has already been mentioned, after the discovery of EOT in subwavelength hole arrays, some of the research effort was directed towards the “equivalent” one-dimensional case: the slit array [TREA 99], [PORT 99]. Now we know that this structure fails in describing the situation of Ebbesen’s experiment since slits propagate without a cut-off while holes have a cut-off frequency. From the equivalent circuit point of view, narrow slits in a thin plate have been classically considered as shunt capacitors [COLL 91], as represented in Fig. 4.37(a). The surface conduction current lines on the metallic face are closed as a displacement current across the capacitor formed by the upper and lower metallic plates. When the slit is transformed into a slot by inserting lateral walls, see Fig. 4.37(b), surface current is allowed to flow around the slot giving as a result an inductive reactance in parallel with the mentioned capacitive reactance. The circuit that describes the operation is an LC-tank.

It has been simulated the spectral response of an array of apertures varying the horizontal dimension. For the simulation, the above described procedure is used: an artificial waveguide is constructed by imposing as boundary conditions magnetic and electric walls, see Fig. 4.1. This makes the structure be infinitely replicated in the

transversal cross-plane. The thickness of the metallic plate is fixed at  $1/10$  the operating wavelength. The vertical dimension of the aperture has been fixed at  $0.4\lambda$ .



(a)



(b)

Fig. 4.38. Simulation results for an infinite array of apertures in a metal of thickness  $w = \lambda/10$ , with vertical dimension  $a = 0.4\lambda$ . (a) Single plate transmission spectra obtained for different horizontal dimensions ranging from  $b = d$  (infinite slit) to  $b = 0.2d$  and (b) stacked hole arrays dispersion diagram particularized to the first band for the cases  $b = 0.8d$  (red curve) and  $b = 0.6d$  (blue curve). The longitudinal period is  $d_z = 2.25$  mm. In dashed line is represented the hole waveguide cut-off frequency.

The results obtained are shown in Fig. 4.38(a) where the width of the slot has been varied from the infinite slit case (black curve) to the very narrow slit,  $b/d = 0.2$ . In all the analyzed cases Wood's anomaly appears at 60 GHz and is preceded by a total transmission narrow peak slightly below it. For an infinite slit array a total transmission is observed at DC and the power level gradually decreases as the frequency increases, in good agreement with the shunt capacitor model – low pass characteristic response. When the slit is transformed into a slot, transmission at DC is completely forbidden, i.e. appears a cut-off frequency, marked with dashed line of the color corresponding to the spectral curve. A peak of total transmission emerges between DC and Wood's anomaly. This total transmission peak moves towards higher frequencies as the slot is made narrower, until the point where it almost collapses with the Wood's anomaly frequency. What is interesting is that after a particular slot width, the peak falls below the slot cut-off frequency. This constitutes the ET regime. Computing now the dispersion diagram of stacked hole arrays with longitudinal period  $d_z = 2.25$  mm for the cases  $b/d = 0.4$  (blue curve) and  $b/d = 0.2$  (red curve), see Fig. 4.38(b), it is interesting to observe that in the first case, when the band falls below the cut-off, the first band obtained has a negative slope, i.e. is LHM. Conversely, in the second case, when the band is above the cut-off, the slope is positive or RHM. Therefore, in order to obtain a LHM by stacking slot arrays, a necessary condition is that ET occurs (transmission below cut-off) or, in other words, the slot horizontal aperture dimension has to be small in order to show a strong inductive character.

It is interesting to see what happens if the horizontal dimension of the slot is left constant and narrow enough such that ET exists, and the vertical dimension is somewhat enlarged. For instance, the vertical dimension is duplicated maintaining a slot width  $b = 0.8d$  and the dispersion diagram for a stacked hole array with longitudinal periodicity  $d_z = 2.25$  mm is computed. The results are presented in Fig. 4.39:  $a = 0.4\lambda$  (blue curve),  $a = 0.8\lambda$  (pink curve). For  $a = 0.8\lambda$  the band obtained is RHM, with a positive slope, while for  $a = 0.4\lambda$  the band is LHM. This can be easily explained with a very intuitive argument: when the vertical dimension of the slot is enlarged, the fraction of metal per unit cell decreases. Moreover, notice that the electric field lines responsible of the electric coupling between adjacent plates emerge just in that region. As the metal fraction is smaller, the mutual capacitance also decreases and eventually disappears the electric coupling along the chain. Therefore,

in order to obtain LHM by stacking hole array three conditions should be fulfilled: first and second, designing the holes small enough in order to enhance the inductive character maintaining at the same time a good power coupling across them. Third, is favour the electric coupling between correlative plates by employing large metal areas. These conditions can be fully satisfied by using stacked ET hole arrays.

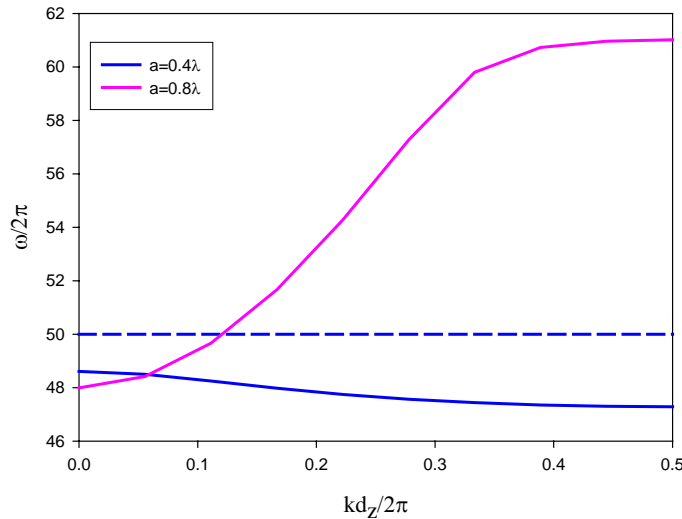


Fig. 4.39. Computed dispersion diagram for a slot array structure with dimensions  $b = 0.8d$ ,  $w = \lambda/10$  and  $a = 0.4\lambda$  (blue curve) and  $a = 0.8\lambda$  (pink curve). The longitudinal period is  $d_z = 2.25$  mm. In dashed line is represented the hole waveguide cut-off frequency.

### 4.11 Metal-dielectric ( $\epsilon > 1$ ) stack.

This point is devoted to the extension of the structures studied in section 2.7. The results obtained there are extended here to the case of stacking hole arrays separated by a dielectric with  $\epsilon > 1$ . Very interesting features appear, as it will be seen.

Consider a double periodicity hole array on a dielectric slab or inserted between two dielectric slabs. It has been seen in section 2.7 that in general the ET band is shifted to lower frequencies. Now, proceeding as before, a bulk material is constructed by stacking such structures, see schematic and picture in Fig. 4.40(a) and (b) respectively. The stack period is the sum of the thickness of the dielectric and conductor layers,  $d_z = h + t = 0.525$  mm. As it is explained below, the resonance is shifted towards lower frequencies when the stack is constructed. In order to observe the resonance in the

measurement frequency range, the vertical periodicity of the hole array needs to be slightly modified to  $d_y = 3.4$  mm. The rest of the hole array parameters are the same as in section 2.7. It is shown in Fig. 4.41 the computed dispersion diagram of the double periodicity structure separated with air and with a dielectric of relative permittivity  $\epsilon = 2.43$ . When the stack is embedded in air, the first band appears between 75 and 87 GHz (red line) and when is embedded in the dielectric it is between 48.4 and 56 GHz. Therefore, with an easy calculation, it is seen that the frequency shift is simply due to dielectric loading ( $f_{\text{diel}} = f_{\text{air}} / \epsilon^{0.5}$ ).

The stacked prototypes separated by dielectric slabs have been measured with the previously described QO bench. The resulting transmission coefficient spectra are shown in Fig. 4.42. In solid cyan curve is shown the response of a single plate between a dielectric sandwich. Notice that the resonance is located around 70 GHz. When two plates are stacked a clear ET peak is detected at 50.4 GHz, see solid red curve. As the number of layers is increased, the level decreases, probably due to losses and to slight misalignments between consecutive layers, but the resonance frequency is locked at 50 GHz.

The shift of the resonance frequency between a single plate response and the stacked structures is due to the electric field distribution. In the single plate case, the electric field lines are spread in the volume surrounding the perforated metallic plate that comprises a mixture of dielectric slab and air, i.e. the effective permittivity is a number between 1 and  $\epsilon$  ( $1 < \epsilon_{\text{eff}} < 2.43$ ). This makes the ET peak shift to lower frequencies (as shown in section 2.7), in a factor proportional to the square root of the effective dielectric permittivity. When a stack is constructed with dielectric slabs separating the metallic plates, all the electric field lines are trapped in the same material, and contribute to the self-capacitance of the single plate hole array and to the mutual capacitance of adjacent plates (this is directly linked to the discussion presented in section 5.3.1 relative to electroinductive waves. It will be seen there, that, for electrically coupled resonators, the total capacitance is splitted in self and mutual capacitance terms). Thus, as all the electric field lines are confined in the dielectric material, the frequency of the LHM band is consequently shifted in a factor  $\epsilon^{-1/2}$ . What is more, this frequency shift towards lower frequencies in stacked structures can also explain the reduction in the measured power level, since now the hole diameter,  $a$ , is smaller in units of wavelength and, following the discussion presented in section 2.4 (also in *Article 2.2*), the smaller the hole in units of wavelength, the narrower the

passband which for finite size structures results in a reduction of the peak level.

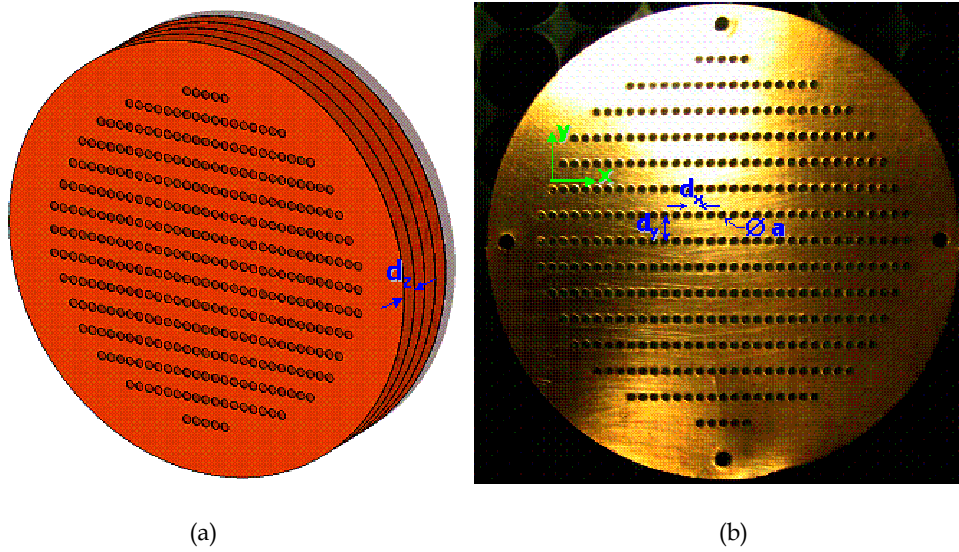


Fig. 4.40. Schematic (a) and picture (b) of the stacked hole array. The parameters are  $d_x = 1.5$  mm,  $d_y = 4$  mm,  $d_z = 0.525$  mm, hole diameter  $a = 1.2$  mm, metallization thickness (copper)  $t = 35$  microns, dielectric thickness  $h = 0.49$  mm and dielectric permittivity  $\epsilon = 2.43$

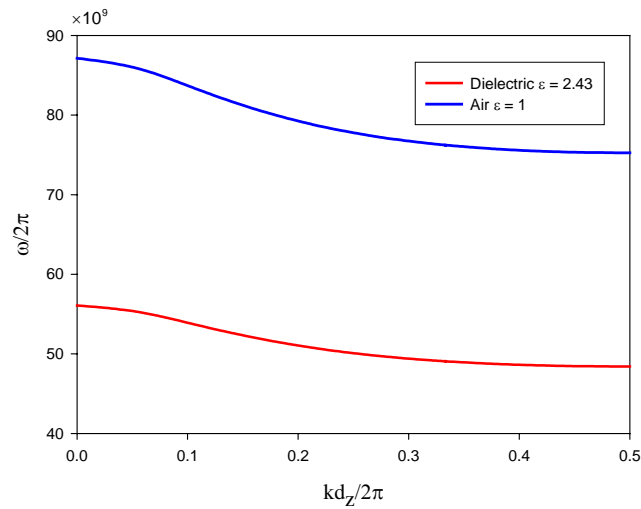


Fig. 4.41. Dispersion diagram particularized to the first band of the stacked hole array separated by air slabs (blue) and by  $\epsilon = 2.43$  dielectric slabs (red).

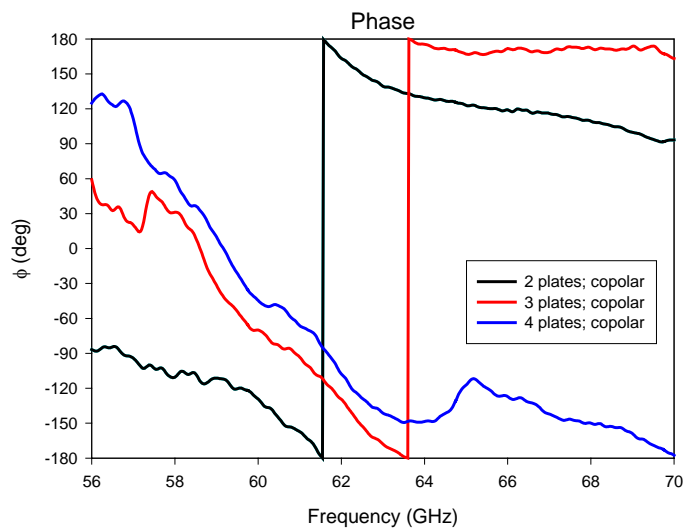
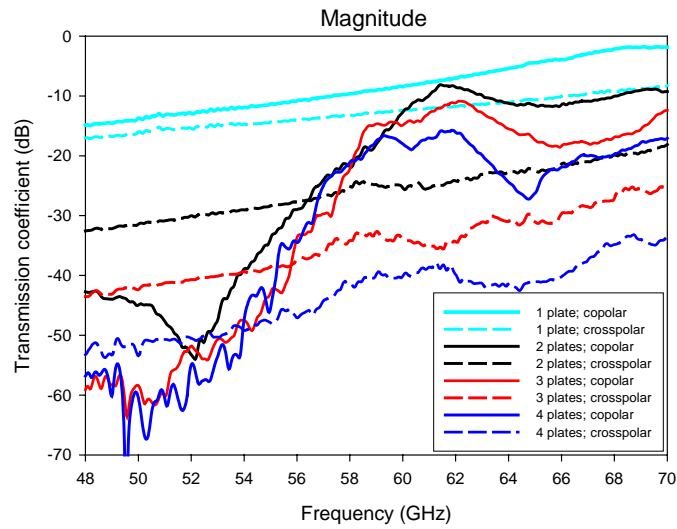


Fig. 4.42. Experimental transmission coefficient magnitude (a) and phase (b) of stacked hole arrays. Solid lines correspond to copolar excitation of the double periodic hole array on dielectric slab structure, i.e. E-field in the direction of the large periodicity and dashed lines to the orthogonal polarization. Black is for two plates, red three plates and blue four plates.

It has also been depicted in Fig. 4.42(a) the frequency response for the cross polarization. No resonance is observed in any of the measured cases, and it is observed that as the stack is enlarged the power level decreases monotonously.

Attending now to the phase in Fig. 4.42(b), it is clear that as the number of plates increases, the phase increases at the EOT band, as happened in 4, giving evidence of LHM inside the stack.

## 4.12 Concluding remarks.

Summing up, an artificial waveguide defined by introducing a set of parallel electric and magnetic conductors can be employed to analyze the diffraction problem of a plane wave impinging normally to a sub-wavelength hole array. Simulation results have demonstrated the key role of the evanescent higher order modes to explain the ET effect. Even more unexpected results appear if a periodic structure is made by stacking several of such plates.

It has been shown how a left-handed metamaterial can be achieved by the periodic stacking of sub-wavelength hole array plates to form a photonic band-gap structure. It has been shown that the stack period with LH behavior can be made much smaller than the operating wavelength and, therefore, it can be safely stated that the structure works in that dimension as an effective metamaterial.

In addition to this, the simulation and experimental results presented show that left-handed propagation effects appearing in the band where EOT happens can be allowed or inhibited by a proper engineering of the band gap position of the photonic crystal made of stacked subwavelength hole-arrays. Moreover, in the transition from LH to RH behavior a nearly zero slope band is observed, which can evidence a frozen mode propagation regime inside the structure.

A simplified model based on inverse line equivalent circuit has been exposed to explain the LH and RH behavior. This model has been complemented with some simulation results. Some future work has been advanced with interesting simulation results showing potential applications of the structure such as the implementation of metamaterial based prisms and parabolic shaped lenses. Finally, it has been explored the case of stacked double-period hole arrays separated with dielectric slabs.

The reported results have been achieved for the millimetre range, but similar results

are expected to happen at optical frequencies since extraordinary transmission has been shown at optical frequencies and the kind of structure presented here will present low losses in higher frequency regime. The control of the EOT-LHM could lead to a new class of practical devices both in the microwave and in the optical range. Further experiments and theoretical analysis are needed to grasp the full implications of these findings.



# Chapter 5

## Alternative Structures.

---

---

*In this section other structures are shown. They stem from novel electromagnetic phenomena, namely the so-called Left-Handed Metamaterials. The key particle in the development of this subject has been the Split-Ring Resonator (SRR) proposed by Prof. Pendry in 1999.*

*Here, this particle is used in the implementation of planar screens or Metasurfaces. It will be seen that due to the peculiar properties of the SRRs the response of the metasurfaces obtained show strong resonance and cross-polarization effects. Complementarity is applied to construct prototypes with the dual particle of the SRR, the CSRR, presented for the first time by Falcone in 2004. Analytical as well as experimental results are given.*

*The strong resonance of these particles allow for the coupling and the energy transport along a chain made by arraying several of them. When the coupling is magnetic the wave supported is referred as Magnetoinductive Wave (MIW). If the coupling is electric is referred as Electroinductive Wave (EIW). Here it is presented the first realization of a Electroinductive wave (EIW) transducer. Several simulation results that illustrate the energy transport with EIWs are given. Also an analytical discussion that shows that EIWs and MIWs are complementary is presented.*

*Finally, a comparison of these alternative structures with enhanced transmission structures is made.*

## 5.1 Introduction: SRR, Babinet, bianisotropy.

In the last few years, an issue of great research interest has been the study of materials with artificial exotic electromagnetic properties. Amongst them, the investigation in the so-called Left-Handed Metamaterials (LHM) has occupied a prominent role. The term Left-Handed comes from the fact that for a plane wave propagating inside these artificial materials the electric field vector,  $\mathbf{E}$ , magnetic field vector,  $\mathbf{H}$ , and wave vector,  $\mathbf{k}$ , form a Left-Handed triplet. This is in contrast with usual media in which the vectors form a Right-Handed triplet. This fact is highlighted in Fig.5.1(a) and (b).

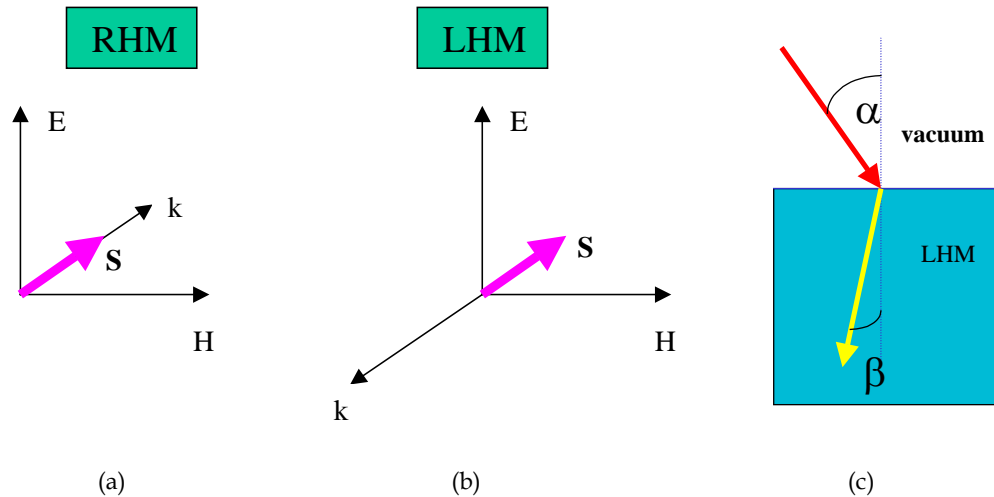


Fig. 5.1. (a) Electric field, magnetic field and wave vectors form a right-handed triplet in a standard media. (b) This triplet is left-handed in the media described by Veselago. Note that Poynting vector is always in the same direction. (c) Sketch of the Snell's law reversal in the interface between a standard medium and a left-handed medium

The origin of this terminology dates back to 1968, when Veselago studied from a theoretical point of view the properties of media having simultaneously negative values of electric permittivity and magnetic permeability [VESE 68]. He found the aforementioned Left-Handed propagation characteristic along with other surprising properties: inversion of Snell's law in the interface between a standard and a left-handed medium, Doppler effect reversal, Cerenkov effect reversal among others.

The synthesis of a negative electric permittivity was feasible by that time, for example by means of a plasma or a metal at optical frequencies. Negative values of magnetic permeability in contrast were not attainable. It was in 1999 when Pendry [PEND 99]

proposed for the first time a particle which can give a negative magnetic response in a certain frequency range: the Split-Ring Resonator (SRR) depicted schematically in Fig.5.2(a). The first medium showing simultaneously negative values of permittivity and permeability was developed in the next year by Smith et al. [SMITH 00].

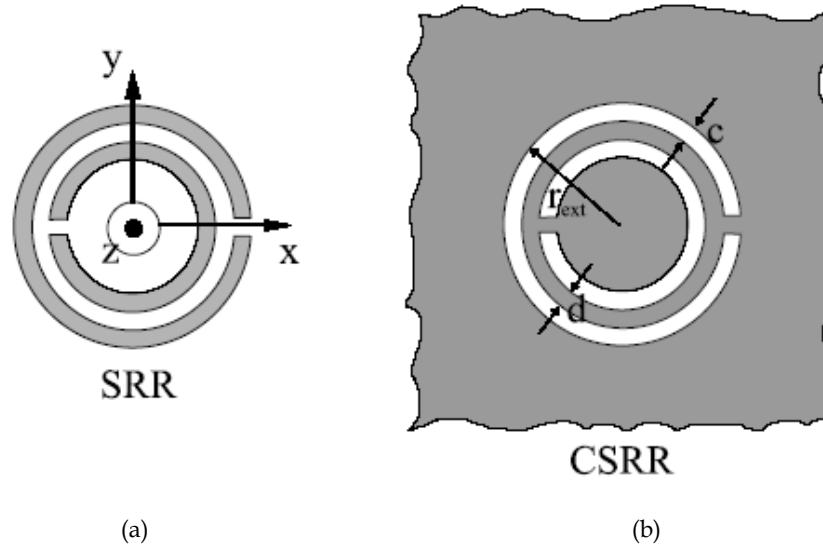


Fig. 5.2. Geometries of the SRR (a) and CSRR (b). Metal parts are represented in gray and air in white. Notice that the structures are complementary in the sense of Babinet's principle

These results attracted great interest and many other works were advanced. It was soon realized that conventional SRRs present cross-polarization effects [GAY 02], [MARQ 02], [MARQ 03], so that artificial LHM designed with these elements also become bi-anisotropic [MARQ 02]. Two characteristics make SRRs very interesting in the design of artificial media. The first one is that they are high Q resonators, which produce a strong diamagnetic response above the resonance, so that they can potentially produce a negative effective  $\mu$ . The second one is that the first SRR resonance is quasi-static [MARQ 03], so that SRRs electrical size at such resonance is small enough to allow for a continuous media modelling of the composite. Actually, artificial media design is not the only application of these elements coming from the aforementioned properties. They also make SRRs very useful for applications in microwave technology (see, for instance, [FALC 05] and references therein).

More recently, the dual configuration or *complementary SRR* (CSRR), shown in Fig. 5.2(b), began to be studied as an alternative to SRRs for some applications [BAEN 04],

[FALC 04], [FALC 05]. The term complementary arises from the Babinet's principle. This principle states that the total field transmitted by a metallic screen with an arbitrary aperture, added to the total field transmitted by its complementary screen (illuminated by the complementary incident wave), gives the incident wave over this last structure.

Similarly to SRRs, CSRRs also behave - at its first resonance - as quasi static LC resonators. However, due to Babinet's principle, a strong electric dipole generation is the dominant effect at this resonance and cross polarization effects are also present.

## 5.2 Metasurfaces.

Frequency selective surfaces (FSS) are periodic structures with a frequency filtering behaviour for an incident wave [MUNK 00], [WU 95]. These devices are well-known in microwave and millimeter wave ranges. Usually they consist of a periodic array of resonant metallic elements or apertures on a metallic screen. Depending on the construction, material and geometry of elements, FSSs can be classified in high-pass, low-pass, band-pass and rejected-band filters. As a simple rule, disconnected or patch elements usually present low-pass or rejected-band behavior, whereas connected or slot elements usually present high-pass or band-pass behavior.

According to diffraction theory, for secondary-grating lobe suppression the size and periodicity of the resonant elements should be smaller than the wavelength of the incident radiation. Otherwise, the resonant optical properties of the FSS may be related to the coupling between adjacent elements, thus depending on the angle of incidence of the incoming radiation. The small electrical size of the SRR and CSRR particles described in the previous section makes them very attractive in the application to FSSs. These particles have usually been excited by means of axial fields, see [PEND 99], but they can also be excited by transversal fields, due to their bianisotropy characteristic [MARQ 02]. This last feature permits the plane wave excitation of a surface constructed with these particles. Besides, a rich variety of cross-polarization effects are observed by changing the angle of incidence.

### 5.2.1 SRR/CSRR Metasurfaces under normal incidence.

In this section are given the results of an *ab-initio* analytical theory for the design of SRR-made and CSRR-made FSSs under normal incidence plane wave excitation. The

validity of this analysis is restricted to the conditions: infinitely thin metallic perfectly conducting screens in free space (conditions of Babinet's principle), and SRR/CSRR sizes much smaller than the free space wavelength. This condition can be easily fulfilled owing to the small electrical size of the SRRs. In consequence, the analysis can be simplified by using the surface admittance approach. CSRR-based FSSs can be analyzed as the complementary counterpart of SRR-based FSSs.

The electromagnetic response of the SRR at its first resonance can be described in terms of four polarizabilities [MARQ 03]. The expressions are reproduced here:

$$m_z = \alpha_{zz}^{mm} B_z^{ext} - \alpha_{yz}^{em} E_y^{ext} \quad (5.1)$$

$$p_y = \alpha_{yy}^{ee} E_y^{ext} + \alpha_{yz}^{em} B_z^{ext} \quad (5.2)$$

$$p_x = \alpha_{xx}^{ee} E_x^{ext} \quad (5.3)$$

where the axis orientation is seen in Fig. 5.2 and  $E_{ext}$  and  $B_{ext}$  are the externally applied field. From the above polarizabilities,  $\alpha_{yy}^{ee}$ ,  $\alpha_{yz}^{em}$  and  $\alpha_{zz}^{mm}$  have a resonant behavior, with a generic  $\omega$  dependence near the resonance of the kind:

$$\alpha \approx \alpha_0 \left( \frac{\omega_0^2}{\omega^2} - 1 \right)^{-1} \quad (5.4)$$

where  $\alpha_0$  is a constant and  $\omega_0$  is the first frequency of resonance of the SRR. It is worth to note that the dipoles  $m_z$  and  $p_y$  are resonantly excited in the first or quasi-static resonance of the SRR whereas the dipole  $p_x$  does not present a resonant response at that frequency.

By using the complementarity concept, the response of CSRRs can be described with the complementary polarizabilities [BAEN 04]; [FALC 04].

$$p_z = \beta_{zz}^{ee} E_z^{ext} - \beta_{yz}^{em} B_y^{ext} \quad (5.5)$$

$$m_y = \beta_{yy}^{mm} B_y^{ext} + \beta_{yz}^{em} E_z^{ext} \quad (5.6)$$

$$m_x = \beta_{xx}^{mm} B_x^{ext} \quad (5.7)$$

$\beta_{yy}^{ee}$ ,  $\beta_{yz}^{em}$  and  $\beta_{zz}^{mm}$  having a resonant behavior near the resonance of the kind:

$$\beta \approx \beta_0 \left( \frac{\omega_{c,0}^2}{\omega^2} - 1 \right)^{-1} \quad (5.8)$$

where the CSRR frequency of resonance  $\omega_{c,0}$  is, in general, different from  $\omega_0$  due the influence of the dielectric board [BAEN 04]. However, if the dielectric is removed, by duality  $\omega_{c,0} = \omega_0$ . In this case, from Babinet principle [FALC 04] and from the well known expressions for the electromagnetic fields of the electric and magnetic dipole, it is shown that:

$$\beta_{xx}^{mm} = -c^2 \alpha_{xx}^{ee}; \beta_{yy}^{mm} = -c^2 \alpha_{yy}^{ee}; \beta_{yz}^{em} = -\alpha_{yz}^{em}; \beta_{zz}^{ee} = -\frac{1}{c^2} \alpha_{zz}^{mm} \quad (5.9)$$

where  $c$  is the speed of light in vacuum.

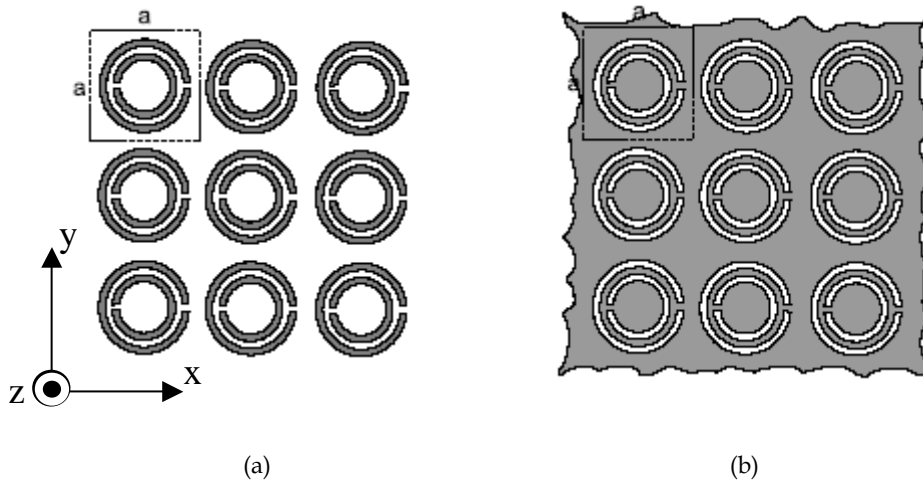


Fig.5.3. Geometries of the analyzed square array of SRRs (a) and CSRRs (b).

It is studied now a planar square array of SRRs of periodicity  $a$  (see Fig.5.3), and a plane wave of arbitrary polarization incident on this array from the left-hand side ( $z < 0$ ). As far as the size of the SRRs can be considered small with regard to the wavelength, the far field produced by the surface currents on the array will approach to that of the mean currents on it. These mean currents arise from the mean electric  $\langle p \rangle$  and magnetic  $\langle m \rangle$  dipoles generated in the SRR array. These dipoles are generated from the electric and magnetic fields incident upon each SRR through (5.1)-(5.3). Therefore, there is a linear relation between the mean surface currents and the

mean fields on the array of the kind:

$$\begin{pmatrix} J_{xx} \\ J_{yy} \end{pmatrix} = \begin{pmatrix} Y_{xx} & Y_{xy} \\ Y_{yx} & Y_{yy} \end{pmatrix} \begin{pmatrix} E_x \\ E_y \end{pmatrix} \quad (5.10)$$

The theory leading to the first order approximate values of the admittances  $Y$  is developed in *Article 5.1*. The results are:

$$Y_{xx} = j\omega \left\{ \frac{\alpha_{xx}^{ee}}{a^2} + \frac{k_y^2 \alpha_{zz}^{mm}}{\omega^2 a^2} \right\} \quad (5.11)$$

$$Y_{yy} = j\omega \left\{ \frac{\alpha_{yy}^{ee}}{a^2} + \frac{k_x^2 \alpha_{zz}^{mm}}{\omega^2 a^2} \right\} \quad (5.12)$$

$$Y_{xy} = j\omega \left\{ \frac{\alpha_{yz}^{em} k_y}{\omega a^2} - \frac{k_x k_y \alpha_{zz}^{mm}}{\omega^2 a^2} \right\} \quad (5.13)$$

$$Y_{yx} = j\omega \left\{ -\frac{\alpha_{yz}^{em} k_y}{a^2} - \frac{k_x k_y \alpha_{zz}^{mm}}{\omega^2 a^2} \right\} \quad (5.14)$$

where  $k_x$  and  $k_y$  are the transverse components of the wave vectors of the incident field. The theory behind these results is based on the the simplest homogenization procedure, i.e. on the assumption of that the incident field on each SRR coincides with the mean field on the array.

Under normal incidence  $k_x = k_y = 0$ . Thus, the surface admittance matrix (5.10) becomes diagonal. Although no crosspolarization effects can occur (the non-diagonal elements are zero), since  $\alpha_{yy}$  is resonant and  $\alpha_{xx}$  is not, the behavior of the FSS for the two orthogonal polarizations of the incident wave are quite different: for waves polarized with the electric field parallel to the y-axis (see Fig. 5.2) a strong reflectivity is expected near the resonance, whereas for incident waves having the orthogonal polarization it is not. Therefore, for normal incidence and near the resonance, the FSS will act as a polarizer.

Now the analysis is restricted to the resonant case. The excitation is made with a plane wave polarized in the  $y$  axis:  $\mathbf{E}^{\text{inc}} = E_0 \mathbf{y} e^{-jk_z z} e^{j\omega t}$ . In these conditions the FSS is

characterized by a scalar surface admittance:

$$\mathbf{J}_s = Y_s \mathbf{E} \quad Y_s = \frac{j\omega\alpha_{yy}^{ee}}{a^2} \quad (5.15)$$

The admittance can be decomposed into the sum of two admittances, see *Article 5.1*:

$$Y_s = Y_D + \left( \frac{4\omega d_{eff}}{\pi\omega_0 a} \right)^2 Y_{LC} \quad (5.16)$$

Here  $Y_D$  is the admittance of a disk of radius equal to that of the SRR [COLL 91]. This choice for the non-resonant part of the SRR admittance is justified by the similarity in behaviour of the SRR and the aforementioned disk far from the resonance [MARQ 03]. The second summand on the right-hand side of the previous equation,  $Y_{LC}$ , is the series connection of the SRR equivalent inductance,  $L$ , and capacitance,  $C = \pi r_0 C_{pu}/2$  [MARQ 03], giving the resonance frequency  $\omega_0 = \sqrt{(LC)^{-1}}$ .

$$Y_{LC} = \frac{j\omega C}{1 - \omega^2 LC} \quad (5.17)$$

Now the transmission and reflection coefficients can be extracted from the admittance following the standard procedure.

$$t = 1 + r = \frac{2}{Y_s \eta_0 + 2} \quad (5.18)$$

where  $\eta_0$  is the free-space impedance. At resonance the equivalent SRR admittance goes to infinite and there is total reflection. Total transmission is achieved when the admittance vanishes. According to (5.16) and (5.18) this happens above the SRR resonance frequency.

The same analysis can be reproduced for the CSRR case. However, for thin and lossless plates the Babinet's principle can be applied. This principle states that the total field transmitted by a metallic screen with an arbitrary aperture, added to the total field transmitted by its complementary screen (illuminated by the complementary incident wave), gives the incident wave over this last structure. After some algebra, see *Article 5.1*, the transmission coefficient for the CSRR-FSS,  $t_c$ , and for the SRR-FSS,  $t$ , are related by  $t + t_c = 1$ . So  $t_c = -r$  and  $r_c = -t$ , where  $t_c$  and  $r_c$  are the transmission and

reflection coefficients for the CSRR-FSS when it is illuminated by the complementary wave. With this, the response of CSRR-FSSs is readily obtained from that of the SRR-FSSs.

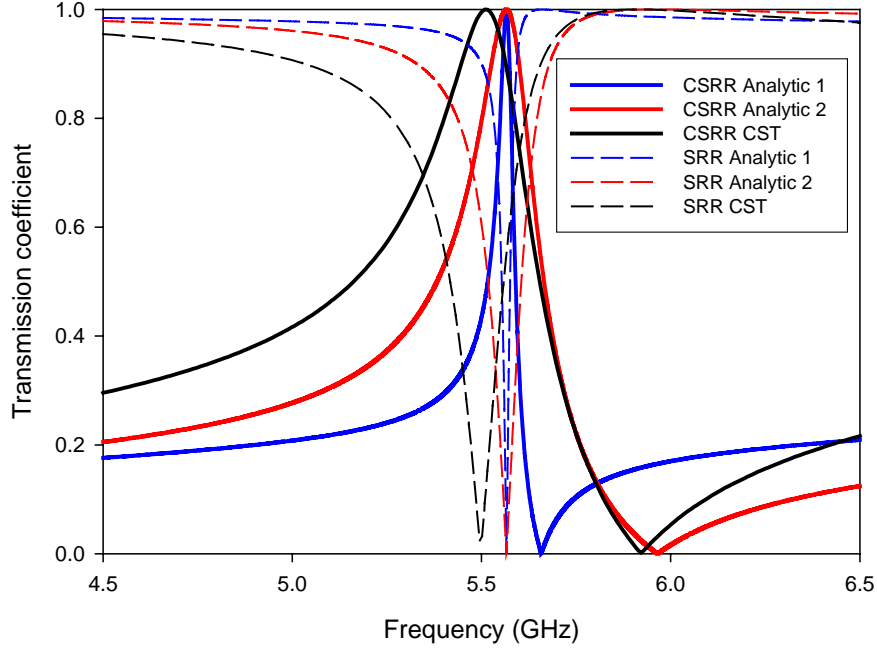


Fig. 5.4. The transmission coefficient for a metasurfaces of SRRs and CSRRs with lattice parameter  $a = 8 \text{ mm}$ . The resonators dimensions are  $r_{ext} = 3.5 \text{ mm}$  and  $c = d = 0.4 \text{ mm}$ . Solid lines are for the CSRR-FSSs and dashed lines for the SRR-FSSs. Black curve: simulation results obtained using CST Microwave Studio. Blue curve: theoretical results computed from the proposed analytical model with  $d_{eff} = c + d$ . Red curve: results computed using the same model with  $d_{eff} = 2(c + d)$ .

To verify the analysis quantitatively, the theoretical results obtained for a specific CSRR-FSS and SRR-FSS have been compared with those obtained from the commercial software *CST Microwave Studio*<sup>TM</sup>. This comparison is shown in Fig. 5.4 for the resonant polarization, i.e. when  $\mathbf{E}^{inc} = E_0 \hat{\mathbf{y}} e^{-jk_z z} e^{j\omega t}$  in the SRR screen and when  $\mathbf{H}^{inc} = H_0 \hat{\mathbf{y}} e^{-jk_z z} e^{j\omega t}$  (as expected, a near zero transmission coefficient was obtained for the orthogonal polarization at all frequencies). For the theoretical computations the values of  $L$  and  $C_{pul}$  have been extracted from [MARQ 03]. Two different values have been tested for the effective diameter:  $d_{eff} = c + d$  (blue curve) which is the expression

usually used in the analysis of SRRs and  $d_{eff} = 2(c + d)$  (red curve) which is an unrealistic value tested in order to fit the numerical results. A good qualitative agreement can be seen between theoretical and numerical results (black curve), as well as an accurate quantitative prediction of the frequency of the transmission peak. The good qualitative agreement includes the zero-transmission point above the transmission peak, although the bandwidth is not accurately predicted. The fitted curve closely resembles the numerical results. Similar results were obtained for different resonator dimensions and periodicities. Thus, it can be concluded that the proposed theory qualitatively reproduces the behaviour of the analysed FSSs for normal incidence. It also gives quantitatively accurate predictions for the frequency of resonance, although it underestimates the bandwidth. This fact is probably related to the limitations of the SRR model reported in [MARQ 02].

Focusing now on the simulation results (black curves) it can be seen that the full-wave simulator clearly predicts a complementary response for SRR-based (dashed black) and CSRR-based (solid black) FSSs. Due to the non-connected nature of the SRR-FSS a rejected band is seen, while for CSRRs the filter is of the bandpass type.

### 5.2.2 SRR/CSRR Metasurfaces under oblique incidence.

The bianisotropy property of SRR/CSRR gives a rich variety of cross-polarization effects when the incoming wave impinges on the screen at an angle.

The previous analysis is extended here to the oblique incidence case. The results obtained will be applicable to infinitely thin metallic perfectly conducting screens of SRRs in free space. Under these conditions, the results can be extended as well to CSRR-FSSs by means of the Babinet's principle. To compute the transmission and reflection coefficients the boundary conditions on the surface  $z = 0$ :

$$J_{sx} = H_y^i + H_y^r - H_y^t \quad (5.19)$$

$$J_{sy} = -H_x^i - H_x^r + H_x^t \quad (5.20)$$

$$0 = E_x^i + E_x^r - E_x^t \quad (5.21)$$

$$0 = E_y^i + E_y^r - E_y^t \quad (5.22)$$

are substituted in (5.10) and after some manipulations the following relations are obtained for the fields of the reflected and transmitted waves at  $z = 0$ :

$$\begin{pmatrix} E_x \\ E_y \end{pmatrix}^r = \begin{pmatrix} A - Y_{xx} & B - Y_{xy} \\ B - Y_{yx} & C - Y_{yy} \end{pmatrix}^{-1} \begin{pmatrix} Y_{xx} & Y_{xy} \\ Y_{yx} & Y_{yy} \end{pmatrix} \begin{pmatrix} E_x \\ E_y \end{pmatrix}^i \quad (5.23)$$

$$\begin{pmatrix} E_x \\ E_y \end{pmatrix}^t = \begin{pmatrix} A - Y_{xx} & B - Y_{xy} \\ B - Y_{yx} & C - Y_{yy} \end{pmatrix}^{-1} \begin{pmatrix} A & B \\ B & C \end{pmatrix} \begin{pmatrix} E_x \\ E_y \end{pmatrix}^i \quad (5.24)$$

where  $A$ ,  $B$ , and  $C$  are given by:

$$A = -2Y_0 \frac{(\xi_x^2 + \xi_z^2)}{\xi_z} \quad (5.25)$$

$$B = -2Y_0 \xi_x \xi_y \quad (5.26)$$

$$C = -2Y_0 \frac{(\xi_y^2 + \xi_z^2)}{\xi_z} \quad (5.27)$$

with

$$k_0 \xi_x = k_x^i = k_x^r = k_x^t \quad (5.28)$$

$$k_0 \xi_y = k_y^i = k_y^r = k_y^t \quad (5.29)$$

$$k_0 \xi_z = k_z^i = -k_z^r = k_z^t \quad (5.30)$$

From the above equations, the transmission and reflection coefficients for the co- and cross-polar polarizations are readily obtained for any polarization and angle of incidence. It is deduced that cross-polarization effects should be present, in general, in SRR arrays. However, for the two orthogonal main planes of incidence (i.e., the  $x - z$  and the  $y - z$  planes), from (5.13), (5.14) and (5.26) it is deduced that cross-polarization only occurs  $k_y \neq 0$ , which implies that  $Y_{yx}$  and/or  $Y_{xy}$  are non-zero. Or, in other words, cross-polarization does not happen for incidence in the  $x - z$  plane. In the remaining cases, cross-polarization effects are unavoidable.

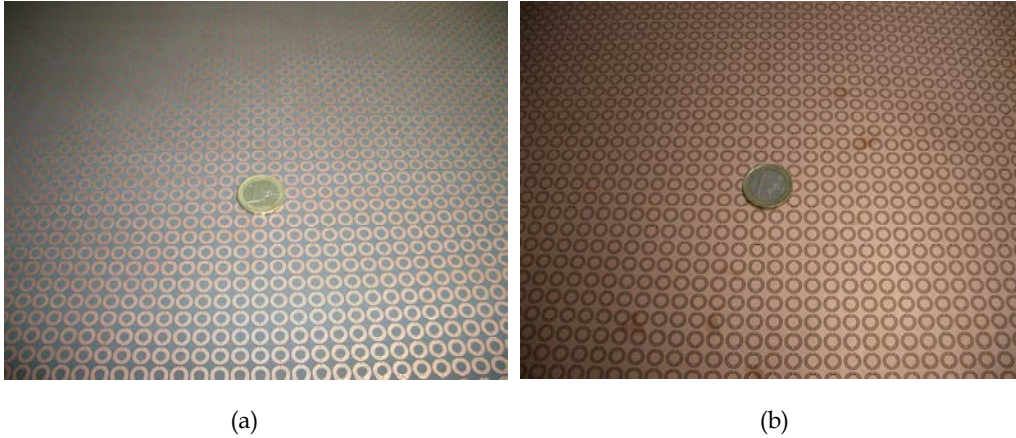


Fig. 5.5. Fabricated metasurfaces of SRRs (a) and CSRRs (b). The parameters of the resonators are  $r_{ext} = 3.5$  mm  $c = d = 0.4$  mm (see Fig. 5.2 for the parameter definition). The dielectric used has  $\epsilon = 2.43$  and  $h = 0.49$  mm.

This analytical theory is checked with the experiments. Two planar screens of  $49 \times 49$  SRRs/CSRRs (with a total size of  $400 \times 400$  mm) were prepared, see Fig. 5.5. The SRRs/CSRRs were etched on a commercial low loss microwave substrate with relative dielectric permittivity  $\epsilon = 2.43$  and height  $h = 0.49$  mm, coated with a conductive layer of copper of thickness  $t = 35$   $\mu$ m. The SRR/CSRR parameters are (see Fig. 5.2 and 5.3)  $r_{ext} = 3.5$  mm and  $c = d = 0.4$  mm, which gives a theoretical frequency of resonance of 4.41 GHz for the SRR, and of 4.65 GHz for the CSRR, according with the theories developed in [MARQ 03] and [BAEN 04] respectively. The periodicity of both screens was  $a = 8$  mm, which is approximately  $1/8$  of the free space wavelength at resonance. The experimental setup is sketched in Fig. 5.6. In order to avoid diffraction and multiple reflection effects, the SRR/CSRR array was surrounded by microwave absorbers and the whole setup was placed in an anechoic chamber. Two standard horn antennas were placed at a distance of 185 cm ( $27 \lambda_0$  approximately) from the screens, as is shown in the Figure. The transmission level ( $|S_{21}|$ ) was measured in a Vector Network Analyzer for the co- and the cross-polar polarizations, and for the appropriate orientations of the screens, for angles of incidence of  $0^\circ$ ,  $30^\circ$ ,  $45^\circ$  and  $60^\circ$ .

Simulation results for the analyzed cases have also been obtained. It serves as a check of the experiment as an alternative to the analytical theory. The simulations are carried out by using the Frequency Domain solver available in the commercial simulator *CST Microwave Studio*<sup>TM</sup>. The solver is based on Maxwell's Grid Equations in

the time harmonic case. With this module it is possible to simulate the oblique incidence for infinitely periodic structures. However, it is limited to lossless structures. Thus, the simulation will be restricted to perfect electrically conducting metals and lossless dielectrics.

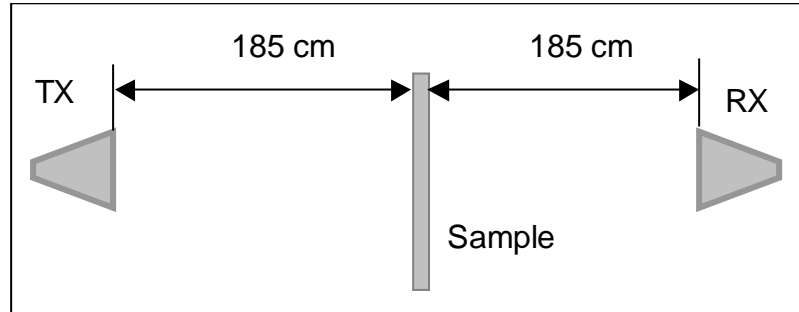


Fig.5.6. Sketch of the experimental setup. Two horn antennas, located at 185 cm from the array are used as emitter and receiver.

### A Incidence in the $x - z$ plane.

In this case, since  $k_y = 0$ ,  $Y_{xy} = Y_{yx} = 0$  in (5.13) and (5.14). Therefore, the admittance matrix (5.10) is diagonal and, according to (5.23)-(5.30), there are no cross-polarization effects. However, for the SRR (CSRR) screen, due to the presence of a resonant  $\alpha_{yy}^{ee} (\beta_{yy}^{mm})$  electric (magnetic) polarizability, there is a resonant response when the screen is illuminated by a plane wave with the electric (magnetic) field polarized along the  $y$ -axis [FALC 04]. For the orthogonal polarizations, since there is no resonant excitation of the SRRs or the CSRRs, resonant responses are not expected in both screens.

#### A.1 Polarization in the plane of incidence (SRR screen).

If the incident wave is polarized in the plane of incidence ( $x - z$  plane), the resulting wave is a  $TM_y$  wave ( $H_z = H_x = 0$ ,  $E_y = 0$ ). According to (5.1)-(5.3) there is no resonant excitation of the SRRs (the polarizability  $\alpha_{xx}^{ee}$  is non-resonant [MARQ 03]). The theoretical calculations for a lossless and infinitely thin screen in the absence of substrate are shown in Fig. 5.7(a) (the expressions proposed in [MARQ 03] were used for the polarizabilities). It predicts almost transparency for all the angles of incidence. The experimental results (Fig. 5.7(c)) confirm these predictions: the screen is almost

transparent for the co-polar component and the cross-polar component is almost not excited. The simulation results (Fig. 5.7(e)) follow very accurately the measurements with small discrepancies in the level of the curves, probably due to the fact that simulation neglects losses which are present in the measurement.

#### A.2 *Polarization perpendicular to the plane of incidence (SRR screen).*

For this polarization, the resulting wave is a  $TE_y$  wave, with  $E_z = E_x = 0$  and  $H_y = 0$ . In this case, resonances occur via the excitation of the SRRs by the field components  $E_y$  and  $H_z$  (5.1)-(5.3). The analytical results are given in Fig. 5.7(b) and the measurements in panel (d). The comparison between both figures shows a good qualitative agreement: a resonant behavior for the transmission coefficient of the co-polar component, without cross-polarization effects. The discrepancies in the frequency of resonance can be attributed to the presence of the substrate in the actual structure, which affects this frequency. The frequency of resonance predicted for the SRRs in the presence of the substrate is 4.41 GHz [MARQ 03]. This value agrees, within a few percent of error, with the measurements. The main quantitative discrepancies with the theory are again in the bandwidths. The experimental bandwidths grow with the angle of incidence, as is predicted by the theory. However, the experimental bandwidth is always wider than the calculated one. Losses and the presence of the substrate may partially explain this disagreement. Moreover, the theory behind the expressions for the polarizabilities is based on a perfect quasi-static behavior, whereas the SRR perimeter (approximately 22 mm) is about 1/3 of the wavelength at resonance. The screen periodicity  $a = 8$  mm, although smaller than the wavelength by a factor of 8, may be big enough to affect these particular results. Finally, the chosen homogenization procedure may not be the appropriate one.

The simulation results of Fig. 5.7(f) are in very good agreement with the experimental ones. A slight disagreement is observed in the position of the zero of transmission. It is at 4.45 GHz in the simulation and at 4.54 GHz in the measurement. However, note that the simulation is closer to the theoretical value of 4.41 GHz. The larger deviation of the experimental result can be due to the inherent fabrication tolerances. A very good agreement is seen in the bandwidth predicted by the simulation and measured in the experiment. The simulated signal level follows quite accurately the measurement.

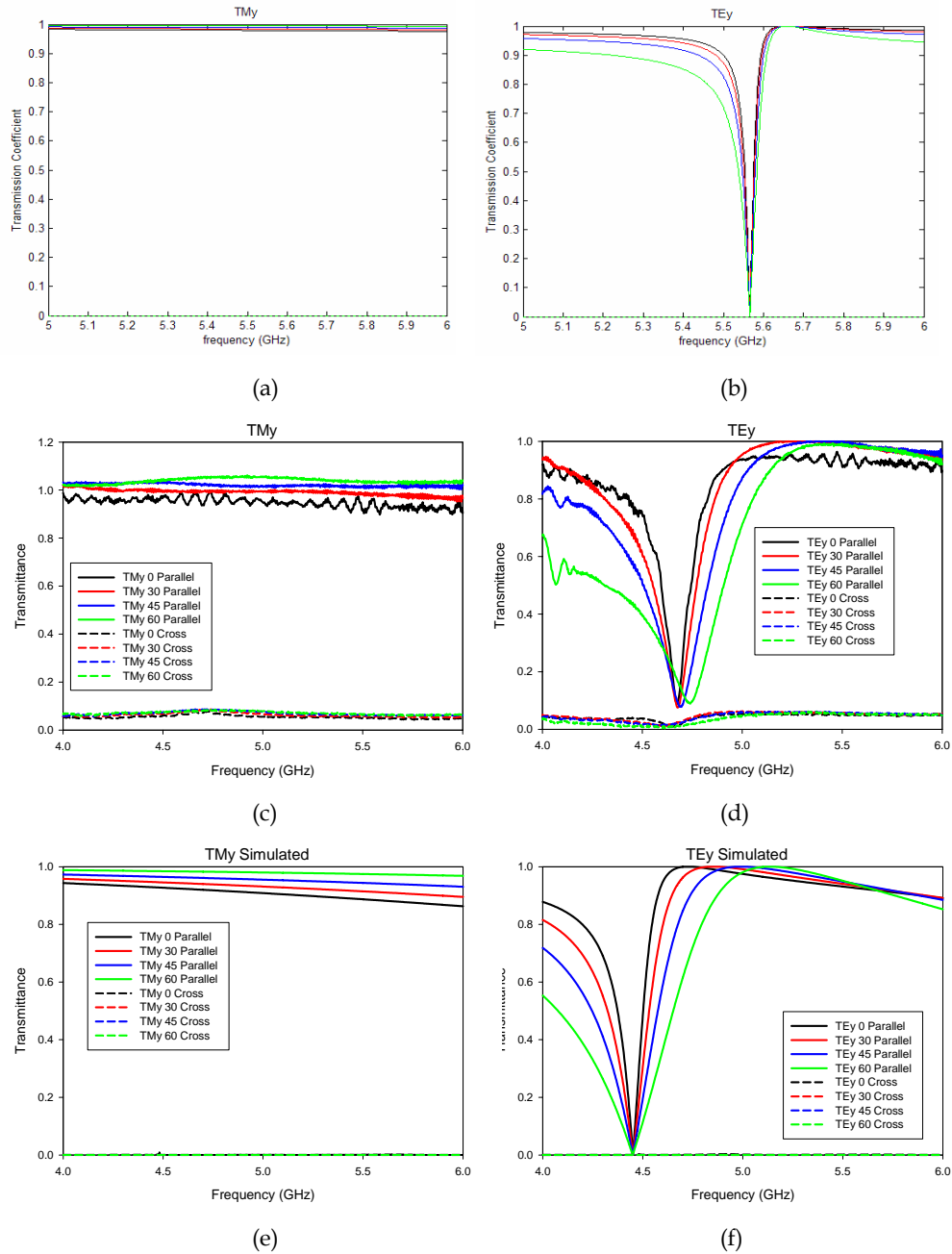


Fig. 5.7. Theoretical (a), experimental (c) and simulated (e) results for a SRR-FSS with plane wave incidence on the  $x - z$  plane and polarization in that plane. The same for polarization perpendicular to the plane of incidence. Theoretical (b) experimental (d) and simulated (f). The angle of incidence is defined with regard to the normal ( $z$ -axis).

A.3 CSRR screen.

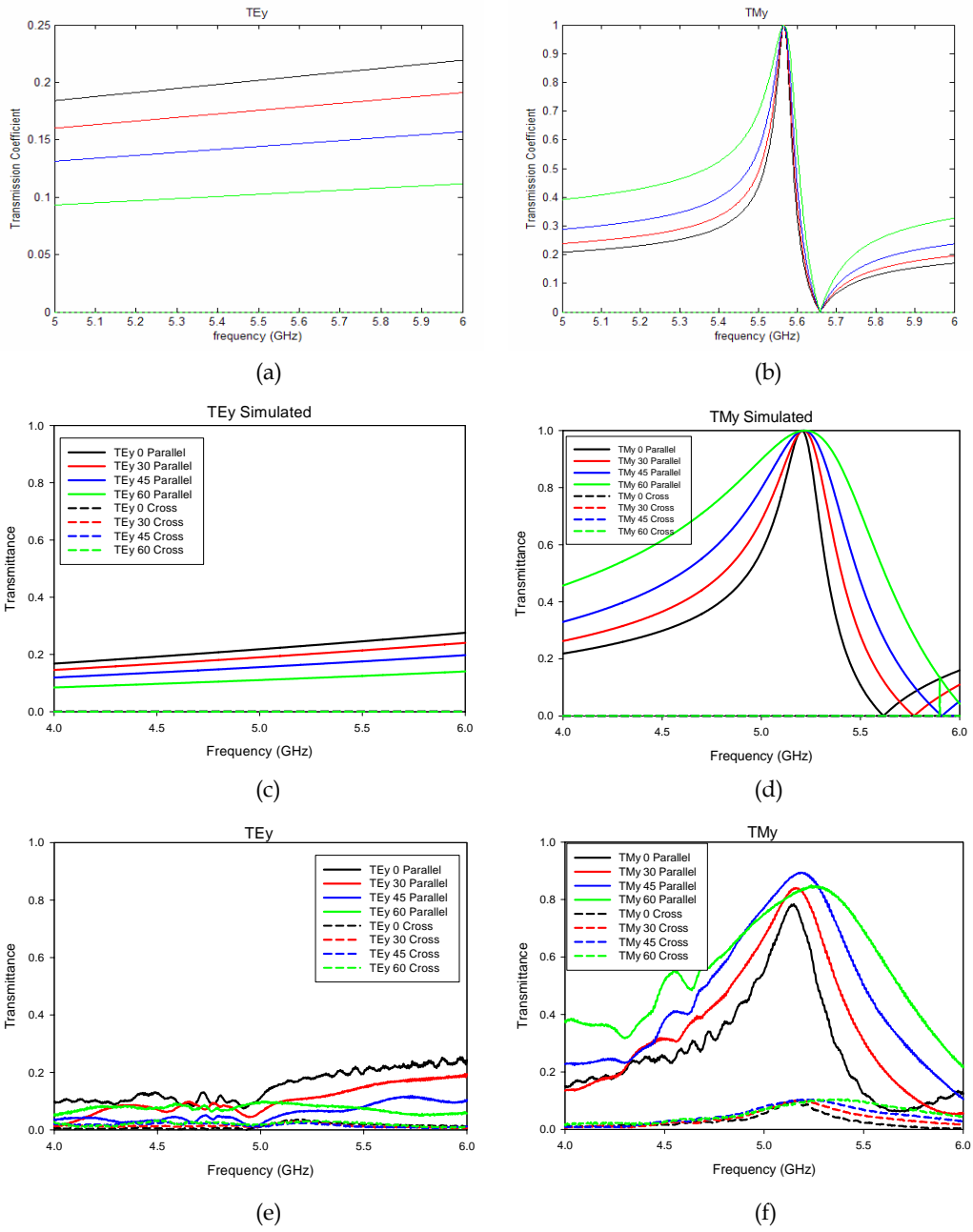


Fig. 5.8. Theoretical (a), experimental (c) and simulated (e) results for a CSRR-FSS with plane wave incidence on the  $x - z$  plane and polarization in that plane. The same for polarization perpendicular to the plane of incidence. Theoretical (b) experimental (d) and simulated (f). The angle of incidence is defined with regard to the normal ( $z$ -axis)

As usual, to compute CSRR screen response, the Babinet's principle will be applied. The transmission coefficients are related by the expression:

$$t + t_c = n; n = 0, 1 \quad (5.31)$$

where  $t$  and  $t_c$  are the transmission coefficients for the *SRR* and the *CSRR* screens respectively, and  $n = 1$  for the co-polar component and  $n = 0$  for the cross-polar one.

The analytical and experimental results for the polarization in the plane of incidence are shown in panels (a) and (c) of Fig. 5.8. A good qualitative agreement can be seen. The frequency shift between the resonances can be attributed to the presence of the substrate. The frequency of resonance for the individual CSRRs in the presence of the substrate, obtained from the theory developed in [BAEN 04] is 4.7 GHz, which is near the experimental value.

A strong disagreement is again seen in the bandwidth. The conformity of the simulation (panel (e)) with the measurement is very good. The position of the peak is at 5.22 GHz very close to the measurement value. The bandwidth is also similar. The only disagreement is on the level of the signal, which is higher in the simulation. It is more noticeable in the case of CSRR-FSSs due to the passband characteristic of the screen, with the bandpass determined by the first resonance of the particles. In the case of SRR-FSSs, the rejected band characteristic does not suffer appreciably and the losses may even contribute to stop transmission.

Finally, for the polarization orthogonal to the plane of incidence, no resonance is observed as expected, see Fig. 5.8(b). The experimental results (Fig. 5.8(d)) confirm this prediction. The simulation (Fig. 5.8(f)) points in the same direction.

## **B Incidence on the $y - z$ plane.**

If the incidence occurs in this plane  $k_y \neq 0$  and, therefore, the admittance matrix (5.10) is non-diagonal. Thus, from (5.23)-(5.30), cross-polarization effects are expected. What is more, for lossless media the cross-polarizabilities  $\alpha_{yz}^{em}$  are imaginary [MARQ 02], whereas the remaining terms are real.

Thus, the non-diagonal terms of (5.10) should be imaginary, whereas the diagonal terms are real, as is deduced from (5.11)-(5.14). Therefore, from (5.23), (5.20), the co- and the cross-polar components of the transmitted and the reflected waves are in

quadrature, so that the reflected and transmitted waves are elliptically polarized.

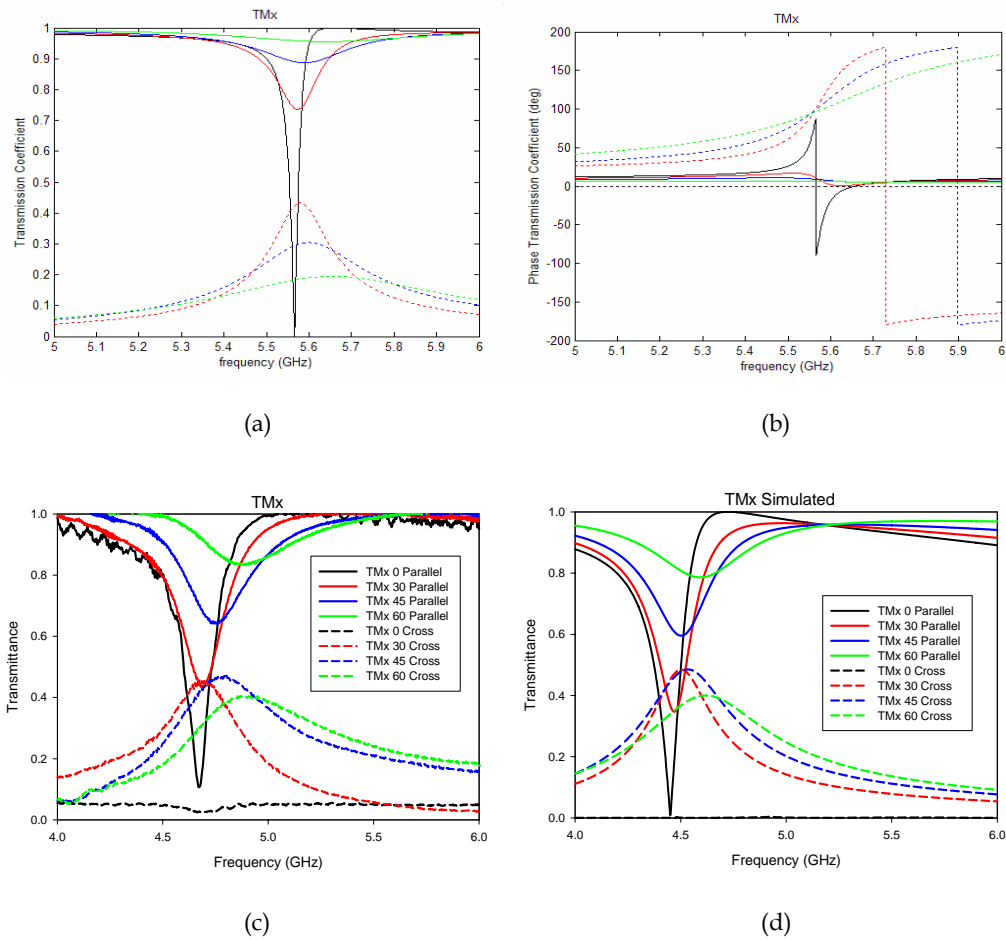


Fig. 5.9. Theoretical magnitude (a) and phase (b) response of a SRR-FSS with plane wave incidence on the  $y - z$  plane and polarization in that plane. In (c) is shown the magnitude of the experimental transmission coefficient for that case and in (d) the simulation result. The angle of incidence is defined with regard to the normal ( $z$ -axis).

### B.1 Polarization in the plane of incidence (SRR screen).

In this case, the wave is a  $TM_x$  wave ( $E_x = 0, H_y = H_z = 0$ ). The theoretical results for the transmission coefficient are shown in Fig. 5.9(a) (magnitude) and in Fig. 5.9(b) (phase). The experimental results for the magnitude of the transmitted wave are

shown in Fig.5.9(c). As in the previous section, the comparison between theory and experiment shows a good qualitative agreement.

Quantitative discrepancies are mainly in the bandwidth. On the other hand, the simulation results of Fig. 5.9 (d) are in very good agreement with the measurements. The simulation bandwidth is similar to the experimental one, and the main discrepancy is in the level of signal, more easily appreciable in the passbands of the cross-polarization curves. Again, this can be due to the effect of neglecting losses in the simulation.

An interesting feature of this device, revealed by both theory, experiments and simulation, is the possibility of obtaining circularly polarized transmitted and reflected waves for the appropriate angle of incidence: that for which the amplitudes of the co- and cross-polar waves equal.

### *B.2 Polarization perpendicular to the plane of incidence (SRR screen).*

The results for this case are very similar to those reported in the previous paragraph. In this case the wave is a TE<sub>x</sub> wave ( $E_y = E_z = 0, B_x = 0$ ), with the electric field polarized along the  $x$ -axis. The theoretical results for the magnitude and phase of the transmission coefficient are shown in Fig. 5.10(a) and Fig. 5.10(b) respectively, whereas the experimental results for the magnitude of the transmitted wave are shown in Fig. 5.10(c).

The main difference with the results of Fig.5.9 (a)-(c) is in the bandwidth, which is bigger for the present polarization. This result is expected from the fact that the magnetic excitation - the main excitation mechanism of the SRRs - is present for this polarization, whereas it is not present in the previous one. Attending to the simulation results of Fig. 5.10(d) it is seen again a very good agreement with the experiment, being the main discrepancies the level of the peaks observed, directly related to the neglect of losses in the simulation.

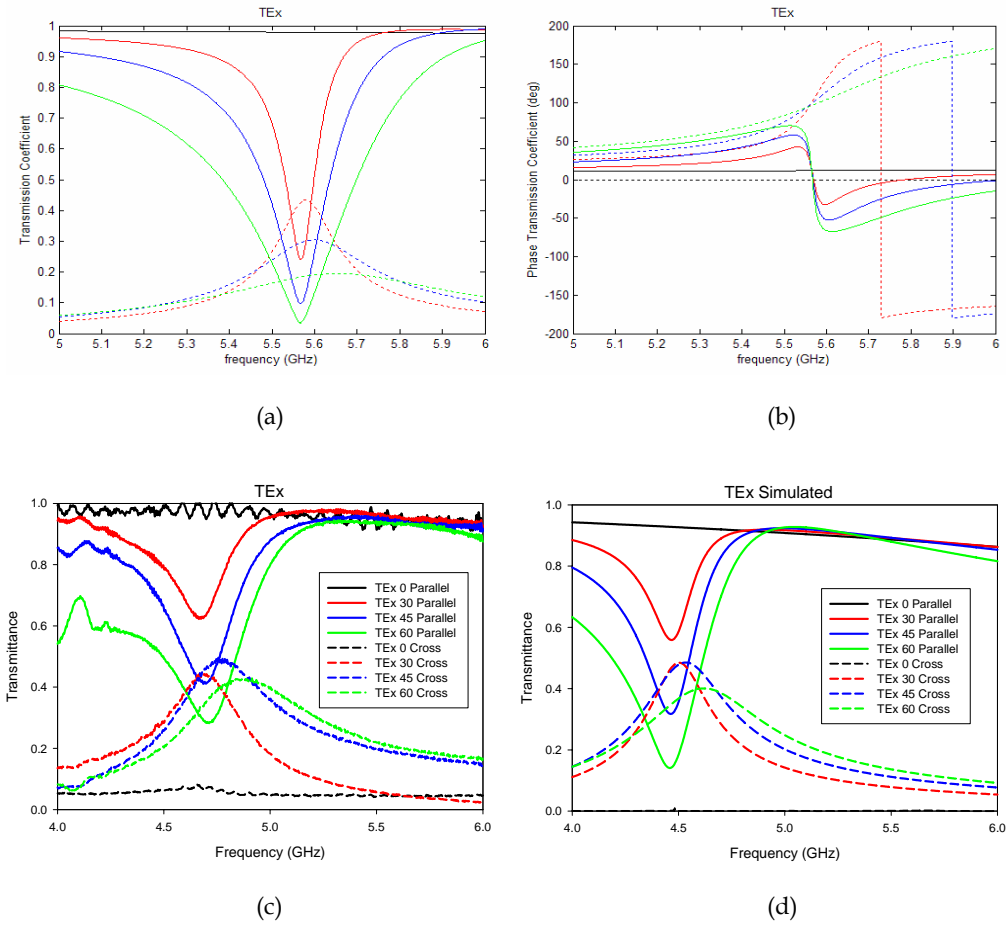


Fig. 5.10. Theoretical magnitude (a) and phase (b) response of a SRR-FSS with plane wave incidence on the  $y - z$  plane and polarization in perpendicular to that plane. In (c) is shown the magnitude of the experimental transmission coefficient for that case and in (d) the simulation result. The angle of incidence is defined with regard to the normal ( $z$ -axis).

### B.3 Behavior of the CSRR screen.

The experimental results for the CSRR screen are shown in Fig. 5.11. The transmission coefficient for the polarization parallel to the plane of incidence ( $TM_x$ ) is plotted in panels (a), (c) and (e), theoretical, experimental and simulation results respectively.

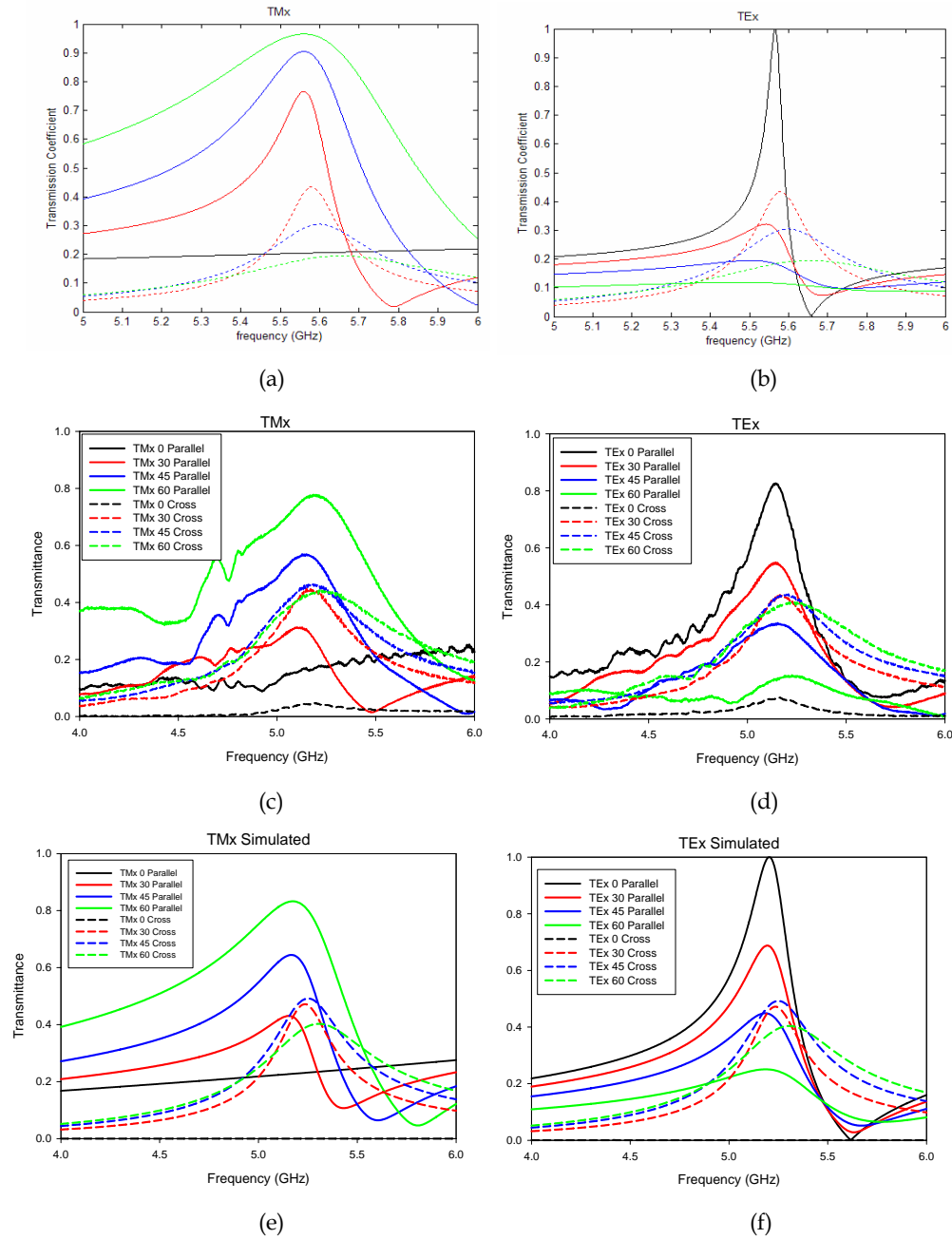


Fig. 5.11. Theoretical (a), experimental (b) and simulated (c) results for a CSRR-FSS with plane wave incidence on the  $y - z$  plane and polarization in that plane. The same for polarization perpendicular to the plane of incidence. Theoretical (d), experimental (e) and simulated (f). The angle of incidence is defined with regard to the normal ( $z$ -axis)

The case of polarization perpendicular to the plane of incidence ( $TE_x$ ) is shown in panels (b), (d) and (f), theoretical, experimental and simulation, respectively.

For a lossless and thin screen, without substrate, the results of Fig. 5.11 (a), (c) and (e) should be related to those in Fig. 5.10 (a), (c) and (d) respectively and those of Fig. 5.11 (b), (d) and (f) to those in Fig. 5.9 (a), (c) and (d) respectively, by means of Eq. (5.31). For the more realistic case reported in the experiments, this relation is only approximate. As it can be seen in the Figures, the experimental results follow this pattern. The simulation results match very accurately the experiment. Note that apart from the different power level, the bandwidth as well as the main features such as the resonance frequency and the relative position of the curves fits very well with the experiment.

### 5.2.3 Concluding remarks.

It has been seen that surfaces made by the periodical arrangement of SRRs and CSRRs illuminated by a plane wave show a high variety of cross-polarization effects. The analytical discussion based on the homogenization principle has been compared with the experimental results. It is able to catch the qualitative features in the response of the screens. The complementarity in the response of SRRs and CSRRs has been checked.

On the other hand, quantitative disagreements still appear, mainly in the predicted bandwidth for the transmitted and reflected beams. More theoretical and experimental work is needed in order to explain these discrepancies. Applications of the studied devices to frequency selective surfaces, polarizers and polarization converters can be envisaged.

Metasurfaces have been discussed in *Article 5.1* in the easier normal incidence case and in *Article 5.2* for oblique incidence.

## 5.3 Electroinductive waves

### 5.3.1 Dispersion relation and duality

After the seminal paper of Pendry [PEND 99], where he predicted that artificial media with negative permeability could be designed by using split ring resonators (SRRs), many researchers became interested in the properties of these particles. Apart from the obvious interest in achieving the left-handed materials described by Veselago [VESE 68], some of the research was concentrated on the guiding properties of the particles. Shamonina et al. analyzed both theoretically [SHAM 02], [SHAM 02b], [SHAM 03] and experimentally [WILT 03] the properties of a new kind of waves supported by arrays of SRRs, the Magnetoinductive Waves (MIW). These waves owe their existence to the magnetic coupling between adjacent resonators, so they can exist in any periodic structure with magnetic coupling between elements. In that series of papers, Shamonina et al. described exhaustively the properties of the waves and the effects of unmatched loading, losses in conductors, tolerances in fabrication, etc, and compared the characteristics of MI waveguides with standard transmission lines. Soon after, Freire et al. [FREI 04] explored a practical application of these waves as a planar wave transducer. There, a delay line in microstrip technology was implemented using modified SRRs. By using the complementarity concepts previously detailed, that result has been extended to the case of resonators electrically coupled. The waves supported by this structure have been termed Electroinductive Waves (EIW) in analogy with MIW.

The resonator proposed for EIW is the complementary of the SRR, the CSRR [FALC 04], see Fig.5.2(b). CSRRs are modelled in their first resonance like LC resonators [BAEN 05]. When a chain of CSRRs is formed by arraying particles, a mutual capacitance,  $C_M$  in Fig. 5.12, arises between the central disks of correlative rings, which gives as a result a transmission line for EIW. The circuit model reported in [BAEN 05] should be modified in order to include the mutual capacitance between adjacent resonators. Furthermore, the capacitance between the central disk of the CSRR and the ground should be modified since this ground is partly reduced by the presence of the nearest neighbours in the chain. Therefore, as a first approximation,  $C_C \approx 2C_M + C$ , where  $C_C$  is the CSRR capacitance defined in [BAEN 05], and  $C$  is the capacitance to ground in the chain of CSRRs. The dispersion equation is calculated with the

equivalent circuit of Fig.5.12.

$$I_n = YV_{n+1} + I_{n+1} \quad (5.32)$$

$$V_n = V_{n+1} + ZI_n = (1 + ZY)V_{n+1} + ZI_{n+1} \quad (5.33)$$

with  $Z = (j\omega C_M)^{-1}$  and  $Y = (1 - \omega^2 LC) / j\omega L$ . For any wave propagating inside a periodic structure and travelling in the +z direction the following relations apply:

$$V_{n+1} = V_n e^{-jka} \quad (5.34)$$

$$I_{n+1} = I_n e^{-jka} \quad (5.35)$$

where  $k$  is the wave number and  $a$  is the periodicity of the array. With all the previous equations and after some algebra, the dispersion relation is given as:

$$\frac{\omega^2}{\omega_0^2} = \left( 1 - \frac{2C_M}{C + 2C_M} \cos(ka) \right)^{-1} \quad (5.36)$$

where  $\omega_0 = [L(C + 2C_M)]^{-1/2}$ . Note that this resonant frequency is not simply that of the LC-parallel for an isolated resonator. In fact, the capacitance seen by the central conductor is modified by the presence of the two adjacent neighbours and gives as a result the equivalent capacitance for the parallel of the capacitance to ground plane,  $C$ , and the two mutual capacitances,  $2C_M$ . In all the previous equations only the nearest neighbour interaction has been taken into account which is enough to obtain the salient features in this kind of one-dimensional systems. For planar arrays, this choice is fully justified due to the small coupling to far located resonators.

The dispersion equation obtained shows a great resemblance with that of a MIW guide in the case of nearest neighbour interaction [SHAM 02], [FREI 04], reproduced here for comparison purposes:

$$\frac{\omega^2}{\omega_0^2} = \left( 1 + \frac{2M}{L} \cos(ka) \right)^{-1} \quad (5.37)$$

where  $M$  and  $L$  are the mutual inductance and self-inductance of an array of SRRs and  $\omega_0 = (LC)^{-1}$  is the resonant frequency of an isolated resonator. Both relations (5.36) and (5.37) coincide if the resonant frequency of the CSRRs and the SRRs is the same and

we change:

$$-C_M \rightarrow KM \quad (5.38)$$

$$C + 2C_M \rightarrow KL \quad (5.39)$$

where  $K$  is an arbitrary constant. If the CSRRs and the SRRs are embedded in an homogeneous isotropic medium, these conditions are fulfilled with  $K = 4(\varepsilon / \mu)$  [BAEN 05].

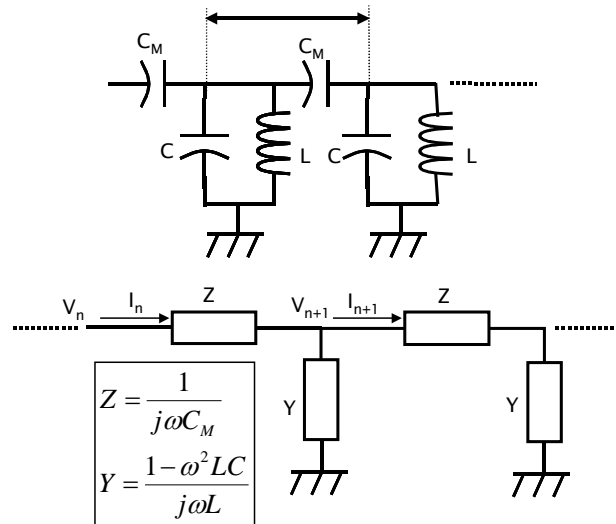


Fig. 5.12. Equivalent circuit for the unit cell of an infinite chain of LC resonators. Electric coupling between resonators is represented by a mutual capacitance  $C_M$

Similar relations – although with different values of  $K$  – arise when both elements are etched on the plane interface between two semi-infinite media [BAEN 05]. For intermediate situations, this equivalence will be only approximated. To sum up, EIWs can be considered as the dual counterparts of MIWs, having a similar electromagnetic behavior (in the sense of Babinet's principle [FALC 04]).

A linear chain of 50 CSRRs drilled on a perfectly conducting metallic plane has been simulated with the commercial full-wave simulator *CST Microwave Studio™*. The structure is excited by a vertical monopole. With this set-up the resonators are properly excited by the axial electric field component. Also, for comparison purposes, a single ring located at the same distance as the last one of the chain has been simulated. The results for the electric energy density are depicted in Fig. 5.13.

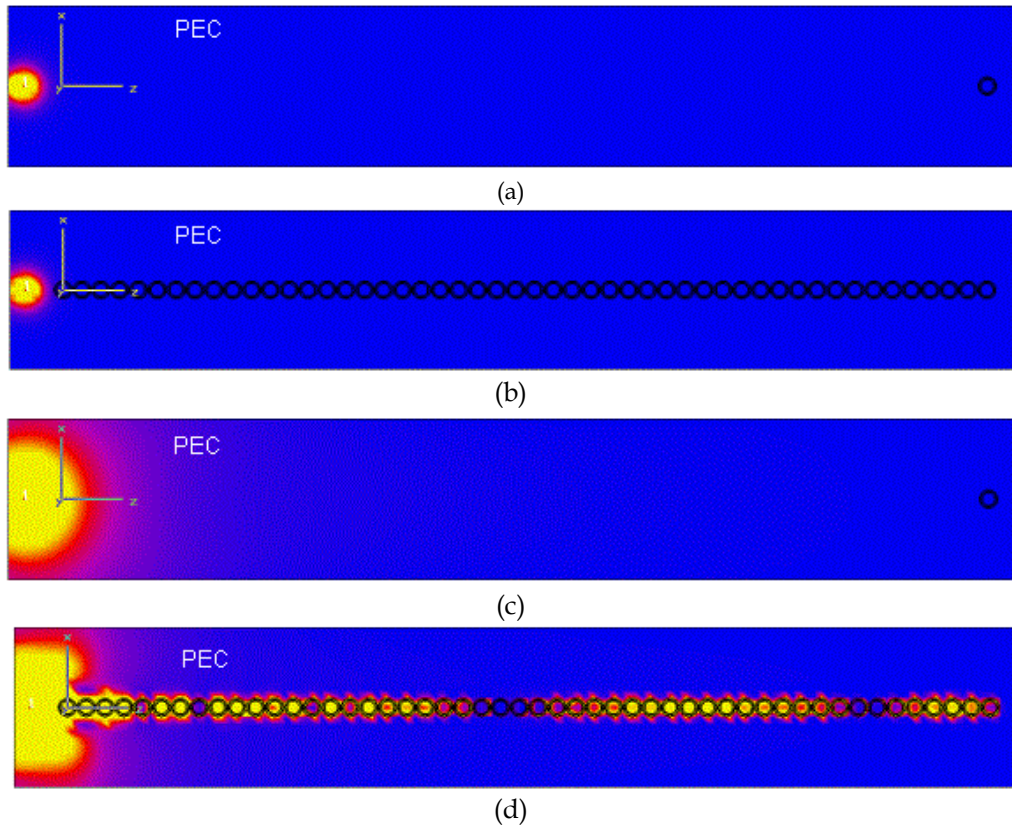
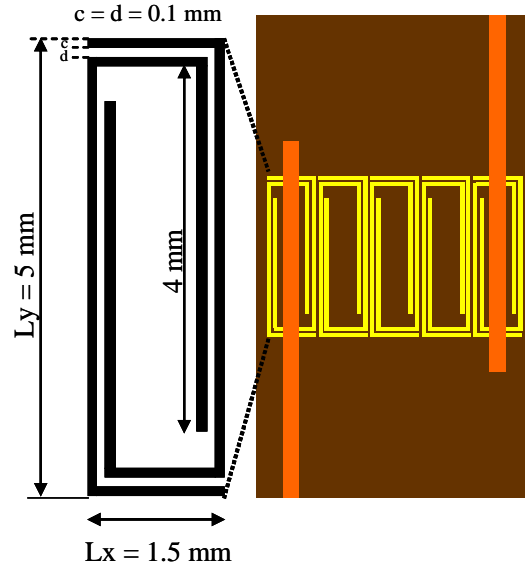


Fig. 5.13. Electric energy density created by a monopole located (on the left) on a perfect conductor ground plane drilled with CSRR resonators. A chain of 50 resonators is etched and tested well below the first particle resonance (b) and near the resonance (d). It is also shown that a single ring at a distance equal to that of the last resonator in the chain cannot be substantially excited by the source itself, neither below resonance (a) nor near resonance (c). The parameters of the resonators are (as shown in Fig.5.2(b)):  $r_{ext} = 3.5$  mm,  $c = d = 0.4$  mm,  $a = 8$  mm.

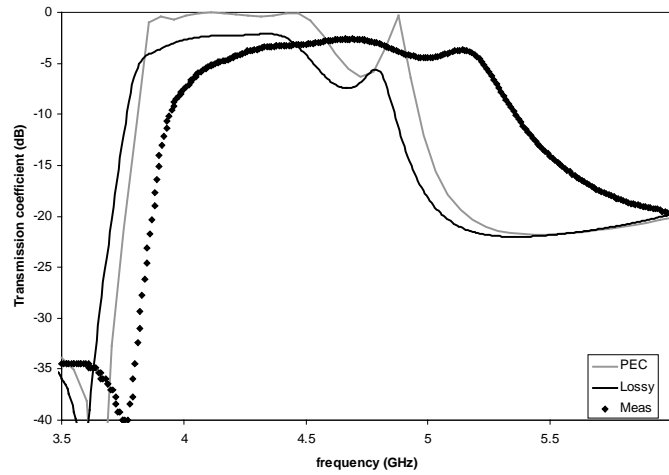
In panels (a) and (b) the rings are at a frequency below the first resonance. No traces of energy transport is seen neither for the isolated ring nor for the chain. In panels (c) and (d) the rings are on the quasi-static frequency. In panel (c) the source by itself is not able to excite appreciable energy in the ring. When the chain is introduced a clear energy transport is observed and the ring at the end shows an obvious concentration of energy. Electric energy is trapped in the vicinity of the particles being negligible out of them. It is worth noting that the standing wave pattern along the chain of resonators, due to the mismatch introduced at the end of the chain by the presence of the perfect conductor plane.

### 5.3.2 Practical implementation in planar technology.

With the given results, the existence of EIW has been well established. Now, a further step towards a more practical prototype is given. Many of the present microwave devices are fabricated in planar technology, thus these results have been extended to the implementation of a prototype in microstrip technology. For this analysis, both simulations and experiments have been carried out. The analyzed structure is shown schematically in Fig. 5.14(a). It is a transducer which transforms EM waves to EI waves. It consists of a chain of five resonators drilled on the ground plane of a microstrip circuit. The excitation of EIW is made by means of two symmetrically disposed microstrip lines. These are located just over the resonators at the end of the row. Here, the electric field is maximum and thus, the electric coupling between the microstrip and the resonators is optimal. The resonators are essentially the complementary ones of the split squared ring resonator (CSSRR) previously used in [FREI 04]. At difference with that the slots of the CSSRRs have been enlarged by comparison with the arms of the SSRR presented in that work. It has been found that this modification contributes to a reduction in the ohmic losses in the resonator. Another difference with that work is the location of the resonators, which for MI waves must be at a distance  $\lambda/4$  from the microstrip open end, in order to enhance the magnetic coupling. The circuit has been simulated with the commercial electromagnetic solver *Ensemble™*. A commercial low loss microwave substrate with relative dielectric permittivity  $\varepsilon = 10$  and height  $h = 0.635$  mm, coated with a conductive layer of copper of thickness  $t = 35$   $\mu\text{m}$  has been used. The parameters of the resonators are given in Fig. 5.14(a). The simulation results for the lossless case (Fig. 5.14(b) solid gray curve) show a passband near the resonance of the individual CSSRRs, well defined and with small ripples. When losses are taken into account in the simulation (Fig. 5.14(b) solid black curve), the shape of the passband remains basically the same as for the lossless case, but with some attenuation. The circuit has been fabricated and measured with a *HP 8510 B Vector Network Analyzer*. The experimental response (Fig. 5.13(b) black markers) presents similar features as the lossy simulation, but it is shifted in frequency, probably due to tolerances in the fabrication process.



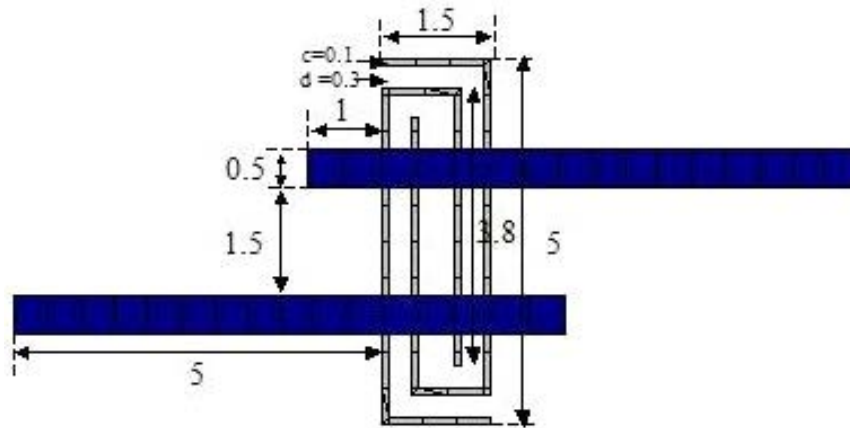
(a)



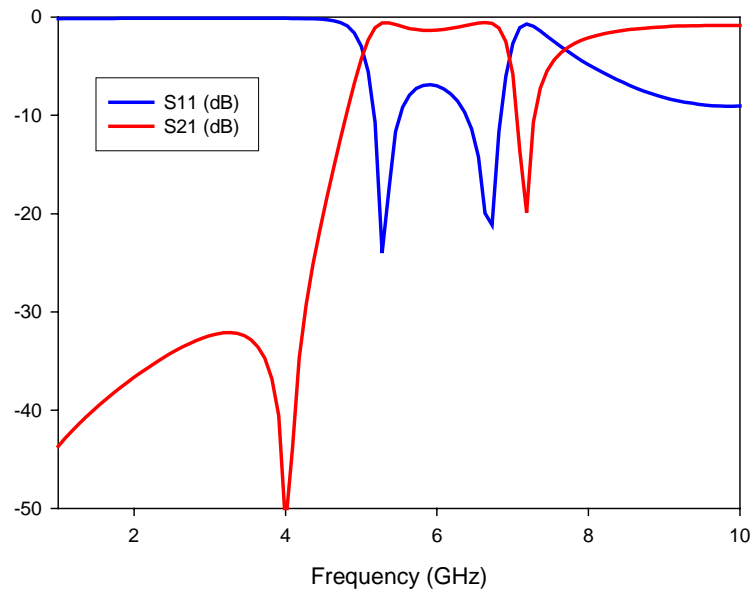
(b)

Fig. 5.14. (a) Sketch of the CSSRR transducer in microstrip technology. The parameters of the resonators are:  $L_x = 1.5$  mm,  $L_y = 5$  mm,  $c = d = 0.1$  mm. The periodicity is  $a = 1.6$  mm. The substrate thickness is  $h = 0.635$  mm and the dielectric permittivity  $\epsilon_r = 10$ . The microstrip lines have been designed to have  $50 \Omega$  of characteristic impedance. (b) Simulated transmission response for the lossless case or perfect conductor metallization (gray), and for the lossy or copper ( $\sigma = 5.8 \cdot 10^7$  S/m) metallization (black). Experimental transmission for the fabricated prototype (black marker).

### 5.3.3 UWB filter based on EIW.



(a)



(b)

Fig. 5.15. UWB filter based on EI waves. (a) Schematic and (b) frequency response. The dimensions of the circuit are given in the figure and the substrate used has the next parameters: thickness  $h = 0.635$  mm, permittivity  $\epsilon = 10$ .

The previous results have been engineered to the design of a ultra wide band (UWB) filter in microstrip technology. The circuit consists of a pair of feeding microstrip lines and the filtering section is made by using a particle similar to those described above, see Fig. 5.15(a). In the figure are represented in blue the metallic microstrip lines and in gray the filtering resonator etched on the ground plane. The feeding lines have been designed to present a  $50 \Omega$  impedance at the working frequency. The circuit is designed on a substrate of thickness  $h = 0.635$  mm and relative dielectric permittivity  $\epsilon = 10$ . This design has been simulated with the commercial solver *Ensemble™*. The  $S_{11}$  and  $S_{21}$  parameters are shown in Fig. 5.15(b), where metal losses have been taken into account (metallization is made with copper of thickness  $t = 35$  microns). As it is seen, a clear bandpass response is obtained, with a band that extends from 5 to 7 GHz and with a minimum value of  $-1.33$  dB in the band. The rejection in the low frequency region is below 30 dB, with a steep slope towards the band. In the high frequency region, however, the rejection is not good. This last point can be mended by inserting a stop band filter structure such as a chain of multiple tuned CSRR in the line proposed by Falcone in his Ph. D. Thesis [FALC 05]. This has been explored and succesfully accomplished in [NAVA 06].

#### 5.3.4 Concluding remarks.

The existence of EIWs in chains of electrically coupled CSRRs has been demonstrated both theoretically and experimentally. The duality between EIWs and previously reported MIWs has been discussed, and the ability of long CSRR chains to transport electromagnetic energy along many periods has been shown. A practical transducer between electromagnetic and EIWs in planar technology has been proposed and analyzed. Regarding practical applications, EIWs can be an alternative to MIWs for the guidance of electromagnetic energy, as well as for the design of couplers, delay lines and other planar devices, when electric couplings rather than magnetic couplings are imposed, or simply desired for the design.

Taking as a basis the resonators used to implement an EI waveguide, a further step has been given in the design of a UWB filter in microstrip technology. This filter can be improved by inserting CSRRs to reject the higher frequencies.

Electroinductive Waves were presented in *Article 5.3*

## 5.4 Comparison with Enhanced Transmission structures.

In this section are compared the fundamental features of the alternative structures presented in this chapter and the enhanced transmission structures explained along the text. In particular the CSRR-based metasurfaces are compared with single plate hole arrays, since both present a bandpass response. On the other hand, MIWs and EIWs are compared with stacked hole arrays.

### 5.4.1 Metasurfaces vs. Enhanced Transmission structures.

CSRR-based metasurfaces and a single plate metallic subwavelength hole arrays consist of a metallic screen with or without dielectric substrate with a bandpass response characteristic. Both can be considered as a special kind of Frequency Selective Surfaces.

From the structural details both are built with small particles (in terms of working wavelength) but with an important difference: CSRRs in the metasurface are self-resonant and the working frequency is chosen at this resonance; holes in subwavelength hole arrays are not resonant at the working frequency. Rather, the passband is directly related on a joint hole resonance, i.e. a structure resonance. This imposes a strong constraint in the number of illuminated holes, that must be large enough ( $31 \times 31$  has been proven to be a good number) in order to observe high transmittance. The passband in CSRR-Metasurfaces is well defined for an arbitrarily small number of particles. Related to this, periodicity only modifies the bandwidth of the passband: the more coarse the array is, the narrower the band, see Fig. 5.16. Periodicity in hole arrays is a fundamental parameter and must be tuned to be approximately equal to the working wavelength in order to obtain the band. Thus, close-packing is not possible in these structures, while in CSRR metasurfaces not only it is possible, but also it is associated with an increment in the bandwidth.

Both structures are very dependent on the metal thickness. The evanescent mode inside the hole of a subwavelength hole array decays rapidly, so the thickness must be in the order of  $\lambda/10$ . It is observed in metasurfaces that as the thickness is increased, the first (quasi-static) resonance frequency is shifted towards larger values, i.e. shorter wavelengths, and eventually happens at a frequency near the second (dynamic)

resonance. Then, the size of the CSRRs becomes larger in terms of wavelength, and the quasi-static operation is no longer present.

Regarding losses, subwavelength hole arrays present a higher level of transmission. Due to the self-resonant nature of individual resonators, where losses are important, losses in CSRR metasurfaces are moderately high.

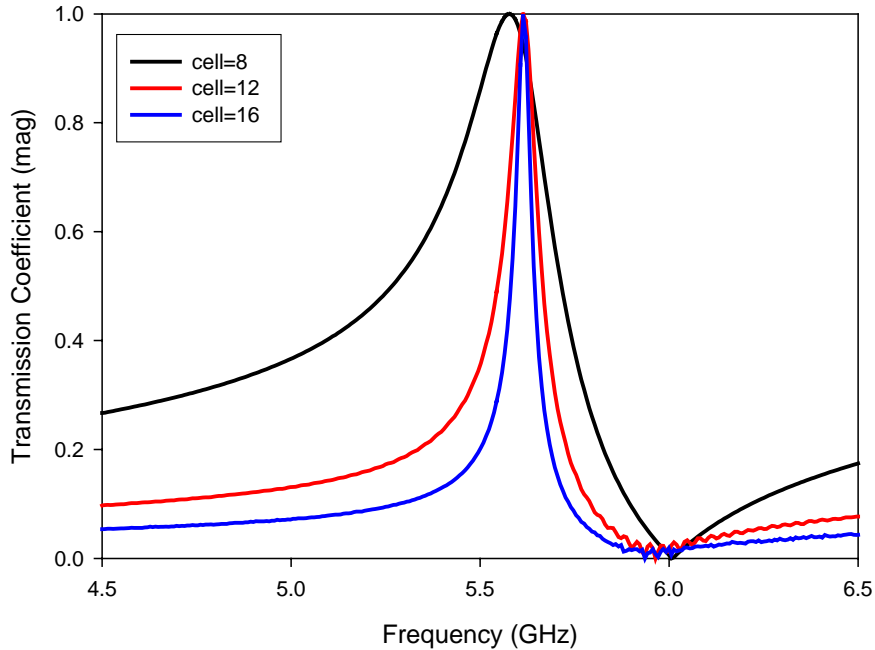


Fig. 5.16. Frequency response of a CSRR-based metasurface for different lattice constants. It is observed that as the periodicity is increased the band is made narrower.

Other relevant aspect is that since CSRRs are bianisotropic particles, metasurfaces can present cross-polarization, as discussed extensively in section 5.2. For certain applications this can be a desired effect, for example in polarization converters. In other circumstances it can be a disadvantage. This is a feature that subwavelength hole arrays do not show.

In summary, hole arrays are better in terms of losses but do not allow for close-packing and they need a large number of holes to work properly. Thus, they are very valuable in the design of narrowband filters at high frequencies like millimeter-waves, terahertz, infrared and visible spectrum, where a large size is not a problem. CSRR-based metasurfaces can be strongly close-packed although losses are relatively high.

These particles are ideal in the design of Frequency Selective Surfaces, polarization converters, etc., at low frequencies like microwaves.

#### 5.4.2 Electroinductive Waveguides vs. Stacked Hole Arrays.

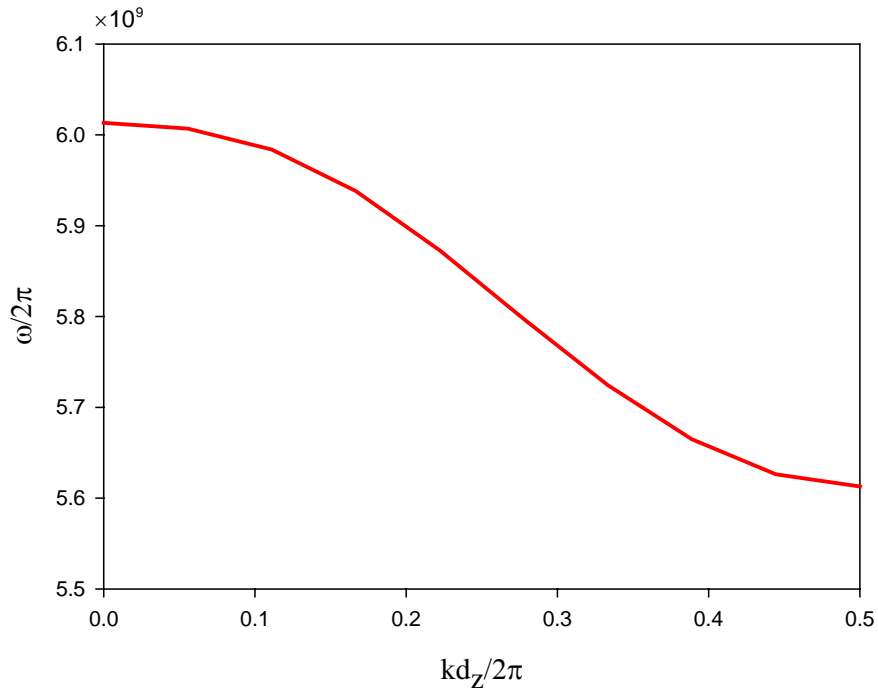


Fig. 5.17. Simulated dispersion diagram of a chain of CSRR-based metasurfaces with the next parameters:  $r_{ext} = 3.5$  mm and  $c = d = 0.4$  mm, with a lattice constant  $a = 8$  mm. The longitudinal periodicity is  $d_z = 5$  mm. The CSRRs are etched on a perfect electrically conducting layer with thickness  $t = 35$  microns. Correlative plates are separated by air.

Electroinductive waves arise in chains of electrically coupled resonators. Therefore, an EI waveguide can be constructed by just stacking CSRR-based metasurfaces. In that sense, the comparison between EI waveguides and Stacked Hole Arrays is essentially the same mentioned in the previous section. In short, EI waveguides constructed by stacking CSRR-based metasurfaces have the advantage of being easily close-packed, but at the cost of high losses. One important aspect mentioned in chapter 4 is that for any chain of electrically coupled resonators the first band has a negative slope. It has been simulated the case of stacked CSRR-based metasurfaces with the next

parameters:  $r_{ext} = 3.5$  mm and  $c = d = 0.4$  mm, with a lattice constant  $a = 8$  mm. The longitudinal periodicity has been fixed at  $d_z = 5$  mm. The CSRRs are etched on a perfect electrically conducting layer with thickness  $t = 35$  microns. It has been considered the easiest case of an air slab between correlative plates. The result of the dispersion diagram calculated with *CST Microwave Studio™* is shown in Fig. 5.17. It is clearly left-handed with a band that extends from 5.6 GHz to 6 GHz.

## **Chapter 6**

### **Conclusions And Future Work.**

---

---

## 6.1 Conclusions.

- The phenomenon of Enhanced Transmission also happens in the millimeter wave range, as it happened in optical frequencies. This experimental fact shows that this is a phenomenon mostly linked to the periodic structure regardless of the model used to describe the metal.
- The number of illuminated holes is a key parameter to observe the Enhanced Transmission band. Measurements in Fresnel zone show a weak band, and with the farfield illumination a good level is obtained.
- It has been shown that ET is mainly governed by one of the transversal periodicities, the one in the direction of the electric field (under normal incidence).
- The presence of dielectrics can produce a great field confinement and therefore a more efficient illumination of holes.
- Enhancement of transmission through a narrow slot on a metallic plane achieved by corrugating the metallic plane has been experimentally proven in the range of microwaves and millimeter waves. This result links the enhancement to the geometry of the metallic substrate rather than to the metallic model.
- It has been checked the ability to produce a strong beaming at broadside in the configuration of corrugations drilled on the output face.
- Several low-profile and all-metallic antenna prototypes have been designed and measured in the microwave range. The feeding is made by means of a waveguide. By changing the central (ideally) infinite slit to a finite slot several improvements can be done, fundamentally the thickness of the antenna can be reduced and a dual-band operation can be achieved. A great variety of farfield characteristics can be obtained by changing the number of corrugations.
- High gain antennas can be attained by using annular corrugations, the so-called Bull's-Eye antenna. Further improvements deal with the insertion of dielectric inside the corrugations and with changes in the shape of the

corrugations, for example sinusoidal profile.

- An artificial waveguide defined by introducing a set of parallel electric and magnetic conductors can be employed to analyze the diffraction problem of an incident plane wave normally to a sub-wavelength hole array. Evanescent higher order modes play a key role in the ET effect.
- Even more unexpected results appear if a periodic structure is made by stacking several of such plates: a left-handed metamaterial can be achieved by the periodic stacking of sub-wavelength hole array plates to form a photonic band-gap structure.
- The stack period with LH behavior can be made much smaller than the operating wavelength, and therefore it can be safely stated that the structure works in that dimension as an effective metamaterial.
- Simulation and experimental results presented show that left-handed propagation effects appearing in the band where EOT happens can be allowed or inhibited by a proper engineering of the band gap position of the photonic crystal made of stacked subwavelength hole-arrays.
- In the transition from LH to RH behavior a nearly zero slope band is observed, which can evidence a frozen mode propagation regime inside the structure.
- A simplified model based on inverse line equivalent circuit has been exposed to explain the LH and RH behavior.
- The stacked hole array structure can be engineered to construct prisms with anomalous behavior. Other geometries such as parabolic lenses can also be achieved.
- It has been seen that surfaces made by the periodical arrangement of Split-Ring Resonators (SRRs) and its complementary particle (CSRRs) illuminated by a plane wave show a high variety of cross-polarization effects. The analytical discussion based on the homogenization principle has been compared with the experimental results. It is able to catch the qualitative features in the response of the screens. The complementarity in the response of SRRs and CSRRs has been checked. Applications of the studied devices to

frequency selective surfaces, polarizers and polarization converters can be envisaged.

- The existence of electroinductive waves (EIWs) in chains of electrically coupled CSRRs has been demonstrated both theoretically and experimentally.
- The duality between EIWs and previously reported MIWs has been discussed, and the ability of long CSRR chains to transport electromagnetic energy along many periods has been shown.
- A practical transducer between electromagnetic and EIWs in planar technology has been proposed and analyzed.
- Regarding practical applications, EIWs can be an alternative to MIWs for the guidance of electromagnetic energy, as well as for the design of couplers, delay lines and other planar devices, when electric couplings rather than magnetic couplings are imposed, or simply desired for the design.
- Taking as a basis the resonators used to implement an EI waveguide, a further step has been given in the design of a UWB filter in microstrip technology. This filter can be improved by inserting CSRRs to reject the higher frequencies.
- A final word fundamentally related to the ET results presented here: The reported results have been achieved for the millimetre range, but similar results are expected to happen at optical frequencies since extraordinary transmission has been shown at optical frequencies and the kind of structure presented here will present low losses in higher frequency regime. The control of the EOT-LHM could lead to a new class of practical devices both in the microwave and in the optical range.

## 6.2 Future work.

- Theoretical study of the hole array using the Mode Matching Technique and development of a surface admittance equivalent circuit model.
- Refinement of the model used to explain the gain obtained with a hole array under normal incidence.
- Further experimental study of the double periodicity subwavelength hole

array samples with and without dielectric.

- Construction and measurement of the sinusoidal profile Bull's-Eye antenna in the microwave and millimeter wave ranges.
- Theoretical analysis of the corrugated antennas using the coupled mode theory to design prototypes of arbitrary (if possible) radiation characteristics.
- Theoretical study of the stacked hole array using the Mode Matching Technique and development of an equivalent circuit model.
- Study of the stacked hole array behavior under oblique incidence illumination.
- Study of the frozen mode regime in stacked hole arrays.
- Characterization of the effective permittivity and permeability of the stacked hole array metamaterial.
- Experimental exploration of the Left Handed behavior at optics wavelengths.
- Design, construction and measurement of SRR-based and CSRR-based Metasurfaces at millimeter wave and optics wavelengths.
- Construction and measurement of the planar ultra-wideband filter based on electroinductive waves.



# References

---

---

## A

- [ALU 03] A. Alu and N. Engheta, "Pairing an epsilon-negative slab with a mu-negative, slab: resonance, tunneling and transparency", *IEEE Transactions on Antennas and Propagation*, Vol. 51, pp. 2558-2271, (2003).
- [ALU 05] A. Alu and N. Engheta, "Evanescent growth and tunneling through stacks of frequency-selective surfaces", *IEEE Antennas and Wireless Propagation Letters*, Vol. 4, pp. 417-420, (2005).
- [AVRU 00] I Avrutsky, Y Zhao. V Kochergin, "Surface-plasmon-assisted resonant tunneling of light through a periodically corrugated thin metal film", *Optics Letters*, Vol. 25, pp. 595-597, (2000).

## B

- [BAEN 04] J.D. Baena, J. Bonache, F. Martin, R. Marques, F. Falcone, T. Lopetegi, M. Beruete, M.A.G. Laso, J. Garcia, F. Medina and M. Sorolla, "Modified and Complementary Split Ring Resonators for Metasurface and Metamaterial Design", *Proceedings of the 10th Bianisotropics Conference*, Ghent, Belgium, 168-171, (2004).
- [BAEN 05] J.D. Baena, J. Bonache, F. Martin, R. Marques, F. Falcone, T. Lopetegi, M.A.G. Laso, J. Garcia, I. Gil, M. Flores and M. Sorolla, "Equivalent Circuit Models for Split Ring Resonators and Complementary Split Ring Resonators Coupled to Planar Transmission Lines", *IEEE Transactions on Microwave Theory and Techniques*, Vol. 53, pp. 1451-1461, (2005).
- [BARN 03] W.L. Barnes, A. Dereux and T.W. Ebbesen, "Surface plasmon

- subwavelength optics," *Nature*, Vol. 424, pp. 824-829, (2003).
- [BARN 03b] W.L. Barnes, W.A. Murray, J. Dintinger, E. Devaux, and T.W. Ebbesen, "Surface Plasmon Polaritons and Their Role in the Enhanced Transmission of Light through Periodic Arrays of Subwavelength Holes in a Metal Film", *Physical Review Letters*, Vol. 92, No. 10, 107401-1-4, (2003).
- [BETH 44] H.A. Bethe, "Theory of Diffraction by Small Holes", *Physical Review*, Vol. 66, pp. 163-182, (1944).
- [BERU 04] M. Beruete, M. Sorolla, I. Campillo, J.S. Dolado, L. Martín-Moreno, J. Bravo-Abad and F.J. García-Vidal, "Enhanced millimeter-wave transmission through subwavelength hole arrays", *Optics Letters*, Vol. 29, pp. 2500-2502 (2004).
- [BERU 05] M. Beruete, I. Campillo, J. S. Dolado, M. Sorolla, V. Lomakin and E. Michielsen, "Phase Response of Cut-Off Metallic Hole Arrays", in *Proceedings IEEE AP-S Symposium/Radio Science Meeting*, Washington, (2005).
- [BERU 05b] M. Beruete, M. Sorolla, I. Campillo, J.S. Dolado, L. Martín-Moreno, J. Bravo-Abad and F.J. García-Vidal, "Enhanced millimeter wave transmission through quasioptical subwavelength perforated plates", *IEEE Transactions on Antennas and Propagation*, Vol. 53, pp. 1897-1902, (2005).
- [BERU 05c] M. Beruete, M. Sorolla, I. Campillo and J.S. Dolado, "Increase of the transmission in cut-off metallic hole arrays", *IEEE Microwave Wireless Components Letters*, Vol. 15, pp. 116-118, (2005).
- [BOUW 50] C.J. Bouwkamp. "On the diffraction of electromagnetic waves by small circular disks and holes", *Philips Res. Rep.*, Vol. 5, pp. 401-422, (1950).
- [BOUW 54] C.J. Bouwkamp. "Diffraction theory", *Rep. Prog. Phys.*, Vol. 17, pp. 35-100, (1954).
- [BRAV 04] J. Bravo-Abad, F.J. García-Vidal, L. Martín-Moreno, "Resonant Transmission of Light Through Finite Chains of Subwavelength Holes

in a Metallic Film", *Physical Review Letters*, Vol. 93, pp. 227401-1-4, (2004).

- [BRIL 46] L. Brillouin, *Wave Propagation in Periodic Structures*, Mc-Graw Hill (Dover), (1946).

## C

- [CAGL 06] H. Caglayan, I. Bulu, and E. Ozbay, "Beaming of electromagnetic waves emitted through a subwavelength annular aperture", *Journal of the Optical Society of America B*, Vol. 23, No. 3, pp. 419-422, (March 2006).
- [CAO 02] Q. Cao and P. Lalanne, "Negative role of surface plasmons in the transmission of metallic gratings with very narrow slits", *Physical Review Letters*, Vol. 88, pp. 7403, (2002).
- [CHEN 73] C.C. Chen, "Transmission of Microwave Through Perforated Flat Plates of Finite Thickness", *IEEE Transactions on Microwave Theory and Techniques*, Vol. MTT-21, No. 1, pp. 1-7, (January 1973).
- [COLL 69] R.E. Collin, F.J. Zucker, *Antenna Theory - Part 2*, McGraw-Hill, (December 1969).
- [COLL 91] R.E. Collin, *Field Theory of Guided Waves*, Wiley-Interscience-IEEE, 2<sup>nd</sup> Edition, (1991).
- [CORN 94] S. Cornbleet, *Microwave and Geometrical Optics*", Academic Press, (1994).
- [CUBU 03] E. Cubukcu, K. Aydin, E. Ozbay, S. Foteinopoulou and C. M. Soukoulis, "Electromagnetic waves - negative refraction by photonic crystals," *Nature*, Vol. 423, pp. 604-605 (2003).

## D

- [DOLL 06] G. Dolling, C. Enkrich, M. Wegener, C.M. Soukoulis, S. Linden, "Simultaneous Negative Phase and Group Velocity of Light in a Metamaterial", *Science*, Vol. 312, pp. 892-894, (12 May 2006).

## E

- [EBBE 98] T.W. Ebbesen, H.J. Lezec, H. Ghaemi, T. Thio, and P.A. Wolf, "Extraordinary optical transmission through sub-wavelength hole arrays", *Nature*, Vol. 391, pp. 667-669, (Feb. 1998).
- [ELLI 03] R.S. Elliot, *Antenna Theory and Design*", IEEE Press, (2003).
- [ENOC 03] S. Enoch, G. Tayeb and B. Gralak, "The Richness of the Dispersion Relation of Electromagnetic Bandgap Materials", *IEEE Transactions on Antennas and Propagation*, Vol. 51, No. 10, pp. 2659-2666, (October 2003)

## F

- [FALC 04] F. Falcone, T. Lopetegi, M.A.G. Laso, J.D. Baena, J. Bonache, M. Beruete, R. Marqués, F. Martín and M. Sorolla, "Babinet principle applied to metasurface and metamaterial design," *Physical Review Letters*, Vol. 93, pp. 197401-1-4, (2004).
- [FALC 05] F. Falcone, "Synthesis and applications of Microwave Metamaterials in Planar Circuit Technology: From Electromagnetic Bandgaps to Left-Handed Materials", *Ph.D. Thesis*, (2005).
- [FREI 04] M.J. Freire, R. Marqués, F. Medina, M.A.G. Laso, F. Martín, "Planar magnetoinductive wave transducers: Theory and applications", *Applied Physics Letters*, Vol. 85, pp. 4439-4441, (2004).

## G

- [GARC 03] F.J. García-Vidal, H.J. Lezec, T.W. Ebbesen, L. Martín-Moreno, "Multiple Paths to Enhance Optical Transmission through a Single Subwavelength Slit", *Physical Review Letters*, Vol. 90, 213901, (2003).
- [GAY 02] Ph. Gay-Balmaz and O.J.F. Martin, "Electromagnetic resonances in individual and coupled split-ring resonators", *Journal of Applied Physics*, Vol. 92, pp. 2929-2936, (2002).

- [GHAE 98] H.F. Ghaemi, T. Thio, D.E. Grupp, T.W. Ebbesen, H.J. Lezec, "Surface Plasmons Enhance Optical Transmission Through Sub-wavelength Holes", *Physical Review B*, Vol. 58, 6779, (1998).
- [GOLD 98] P.F. Goldsmith, *Quasioptical Systems-Gaussian Beam, Quasioptical Propagation, and Applications*, IEE Press, (1998).
- [GOME 03] G. Gomez-Santos, "Universal features of the time evolution of evanescent modes in a left-handed perfect lens," *Physical Review Letters*, Vol. 90, pp. 077401-1-4 (2003).
- [GRIG 05] A.N. Grigorenko, , A.K. Geim, H.F. Gleeson, Y. Zhang, A.A. Firsov, I.Y. Khrushchev and J. Petrovic, "Nanofabricated media with negative permeability at visible frequencies", *Nature*, Vol. 438, pp. 335-338 (2005).
- [GRUP 99] D.E. Grupp, H.J. Lezec, T Thio and T.W. Ebbesen, "Beyond the Bethe Limit: Tunable Enhanced Light Transmission Through a Single Subwavelength Aperture", *Advanced Materials*, Vol. 11, pp. 860, (1999).
- [GRUP 00] D.E. Grupp, H.J. Lezec, T.W. Ebbesen, K.M. Pellerin, and T. Thio, "Crucial role of metal surface in enhanced transmission through subwavelength apertures", *Appl. Phys. Lett.*, Vol. 77, pp. 1569-1571, (2000).

## H

- [HESS 65] A. Hessel and A.A. Oliner, "A new theory of Wood 's anomalies on optical gratings", *Applied Optics*, Vol. 4, No. 10, pp. 1275-1297, (1965).
- [HIBB 01] A.P. Hibbins, J.R. Sambles, C.R. Lawrence, D.M. Robinson, "Remarkable transmission of microwaves through a wall of metallic bricks.", *Applied Physics Letters*, Vol. 79, pp. 2844, (2001).
- [HIBB 02] A.P. Hibbins, J.R. Sambles, and C.R. Lawrence, "Gratingless enhanced microwave transmission through a subwavelength aperture in a thick metal plate", *Applied Physics Letters*, Vol. 81, pp. 4461-4463, (Dec. 2002).

- [HRIS 00] H.D. Hristov, *Fresnel Zones in wireless links, zone plate lenses and antennas*, Artech House, (2000).

## I

- [IEEE 79] IEEE Standard Test Procedures for Antennas, Dec. 1979. ANSI/IEEE Std 149-(1979).
- [ISHI 91] A. Ishimaru, *Electromagnetic Wave Propagation, Radiation, and Scattering*, Prentice Hall, (1991).

## J

- [JOAN 95] J.D. Joannopoulos, R.D. Meade, and J.N. Winn, *Photonic Crystals: Molding the Flow of Light*, Princeton, NJ: Princeton Univ. Press, (1995).
- [JOAN 97] J.D. Joannopoulos, P.R. Villeneuve and S. Fan, "Photonic crystals: putting a new twist on light.", *Nature*, Vol. 386, pp. 143-149, (1997).
- [JOHN 87] S. John, "Strong localization of photons in certain disordered dielectric superlattices", *Physical Review Letters*, Vol. 58, pp. 2486- 2489, (1987).

## K

- [KATS 60] B.Z. Katsenelenbaum, "Problem of normal incidence of a plane electromagnetic wave on a periodic boundary separating two dielectrics", *Radio Engineering and Electronics*, Vol. 5, No. 12, pp. 77-82, (1960).
- [KATS 98] B.Z. Katsenelenbaum, L. Mercader del Río, M. Pereyaslavets, M. Sorolla Ayza, and M. Thumm, *Theory of Nonuniform Waveguides - The cross-section method*, The Institution of Electrical Engineers, IEE Electromagnetic Waves Series, London, (1998).
- [KEIL 81] F. Keilmann, "Infrared high-pass filter with high contrast", *International Journal of Infrared and Millimeter Waves*, Vol. 2, No.2, pp. 259-272, (1981).

- [KIM 99] T.J. Kim, T. Thio, T.W. Ebbesen, D.E. Grupp and H.J. Lezec, "Control of Optical Transmission Through Metals Perforated with Subwavelength Hole Arrays", *Optics Letters*, Vol. 24, 256, (1999).
- [KOBR 04] M.J. Kobrinsky, B.A. Block, J.-F. Zheng, B.C. Barnett, E. Mohammed, M. Reshotko, F. Robertson, S. List, I. Young, and K. Cadien, "On-chip optical interconnects", *Intel Technology Journal*, Vol. 8, No.2, pp. 129-143, (2004).
- [KOSA 98] H. Kosaka, T. Kawashima, A. Tomita, M. Notomi, T. Tamamura, T. Sato, and S. Kawakami, "Superprism phenomena in photonic crystals", *Physical Review B*, Vol. 58, pp. 10096-10099, (1998).
- [KRAU 02] J.D. Krauss, R.J. Marhefka, *Antennas: For All Applications*, Third Edition, McGraw-Hill, (2002).
- [KRIS 01] A. Krishnan, T. Thio, T.J. Kim, H.J. Lezec, T.W. Ebbesen, P.A Wolff, J.B. Pendry, L. Martín-Moreno, F.J. García-Vidal, "Evanesciently coupled resonance in surface plasmon enhanced transmission", *Optics Communications*, Vol. 200, 1, (2001).

**L**

- [LEZE 02] H.J. Lezec, A. Degiron, E. Deveaux, R.A. Linke, L. Martín-Moreno, F.J. García-Vidal, T.W. Ebbesen, "Beaming light from a sub-wavelength aperture", *Science*, Vol. 97, pp. 820-822, (2002).
- [LOCK 05] M.J. Lockyear, A.P. Hibbins, J.R. Sambles and C.R. Lawrence "Enhanced microwave transmission through a single subwavelength aperture surrounded by concentric grooves", *Journal of the Optical Society of America A*, Vol. 7, pp. S152-S158, (2005).
- [LOMA 04] V. Lomakin, N.W. Chen, S. Q. Li, and E. Michielssen, "Enhanced transmission through two-period arrays of sub-wavelength holes", *IEEE Microwave and Wireless Components Letters*, Vol. 14, No. 7, pp. 355-357, (2004).
- [LOMA 05] V. Lomakin and E. Michielssen, "Enhanced transmission through

metallic plates perforated by arrays of subwavelength holes and sandwiched in between dielectric slabs", *Physical Review B*, Vol. 71, pp. 235117-1-10, (2005).

## M

- [MARQ 02] R. Marqués, F. Medina, R.R. El-Idrissi, "Role of Bianisotropy in Negative Permeability and Left-Handed Metamaterials", *Physical Review B*, Vol. 65, pp. 144440 1-6, (April 2002).
- [MARQ 03] R. Marqués, F. Mesa, J. Martel and F. Medina, "Comparative Analysis of Edge- and Broadside- Coupled Split Ring Resonators for Metamaterial Design – Theory and Experiments", *IEEE Transactions on Antennas and Propagation*, Vol. 51, No. 10, pp. 2572-2581, (2003).
- [MART 01] L. Martín-Moreno, F.J. García-Vidal, H.J. Lezec, K.M. Pellerin, T. Thio, J.B. Pendry, and T.W. Ebbesen, "Theory of Extraordinary Optical Transmission through Subwavelength Hole Arrays", *Physical Review Letters*, vol. 86, pp. 1114-1117, (Feb. 2001).
- [MUNK 00] B.A. Munk, *Frequency selective surfaces: theory and design*, J.Wiley, US, 2000.

## N

- [NAVA 06] M. Navarro, "Efectos de Interacción EBG / Metamateriales en Tecnología Plana de Microondas", *Final Degree Project*, (2006)
- [NODA 00] S. Noda, A. Chutinan and M. Imada, "Trapping and emission of photons by a single defect in a photonic bandgap structure," *Nature*, vol. 407, pp. 608-610 (2000).
- [NOTO 02] M. Notomi, "Negative refraction in photonic crystals," *Opt. Quantum Electron.*, Vol. 34, pp. 133-143, (2002).

**O**

- [OLIN 63] A.A. Oliner, *Radiating Periodic Structures: Analysis in Terms of  $k$  vs.  $\beta$  Diagrams*, Polytechnic Institute of Brooklyn, Graduate Center, Electrophysics Department, Short Course on "Microwave Field and Network Techniques", Tuesday, June 4, (1963).
- [OLIN 03] A.A. Oliner and D.R. Jackson, "Leaky surface-plasmon theory for dramatically enhanced transmission through a subwavelength aperture, part I: Basic features", in *Proc. IEEE AP-S Symp. Radio Science Meeting*, Columbus, OH, (2003).
- [OZBA 06] E. Ozbay, "Plasmonics: Merging Photonics and Electronics at Nanoscale Dimensions", *Science*, vol. 311, pp.189-193, (Jan. 2006).

**P**

- [PEND 96] J.B. Pendry, A.J. Holden, W.J. Stewart and I. Youngs, "Extremely low frequency plasmons in metallic mesostructures", *Physical Review Letters*, Vol. 76, pp. 4773-4776, (1996).
- [PEND 99] J.B. Pendry, A.J. Holden, D.J. Robbins, W.J. Stewart, "Magnetism from Conductors and Enhanced Nonlinear Phenomena", *IEEE Transactions on Microwave Theory and Techniques*, Vol. 47, No.11, pp.2075-2084, (November 1999).
- [PEND 00] J.B. Pendry, "Negative Refraction Makes a Perfect Lens", *Physical Review Letters*, vol. 85, No. 18, pp. 3966-3969, (October 2000).
- [PEND 04] J.B. Pendry, L. Martín-Moreno and F.J. García-Vidal, "Mimicking surface plasmons with structured surfaces", *Science*, Vol. 305, pp. 847-848, (2004).
- [PEND 05] D.R. Smith, J.B. Pendry and M.C.K. Wiltshire, "Metamaterials and negative refractive index", *Science*, Vol. 305, pp. 788-792, (2005).
- [POPO 00] E. Popov, M. Neviere, S. Enoch, and R. Reinisch, "Theory of light transmission through subwavelength periodic hole arrays", *Physical*

*Review B*, Vol. 62, pp. 16 100–16 108, (Dec. 2000).

- [PORT 99] J.A. Porto, F.J. García-Vidal and J.B. Pendry, "Transmission resonances on metallic gratings with very narrow slits", *Physical Review Letters*, Vol. 83, pp. 2845–2848, (1999).

## Q

- [QIU 05] M. Qiu, "Photonic band structures for surface waves on structured metal surfaces", *Optics Express*, Vol. 13, pp. 7583-7588 (2005).

## R

- [RAMO 94] S. Ramo, J.R. Whinnery and T. Van Duzer, *Fields and Waves in Communication Electronics*, Third Edition, John Wiley & Sons, Inc, New York, (1994).
- [RAYL 07] Lord Rayleigh, "On the dynamical theory of gratings", *Proc. R. Soc. London A*, Vol. 79, pp. 399-416, (1907); "Note on the remarkable case of diffraction spectra described by Prof. Wood", *Philos Mag.*, Vol. 14, 60, (1907).
- [RHOA 82] C.M. Rhoads, E.K. Damon, and B.A. Munk, "Mid-infrared filters using conducting elements", *Applied Optics*, Vol. 21, pp. 2814-2816, (1982).
- [ROBI 60] L.A. Robinson, "Electrical properties of metal loaded radomes", *Wright Air Develop. Div. Rep. WADD-TR-60-84* (ASTIA no.249-410) February, (1960).

## S

- [SAMB 05] R. Sambles, "Gold loses its lustre", *Nature*, Vol. 438, pp. 295-296, (2005).
- [SARR 03] M. Sarrazin, J.P. Vigneron and J.M. Vigoureux, "Role of Wood anomalies in optical properties of thin metallic films with a bidimensional array of subwavelength holes", *Physical Review B*, Vol.

- 67, pp. 085415, (2003).
- [SCHW 68] J. Schwinger and D.E. Saxon, *Discontinuities in Waveguides, Notes on Lectures by Julian Schwinger*, Gordon and Breach, New York, (1968)
- [SENA 05] S. Sena, Akarca-Biyikli, I. Bulu and E. Ozbay, "Resonant excitation of surface plasmons in one-dimensional metallic grating structures at microwave frequencies", *Journal of the Optical Society of America A*, Vol. 7, pp. S159-S164, (2005).
- [SHAM 02] E. Shamonina, V.A. Kalinin, K.H. Ringhofer and L. Solymar, "Magneto-inductive waveguide", *Electronics Letters*, Vol. 38, pp. 371-373, (2002).
- [SHAM 02b] E. Shamonina, V.A. Kalinin, K.H. Ringhofer and L. Solymar, "Properties of a metamaterial element: analytical solutions and numerical simulations for a Singly Split Double Ring", *Journal of Applied Physics.*, Vol. 92, pp. 6252-6261, (2002).
- [SHAM 04] E. Shamonina and L. Solymar, "Magneto-inductive waves supported by metamaterial elements: components for a one-dimensional waveguide", *Journal Physics D*, Vol. 37, pp. 362-367, (2004).
- [SHEL 01] R.A. Shelby, D.R. Smith and S. Schultz, "Experimental verification of a negative index of refraction", *Science*, Vol. 292, pp. 77-79, (2001).
- [SMIT 00] D.R. Smith, W.J. Padilla, D.C. Vier, S.C. Nemat-Nasser, S. Schultz, "Composite Medium with Simultaneously Negative Permeability and Permittivity", *Physical Review Letters*, Vol. 84, No. 18, pp. 4184-4187, (May 2000).
- [SMIT 04] D.R. Smith, P.M. Rye, J.J. Mock, D.C. Vier and A.F. Starr, "Enhanced Diffraction from a grating on the Surface of a Negative Index Material", *Physical Review Letters*, Vol. 93, No. 13, pp. 137405-1-4, (September 2003).
- [SMIT 05] D.R. Smith, "How to build a superlens", *Science*, Vol. 308, pp. 502-503, (2005).

## T

- [TAKA 01] Y Takakura, "Optical resonance in a narrow slit in a thick metallic screen", *Physical Review Letters*, Vol. 86, pp. 5601, (2001).
- [THIO 01] T Thio, K.M. Pellerin, R.A. Linke, T.W. Ebbesen, H.J. Lezec, "Enhanced Light Transmission through a Single Sub-Wavelength Aperture", *Optics Letters*, Vol. 26, pp. 1972, (2001).
- [THIO 02] T Thio, H.J. Lezec, T.W. Ebbesen, K.M. Pellerin, G.D. Lewen, A. Nahata, R.A. Linke, "Giant optical transmission of sub-wavelength apertures: physics and applications", *Nanotechnology*, Vol. 13, pp. 429, (2002)
- [TREA 99] M.M.J. Treacy, "Dynamical diffraction in metallic optical gratings", *Applied Physics Letters*, Vol. 75, No. 5, pp. 606-608, (1999).
- [TREA 02] M.M.J. Treacy, "Dynamical diffraction explanation of the anomalous transmission of light through metallic gratings", *Physical Review B*, Vol. 66, pp. 195105, (2002).

## U

- [ULRI 67] R. Ulrich, "Far-infrared properties of metallic mesh and its complementary structure", *Infrared Physics*, Vol. 7, pp. 37-55, (1967)

## V

- [VESE 68] V.G. Veselago, "The Electrodynamics of Substances with Simultaneously Negative Values of  $\epsilon$  and  $\mu$ ", *Soviet Physics Uspekhi*, Vol. 10, No. 4, pp. 509-514, (January-February 1968).
- [VIGO 01] J.M. Vigoureux, "Analysis of the Ebbesen experiment in the light of evanescent short range diffraction", *Optics Communications*, Vol. 198, pp. 257, (2001).

**W**

- [WARR 90] B.E. Warren, *X-Ray Diffraction*, Dover Publications Inc., 1990.
- [WENT 00] H.E. Went, A.P. Hibbins, J.R. Sambles, C.R. Lawrence, A.P. Crick, "Selective transmission through very deep zero-order metallic gratings at microwave frequencies", *Applied Physics Letters*, Vol. 77, pp. 2789, (2000).
- [WENT 01] H.E. Went and J.R. Sambles, "Resonantly coupled surface plasmon polaritons in the grooves of very deep highly blazed zero order metallic gratings at microwave frequencies.", *Applied Physics Letters*, Vol. 79, pp. 575, (2001).
- [WILT 03] M.C.K. Wiltshire, E. Shamonina, I. R. Young, and L. Solymar, "Dispersion characteristics of magneto-inductive waves: comparison between theory and experiment", *Electronics Letters*, Vol. 39, pp. 215-217, (2003).
- [WOOD 02] R.W. Wood, "On a remarkable case of uneven distribution of light in a diffraction grating spectrum", *Phil. Mag.*, Vol. 4, pp. 396-408, (1902)
- [WU 95] T.K.Wu, *Frequency selective surface and grid array*, J.Wiley, US, 1995.

**Y**

- [YABL 87] E. Yablonovitch, "Inhibited Spontaneous Emission in Solid-State Physics and Electronics", *Physical Review Letters*, vol. 58, No. 20, pp. 2059-2062, May 1987.
- [YABL 93] E. Yablonovitch, "Photonic Band-Gap Crystals", *J. Phys. Condens. Matter*, Vol. 5, pp. 2443-2460, (1993).
- [YABL 93b] E. Yablonovitch, "Photonic Band-Gap Structures", *Journal of the Optical Society of America B*, vol. 10, No. 2, pp. 283-295, (February 1993).
- [YE 05] Y-H Ye and J-Y Zhang, "Enhanced light transmission through cascaded metal films perforated with periodic hole arrays", *Optics*

*Letters*, Vol. 30, pp. 1521-1523 (2005).

- [YANG 02] F Yang and J.R. Sambles, "Resonant transmission of microwaves through a narrow metallic slit.", *Physical Review Letters*, Vol. 89, 63901, (2002).

## Z

- [ZHAN 05] S. Zhang, W. Fan, N. C. Panoiu, K.J. Malloy, R.M. Osgood, and S.R.J. Brueck, "Experimental Demonstration of Near-Infrared Negative-Index Metamaterials", *Physical Review Letters*, Vol. 95, pp. 137404-1-4, 25 September 2005.
- [ZHAN 05b] S. Zhang, W. Fan, K.J. Malloy and S.R.J. Brueck, "Near-infrared double negative metamaterials", *Optics Express*, Vol. 13, No. 13, pp. 4922-4930, 27 June 2005.
- [ZHAO 03] T. Zhao, D.R. Jackson, J.T. Williams, and A.A. Oliner, "Leaky-wave theory for enhanced transmission through subwavelength apertures, part II: Leaky-wave antenna model", in *Proc. IEEE AP-S Symp. Radio Science Meeting*, Columbus, OH, (2003).

# Author's Publications

---

---

## Journal Papers:

- **M. Beruete**, M. Sorolla, I. Campillo, "Inhibiting Left-Handed Wave Propagation by a Band Gap of Stacked Cut-Off Metallic Hole Arrays.", *IEEE - Microwave and Wireless Components Letters*, accepted for publication.
- **M. Beruete**, M. Sorolla, I. Campillo, "Molding Left- or Right-Handed Metamaterials by Stacked Cut-Off Metallic Hole Arrays.", *IEEE - Transactions on antennas and propagation*, submitted for publication.
- **M. Beruete**, I. Campillo, J.S. Dolado, J.E. Rodríguez-Seco, E. Perea, F. Falcone, and M. Sorolla, "Very Low Profile and Dielectric Loaded Feeder Antenna.", *IEEE - Antennas and Wireless Propagation Letters*, submitted for publication.
- **Miguel Beruete**, Mario Sorolla, Igor Campillo, "Left-handed extraordinary optical transmission through a photonic crystal of subwavelength hole arrays", *Optics Express*, Vol. 14, No. 12, pp. 5445-5455, (Jun 2006).
- E. Jarauta, M. A. G. Laso, T. Lopetegui, F. Falcone, **M. Beruete**, J. D. Baena, A. Marcotegui, J. Bonache, J. García, R. Marqués, F. Martín, "Novel microstrip backward coupler with metamaterial cells for fully planar fabrication techniques", *Microwave and Optical Technology Letters*, Vol. 48, No. 6, pp. 1205-1209, (Jun. 2006).
- **M. Beruete**, M. Sorolla, R. Marqués, J.D. Baena, M.J. Freire, "Resonance and Cross-Polarization Effects in Conventional and Complementary Split Ring Resonator Periodic Screens", *Electromagnetics*, Vol. 26, No. 3-4, pp 247-260, (Apr. 2006).
- **M. Beruete**, M.J. Freire, R. Marqués, F. Falcone, J. D. Baena, "Electroinductive waves in chains of complementary metamaterial elements", *Applied Physics*

*Letters*, Vol. 88, pp. 083503-1-3, (Feb. 2006).

- **M. Beruete**, I. Campillo, J.S. Dolado, J.E. Rodríguez-Seco, E. Perea, F. Falcone, M. Sorolla, "Dual Band Low-Profile Corrugated Feeder Antenna.", *IEEE - Transactions on antennas and propagation*, Vol. 54, No. 2, pp. 340-350, (Feb. 2006).
- **M. Beruete**, I. Campillo, J.S. Dolado, J.E. Rodríguez-Seco, E. Perea, F. Falcone, M. Sorolla, "Low-Profile Corrugated Feeder Antenna.", *IEEE - Antennas and Wireless Propagation Letters*, Vol. 4, pp. 378-380, (2005).
- A. Gastón, **M. Beruete**, F. Meseguer, M. Sorolla, and J. Sevilla, "Strong Microwave Second Order Rejection Band In Opal-like Structures", *Microwave and Optical Technology Letters*, Vol. 47, No. 5, pp. 472-475, (Dic. 2005).
- **M. Beruete**, I. Campillo, J.S. Dolado, J.E. Rodríguez-Seco, E. Perea, F. Falcone, M. Sorolla, "Very Low-Profile "Bull's-Eye" Feeder Antenna.", *IEEE - Antennas and Wireless Propagation Letters*, Vol. 4, pp. 365-368, (2005).
- **M. Beruete**, M. Sorolla, I. Campillo, J.S. Dolado, L. Martín-Moreno, and F. J. García-Vidal, "Enhanced millimeter wave transmission through quasioptical subwavelength perforated plates", *IEEE - Transactions on antennas and propagation*, Vol. 53, No.6, pp. 1897-1903, (Jun. 2005).
- N. Ortiz, J.D. Baena, **M. Beruete**, F. Falcone, M.A.G.Laso, T. Lopetegi, R. Marqués, F. Martín, J.García-García and M. Sorolla, "Complementary Split Ring Resonator for Compact Waveguide Filter Design", *Microwave and Optical Technology Letters*, Vol. 46, No. 1, pp. 88-92, (May. 2005).
- **M. Beruete**, M. Sorolla, I. Campillo, J.S. Dolado, "Subwavelength Slotted Corrugated Plate with Enhanced Quasioptical Millimeter Wave Transmission.", *IEEE - Microwave and Wireless Components Letters*, Vol. 15, No.4, pp. 286-288, (Abr. 2005).
- **M. Beruete**, M. Sorolla, I. Campillo, J.S. Dolado, "Increase of the Transmission in Cut-Off Metallic Hole Arrays.", *IEEE - Microwave and Wireless Components Letters*, Vol. 15, No. 2, pp. 116-118, (Feb. 2005).
- R. Marqués, J.D. Baena, **M. Beruete**, F. Falcone, T. Lopetegi, and M. Sorolla, F. Martín and J. Garcia, "Ab Initio Analysis of Frequency Selective Surfaces

based on Conventional and Complementary Split Rings Resonators", *Journal of the Optical Society of America A*, Vol. 7, No. 2, pp. S38-S43, (Feb 2005).

- **M. Beruete**, I. Campillo, J.S. Dolado, J.E. Rodríguez-Seco, E. Perea, M. Sorolla, "Enhanced Microwave Transmission and Beaming using a Subwavelength Slot in Corrugated Plate.", *IEEE - Antennas and Wireless Propagation Letters*, Vol. 3, No. 16, pp. 328-331, (Dic. 2004).
- F. Falcone, T. Lopetegi, M.A.G. Laso, J.D. Baena, J. Bonache, **M. Beruete**, R. Marqués, F. Martín, and M. Sorolla, "Babinet principle applied to metasurface and metamaterial design", *Physical Review Letters*, Vol. 93, No. 19, pp. 197401-1-4, (Nov. 2004).
- **M. Beruete**, M. Sorolla, I. Campillo, J.S. Dolado, L. Martín-Moreno, J. Bravo-Abad and F.J. García-Vidal, "Enhanced millimeter wave transmission through subwavelength hole arrays.", *Optics Letters*, Vol. 29, No. 21, pp. 2500-2502, (Nov. 2004).

## International Conferences:

- **M. Beruete**, M. Sorolla-Ayza, I. Campillo, M. Navarro, F. Falcone, M.A.G. Laso, "Enhanced transmission in photonic crystal of hole arrays", Conference Digest of the *Joint 31st International Conference on Infrared and Millimeter Waves and 14th International Conference on Terahertz Electronics*, September 18-22, 2006, Shanghai, China.
- **M. Beruete**, M. Sorolla, I. Campillo, "Waveguiding By Dichroic Filters Metamaterial", Proceedings of the *Progress In Electromagnetics Research Symposium (PIERS 2006)*, Aug. 2006, Tokyo, Japan.
- F. Falcone, M. Navarro, **M. Beruete**, T. Lopetegi, M.A. Gómez-Laso and M. Sorolla, "Topological considerations in the frequency response of SRR loaded microstrip line", Proceedings of the *Progress In Electromagnetics Research Symposium (PIERS 2006)*, Aug. 2006, Tokyo, Japan.
- A. Andueza, **M. Beruete**, M. Sorolla and J. Sevilla, "Study of the

Electromagnetic Behaviour of non Compact Single-layers of Dielectric Spheres”, Proceedings of the *International Workshop on Physics of Photonic Crystals and Metamaterials*, Jun. 2006, Brussels, Belgium.

- **M. Beruete**, M. Laso, M. Navarro, F. Falcone, M. Sorolla, I. Campillo, “Stacked hole arrays filters metamaterial”, Proceedings of the *International Workshop on Physics of Photonic Crystals and Metamaterials*, Jun. 2006, Brussels, Belgium.
- **Miguel Beruete**, I. Campillo, J. S. Dolado, J.E. Rodríguez-Seco, E. Perea, Francisco Falcone, Mario Sorolla, “Low profile antenna feeders based of enhanced microwave transmission through a narrow slot on a corrugated plane”, Proceedings of the *Microwave Technology and Techniques Workshop*, May. 2006, ESTEC, Noordwijk, The Netherlands.
- Francisco Falcone, Miguel Navarro, **Miguel Beruete**, Mario Sorolla, “Left-handed microstrip line based on composite SRR-EBG topology”, Proceedings of the *Microwave Technology and Techniques Workshop*, May. 2006, ESTEC, Noordwijk, The Netherlands.
- **M. Beruete**, M. Sorolla, I. Campillo, “Electromagnetic Band Gap made of stacked hole arrays and metallic disks”, Proceedings of the *13th IEEE Mediterranean Electrotechnical Conference, MELECON 2006*, May. 2006, Málaga, Spain.
- M. Navarro, F. Falcone, T. Lopetegi, M.A.Gómez-Laso, **M. Beruete**, I. Arnedo, E. Jarauta, J.A. Marcotegui and M. Sorolla, “Interaction Effects between Electromagnetic Bandgap Structures and Split Ring Resonators in Microstrip Technology”, Proceedings of the *13th IEEE Mediterranean Electrotechnical Conference, MELECON 2006*, May. 2006, Málaga, Spain.
- **M. Beruete**, I. Campillo, J. S. Dolado, J.E. Rodríguez-Seco, E. Perea, F. Falcone, M. Sorolla, “Experimental realization of a Low Profile metallic Bull’s Eye Antenna”, Abstracts of the *Progress In Electromagnetics Research Symposium (PIERS 2006)*, par. 350, Mar. 2006, Cambridge (MA), USA.
- **M. Beruete**, M. J. Freire, R. Marqués, F. Falcone, J.D.Baena, “Electroinductive waves on chains of resonators”, Abstracts of the *Progress In Electromagnetics Research Symposium (PIERS 2006)*, pag. 264, Mar. 2006, Cambridge (MA), USA.

- **M. Beruete**, M. Sorolla, I. Campillo, "Photonic crystal made of dichroic filters", Abstracts of the *Progress In Electromagnetics Research Symposium (PIERS 2006)*, pag. 275, Mar. 2006, Cambridge (MA), USA.
- Francisco Falcone, **Miguel Beruete** and Mario Sorolla, "Simulation of planar metamaterial devices and metasurfaces employing Split Ring Resonators (SRR) and Complementary Split Ring Resonators (CSRR)", Presented at the *European User Group Meeting CST-UGM 2006*, Mar. 2006, Boppard, Germany.
- **Miguel Beruete**, Francisco Falcone, Mario Sorolla, "Frequency response and dispersion diagrams of single and stacked hole arrays and metallic disks", Presented at the *European User Group Meeting CST-UGM 2006*, Mar. 2006, Boppard, Germany.
- **M. Beruete**, I. Campillo, J. S. Dolado, J.E. Rodríguez-Seco, E. Perea, M. Sorolla, "Enhanced Microwave Transmission Using a Subwavelength Slot in Corrugated Plate", *Proceedings of the IEEE -Antennas and Propagation Society International Symposium, AP/S-2005*, pp. 14-17, Jun. 2005, Washington, USA.
- **M. Beruete**, I. Campillo, J. S. Dolado, M. Sorolla, V. Lomakin, E. Michielsen, "Phase Response of Cut-Off Metallic Hole Arrays", *Proceedings of the IEEE - Antennas and Propagation Society International Symposium*, pp. 734-737, Jun. 2005, Washington, USA.
- **M. Beruete**, R. Marqués, J.D. Baena, M. Sorolla, "Resonance and Cross-Polarization Effects in Conventional and Complementary Split Ring Resonators Periodic Screens", *Proceedings of the IEEE -Antennas and Propagation Society International Symposium*, pp. 794-797, Jun. 2005, Washington, USA.
- Francisco Falcone, **Miguel Beruete**, Juan Baena, Miguel Angel Gómez Laso, Txema Lopetegui, Jordi Bonache, Ferran Martin, Ricardo Marques, Mario Sorolla, "Coupling effects in Left-Handed structures in Coplanar Waveguide Technology", Presented at the *Donostia International Physics Center (DIPC) Workshop on Metamaterials for Microwave and Optical Technologies*, Jul. 2005, San Sebastián, Spain.
- **Miguel Beruete**, Francisco Falcone, Juan Baena, Ricardo Marqués, Mario Sorolla, "Frequency Selective Surfaces based on Complementary Spiral

Resonators", Presented at the *Donostia International Physics Center (DIPC) Workshop on Metamaterials for Microwave and Optical Technologies*, Jul. 2005, San Sebastián, Spain.

- **M. Beruete**, M. J. Freire, R. Marqués, J. D. Baena and M. Sorolla, "Electroinductive wave propagation in CSRR arrays", *Proceedings of the Photonic and Electromagnetic Crystals Symposium (PECS VI)*, Jun. 2005, Aghia Pelaghia, Crete, Greece.
- **M. Beruete**, J. D. Baena, F. Falcone, I. Campillo, J. S. Dolado, T. Lopetegi, M.A.G. Laso, J. Bonache, J. García-García, A. Marcotegui, F. Martín, R. Marqués, and M. Sorolla, "Subwavelength Hole Arrays and Split Ring Resonators Based Metasurfaces for Frequency Selective Surfaces", *Conference Digest of the 2004 Joint 29th International Conference on Infrared and Millimeter Waves, 2004 and 12th International Conference on Terahertz Electronics, 2004*, pp. 97-98, Oct. 2004, Karlsruhe, Germany.
- E. Jarauta, M.A.G. Laso, T. Lopetegi, F. Falcone, **M. Beruete**, J.D. Baena, J. Bonache, I. Gil, J. García-García, A. Marcotegui, F. Martín, R. Marqués, and M. Sorolla, "Metamaterial Microstrip Backward Couplers for Fully Planar Fabrication Techniques", *Conference Digest of the 2004 Joint 29th International Conference on Infrared and Millimeter Waves, 2004 and 12th International Conference on Terahertz Electronics, 2004*, pp. 185-186, Oct. 2004, Karlsruhe, Germany.
- J.D. Baena, J. Bonache, F. Martín, R. Marqués, F. Falcone, T. Lopetegi, **M. Beruete**, M.A.G. Laso, J. García-García, F. Medina, M. Sorolla, "Modified and complementary split ring resonators for metasurface and metamaterial design", *Proceedings of the Bianisotropics 2004*, Sept. 2004, Ghent, Belgium.
- María Flores, Francisco Falcone, Ferran Martín, Jordi Bonache, Juan Baena, Txema Lopetegi, Miguel Angel Gomez Laso, **Miguel Beruete**, J.A. Marcotegui, Joan Garcia, Ricardo Marqués and Mario Sorolla, "Radiation phenomena in left-handed materials implemented in coplanar waveguide technology", *Proceedings of the International Symposium on Antennas and Propagation - ISAP'04*, pp. 465-468, Aug. 2004, Sendai, Japan.
- **M. Beruete**, M. Sorolla, I. Campillo, J. S. Dolado, L. Martín-Moreno, and F. J.

- García-Vidal, "Transmission in Cut-Off Hole Arrays", Proceedings of the *IEEE -Antennas and Propagation Society International Symposium*, pp. 1327-1330, Jun. 2004, Monterey (CA), USA.
- R. Marques, J. Baena, F. Martin, J. Bonache, F. Falcone, T. Lopetegi, **M. Beruete**, M. Sorolla, "Left-Handed Metamaterial Based on Dual Split Ring Resonators in Microstrip Technology", Proceedings of the *2004 URSI International Symposium on Electromagnetic Theory*, May. 2004, Pisa, Italy.
  - F. Falcone, F. Martin, J. Bonache, J. Baena, **M. Beruete**, T. Lopetegi, R. Marqués and M. Sorolla, "Application of Split Ring Resonator Particles in Planar Circuit Technology", Proceedings of the *27th ESA Antenna Technology Workshop on Innovative Periodic Antennas: Electromagnetic Bandgap, Left-handed Materials, Fractal and Frequency Selective Surfaces*, Santiago, Spain, March 2003.
  - **M. Beruete**, M. Sorolla, I. Campillo, J. S. Dolado, L. Martín-Moreno, and F. J. García-Vidal, "Enhanced Millimeter Wave Transmission Through Quasioptical Subwavelength Patterned Structures", Proceedings of the *Progress In Electromagnetics Research Symposium (PIERS 2004)*, pp. 595-598, Mar. 2004, Pisa, Italy.
  - **M. Beruete**, M. Sorolla, I. Campillo, J. S. Dolado, L. Martín-Moreno, and F. J. García-Vidal, "Enhanced Millimeter Wave Transmission Through Subwavelength Hole Arrays", Presented at the *Surface Plasmon Photonics Euro-Conference on Nano-Optics (EURESCO 2003)*, Sep. 2003, Granada, Spain.
  - I. Campillo, J. S. Dolado, **M. Beruete**, M. Sorolla, L. Martín- Moreno, and F. J. García- Vidal, "Highly Directional Transmission from a Single Subwavelength Slit Surrounded by Parallel Grooves in the Microwave Regime", Presented at the *Surface Plasmon Photonics Euro-Conference on Nano-Optics (EURESCO 2003)*, Sep. 2003, Granada, Spain.
  - Luis Martín-Moreno, F. J. García - Vidal, J. Pendry, T. Ebbesen, H. Lezec, M. Sorolla, **M. Beruete**, I. Campillo, J. S. Dolado, "Extraordinary Optical Properties of Nanostructured Metals", Presented at the *Donostia International Physics Center (DIPC) Workshop on Optical Properties of Complex Materials Over Different Length Scales*, Jul. 2003, San Sebastián, Spain.

## National Conferences:

- **M. Beruete**, F. Falcone, I. Campillo, M. Sorolla, "Guiado de ondas en arrays de agujeros apilados", Libro de Actas del *XXI Simposium Nacional de la Unión Científica Internacional de Radio, URSI 2006*, Sep. 2006, Oviedo.
- **M. Beruete**, I. Campillo, J. S. Dolado, J. E. Rodríguez-Seco, E. Perea, F. Falcone y M. Sorolla, "Antenas metálicas basadas en transmisión extraordinaria", Libro de Actas del *XXI Simposium Nacional de la Unión Científica Internacional de Radio, URSI 2006*, Sep. 2006, Oviedo.
- E. Jarauta, F. Falcone, **M. Beruete**, A. Marcotegui, M. Navarro, T. Lopetegi, M.A.G. Laso, "Duplexores y multiplexores basados en left-handed materials", Libro de Actas del *XXI Simposium Nacional de la Unión Científica Internacional de Radio, URSI 2006*, Sep. 2006, Oviedo.
- M. Navarro, F. Falcone, **M. Beruete**, E. Jarauta, M. Sorolla, "Comportamiento left-handed en una línea microstrip cargada con SSRR y EBG", Libro de Actas del *XXI Simposium Nacional de la Unión Científica Internacional de Radio, URSI 2006*, Sep. 2006, Oviedo.
- M. Navarro, F. Falcone, **M. Beruete**, E. Jarauta, M. Sorolla, "Estudio topológico de los Split Ring Resonators cargando una línea microstrip", Libro de Actas del *XXI Simposium Nacional de la Unión Científica Internacional de Radio, URSI 2006*, Sep. 2006, Oviedo.
- J. Illescas, E. Jarauta, F. Falcone, **M. Beruete**, J.A. Marcotegui, M. Sorolla, "Simulación de antenas planas broadband mediante la aplicación de elementos parásitos", Libro de Actas del *XXI Simposium Nacional de la Unión Científica Internacional de Radio, URSI 2006*, Sep. 2006, Oviedo.
- F. Falcone, F. Martín, J. Bonache, J. Baena, T. Lopetegi, M.A.G. Laso, J. García-García, **M. Beruete**, R. Marqués, M. Sorolla, "Estructuras metamateriales en tecnología plana basadas en partículas SRR y CSRR.", Libro de Actas del *XX Simposium Nacional de la Unión Científica Internacional de Radio, URSI 2005*, Sep. 2005, Gandía.
- **Miguel Beruete**, I. Campillo, J. S. Dolado, J.E. Rodríguez-Seco, E. Perea,

Francisco Falcone, Mario Sorolla, "Antena "Bull's-Eye" de Bajo Perfil Libro de Actas del XX *Simposium Nacional de la Unión Científica Internacional de Radio, URSI 2005*, Sep. 2005, Gandía.

- **M. Beruete**, M. Sorolla, I. Campillo, J. S. Dolado, "Transmisión total en arrays metálicos de agujeros en corte", Libro de Actas del XIX *Simposium Nacional de la Unión Científica Internacional de Radio, URSI 2004*, Sep. 2004, Barcelona.
- María Flores, Francisco Falcone, Juan Baena, Txema Lopetegi, **Miguel Beruete**, Miguel Angel Gomez Laso, J.A. Marcotegui, Jordi Bonache, Joan Garcia, Ferran Martin, Ricardo Marqués and Mario Sorolla, "Fenómenos de radiación en metamateriales basados en tecnología coplanar", Libro de Actas del XIX *Simposium Nacional de la Unión Científica Internacional de Radio, URSI 2004*, Sep. 2004, Barcelona.
- F. Falcone, F. Martín, J. Bonache, T. Lopetegi, M.A.G. Laso, M. Sorolla, **Miguel Beruete**, "Implementación de filtros paso bajo EBG de doble periodicidad en guía coplanar.", Libro de Actas del XVIII *Simposium Nacional de la Unión Científica Internacional de Radio, URSI 2003*, Sep. 2003, A Coruña.